Electronic transport in a type-II GaInAsSb/*p*-InAs heterojunction with different doping levels of the solid solution

T. I. Voronina, T. S. Lagunova, M. P. Mikhaĭlova, K. D. Moiseev, M. A. Sipovskaya, and Yu. P. Yakovlev

A. F. Ioffe Physicotechnical Institute, Russian Academy of Sciences, 194021 St. Petersburg, Russia
(Submitted September 27, 1996; accepted for publication October 25, 1996)
Fiz. Tekh. Poluprovodn. **31**, 897–901 (August 1997)

Galvanomagnetic phenomena and photoconductivity in broken-gap type-II GaInAsSb/*p*-InAs heterojunctions with different levels of doping of the solid solution with donor (Te) or acceptor (Zn) impurities have been investigated. It has been determined that in such structures an electronic channel, which determines the galvanomagnetic effects in a wide range of doping levels, is present at the heterojunction. A sharp decrease of the Hall mobility was observed in the experimental heterostructures with a high level of doping of the epitaxial layer with an acceptor impurity. The observed effect is due to exhaustion of the electronic channel as a result of carrier localization in potential wells at the heterojunction. © *1997 American Institute of Physics.* [S1063-7826(97)00108-7]

Quaternary solid solutions in the system Ga–In–As–Sb are of great interest for optoelectronic devices (lasers[1–3] and photodiodes[4,5]) in the spectral range 2–5 μm, which is important for problems of gas analysis and environmental protection.[6] The present work is a continuation of our series of investigations of the electric and photoelectric properties of the solid solutions GaInAsSb and heterojunctions based on epitaxial layers lattice-matched to GaSb and InAs substrates.[7,8]

We observed a high carrier mobility $\mu_H = 65000$ cm^2/(V·s) at $T = 77$ K (Ref. 9) in the isotypic isolated heterostructures *p*-$Ga_{0.83}In_{0.17}As_{0.22}Sb_{0.78}$/*p*-InAs with undoped layers of the solid solution, and we determined that an electronic channel exists at the heterojunction on the narrow-gap material side.[10] In Ref. 11 we determined the band diagram of a *p*-$Ga_{0.83}In_{0.17}As_{0.22}Sb_{0.78}$/*p*-InAs heterojunction and showed that such a heterojunction is a broken-gap type-II heterojunction.

The parameters of the self-consistent quantum wells, which are formed at the heterojunction in broken-gap type-II heterojunctions, and the properties of the electronic channel should depend to a large degree on the doping level of its constituent semiconductors. For this reason, we considered it important to study the effect of doping of the wide-gap solid solution *p*-$Ga_{0.83}In_{0.17}As_{0.22}Sb_{0.78}$/*p*-InAs ($E_g = 630$ meV at $T = 77$ K) with donor (Te) and acceptor (Zn) impurities on the magnetotransport and optical properties of isolated GaInAsSb/*p*-InAs heterostructures with a solid solution of the *p* as well as *n* type.

The solid-solution layers were grown on semi-insulating *p*-InAs (100) substrates ($p = 10^{16}$ cm^{-3}, $\sigma = 0.1$ $\Omega^{-1}\cdot$cm^{-1} at $T = 77$ K) by liquid-phase epitaxy. To grow the epitaxial layers, a fluxed solution was prepared from pure components In(99.99999%) and Sb(99.9999%) and from undoped weighed portions of GaSb and InAs with carrier density $p = 5\times10^{16}$ cm^{-3} and $n = 2\times10^{16}$ cm^{-3}, respectively. To dope the epitaxial layers with acceptor impurities, zinc was added to the fluxed solution in quantities up to 0.01 at. %, and tellurium in the form of the compound *n*-GaSb:Te with electron density $n = 5\times10^{17}$ cm^{-3} in quantities up to 0.001 at. % and in pure form above 0.001 at.% was used as the donor impurity.

The epitaxial layers ranged in thickness from 1.8 to 2.3 μm. The mismatch with the substrate was equal to $\Delta a/a < +4\times10^{-4}$ at $T = 300$ K. Rectangular samples for investigating the galvanomagnetic effects were cut from the epitaxial structures. Six indium contacts (two current and four potential) were deposited on the surface of the GaInAsSb epitaxial layers. In:Te alloy contacts were deposited on the *n*-type solid-solution layers and In:Zn contacts were deposited on the *p*-type layers. A compensation probe method was used to measure the voltage drop V_σ on the potential probes and the Hall emf V_H in the temperature range $T = 77-200$ K in magnetic fields up to 16 kOe with a current $I < 100$ μA (in the region where Ohm's law holds) flowing through the sample. The electrical conductivity $\sigma_\square$ and the Hall coefficient R_H per unit area and the Hall mobility $\mu_H = R_H\sigma_\square$ were calculated from these data. Investigations of the photoconductivity were conducted on an IKS-12 spectrometer using NaCl and LiF prisms and a synchronous-detection system. A constant electric field with a voltage not exceeding 510 V/cm was applied along the heterojunction. The signal obtained in a light-modulated flux from a globar was recorded.

The main parameters of the experimental samples are presented in Table I. The sign of the Hall voltage for all experimental samples always indicated electronic conductivity, irrespective of the type and quantity of dopant introduced into the melt with Te and Zn concentrations up to 0.01 at. % and 0.008 at. %, respectively. At the same time, the sign of the current carriers according to the thermo-emf measured with a thermal probe on the solid-solution side indicated hole conductivity in all samples except the strongly tellurium-doped samples (samples 3 and 7). This result attests to the fact that the conductivity of the GaInAsSb/*p*-InAs heterostructures with different levels of doping of the solid solution with donor and acceptor impurities, just as in heterostructures with an undoped solid solution, is determined mainly

TABLE I.

Sample No.	Impurity introduced: Type of impurity	Impurity introduced: Concentration, at. %	Sign of current carriers: According to thermo-emf in the solid solution	Sign of current carriers: According to Hall emf in the structure	R_H, 10^6 cm^2/C: H=kOe	R_H, 10^6 cm^2/C: H=10 kOe	μ_H, 10^3 cm^2/(V·s): H=2 kOe	μ_H, 10^3 cm^2/(V·s): H=10 kOe
1	–	–	*p*	*n*	4.5	4.3	65.0	64.0
2	Te	1×10^{-4}	*p*	*n*	4.45	3.85	57.4	55.0
3	Te	2×10^{-4}	*p*	*n*	4.0	3.35	52.8	44.8
4	Te	4×10^{-4}	*p*	*n*	4.1	3.0	46.6	34.5
5	Te	1×10^{-3}	*p*	*n*	3.25	1.6	45.0	18.6
6	Te	5.8×10^{-3}	*n*	*n*	0.19	0.1	11.4	6.2
7	Te	1.2×10^{-2}	*n*	*n*	0.1	0.05	11.8	5.6
8	Zn	3×10^{-3}	*p*	*n*	4.9	3.35	49.0	33.3
9	Zn	4×10^{-3}	*p*	*n*	2.7	2.4	24.4	19.8
10	Zn	8×10^{-3}	*p*	*n*	0.27	0.03	2.1	0.21

by the conductivity of the electronic channel on the heterojunction.[10] The Hall mobility, observed in heterostructures with solid-solution layers lightly doped with donor (Te <0.001 at. %) and acceptor (Zn <0.004 at.%) impurities (samples 2–5, 8, and 9 in Table I), remain just as high as in heterostructures with undoped solid-solution layers (sample 1). A decrease of the mobility was observed with higher levels of Te and Zn doping of the solid solution. The energy structures of the systems GaInAsSb/*p*-InAs for lightly and strongly tellurium- and zinc-doped solid solutions are shown schematically in Fig. 1.

Figures 2a and 2b (solid lines) display the dependence of the Hall mobility on the amount of impurity introduced into the melt for GaInAsSb/*p*-InAs heterostructures. The mobility remains nearly constant for heterostructures with lightly doped solid-solution layers (Te<0.001%, Zn <0.004 at. %). For a substantial level of tellurium doping of the solid solution (Te >0.001 at. %), the absolute value of the Hall mobility decreases by a factor of 4–5 to $\mu_H=10000$ cm^2/(V·s) at $H=2$ kOe. A sharp drop in the Hall mobility is observed with heavy doping with zinc (Zn >0.004 at. %): The Hall mobility drops by more than an order of magnitude (to 2000 cm^2/V/s at $H=2$ kOe), as compared with its values in heterostructures with undoped solid-solution layers. The figure also shows (dashed lines) for comparison the mobility versus the impurity density for solid solutions with the same composition but grown on GaSb substrates. A stepped type-II junction, whose boundary does not contain an electronic channel, is observed in such structures.[12] The measured mobility for such heterostructures characterizes the properties of the epitaxial layer of the GaInAsSb solid solution. The initial undoped samples of the solid solution GaInAsSb possessed *p*-type conductivity with hole density $p=10^{16}$ cm^{-3}and mobility $\mu_H=2000$ cm^2/(V·s). Tellurium doping of the solid solution resulted in overcompensation of the acceptors, and for Te concentration >0.001 at. % the material became *n*-type with mobility $\mu_H=4000-5000$ cm^2/(V·s). When the solid solution was doped with zinc, the acceptor concentration increased and the mobility dropped as a result of an increase in the scattering by impurity ions, and at high zinc concentrations (Zn >0.004 at. %) the mobility remained constant [$\mu_H=200$ cm^2/(V·s)], indicating that the hole gas is degenerate.[13]

As one can see in Fig. 2, the mobility in GaInAsSb/*p*-InAs heterostructures starts to decrease at locations where a transition to *n*-type conductivity is observed in the Te-doped solid solution (the Fermi level lies in the conduction band), and in the case of Zn doping this occurs at locations where the hole gas becomes degenerate (the Fermi level lies in the valence band).

In GaInAsSb/*p*-InAs heterostructures with a heavily doped solid solution, the mobility and Hall coefficient were

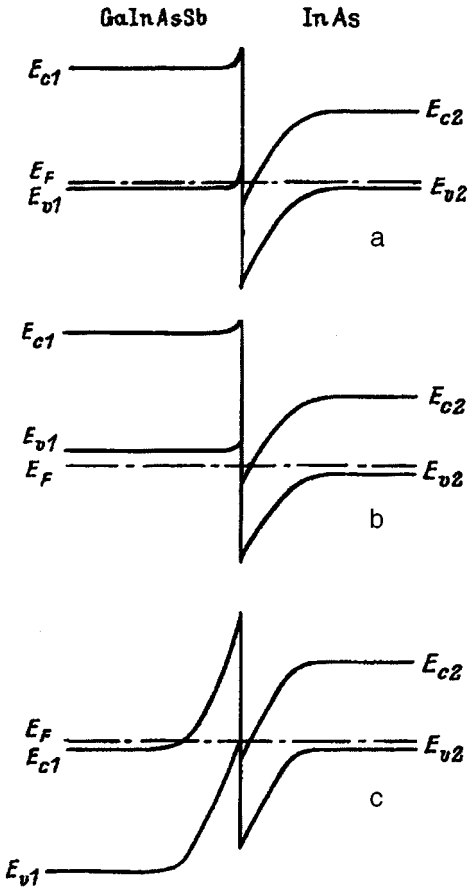

FIG. 1. Energy diagrams of a $Ga_{0.83}In_{0.17}As_{0.22}Sb_{0.78}$/*p*-InAs structure for solid solutions: a — Undoped, b — heavily doped with zinc, c — heavily doped with tellurium.

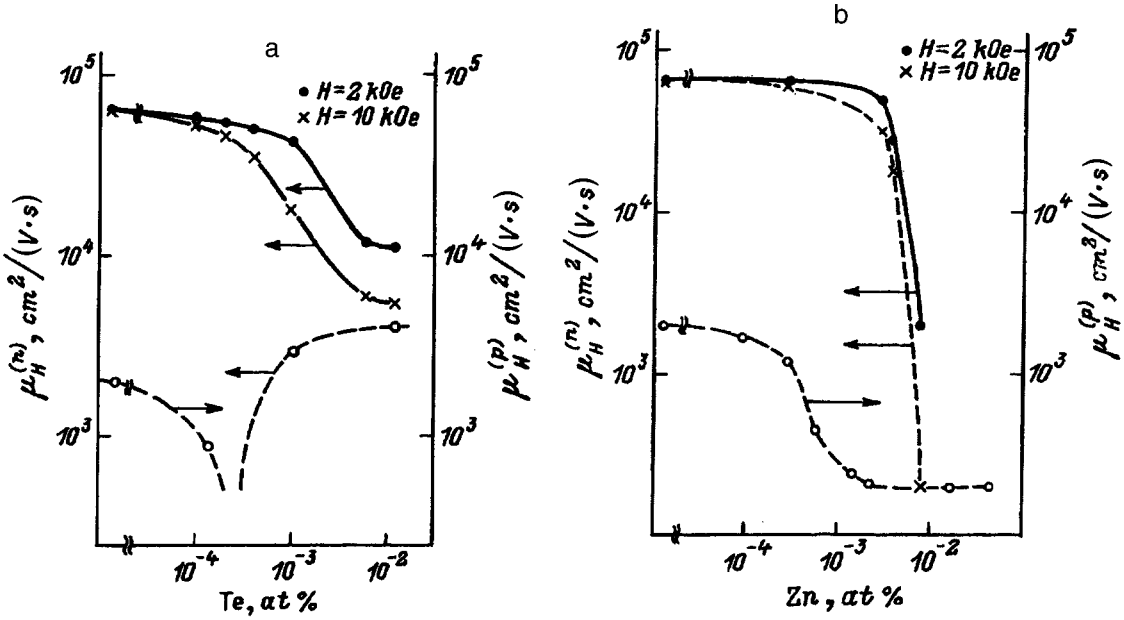

FIG. 2. Electron and hole Hall mobilities $\mu_H^{(n)}$ and $\mu_H^{(p)}$, respectively, versus the doping level of the solid solution: a — with tellurium, b — with zinc, $T=77$ K. Solid lines — GaInAsSb/*p*-InAs, dashed lines — GaInAsSb.

found to depend strongly on the magnetic field intensity; the dependence is different for Te- and Zn-doped samples (see Table I). Figure 3 shows the values of the Hall coefficient R_H as a function of the magnetic field intensity H in the GaInAsSb/*p*-InAs structures with different levels of doping of the solid solution. In samples with undoped and lightly Te- and Zn- doped solid-solution layers (samples 1–3 and 8) the Hall coefficient remains nearly constant as the magnetic field intensity increases. In the case of strong doping with Te (samples 6 and 7) the Hall coefficient for low values of H decreases with increasing magnetic field, and for $H>5$ kOe it no longer depends on the magnetic field intensity. The values of the mobility $\mu_H \approx 5000$ cm^2/(V·s) become comparable to the mobility of the epitaxial layer of the solid solution (see Fig. 3a). This attests to the fact that in samples with a heavily Te-doped epitaxial layer two types of current carriers are involved in conduction — high-mobility electrons in the channel [$\mu_H^{(n)} > 10000$ cm^2/(V·s)], which is manifested in weak magnetic fields, and electrons with a lower mobility [$\mu_H^{(n)} \approx 5000$ cm^2/(V·s)] in the epitaxial layer of the solid solution.

In the case of a heavily zinc-doped solid solution GaInAsSb (Zn concentration >0.005 at. %, sample 10) the de-

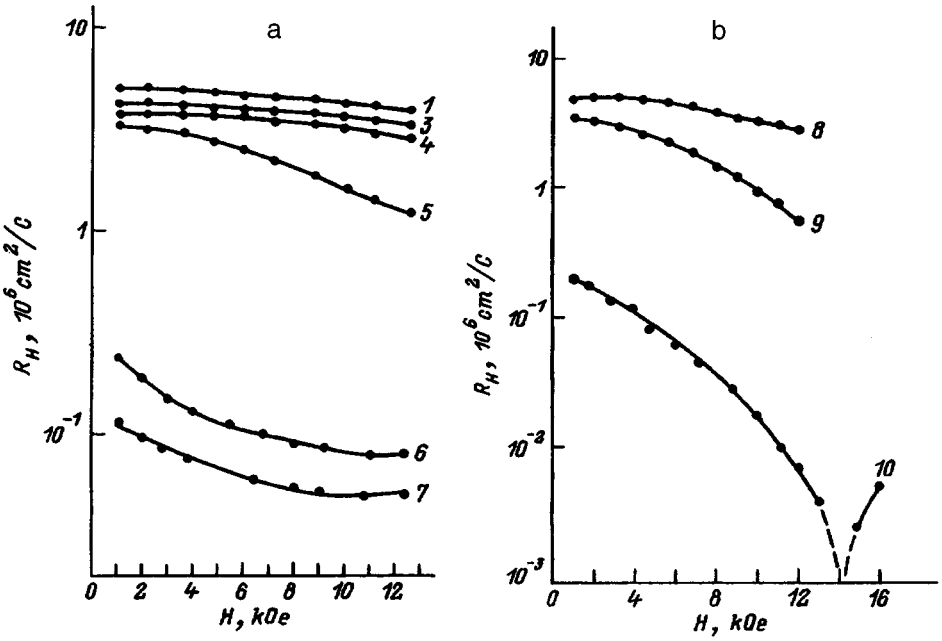

FIG. 3. Hall coefficient R_H as a function of the magnetic field intensity H for samples doped with tellurium (a) and zinc (b). The numbers on the curves correspond to the numbers of the samples in Table I.

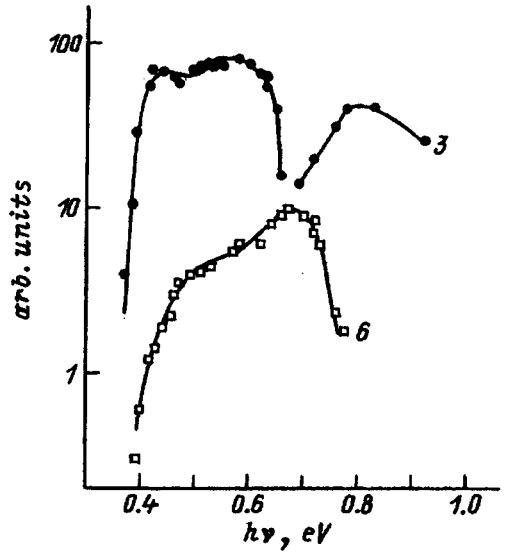

FIG. 4. Spectral dependences of the photoconductivity in GaInAsSb/*p*-InAs structures with a different level of tellurium doping of the solid solution. The numbers on the curves correspond to the numbers of the samples in Table I.

crease in R_H is so large that the sign of the Hall coefficient was found to change for certain values of the magnetic field ($H \approx 15$ kOe). This field dependence of R_H in the entire doping interval of the solid-solution layers is also characteristic of the simultaneous participation in the conductivity of the heterostructure of two types of current carriers, which differ not only in mobility but also in sign. The hole-type conductivity is due, in our opinion, not to a strong increase in the conductivity of the epitaxial layer, where the mobility is very low [200 cm/(V·s)], but rather to a decrease in the mobility in the electronic channel. Apparently, the drop in the mobility in the case of strong zinc doping could be due to the depletion of the electronic channel as a result of the localization of mobile carriers in the wells of the potential well at the heterojunction.[14]

The presence of an electronic channel at the broken-gap heterojunction and of two types of electrons with different mobilities in GaInAsSb/*p*-InAs structures should also be manifested in the photoelectric properties. Figure 4 shows the spectral dependences of the photoconductivity $\Delta\sigma = f(h\nu)$ at $T = 77$ K for two samples which differs in the tellurium-doping level of the solid solution. Aa one can see from Fig. 4, the photoresponse pattern depends strongly on the doping level. For light tellurium doping of the GaInAsSb epitaxial layer (sample 3) we observe, together with a positive photoconductivity, the appearance of a negative photoconductivity for $h\nu > 0.66$ eV. As the tellurium-doping level increases to 0.005 at. % (sample 6), only positive photoconductivity is observed. The dropoff of the long-wavelength edge in all cases corresponds to a photon energy equal to the band gap in InAs at $T = 77$ K ($h\nu_{(1/2)\max} = 0.40 - 0.41$ eV). The obtained spectral dependences of the photoconductivity reflect the contribution of the high-conductivity electronic channel at the heterojunction to the total signal. When a crystal absorbs photons with energy $h\nu > E_c - E_F$, where E_c is the position of the conduction-band bottom of the GaInAsSb solid solution and E_F is the Fermi level, electrons are excited from the electronic channel and are transferred into the wide-gap layer, where their mobility is much lower. As a result of electron transfer into the wide-gap GaInAsSb semiconductor layer, the conductivity of the layer increases and the total photoconductivity is determined by the expression

$$\Delta\sigma = -e\mu_f n_f + e\mu_{2d}(\Delta n_f + \Delta n_{2d}),$$

where μ_{2d} and μ_f are the electron mobility in the channel and in the GaInAsSb layer, Δn_{2d} is the illumination-induced change in the electron density in the channel, and Δn_f is the change occurring in the electron density in the wide gap layer of the solid solution for photon energy $h\nu$ corresponding to interband transitions in the wide gap GaInAsSb layer. Depending on the ratios of the contributions from both terms in this expression, either an increase or a decrease in the photoconductivity signal, right up to the appearance of negative photoconductivity (NPC), can be observed. Since NPC is observed in sample 3 in the entire experimental spectral interval $h\nu > 0.66$ eV, it can be assumed that recombination processes in the electronic channel make the determining contribution to the photoconductivity of the sample. We note that NPC due to the presence of two types of electrons with different mobility has been observed before in GaAlAs/GaAs heterojunctions.[15] The results obtained from an investigation of the photoelectric properties of broken-gap GaInAsSb/InAs heterojunctions supplement the data from galvanomagnetic investigations and are in agreement with our notion that a high-mobility electronic channel strongly affects the properties of the experimental heterostructures.

In summary, our investigation of electronic transport in GaInAsSb/*p*-InAs heterostructures has established that when wide-gap GaInAsSb solid solutions are grown on *p*-InAs substrates, an electronic channel is formed at the heterojunction and the channel remains in a wide range of levels of doping of the epitaxial layer with both donor (Te) and acceptor (Zn) impurities. It was shown that in an isolated $Ga_{0.83}In_{0.17}As_{0.22}Sb_{0.78}$/*p*-InAs heterostructure with a high level of doping of the solid solution with a donor impurity, the galvanomagnetic effects are due to the total contribution of the electronic channel at the heterojunction and epitaxial layer. The sharp mobility drop occurring with heavy doping of a quaternary solid solution with an acceptor impurity is due to the depletion of the electronic channel at the heteroboundary as a result of carrier localization in the potential wells at the heteroboundary and the mutual compensating effect of electrons and holes in the heterojunction itself.

We thank A. M. Monakhov for helpful discussions and valuable remarks. This work was supported, in part, by the Russian Fund for Fundamental Research under grant 96-02-17841a.

[1] A. N. Baranov, B. E. Dzhurtanov, A. N. Imenkov, A. A. Rogachev, Yu. M. Shernyakov, and Yu. P. Yakovlev, Fiz. Tekh. Poluprovodn. **20**, 2217 (1986) [Sov. Phys. Semicond. **20**, 1385 (1986)].
[2] H. K. Choi, S. L. Eglash, and G. W. Turner, Appl. Phys. Lett. **64**, 2474 (1994).
[3] M. P. Mikhaĭlova, G. G. Zegrya, K. D. Moiseev, O. G. Ergakov, and Yu.

P. Yakovlev, Pis'ma Zh. Tekh. Fiz. **21**, 83 (1995) [Tech. Phys. Lett. **21**, 482 (1995)].
[4] Yu. P. Yakovlev, A. N. Baranov, A. N. Imenkov, and M. P. Mikhailova, SPIE **1510**, 120 (1991).
[5] I. A. Andreev, A. N. Baranov, M. P. Mikhaĭlova, K. D. Moiseev, A. V. Pentrsov, Yu. P. Smorchkova, V. V. Sherstnev, and Yu. P. Yakovlev, Pis'ma Zh. Tekh. Fiz. **18**, 50 (1992) [Sov. Tech. Phys. Lett. **18**, 630 (1992)].
[6] A. M. Prokhorov and A. I. Nadezinskiy, SPIE **1724**, 2 (1992).
[7] M. P. Mikhailova and A. N. Titkov, Semicond. Sci. Technol. **9**, 1279 (1994).
[8] T. I. Voronina, T. S. Lagunova, M. P. Mikhaĭlova, M. A. Sipovskaya, V. V. Sherstnev, and Yu. P. Yakovlev, Fiz. Tekh. Poluprovodn. **25**, 276 (1991) [Sov. Phys. Semicond. **25**, 167 (1991)].
[9] T. I. Voronina, T. S. Lagunova, M. P. Mikhaĭlova, K. D. Moiseev, and Yu.P. Yakovlev, Fiz. Tekh. Poluprovodn. **30**, 985 (1996) [Semiconductors **30**, 523 (1996)].
[10] T. I. Voronina, T. S. Lagunova, M. P. Mikhaĭlova, K. D. Moiseev, S. A. Obukhov, A. V. Anikundinov, A. N. Titkov, and Yu. P. Yakovlev in *Abstracts of Reports at the 2nd Russian Conference on Semiconductor Physics* [in Russian], St. Peterssburg, 1996, Vol. 2, p. 158.
[11] M. P. Mikhaĭlova, I. A. Andreev, T. I. Voronina, T. S. Lagunova, K. D. Moiseev, and Yu. P. Yakovlev, Fiz. Tekh. Poluprovodn. **29**, 678 (1995) [Semiconductors **29**, 353 (1995)].
[12] A. N. Baranov, A. N. Imenkov, M. P. Mikhailova, A. A. Rogachev, and Yu. P. Yakovlev, Superlat. Microstruct., **8**, 375 (1990).
[13] T. I. Voronina, B. E. Dzhurtanov, T. S. Lagunova, and Yu. P. Yakovleva, Fiz. Tekh. Poluprovodn. **25**, 283 (1991) [Sov. Phys. Semicond. **25**, 171 (1991)].
[14] C. A. Hoffman, J. R. Meyer, E. R. Youngdall, F. J. Bartoli, R. H. Miles, and L. R. Ram Mohan, Solid−State Electron. **37**, 1203 (1994).
[15] I. M. Grodnenskiĭ, K. V. Starostin, and D. V. Galchenkov, JETP Lett. **43**, 70 (1986).

Translated by M. E. Alferieff

Formation of InGaAs/GaAs nanostructures by submonolayer deposition from molecular beams

G. É. Tsyrlin, V. N. Petrov, V. G. Dubrovskiĭ, N. K. Polyakov, S. Ya. Tipisev, and A. O. Golubok

Institute of Analytical Instrument Building, Russian Academy of Sciences, St. Petersburg, Russia

N. N. Ledentsov

A. F. Ioffe Physicotechnical Institute, Russian Academy of Sciences, 194021 St. Petersburg, Russia
(Submitted October 25, 1996; accepted for publication October 31, 1996)
Fiz. Tekh. Poluprovodn. **31**, 902–907 (August 1997)

The morphological characteristics of an ensemble of nanosize objects InGaAs/GaAs on the singular and vicinal GaAs(100) surfaces have been investigated by means of scanning tunneling microscopy. Different modifications of molecular-beam epitaxy were used to produce the nanostructures. It was determined that both the growth kinetics and a deliberate disorientation of the surface strongly affect surface morphology. © *1997 American Institute of Physics.* [S1063-7826(97)00208-1]

INTRODUCTION

The study of self-organization is one of the main directions in modern fundamental and applied surface physics. For example, nanostructure formation as a result of self-organization of semiconductor surfaces is now under active investigation.[1–5] Self-organization of nanostructures on semiconductor surfaces during heteroepitaxial growth in lattice-mismatched systems is due to the relaxation of elastic stresses in the volume and on the surface. Quantum dots and quantum wires, in which charge-carrier motion is limited in three or two directions, exhibit unique optical properties,[6,7] and they open up ways to develop a new generation of optoelectronic devices.[8,9] The observation of ultranarrow cathodoluminescence lines indicates unequivocally an electronic density of states with a delta-function-like spectrum.[6] The progress made in the theory of nanostructure formation,[10,11] the observation of ordering of quantum-size formations on surfaces in the InGaAs/GaAs system[12,13] and the possibility of ''adjusting,'' by varying the technological conditions of growth (substrate temperature, growth rate, and flux ratio) in the molecular-beam epitaxy (MBE) method[10,14] the characteristic dimensions of nanostructures as well as the disorientation of the substrate surface,[8,15,16] promise production of quantum-size structures with prescribed geometric properties. An additional parameter that can be used to control nanostructure sizes is variation of the growth modes (submonolayer MBE and atomic-layerwise MBE) for growing layers that undergo a phase transition during Stronski–Krastanov growth. In the present study we investigated by scanning tunneling microscopy (STM) the morphological characteristics of an ensemble of InGaAs/GaAs quantum dots, obtained on singular and vicinal GaAs(100) surfaces by different modifications of the MBE method.

1. EXPERIMENT

Growth experiments were conducted on GaAs(100) substrates (singular samples) and GaAs(100) substrates, whose surface was disoriented by 3° and 7° in the [011] direction (vicinal samples), in the EP 1203 system. The method of pregrowth chemical preparation of the plate surfaces is described in Ref. 17 . To investigate the effect of substrate disorientation on surface morphology we glued the singular and vicinal samples, with the aid of indium, on the same molybdenum holder in a manner so as to reduce to a minimum the nonuniformity of the temperature field of the heater that heats the sample and the flux gradients at the surface.

After the oxide layer was removed in the growth chamber at substrate temperature $T_s = 610-630\ ^\circ\mathrm{C}$ in an As_4 flow, a 0.25-μm-thick GaAs buffer layer was grown by the standard molecular-beam epitaxy method while maintaining the (2×4) surface reconstruction and $T_s = 550\ ^\circ\mathrm{C}$. The buffer layer was doped with beryllium to a density $\sim 10^{16}$ cm^3 so as to make sure that the tunneling current is trapped. Then the surface was investigated by scanning tunneling microscopy.

After a buffer layer was grown, the temperature of the sample in the arsenic flow was decreased to $T_s = 470\ ^\circ\mathrm{C}$ [the moment at which the (2×4) surface reconstruction was changed to $c(4\times4)$]. The arsenic pressure in the growth chamber with the arsenic shutter open was maintained constant at a level of 4×10^{-6} Pa in all experiments.

The $In_xGa_{1-x}As$ layers were grown in submonolayer epitaxial growth regimes. The time dependences of the positions of the shutters of the In, Ga, and As molecular sources are shown schematically in Fig. 1. The following growth modes were used: submonolayer MBE (SMBE)[18] (Fig. 1a for InAs and Fig. 1b for $In_xGa_{1-x}As$), submonolayer migration-stimulated epitaxy (SMSE)[19] (Fig. 1c for InAs and Fig. 1d for $In_xGa_{1-x}As$), atomic-layerwise MBE (ALMBE)[20] (Fig. 1e), and (or) combinations of these modes. In each case three monolayers (MLs) of either indium arsenide or the solid solution $In_xGa_{1-x}As$ were deposited. After completion of growth, the heater heating the sample was immediately removed from the sample-holder zone.

The state of the surface was monitored *in situ* by RHEED. The RHEED system included a high-sensitivity video camera, a VCR for recording the dynamics of the

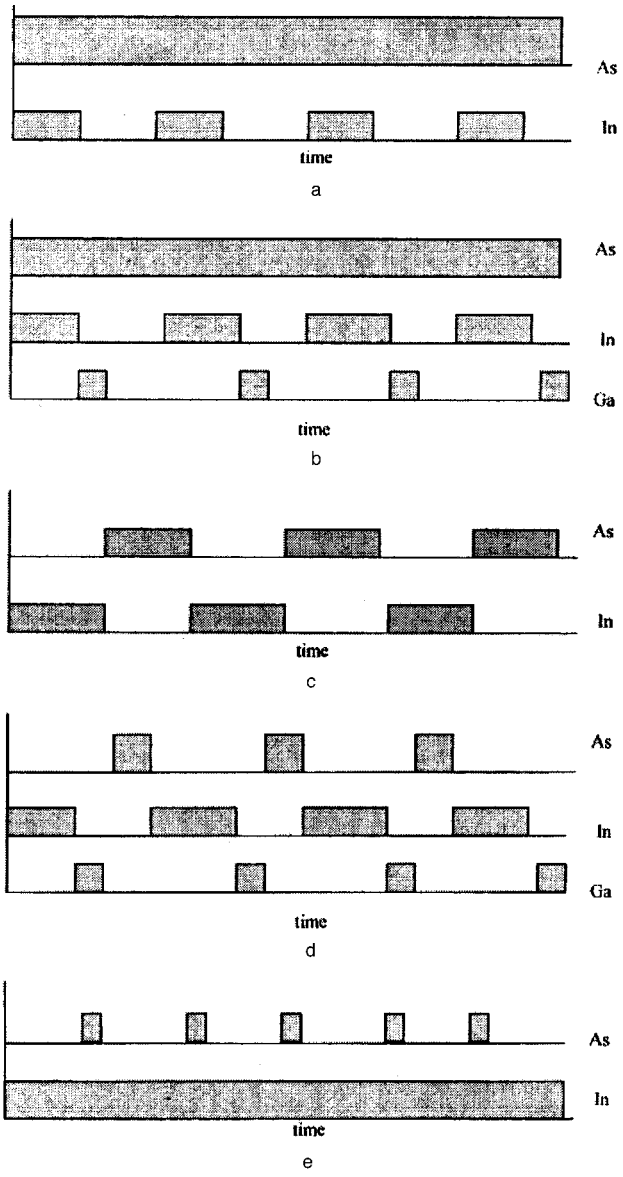

FIG. 1. Time dependences of the shutter positions for SMBE InAs (a) and InGaAs (b), SMSE InAs (c) and InGaAs (d) and ALMBE (e). Shading corresponds to an open-shutter state and no shading corresponds to a closed-shutter state.

RHEED patterns during growth, a computer for processing the recorded information, and an interface for coupling the video camera with the VCR and the computer, and software making it possible to analyze the RHEED patterns in real-time.[21] The GaAs and InAs growth rates were gauged by measuring the oscillations of the intensity of the mirror reflection in the RHEED pattern. The GaAs and InAs growth rates in the course of the experiments were constant and equal to 0.5 and 0.1 monolayers per second, respectively.

The surface morphology of the samples was investigated *ex situ* with a scanning tunneling microscope; the measurement procedures and conditions are described in Refs. 13 and 16 . Reproducible and stable STM images were obtained from different sections of the experimental samples. To conduct prolonged STM measurements, the samples were placed in vacuum oil to protect the surface from oxidation in air. Such shielding made it possible to obtain reproducible STM images in the course of one month after the samples were removed from the vacuum chamber.

2. RESULTS AND DISCUSSION

The experimental samples, enumerated according to their technological parameters and their basic geometric characteristics, are presented in Table I.

The STM images for samples 1 and 2 ($In_xGa_{1-x}As$, SMBE and SMSE technologies) are shown in Figs. 2a and 2b, respectively. One can see from the figure that different growth methods yield qualitatively different surface morphology. Both relatively large ($\sim$15 nm) and small ($\sim$6 nm) quantum dots, which are not clearly separated (i.e., the islands are partially merged), are observed in the case of SMBE. In the case of SMSE growth the quantum dots are separated laterally, they are characterized by a high surface density, and their size dispersion is relatively small.

Figure 3 shows STM images for samples 3–5, respectively (InAs, SMSE growth). As the RHEED data show, as a result of the large lattice mismatch, quantum dots in our case form with a thinner deposited layer than for samples 1 and 2. The presence of well-separated, isotropically-arranged quantum dots is characteristic of the singular surface (Fig. 3a). Predominantly isotropic distribution is also characteristic of the vicinal surfaces, but as the disorientation angle increases, their density increases, while the lateral dimensions remain the same or decrease (Fig. 3b and 3c).

Previous investigations showed that growth kinetics, including that at the initial stage, strongly influences surface

TABLE I. List of experimental samples and their technological parameters and geometric characteristics.

Sample No.	Growth mode	Vicinality	Lateral dimensions, nm	Surface density, cm^{-2}	Composition
1	SMBE	No	6–15	–	$In_{0.66}Ga_{0.33}As$
2	SMSE	No	10	1.5×10^{11}	$In_{0.66}Ga_{0.33}As$
3	SMSE	No	18	1.1×10^{11}	InAs
4	SMSE	3°	19	0.7×10^{11}	InAs
5	SMSE	7°	10	1.3×10^{11}	InAs
6	MBE+SMBE	No	–	–	InAs
7	MBE+SMBE	3°	–	–	InAs
8	MBE+SMBE	7°	14	1.4×10^{11}	InAs
9	ALMBE+SMBE	3°	–	–	InAs
10	ALMBE+SMBE	7°	–	–	InAs

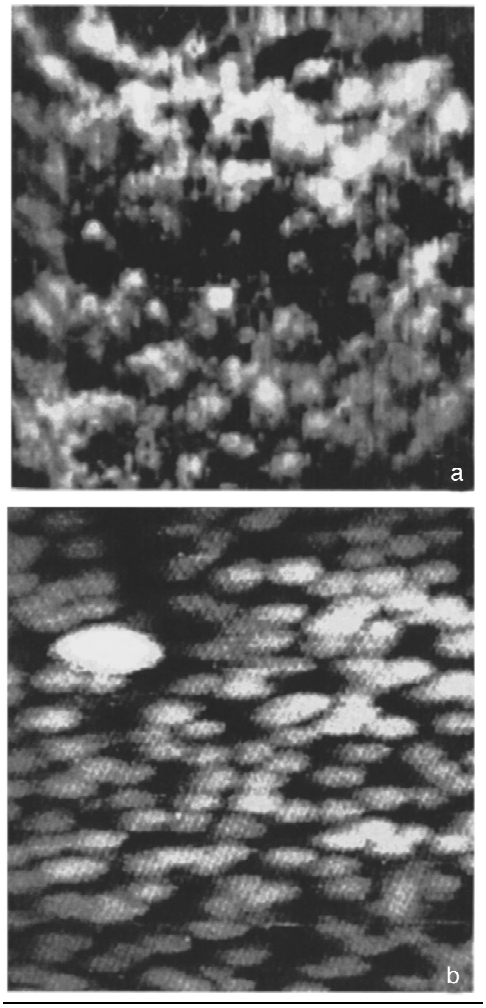

FIG. 2. STM images of sections of a surface after deposition of three $In_{0.66}Ga_{0.33}As$ monolayers on GaAs(100) by SMBE (a) and SMSE (b). The scanning area is 400 nm × 400 nm for both cases. The edges of the images are parallel to the [011] and [011] directions.

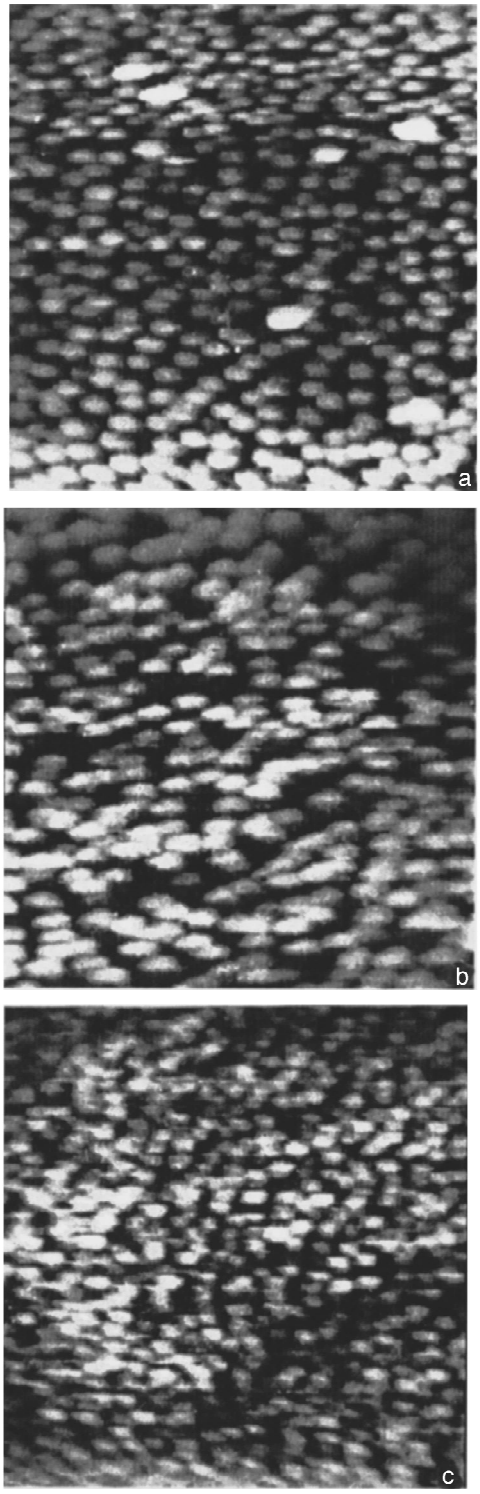

FIG. 3. STM images of sections of a surface after deposition of three InAs monolayers on GaAs(100) during SMSE. a — Singular surface, b — 3° disorientation, c — 7° disorientation. The scan area is 600 nm × 600 nm for all cases. The edges of the images are parallel to the [011] and [011] directions.

morphology. To investigate the effect of the growth modes on the surface morphology, we varied the growth procedure at the initial stage, i.e., during the formation of the first 1.5 InAs monolayers. The traditional MBE and atomic-layerwise MBE were used. The remaining 1.5 monolayers were deposited with the SMBE mode. Figure 4 shows the STM images for samples 6–8, respectively. For the singular and slightly disoriented sample, a mesoscopic structure with a low density of quantum dots is observed on the surface. As the disorientation angle increases, an ensemble of quantum dots arranged in a primitive two-dimensional lattice with vectors along the [001] and [010] directions is formed. When the ALMBE method is used at the initial stage, merging of quantum dots into conglomerates is observed on the vicinal samples (Figs. 5a and 5b, samples 9 and 10, respectively), regardless of the degree of surface disorientation.

Our results attest to a strong effect of growth kinetics and surface disorientation on the morphology of InGaAs/GaAs (100) layers. Previous results concerning the dependence of the structural and optical properties of quantum-well structures in the MBE method on the pressure of the group-V component[14] confirm that the growth kinetics influences the resulting surface morphology. According to our data, SMSE methods give an ensemble of quantum dots with a higher density and a smaller lateral-size dispersion than with other technologies. This effect can apparently be explained by a more rapid accumulation of stress in the hetero-

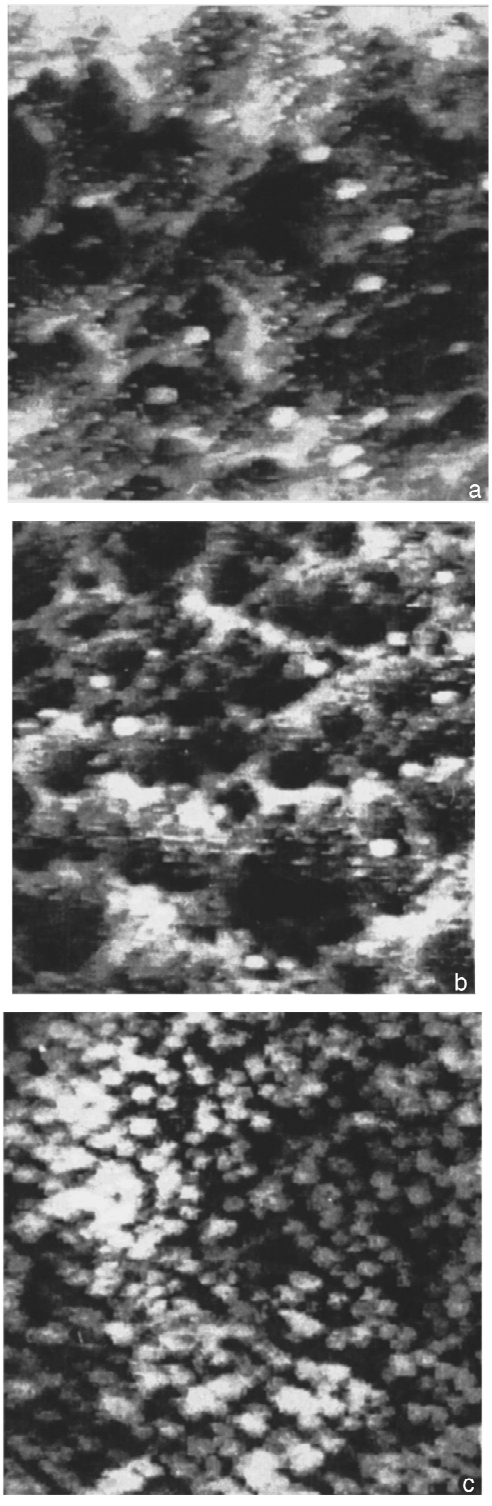

FIG. 4. STM images of sections of a surface after deposition of three InAs monolayers on GaAs(100) by MBE + SMBE. a — Singular surface, b — 3° disorientation, c — 7° disorientation. The scan area is 900 nm × 900 nm for all cases. The edges of the images are parallel to the [011] and [011] directions.

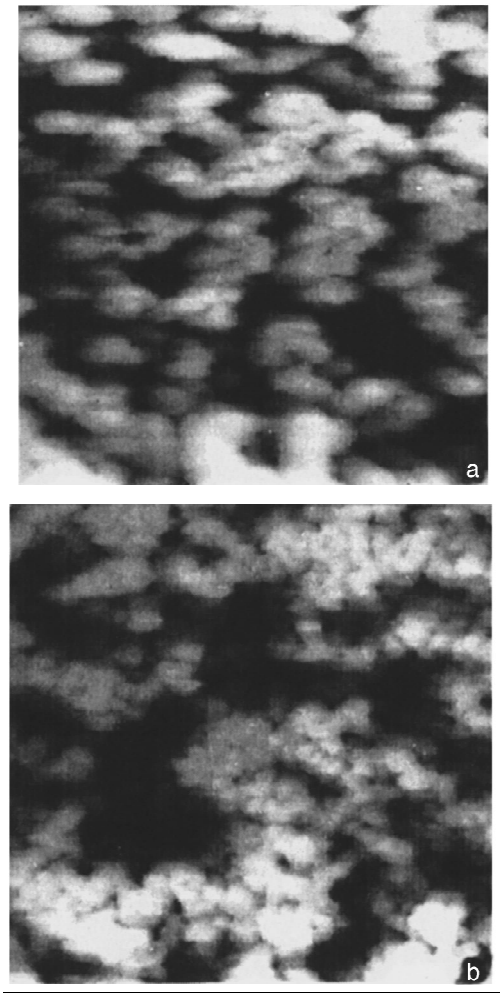

FIG. 5. STM images of sections of a surface after deposition of three InAs monolayers on GaAs(100) by ALMBE + SMBE. a — 3° disorientation, b — 7° disorientation. The scan area is 900 nm × 900 nm for all cases. The edges of the images are parallel to the [011] and [011] directions.

structure, sufficient for the layer to break up into three-dimensional formations under the action of elastic stresses. This in turn accounts for the fact that the thickness of the pseudomorphic layer is less than the thickness obtained with other methods of simultaneous deposition of group-V and -III elements. The effect of the vicinality of the surface on the morphology of the nanostructures is attributable to the additional mechanism of relaxation of elastic stresses as a result of the presence of a collection of monomolecular steps on the surface. In individual cases, their high density can result in a qualitative change in the surface morphology as compared with a singular or slightly disoriented surface, especially in the case of a ''thicker'' pseudomorphous layer (Fig. 4a–4c).

In summary, we have investigated some submonolayer technological methods for producing self-organized ensembles of quantum dots in the heteroepitaxial system InGaAs/GaAs. Our results show unequivocally that the kinetic parameters influence the structural properties of quantum-well formations. The disorientation of the surface also influences the surface morphology, which changes the growth mechanisms in certain cases.

This work was supported, in part, by the Russian Fund for Fundamental Research under grant No. 95-02-05084-a, the INTAS fund under Grant No. 94-1028, and the Scientific Program ''Physics of solid-state nanostructures.''

[1] V. I. Marchenko, Zh. Éksp. Teor. Fiz. **81**, 1141 (1981) [Sov. Phys. JETP **54**, 605 (1981)].
[2] Y.-W. Mo, B. S. Swartzentruber, R. Kariotis, M. B. Webb, and M. G. Lagally, Phys. Rev. Lett. **63**, 2393 (1989).
[3] I. Goldstein, F. Glas, J. Y. Marzin, M. N. Charasse, and G. Le Roux, Appl. Phys. Lett. **47**, 1099 (1985).
[4] R. Nözel, N. N. Ledentsov, L. Däweritz, M. Hohenstein, and K. Ploog K, Phys. Rev. Lett. **67**, 3812 (1991).
[5] J. Tersoff and R. M. Tromp, Phys. Rev. Lett. **70**, 2782 (1993).
[6] M. Grundmann, J. Christen, N. N. Ledentsov, J. Böhrer, D. Bimberg, S. S. Ruvimov, P. Werner, U. Richter, U. Gösele, J. Heydenriech, M. V. Ustinov, A. Yu. Egorov, A. E. Zhukov, P. S. Kop'ev, and Zh. I. Alferov, Phys. Rev. Lett. **74**, 4043 (1995).
[7] R. Leon and S. Fafard, D. Leonard, J. I. Merz, P. M. Petroff. Phys. Rev. B **50**, 11 687 (1994).
[8] N. Kirstaedter, N. N. Ledentsov, M. Grundmann, D. Bimberg, V. M. Ustinov, S. S. Ruvimov, M. V. Maximov, P. S. Kop'ev, Zh. I. Alferov, U. Richter, P. Werner, U. Gösele, and J. Heydenreich, Electron. Lett. **30**, 1416 (1994).
[9] D. S. I. Mui, D. Leonard, L. A. Coldren, and P. M. Petroff, Appl. Phys. Lett. **66**, 1620 (1995).
[10] V. A. Shchukin, N. N. Ledentsov, P. S. Kop'ev, and D. Bimberg, Phys. Rev. Lett. **75**, 2968 (1995).
[11] C. Priester and M. Lanoo, Phys. Rev. Lett. **75**, 93 (1995).
[12] N. N. Ledentsov, M. Grundmann, N. Kirstaedter, J. Christen, R. Heitz, J. Böhrer, F. Heinrichsdorff, D. Bimberg, S. S. Ruvimov, P. Werner, U. Richter, U. Gösele, J. Heydenreich, V. M. Ustinov, A. Yu. Egorov, M. V. Maximov, P. S. Kop'ev, and Zh. I. Alferov, in *Proceedings of the 22nd International Conference on Physics of Semiconductors, Vancouver, Canada, 1994*, edited by D. J. Lookwood, World Scientific, Singapore, 1995, vol. 3, p. 1855.
[13] G. E. Cirlin, G. M. Guryanov, A. O. Golubok, S. Ya. Tipissev, N. N. Ledentsov, P. S. Kop'ev, M. Grundmann, and D. Bimberg, Appl. Phys. Lett. **67**, 97 (1995).
[14] N. N. Ledentsov, M. Grundmann, N. Kirstaedter, O. Schmidt, R. Heitz, J. Böhrer, D. Bimberg, V. M. Ustinov, V. A. Shchukin, A. Yu. Egorov, A. E. Zhukov, S. Zaitsev, P. S. Kop'ev, Zh. I. Alferov, S. S. Ruvimov, A. O. Kosogov, P. Werner, U. Gösele, and J. Heydenriech, Solid–State Electron. **40**, 785 (1996).
[15] N. N. Ledentsov, M. V. Maksimov, G. É. Tsyrlin, V. N. Petrov, and G. M. Gur'yanov, Fiz. Tekh. Poluprovodn. **29**, 1295 (1995) [Semiconductors **29**, 671 (1995)].
[16] G. M. Guryanov, G. E. Cirlin, V. N. Petrov, N. K. Polyakov, A. O. Golubok, S. Ya. Tipissev, E. P. Musikhina, V. B. Gubanov, Yu. B. Samsonenko, and N. N. Ledentsov, Surf. Sci. **331–333**, 414 (1995).
[17] G. M. Gur'yanov, N. N. Ledentsov, V. N. Petrov, Yu. B. Samsonenko, G. É. Tsyrlin, and A. G. Filaretov, Pis'ma Zh. Tekh. Fiz. **19**(18), 64 (1993) [Sov. Tech. Phys. Lett. **19**, 591 (1993)].
[18] P. D. Wang, N. N. Ledentsov, C. M. Sotomayor Torres, P. S. Kop'ev, and V. M. Ustinov, Appl. Phys. Lett. **64**, 1526 (1994).
[19] G. É. Tsyrlin, A. O. Golubok, S. Ya. Tipisev, N. N. Ledentsov, and G. M. Gur'yanov, Fiz. Tekh. Poluprovodn. **29**, 1697 (1995) [Semiconductors **29**, 884 (1995)].
[20] Y. Gonzalez, L. Gonzalez, and F. Briones, J. Cryst. Growth. **111**, 120 (1991).
[21] G. M. Gur'yanov, V. N. Demidov, N. P. Korneeva, and G. É. Tsyrlin, Prib. Tekh. Éksp., No. 3, 167 (1996).

Translated by M. E. Alferieff

Two sources of excitation of photoluminescence of porous silicon

N. E. Korsunskaya, T. V. Torchinskaya,[a)] B. R. Dzhumaev, L. Yu. Khomenkova, and B. M. Bulakh

Institute of Semiconductor Physics National Academy of Sciences, 252650 Kiev, Ukraine
(Submitted August 7, 1996; accepted for publication November 14, 1996)
Fiz. Tekh. Poluprovodn. **31**, 908–911 (August 1997)

The change occurring in the photoluminescence spectra and the photoluminescence excitation spectra during aging of porous-silicon samples in air and in vacuum has been investigated. It was found that the character of the photoluminescence changes occurring during aging depends on the wavelength of the exciting light: In the case of excitation in the visible-range band of the luminescence excitation spectrum ($\lambda_{exc}>490$ nm) the photoluminescence decreases and in the case of excitation in the ultraviolet band it predominantly increases. It is shown that the two bands of the luminescence excitation spectrum (visible and ultraviolet) correspond to two different objects on the surface of the porous layer. © *1997 American Institute of Physics.* [S1063-7826(97)00308-6]

It is well known[1] that the photoluminescence (PL) intensity and spectrum of as-grown samples of porous silicon (PS) change in time (aging process). Investigation of this process evidently can yield useful information about an, as yet, unresolved question concerning the nature of the luminescence of porous silicon.

There are a number of studies on aging processes.[1–4] In these studies, the PL intensity (W), as a rule, was observed to decrease. This decrease was attributed either to the desorption of hydrogen[5] or SiH, SiH_2, and SiH_3 complexes[1,6,7] or to oxidation.[8] It was explained by two factors. One factor is an increase in the density of fast recombination centers (dangling silicon bonds), which form on desorption,[7] and the second factor is destruction of the luminescing material on the surface of silicon filaments, whose components are the desorbing complexes.[6] It has also been reported that the PL intensity increases with time.[9,10]

In the present paper we show that the character of the change occurring in the PL intensity during aging depends on the wavelength of the exciting light. On the basis of an investigation of the PL spectra, the luminescence excitation spectra (LES), and the changes occurring in the spectra when the PS samples are exposed to air or held in vacuum it is concluded that there exist two different objects with which the excitation of the PL of porous silicon is associated.

1. RESULTS

The experimental samples were prepared by anodic etching of *p*-Si plates ($\rho=5-10\ \Omega\cdot$cm) in an alcohol solution of HF with current densities (I_{etc}) of 50 and 200 mA/cm^2. The process of aging of the samples prepared in identical etch regimes was conducted at room temperature either in air or in vacuum (10^{-8} Torr). The PL was excited by light from a xenon lamp through a MDR-23 monochromator or light from a nitrogen laser ($\lambda_{exc}=337$ nm).

The typical PL spectra of as-grown samples measured with excitation by light from the xenon lamp ($\lambda_{exc}=490$ nm) and by light from the nitrogen laser, are shown in Fig. 1. We note that the intensities of the nitrogen-laser radiation which were employed did not appreciably influence the rate of change of the PL intensity. As one can see from the figure, the position of the PL-band maximum lies in the range 650–720 nm and, as a rule, the position in the case of excitation by light from the lamp is different from the position in the case of laser excitation.

The luminescence excitation spectra (LES) consist of two components — a visible component, which consists of a structural maximum in the region 400–550 nm, whose position can vary somewhat from sample to sample, and an ultraviolet (UV) component, which is represented by a section of increasing intensity in the region 400–350 nm (Fig. 2). The position of the PL-band maximum depends on the wavelength of the exciting light. As the latter wavelength decreases, the PL-band maxima shifts to shorter wavelengths, in agreement with the data in Fig. 1.

It should be noted that the PL-intensity ratio between UV and visible range excitation can vary from sample to sample, and that it depends on the conditions under which they are obtained. For example, for an etch current $I_{etc}=20$ mA/cm^2 there is virtually no excitation of visible-range PL.

The LES undergo transformation during aging: For sufficiently long aging times, the intensity of the visible band (primarily its long-wavelength wing) decreases substantially and the intensity of the ultraviolet wing increases (Fig. 2). Accordingly, the PL intensity decreases during aging in the case of long-wavelength excitation ($\lambda_{exc}>490$ nm) and it varies nonmonotonically for excitation at shorter wavelengths: The decreasing intensity is followed by its increase (Fig. 3). Figure 4 shows curves of the relative changes in the PL intensity $[(W_n-W_0)/W_0]$ versus the wavelength of the exciting light at different stages of the aging process. Evidently, the amplitude of the decrease in the PL intensity at first increases with increasing wavelength of the exciting light and then stops changing (for $\lambda_{exc}>490$ nm). This is most clearly seen at the initial stage of aging, when the PL intensity predominantly decreases. The amplitude of the increase in the PL intensity increases as λ_{exc} shifts in the short-wavelength direction. For $\lambda_{exc}=337$ nm the decrease in the PL intensity is, as a rule, very small. In a sample with no

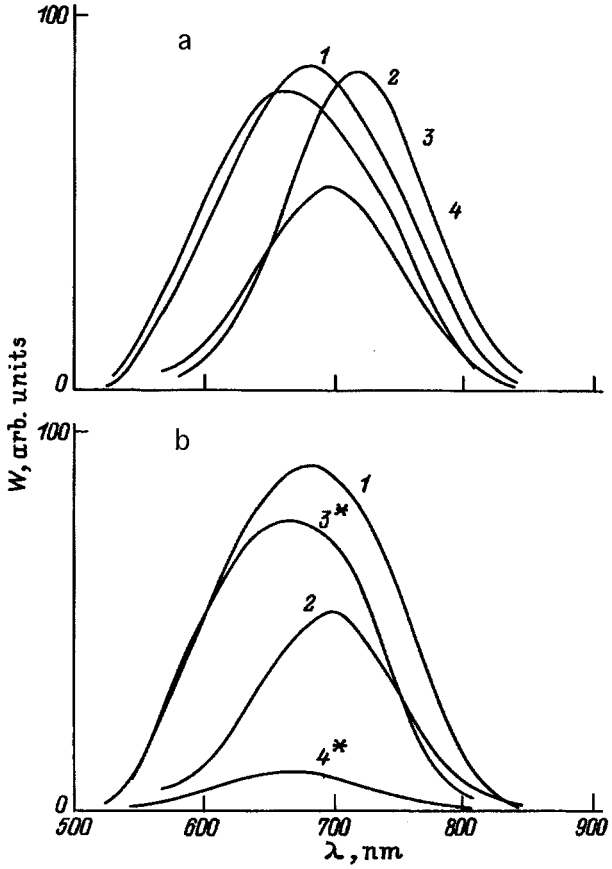

FIG. 1. PL spectra of PS samples stored in air (a) and in vacuum (b). The spectra were measured immediately after preparation (*1* and *2*), 7 days later (*3* and *4*), and 10 days later (*3** and *4**). The luminescence was excited with radiation with $\lambda_{exc}=490$ nm (curves *2*, *4* and *4**) and $\lambda_{exc}=337$ nm (curves *1*, *3*, and *3**) ($I_{etc}=50$ mA/cm^2).

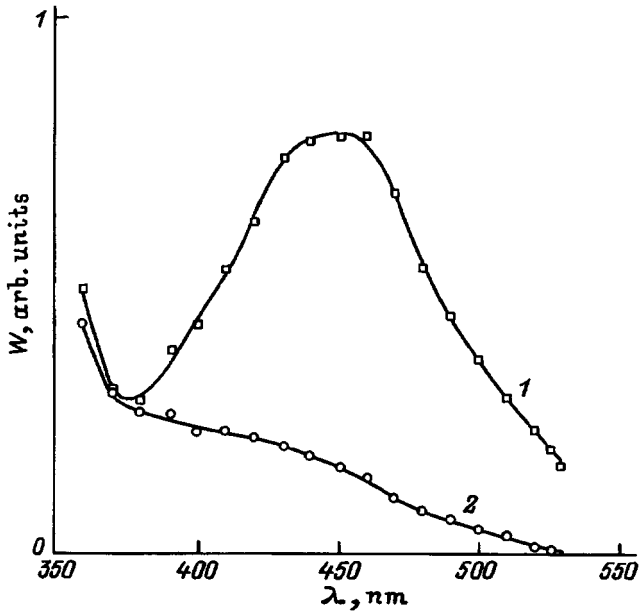

FIG. 2. Luminescence excitation spectra of a PS sample immediately after preparation (*1*) and 7 days laters (*2*) ($I_{etc}=50$ mA/cm^2).

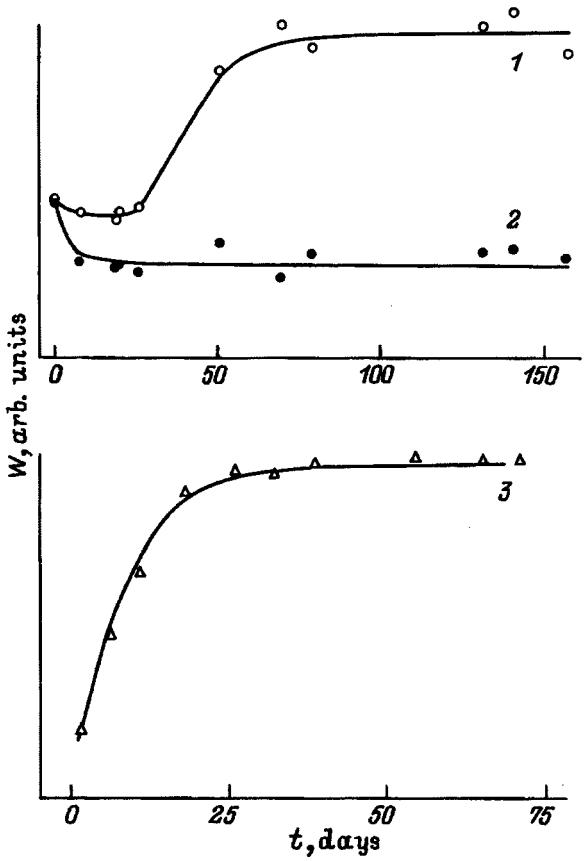

FIG. 3. PL intensity versus aging time in air for samples prepared under different conditions: *1*, *2* — $I_{etc}=50$ mA/cm^2; *1* — $\lambda_{exc}=490$ nm, *2* — $\lambda_{exc}=337$ nm, *3* — $I_{etc}=200$ mA/cm^2, $\lambda_{exc}=337$ nm.

visible-range SEL band ($I_{etc}=200$ mA/cm^2), only an increase in the PL intensity is observed (Fig. 3).

As the PL intensity increases in the case of visible-range excitation, the position of the band maximum generally shifts to shorter wavelengths (Fig. 1). The UV-excited PL band becomes narrower as a result of a decrease in the intensity of the long-wavelength wing. As the PL intensity increases, the position of the band for UV-range excitation shifts very little in the long-wavelength direction, so that with time the positions of the PL-band maxima with visible- and UV-range excitations come closer to each other.

When the samples are stored in vacuum, the PL intensity was observed to decrease, but not increase (Fig. 1b).

If a sample is exposed to air after being stored in vacuum, the PL intensity remains nearly constant in the case of excitation by light with $\lambda_{exc}>490$ nm and increases with time in the case of UV-range excitation.

2. DISCUSSION

As follows from the data presented above, only a decrease of the PL intensity is observed in the case of excitation by light with $\lambda_{exc}>490$ nm. At the same time, in samples where only UV excitation is present, the PL intensity only increases. This enables us to conclude that the drop of the PL intensity corresponds to a visible SEL band and an increase corresponds to an ultraviolet band. The nonmono-

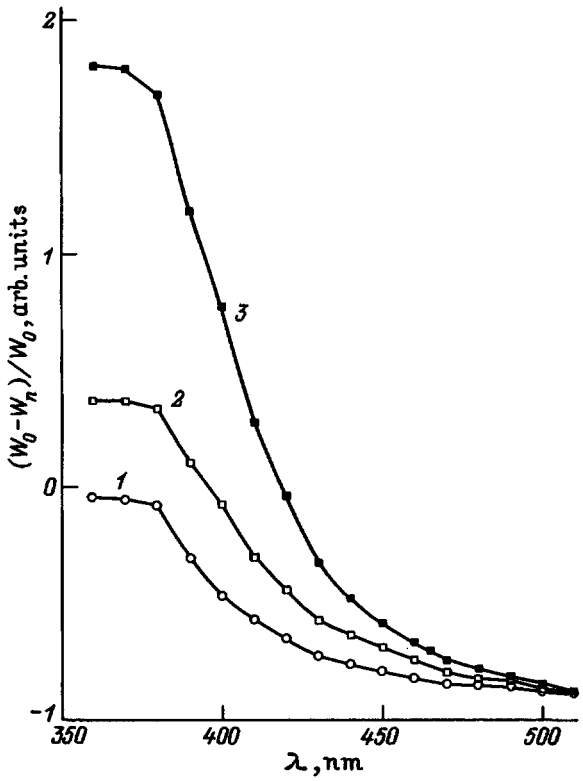

FIG. 4. Relative changes $(W_n-W_0)/W_0$ in the PL intensity versus wavelength of the exciting light at different stages of the etching process: *1* — $\Delta t=7$ days, *2* — $\Delta t=40$ days, *3* — $\Delta t=60$ days ($I_{\text{etc}}=50$ mA/cm^2).

tonic character of the changes in the region $\lambda_{\text{exc}}<490$ nm is explained by overlapping of these bands. As one can see from the dependence of the magnitude of the relative changes in the PL intensity on the wavelength of the exciting light (Fig. 4), the amplitude of the drop in the PL intensity in the region $\lambda_{\text{exc}}>490$ nm does not change. Therefore, it can be assumed that in this region there is no overlapping of the UV and visible SEL bands.

Some conclusions about the nature of the increase and decrease of the PL intensity can be drawn from a comparison of the character of the changes in the PL intensity in air and in vacuum.

The absence of an increase in the PL intensity in the case of excitation by UV light in vacuum and the large increase in the PL intensity in air before and after the samples are stored in vacuum show that this growth is due to an oxidation process. The fact that the quantity of oxide increases during aging is also confirmed by the results of secondary-ion mass spectrometry (SIMS),[11] which likewise shows that the oxide, just as the luminescence, is localized predominantly in a region of thickness ~ 500 nm near the surface of the porous layer. When this layer is removed by an argon beam, the intensity of the UV-excited PL decreases substantially,[11] and the PL intensity increases when the sample is subsequently held in air.

The decrease in the PL intensity can be attributed to desorption, as is ordinarily assumed.[1,5,6] This assumption is in agreement with the corresponding changes occurring in the PL intensity when as-grown samples are stored in air and in vacuum. It is also in agreement with the absence of an increase in intensity when the samples are exposed to air after being held in vacuum. Therefore, two different processes, which influence the PL intensity, occur simultaneously during aging — desorption and oxidation.

The data presented above also attest to the fact that the two SEL bands of porous silicon are associated with two different objects. Indeed, the desorption process results in a decrease of intensity or vanishing of the visible SEL band, which is then not restored with time. At the same time, with UV excitation, the PL intensity changes very little with desorption and then increases with time in air. The different temporal behavior of the PL intensity in the case of visible- and UV-range excitations signifies that the decrease in the PL intensity cannot be explained solely by an increase in the concentration of dangling silicon bonds, as is ordinarily assumed.[7] This process is apparently also associated with the vanishing of absorption centers, which give rise to the visible SEL band of the PL-exciting light. The fact that visible-range excitation is not restored after desorption or aging of the surface layer of PS by an argon-ion beam suggests that the object with which the visible-range SEL band is associated is a component of the etchant or a reaction product. The object responsible for the UV excitation of the PL of PS is apparently an oxide.

As the PL intensity decreases, the density of luminescence centers can, in principle, decrease as well. The dependence of the position of the PL-band maximum on the wavelength of the exciting light attests to its nonelementary nature; this is confirmed by data from Refs. 12 and 13. Therefore, it is logical to assume that the PL is due to a superposition of two bands, one of which is excited in the visible-range SEL band and the other in the ultraviolet band. In this case the dependence of the position of the PL-band maximum on λ_{exc}, just as the nonmonotonic dependence of the PL intensity on the aging time, can be explained by overlapping of the SEL bands. Therefore, it is possible that each object is associated with its own luminescence band. This result is also in agreement with the narrowing of the IV-excited PL band in the process of aging; this can be explained by the decrease in the contribution of the band excited by the visible light.

It follows, however, that a number of factors suggest that the superposition of these two bands is not the only reason for the displacement of the PL maximum during aging. Indeed, a displacement of the PL maximum also occurs, though it is smaller, when there is no overlapping of the SEL bands (for example, in the absence of a visible-range excitation band). This shift could be due, for example, to a desorption-induced change in the electric field at the surface. The data in Refs. 14 and 15 , where a displacement of the PL-band maximum to shorter wavelengths was observed when a negative potential was applied to the sample, attest to this possibility.

Further investigations are required in order to determine finally the nature of the desorbing object and its role in PL processes.

In closing, we wish to make one additional remark concerning the difference in the excitation spectra of the PL that

was observed in different studies.[6,16–21] The results presented above explain this difference, since the form of the SEL was found to depend on the sample preparation technology and on the time elapsed after sample preparation (Fig. 2).

[a)]Electronic-mail: torch@opto.kiev.ua; fax: (044)-265-8344

[1] Y. M. Weng, Zh. N. Fan, and X. F. Zong, Appl. Phys. Lett. **63**, 168 (1993).
[2] R. T. Collins, M. A. Tischler, and J. H. Stathis, Appl. Phys. Lett. **61**, 1649 (1992).
[3] M. A. Tischler, R. T. Collins, J. H. Stathis, and J. C. Tsang, Appl. Phys. Lett. **60**, 639 (1992).
[4] M. S. Brandt, H. D. Fuchs, M. Stuzmann, J. Weber, and M. Cardona, Solid State Commun. **81**, 307 (1992).
[5] B. A. Khan, R. Pinker, Kh. Shahzad, and B. Rossi, Mater. Res. Soc. Symp. Proc. **256**, 143 (1992).
[6] C. Tsai, K. H. Li, D. S. Kinosky, R. Z. Qian, T. C. Hsu, and J. T. Irby, Appl. Phys. Lett. **60**, 1700 (1992).
[7] N. H. Zoubir, M. Vergnat, and Ph. de Donato, Appl. Phys. Lett. **65**, 82 (1994).
[8] A. Bsiesy, J. C. Vial, F. Gaspard, R. Herino, M. Legion, F. Muller, R. Romestain, A. Wasiela, A. Halimaoui, and G. Bomchil, Surf. Sci. **254**, 195 (1991).
[9] P. D. Stevens and R. Glosser, Appl. Phys. Lett. **63**, 803 (1993).
[10] Y. Xiao, M. J. Heben, J. M. McCullough, Y. S. Tsuo, J. I. Pankove, and S. K. Deb, Appl. Phys. Lett. **62**, 1152 (1993).
[11] N. E. Korsunskaya, T. V. Torchinskaya, B. R. Dzhumaev, B. M. Bulakh, O. D. Smiyan, A. L. Kapitanchuk, and S. O. Antonov, Fiz. Tekh. Poluprovodn. **30**, 7 (1996) [Semiconductors **30**, 792 (1996)].
[12] K. L. Harasimhan, S. Banerje, A. K. Srivastava, and A. Sardesai, Appl. Phys. Lett. **62**, 331 (1993).
[13] S. Liu, C. Palsule, S. Yi, and S. Gangopadhyay, Phys. Rev. B **49**, 10 318 (1994).
[14] A. Bsiesy, F. Muller, I. Mihalcescu, M. Ligeon, F. Gaspard, R. Herino, R. Romestain, and J. C. Vial, J. Luminecs. **57**, 29 (1993).
[15] H. Koyama, T. Oguro, and N. Koshida, Appl. Phys. Lett. **62**, 3177 (1993).
[16] Y. Kanemitsu, T. Matsumoto, T. Futagi, and H. Mimura, Jpn. J. Appl. Phys. **32**, 411 (1993).
[17] H. Aoyagi, A. Motohashi, A. Kinoshita, T. Anoto, and A. Satou, Jpn. J. Appl. Phys. **32**, L1 (1993).
[18] T. Motohiro, T. Kachi, F. Miura, Y. Takeda, J. Hyodo, and S. Noda, Jpn. J. Appl. Phys. **31**, L207 (1992).
[19] I. A. Buyanova, S. S. Ostapenko, and M. K. Sheĭnkman, Fiz. Tekh. Poluprovodn. **20**, 1791 (1986) [Sov. Phys. Semicond. **20**, 1123 (1986)].
[20] A. N. Starukhin, A. A. Lebedev, B. S. Razbirin, and L. M. Kapitonov, Pis'ma Zh. Tekh. Fiz. **18**, 60 (1992) [Sov. Tech. Phys. Lett. **18**, 23 (1992)].
[21] I. A. Buyanova, E. I. Oborina, and S. S. Ostapenko, Semicond. Sci. Techn. **4**, 797 (1989).

Translated by M. E. Alferieff

Luminescence properties of InAs/GaAs quantum dots prepared by submonolayer migration-stimulated epitaxy

G. É. Tsyrlin and V. N. Petrov

Institute of Analytical Instrument Building, Russian Academy of Sciences, 198103 St. Petersburg, Russia

M. V. Maksimov and N. N. Ledentsov

A. F. Ioffe Physicotechnical Institute, Russian Academy of Sciences 194021 St. Petersburg, Russia
(Submitted November 12, 1996; accepted for publication November 14, 1996)
Fiz. Tekh. Poluprovodn. **31**, 912–915 (August 1997)

The results of an investigation of the luminescence properties of an ensemble of InAs quantum dots, obtained by submonolayer migration-stimulated epitaxy on singular and vicinal GaAs(100) surfaces, are reported. The largest width at half-height of the photoluminescence line is observed in samples with a 3° disorientation, indicating that the size-variance of the quantum dots is largest in this case. Quasiequilibrium quantum dots are formed either with a long sample holding time in an arsenic flow or with a larger quantity of deposited indium. © *1997 American Institute of Physics.* [S1063-7826(97)00408-0]

1. INTRODUCTION

Self-organization effects on a semiconductor surface, which lead to the spontaneous formation of an ensemble of ordered nanosize islands, are being actively investigated fundamentally and from the point of view of application. It has been shown theoretically that the use of quantum-well structures, in which the motion of charge carriers is limited in two (quantum wires) and three (quantum dots) directions, greatly improves the performance of semiconductor devices.[1] In the case of an InAs/GaAs semiconductor system, an array of quantum dots can be obtained when indium arsenide deposited on the gallium arsenide substrate directly during molecular-beam epitaxy (MBE) reaches a critical thickness.[2–7] This effect is explained by the relaxation of elastic stresses which arise during growth in a lattice-mismatched heteroepitaxial system in accordance with the Stronski–Krastanov mechanism. A semiconductor laser, whose active region includes an array of InGaAs/GaAs quantum dots obtained by submonolayer MBE (SMBE), has recently been constructed.

It is known that both the growth kinetics and surface vicinality influence the structural properties of an ensemble of quantum dots.[9–12] It has been shown that quantum dots with a lateral-size variance of 10% can be obtained by submonolayer migration-stimulated epitaxy (SMSE).[13] This paper reports the results of an experimental study of the luminescence properties of an ensemble of quantum dots obtained on singular and vicinal GaAs(100) surfaces by SMSE.

2. EXPERIMENT

The growth experiments were performed in an ÉP1203 MBE system on singular semi-insulating GaAs(100) substrates and on the same substrates disoriented by 3° and 7° in the [011] direction. Three samples (singular and two vicinal), chemically treated by the method described in Ref. 14 , were glued with the aid of indium on the same molybdenum holder in a manner so as to reduce to a minimum the nonuniformity of the temperature profile of the heater that heats the sample and the flux gradients at the surface. After the oxide layer was removed, a 300-nm-thick GaAs buffer layer with $T_s = 630$ °C was grown in an As flow in the growth chamber. In our case this temperature corresponds to the moment of the transition from (2×4) to (3×1) surface re-

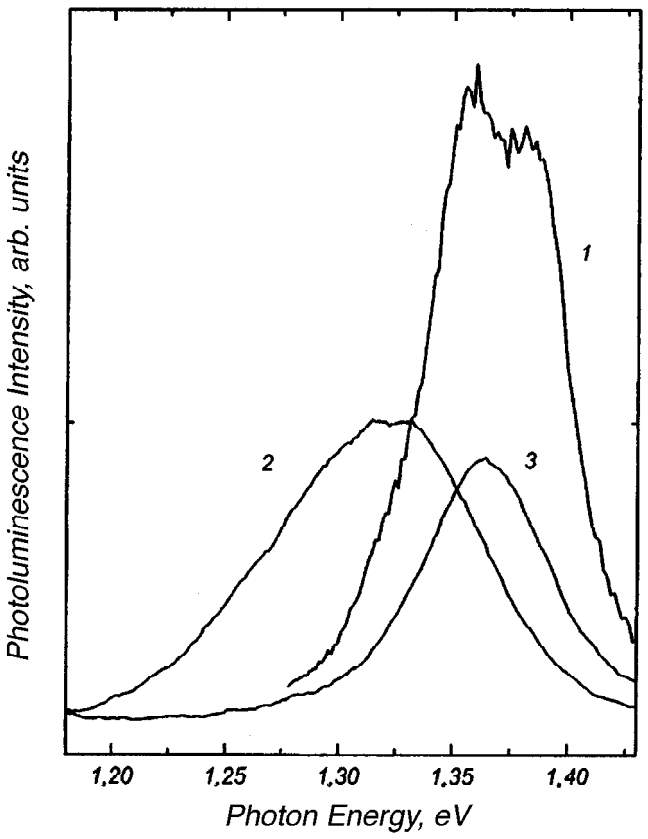

FIG. 1. Photoluminescence spectra for SMSE-grown InAs quantum dots. The nominal thickness is two monolayers and the holding time between cycles is 2 s. *1* — Singular sample; *2* — sample disoriented by 3°; *3* — sample disoriented by 7°.

 1063-7826/97/080777-04$10.00

construction and was chosen so as to improve the electrical and optical parameters of the layers.[15] After the buffer layer, a superlattice consisting of five pairs of GaAs/$Al_{0.25}Ga_{0.75}As$ (20 Å/20 Å) layers was grown so as to prevent the diffusion and drift of nonequilibrium carriers into the semi-insulating substrate with a high density of deep impurities (Cr). Next, a 70-Å-thick GaAs layer was grown and the temperature of the sample in the arsenic flux was lowered to T_s=470 °C [the moment of the transition from (2×4) to (2×2) surface recombination]. The active layer was grown by submonolayer migration-stimulated epitaxy, in which indium was deposited (in the absence of an arsenic flow) in the amount required for a 0.5 monolayer of InAs. It was held in an arsenic flow for 2–30 s (the time τ). The total nominal InAs thickness was equal to two or three monolayers (four or six deposition cycles). After growth of the active layer was completed, a 70-Å-thick GaAs layer was grown at the same temperature. Next, the substrate temperature T_s was set to 630 °C and a 70-Å-thick GaAs layer was grown. A superlattice consisting of five pairs of GaAs/$Al_{0.25}Ga_{0.75}As$ (20 Å/20 Å) layers was then grown so as to prevent any effect from surface recombination. During the growth of the superlattices, after each GaAs layer, the sample surface was held in an As flow for 20 s. The arsenic pressure in the growth chamber was maintained constant at 4×10^{-6} Pa in all experiments. The values of the precalibrated Ga, Al, and In flows were set so that the GaAs, AlGaAs, and InAs growth rates would correspond to 0.53, 0.68, and 0.1 monolayers/s. The growth rates were measured with a system for observing oscillations of the RHEED mirror reflection[16] with a primary beam energy of 12.5 keV, which corresponded to the anti-Bragg diffraction condition.

The photoluminescence (PL) spectra were excited with an argon laser. The excitation density was equal to 1 W/cm^2. The observation temperature was equal to 77 K.

3. RESULTS

The PL spectra from structures with a nominal InAs thickness of two monolayers and a holding time of 2 s in arsenic flow are shown in Fig. 1. In the case of a singular sample the spectrum contains two peaks, which we attribute to the nonequilibrium sizes of the quantum formations at the initial stage of formation of elastically strained islands. This effect is not observed in the case of disoriented samples, where monatomic steps on the substrate surface additionally influence the quantum-dot formation process. As the disorientation angle increases, the PL line shifts into the short-wavelength region (1.32 and 1.36 eV, respectively) with the radiation intensity remaining virtually unchanged. The total width at half-maximum of the PL line decreases from 100 to

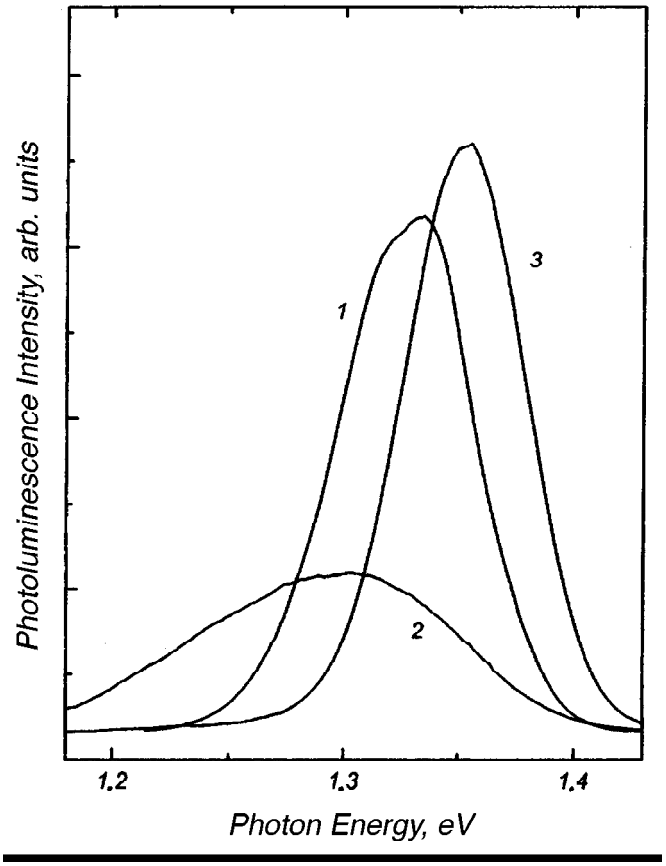

FIG. 2. Photoluminescence spectra for SMSE-grown InAs quantum dots. The nominal thickness is two monolayers and the holding time between cycles is 30 s. *1* — Singular sample; *2* — sample disoriented by 3°; *3* — sample disoriented by 7°.

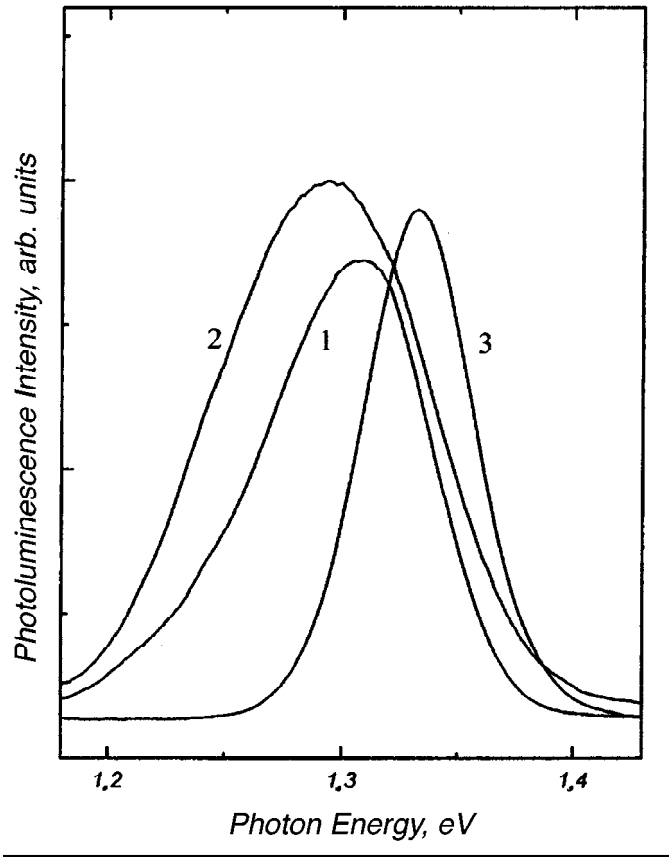

FIG. 3. Photoluminescence spectra for SMSE-grown InAs quantum dots. The nominal thickness is three monolayers and the holding time between cycles is 2 s. *1* — Singular sample; *2* — sample disoriented by 3°; *3* — sample disoriented by 7°.

TABLE I.

Sample No.	InAs layer thickness, ML	τ, s	Disorientation, deg 5	Position of the PL peak from quantum dots, eV	PL-line width at half-maximum, meV	PL intensity, arb. units
1	2	2	0	–	76	0.29
2	2	2	3	1.323	101	0.10
3	2	2	7	1.362	63	0.09
4	2	30	0	1.329	69	0.94
5	2	30	3	1.298	128	0.29
6	2	30	7	1.349	62	1
7	3	2	0	1.305	83	0.48
8	3	2	3	1.291	108	0.56
9	3	2	7	1.344	54	0.51

60 meV for 3° and 7°, respectively. The last two facts show that for a strongly disoriented sample the dimensions and the size-variance decrease.

The PL spectra of samples whose surfaces were held in an arsenic flow for a longer time and which have the same amount of deposited indium are presented in Fig. 2. For all samples, the photoluminescence intensity is substantially higher (by a factor of 3–10) than the data presented in Fig. 1. This indicates that the density of quantum dots is sharply higher in this case. For all positions of the maxima of the PL lines, a shift is observed into the low-energy region (in the range from 1.30 to 1.35 eV); this corresponds to the case of an increase in the characteristic sizes of the quantum dots. The character of the change in the total width at half-maximum, depending on the vicinality of the substrate, remains the same as in the preceding case: The smallest change (60 meV) corresponds to a disorientation by 70°, while the largest value (128 meV) is observed with a disorientation of 3°.

The effect of disorientation of the substrate on the intensity, shape, and position of the maximum of the PL line in the case of quantum dots formed by the deposition of three InAs monolayers is demonstrated in Fig. 3. A characteristic feature of these spectra is that the PL intensity is practically the same and quite high for both singular and vicinal samples. The largest width at half-maximum of the PL line is observed, as before, for samples with a 3° surface disorientation. The positions of the maxima of the PL lines are virtually identical to the positions for samples with an average thickness equal to two InAs monolayers and $\tau = 30$ s. This apparently indicates that the SMSE-grown quantum dots possess quasiequilibrium dimensions in this case. This is also confirmed by our scanning tunneling microscopy (STM) investigations of similar unburied structures,[12,17] where the lateral dimensions of SMSE-grown quantum dots in the cases of deposition of two ($\tau = 30$ s) and three ($\tau = 2$ s) InAs/GaAs monolayers were virtually identical (10–20 nm, depending on the disorientation).

The optical characteristics of the investigation of SMSE-grown quantum dots are presented in Table I. The main conclusions that can be drawn from an analysis of the results are as follows. First, the largest width at half-maximum of the PL line is observed in samples disoriented by 3°; this indicates that the size-variance of the quantum dots is largest in this case. Second, quasiequilibrium quantum dots are obtained either with a long sample holding time in an arsenic flow or with a large amount of deposited indium. Third, a short-wavelength shift of the photoluminescence line compared with samples obtained by MBE and SMBE is observed. This shows that the SMSE method gives smaller quantum dots.[10] The PL-line width at half-maximum is usually smaller for SMSE than for SMBE or, in other words, less than the deviation from the average quantum-dot sizes for the technology under study. This is also confirmed by comparing the profile analysis of STM images for these methods.[11–13] Therefore, submonolayer migration-stimulated epitaxy technology holds promise for producing optoelectronic devices whose active region consists of an ensemble of quantum dots.

We wish to thank D. Bimberg, G. M. Gur'yanov, and V. G. Dubrovskiĭ for helpful discussions of the results. We also thank N. K. Polyakov, D. N. Demidov, and N. P. Korneev for assisting in the growth experiments.

This work was supported, in part, by the Russian Fund for Fundamental Research under Grant No. 95-02-05084-a, the INTAS Fund under Grant No. 94-1028, and the Scientific Program ''Physics of solid-state nanostructures.''

[1] Y. Arakawa and H. Sakaki, Appl. Phys. Lett. **40**, 635 (1982).
[2] L. Goldstein, F. Glas, J. Y. Marzin, M. N. Charasse, and G. Le Roux, Appl. Phys. Lett. **47**, 1099 (1985).
[3] M. Grundmann, J. Christen, N. N. Ledentsov, J. Böhrer, D. Bimberg, S. S. Ruvimov, P. Werner, U. Richter, U. Gösele, J. Heydenreich, V. M. Ustinov, A. Yu. Egorov, A. E. Zhukov, P. S. Kop'ev, and Zh. I. Alferov, Phys. Rev. Lett. **74**, 4043 (1995).
[4] R. Leon, S. Fafard, D. Leonard, J. I. Merz, and P. M. Petroff, Phys. Rev. B **50**, 11 687 (1994).
[5] D. S. I. Mui, D. Leonard, L. A. Colden, and P. M. Petroff, Appl. Phys. Lett. **66**, 1620 (1995).
[6] N. N. Ledentsov, M. Grundmann, N. Kirstaedter, J. Christen, R. Heitz, J. Böhrer, F. Heinrichsdoff, D. Bimberg, S. S. Ruvimov, P. Werner, U. Richter, U. Gösele, J. Heydenreich, V. M. Ustinov, A. Yu. Egorov, M. V. Maximov, P. S. Kop'ev, and Zh. I. Alferov, in *Proceedings of the 22nd International Conference on the Physics of Semiconductors*, Vancouver, Canada, 1994, edited by D. J. Lookwood, World Scientific, Singapore, 1995, Vol. 3, p. 1855.
[7] N. N. Ledentsov, M. Grundmann, N. Kirstaedter, O. Schmidt, R. Heitz, J. Böhrer, D. Bimberg, V. M. Ustinov, V. A. Shchukin, A. Yu. Egorov, A. E. Zhukov, S. Zaitsev, P. S. Kop'ev, Zh. I. Alferov, S. S. Ruvimov, A. O. Kosogov, P. Werner, U. Gösele, and J. Heydenreich, Solid–State Electron. **40**, 785 (1996).
[8] N. Kirstaedter, N. N. Ledentsov, M. Grundmann, D. Bimberg, V. M. Ustinov, S. S. Ruvimov, M. V. Maximov, P. S. Kop'ev, Zh. I. Alferov, U. Richter, P. Werner, U. Gösele, and J. Heydenreich, Electron. Lett. **30**, 1416 (1994).

[9] G. E. Cirlin, G. M. Guryanov, A. O. Golubok, S. Ya. Tipissev, N. N. Ledentsov, P. S. Kop'ev, M. Grundmann, and D. Bimberg, Appl. Phys. Lett. **67**, 97 (1995).
[10] N. N. Ledentsov, M. V. Maksimov, G. É. Tsyrlin, V. N. Petrov, and G. M. Gur'yanov, Fiz. Tekh. Poluprovodn. **29**, 1295 (1995) [Semiconductors **29**, 671 (1995)].
[11] G. M. Guryanov, G. E. Cirlin, V. N. Petrov, N. K. Polyakov, A. O. Golubok, S. Ya. Tipissev, E. P. Musikhina, V. B. Gubanov, Yu. B. Samsonenko, and N. N. Ledentsov, Surf. Sci. **331–333**, 414 (1995).
[12] G. M. Gubanov, G. E. Cirlin, V. N. Petrov, N. K. Polyakov, A. O. Golubok, S. Ya. Tipissev, V. B. Gubanov, Yu. B. Samsonenko, N. N. Ledentsov, V. A. Shchukin, M. Grundmann, D. Bimberg, and Zh. I. Alferov, Surf. Sci. **352–354**, 651 (1996).
[13] G. É. Tsyrlin, A. O. Golubok, S. Ya. Tipisev, N. N. Ledentsov, and G. M. Gur'yanov, Fiz. Tekh. Poluprovodn. **29**, 1697 (1995) [Semiconductors **29**, 884 (1995)].
[14] G. M. Gur'yanov, N. N. Ledentsov, V. N. Petrov, Yu. B. Samsonenko, G. É. Tsyrlin, and A. G. Filaretov, Pis'ma Zh. Tekh. Fiz. **19**(18), 64 (1993) [Tech. Phys. Lett. **18**, 591 (1993)].
[15] V. B. Gubanov, G. M. Gur'yanov, N. N. Ledentsov, V. N. Petrov, Yu. B. Samsonenko, and G. É. Tsyrlin, Pis'ma Zh. Tekh. Fiz. **19**(21), 73 (1993) [Tech. Phys. Lett. **19**, 254 (1993)].
[16] G. M. Gur'yanov, V. N. Demidov, N. P. Korneeva, and G. É. Tsyrlin, Prib. Tekh. Éksp., No. 3, 167 (1996).
[17] G. E. Cirlin, V. N. Petrov, A. O. Golubok, S. Ya. Tipissev, V. G. Dubrovskii, G. M. Guryanov, N. N. Ledentsov, and D. Bimberg, Surf. Sci. (1997) (in press).

Translated by M. E. Alferieff

Hall effect in quasi-two-dimensional superlattices in nonquantizing magnetic and strong electric fields

G. M. Shmelev, É. M. Épshteĭn, and I. I. Maglevannyĭ

Volgograd State Pedagogical University, 400013 Volgograd, Russia
(Submitted June 29, 1995; accepted for publication November 18, 1996)
Fiz. Tekh. Poluprovodn. **31**, 916–919 (August 1997)

The transverse electric field E_y arising in quasi-two-dimensional superlattices (SLs) in a strong pulling electric field E_x and a weak magnetic field oriented in a direction perpendicular to the plane of the SL ($\mathbf{H} \parallel Z$) is calculated. In the case where the electronic energy spectrum is nonadditive, the field E_y includes the Hall factor and the spontaneous transverse electric field that exists without **H**. The field E_y is a multivalued and sign-variable function of E_x. The asymptotically stable branches of the function E_y are determined. The (kinetic) ''potential,'' whose minimum corresponds to a stationary state of the nonequilibrium electron gas, is used.
 [S1063-7826(97)00508-5]

In this paper we report the results of a calculation of the Hall field as a function of the strong pulling electric field in quasi-two-dimensional superlattices (2-SLs). Superlattices of this kind are fabricated on the basis of size-quantized $Al_xGa_{1-x}As$ layers with an energy miniband bounded in two directions and fixed energy in a direction perpendicular to the layers:[1]

$$\varepsilon(\mathbf{p}) = \varepsilon_0 - \frac{1}{2}\Delta\left(\cos\frac{p_1 d_0}{\hbar} + \cos\frac{p_2 d_0}{\hbar}\right), \tag{1}$$

where 2Δ is the width of the miniband, p_1 and p_2 are the Cartesian components of the quasimomentum **p** of the charge carrier, and d_0 is the period of the SL. In application to the spectrum (1), the characteristic features of the Hall effect, which are discussed below, are related primarily to the choice of the direction of the pulling field relative to the principal axes of the 2-SL: We assume that it makes an angle of 45° with one of the axes. Correspondingly, we orient the X axis along the pulling field. The spectrum (1) then becomes nonadditive in this coordinate system:

$$\varepsilon(\mathbf{p}) = \varepsilon_0 - \Delta\,\cos\frac{p_x d}{\hbar}\cos\frac{p_y d}{\hbar}, \tag{2}$$

where $d = d_0\sqrt{2}$. Of course, a spectrum of the type (2) is also possible in the principal axes, for example, in crystals with a volume-centered cubic lattice.[2] In this case the second term in Eq. (2) contains an additional factor $\cos(p_z d/\hbar)$, which for the field geometry chosen here is not important for the effects of interest to us. Zeolite-based three-dimensional cluster SLs also belong to this class of crystals.[3] Of course, this list of materials with the electronic spectrum (1) [or (2)] is not limited to the examples presented above.

We note that galvanomagnetic phenomena in a one-dimensional SL have been studied by many authors (see Ref. 4 and the references cited there). The Hall effect in a 1-SL in a strong electric field was investigated directly in Refs. 5 and 6.

In Ref. 7 it is shown that in the absence of a magnetic field, the spontaneous appearance of a transverse (relative to the pulling field E_x) voltage is possible in a conductor with a nonadditive nonparabolic dispersion law (2) and open in the transverse direction. This effect is an example of a nonequilibrium second-order phase transition, in which the transverse voltage plays the role of the order parameter and the pulling field is a controlling parameter. The existence of a transverse EMF with $\mathbf{H}=0$ evidently should also affect the magnitude of the transverse field in the presence of a magnetic field ($\mathbf{H} \parallel Z$), and since we are concerned with nonlinear effects, it is generally impossible to separate a ''pure'' Hall effect in this case. A similar situation occurs in multivalley semiconductors under conditions of a multiple-valued Sasaki effect.[8] Therefore, speaking about the Hall field, we have in mind the transverse field which includes both factors indicated above.

To calculate the current density $\mathbf{j}_0$ produced by charge carriers with the dispersion law (2), we restrict the analysis to the quasiclassical and one-band approximations: $\Delta \gg \tau^{-1}\hbar$; eEd and $eEd \ll \varepsilon_g$, where ε_g is the band gap, and τ is the mean free time of the electrons. We assume that the magnetic field is nonquantizing, $\hbar\omega_c \equiv |eH\Delta d^2/c\hbar| \ll T$ (T is the temperature in energy units), and that it is weak, $\omega_c\tau \ll 1$.

To solve the problem posed above, it is convenient to write the required equation of motion of a charge in dimensionless variables. We thus make the substitutions $\mathbf{p}d/\hbar \to \mathbf{p}$, $\mathbf{E}e\tau d/\hbar \to \mathbf{E}$, $\omega_c\tau \to \omega_c$, and $t/\tau \to t$. In the new notation we have

$$\frac{d\mathbf{p}}{dt} = \mathbf{E} + [\mathbf{v}(\mathbf{p}), \omega_c], \quad (\omega_c \| \mathbf{H}), \tag{3}$$

where $\mathbf{v} = 1/\Delta\ \partial\varepsilon/\partial\mathbf{p}$ is the dimensionless velocity of the charge.

To calculate the current we employ Boltzmann's equation with the collision integral in the $\tau = \text{const}$ approximation. The general formula obtained for the current density using the solution of this equation has the form (see, for example, Ref. 4)

$$\mathbf{j} = \int_0^\infty \mathbf{v}(\mathbf{p}(t))e^{-t}dt, \quad (\mathbf{p}(0) = 0). \tag{4}$$

Here $\mathbf{j}=\mathbf{j}_0\hbar/(en\Delta d)$ is the dimensionless current density and n is the carrier density in the layer. In the linear approximation in ω_c, we have the following expression from Eqs. (3) and (2):

$$P_x=E_xt-\frac{\omega_c}{2}\left\{\frac{\cos(E_x+E_y)t-1}{E_x+E_y}+\frac{\cos(E_y-E_x)t-1}{E_y-E_x}\right\}. \tag{5}$$

Substituting expression (5) into Eq. (4) we find

$$j_x=j_x^{(0)}+\frac{\omega_cE_y}{E_x^2-E_y^2}\left\{\frac{1+2(E_x^2+E_y^2)}{(1+4E_x^2)(1+4E_y^2)}-\frac{j_y^{(0)}}{E_y}\right\}, \tag{6}$$

$$j_x^{(0)}=\frac{E_x(1+E_x^2-E_y^2)}{(1+E_x^2+E_y^2)^2-4E_x^2E_y^2}. \tag{7}$$

The expressions p_y, j_y, and $j_y^{(0)}$ have the form (5)–(7) with the substitutions $y\leftrightarrow x$ and $\omega_c\rightarrow-\omega_c$. We underscore that the expressions found for j_x and j_y in the linear approximation in the magnetic field are exact in the electric field.

For a fixed pulling field E_x, which we assume to be the case below, the transverse field E_y is determined by the boundary conditions.

1. SHORT-CIRCUITED HALL CONTACTS (CORBINO DISK)

In this case $E_y=0$, and we find from Eqs. (6) and (7)

$$j_x=\frac{E_x}{1+E_x^2}, \tag{8}$$

$$j_y=\omega_cE_x\frac{2E_x^2-1}{(1+E_x^2)(1+4E_x^2)}. \tag{9}$$

Equation (8) has the same form as the formula for the current density flowing along the axis of a 1-SL.[1,4] The function $j_y(E_x)$ is nonmonotonic and sign-variable (the sign change occurs at $E_x=1/\sqrt{2}$). As should happen in this case, for $E_x\ll1$ the expressions (8) and (9) pass into the corresponding expressions for a parabolic spectrum: $j_x=E_x$ and $j_y=-\omega_cj_x$.

2. SAMPLE (PLATE) OPEN IN THE *Y* DIRECTION

In this case we have the condition

$$j_y=0, \tag{10}$$

which is an equation for the transverse field $E_y=E_y(E_x)$.

For $\omega_c=0$ the solutions of Eq. (10) have the form

$$E_y=0, \tag{11}$$

$$E_y=\pm\sqrt{E_x^2-1}, \quad (|E_x|>1), \tag{12}$$

and the solution (11) with $|E_x|<1$ and solution (12) with $|E_x|>1$ are stable with respect to fluctuations of the field E_y. Therefore, for $|E_x|>1$ a transverse field appears in the sample in one of two mutually opposite directions. The choice of direction is determined by a random fluctuation or an initial inhomogeneity. In this case, a nonequilibrium (kinetic) second-order phase transition, mentioned above, occurs at the bifurcation point $|E_x|=1$. The appearance of the transverse field (12) is the simplest example of self-organization in a nonequilibrium quasi-two-dimensional electron gas.

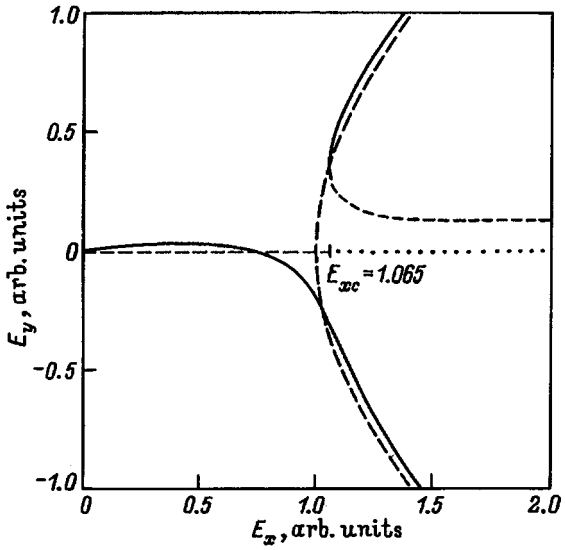

FIG. 1. Transverse field E_y versus the pulling field E_x. The solid and dashed lines represent stable states with $\omega_c=0.1$ and $\omega_c=0$, respectively. Dotted lines — unstable states.

For $\omega_c\neq0$ Eq. (10) becomes much more complex, transforming into an equation of degree 7 in E_y. Since it is impossible to find exact real solutions analytically, this equation was solved numerically. The computational results obtained with $\omega_c=0.1$ and $\omega_c=0$ are presented in Fig. 1.

The region $E_x<1$ is worth noting. Here, on the one hand, we have $E_y=0$ in the absence of a magnetic field and, on the other, the Hall effect does not usually manifest itself (the field E_y has a maximum and changes sign). For $E_x>1$ the situation is close to a ''seed situation.'' This is entirely natural, since the magnetic field is assumed to be weak ($\omega_c\ll1$) and the corrections due to the magnetic field are small. Nonetheless, the magnetic field plays a fundamental role: It washes out the phase transition and forces the system to choose between equally probable (for $\omega_c=0$) states (12) (forced bifurcation).

To investigate the stability of the solutions E_y found, we start from the condition (see, for example, Ref. 9)

$$\frac{dj_y}{dE_y}>0, \quad (E_x=\text{fix}) \tag{13}$$

whose satisfaction means that near the stable stationary values of E_y determined by the condition (10), a small fluctuation of the transverse field asymptotically approaches zero. The asymptotically stable states determined with the aid of the criterion (13) are shown in Fig. 1 (solid lines). It follows from Fig. 1 that for $E_x>1.065$ the Hall field has two stable values (bistability) for fixed E_x. (The possibility that the Hall field ''switches'' with a change in sign in a 1-SL was noted in Ref. 5). Figure 2 shows the I–V characteristic calculated from Eqs. (6) and (7) and the values found for E_y (for $\omega_c=0.1$).

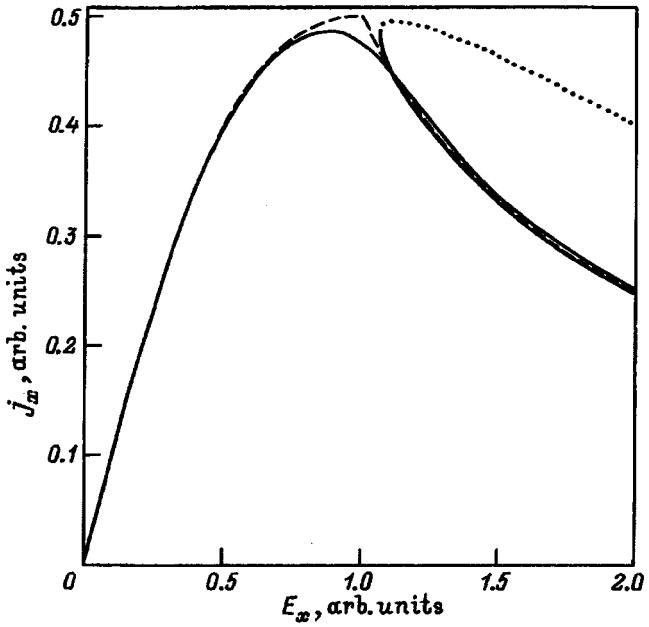

FIG. 2. Current-voltage characteristic for $\omega_c=0$ (dashed line) and $\omega_c=0.1$ (solid line). The dotted line corresponds to an unstable state E_y (see Fig. 1) with $\omega_c=0.1$.

It is convenient to investigate stability by the method proposed in Ref. 7. This method can be described as follows. The function

$$\Phi(E_y)=\int_0^{E_y} j_y(E_y')dE_y' + \text{ const}, \quad (E_x=\text{ fix}) \tag{14}$$

is studied. With the aid of this function the conditions (10) and (13) can be written in the form

$$\frac{d\Phi}{dE_y}=0, \quad \frac{d^2\Phi}{dE_y^2}>0. \tag{15}$$

Equations (15), which express the conditions for a minimum of the function Φ, mean that in the present nonequilibrium situation this function reaches a minimum in the stationary state under study. Consequently, the function Φ can be viewed as an analog of the thermodynamic potential for equilibrium systems. This analogy makes it possible to investigate the stability of the solutions of Eq. (10) by the standard Landau method employed in the theory of equilibrium phase transitions. This approach not only confirms the results obtained with the aid of Eq. (13), but also makes it possible to easily find the absolute minimum among local minima. The result of the integration in Eq. (14) (with const $=0$) is illustrated in Fig. 3 for $\omega_c=0.1$ near the point $E_x=1$. It follows from this figure that the minimum of the potential Φ on the lower stable branch (Fig. 1) is less than the minimum of the potential on the upper stable branch. For $E_x \gg 1$ the difference between the indicated minima approaches zero. The dotted curve in Fig. 3 shows the potential Φ for $E_{xc}=1.065$ (see also Fig. 1) (at the corresponding point $E_{yc}=0.45$ we have $d^2\Phi/dE_y^2=0$).

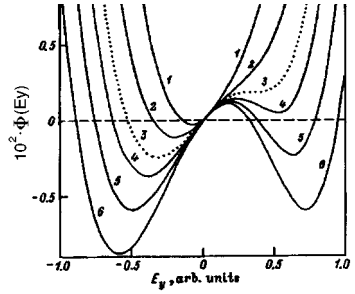

FIG. 3. ''Potential'' curves $10^2\cdot\Phi(E_y)$ with $\omega_c=0.1$. Controlling parameter E_x (arb. units): *1* — 0.9, *2* — 1.0, *3* — 1.065, *4* — 1.1, *5* — 1.15, *6* — 1.2.

The characteristic features of the Hall effect which were found above are ultimately associated with the limited nature, the nonlinearity, and primarily the nonadditivity of the energy spectrum (2). For additivity of the spectrum (1) (the X and Y axes are directed along the principal axes of the SL) we obtain in the linear approximation in ω_c: a) $j_y=-\omega_c j_x$ and b) $E_y=\omega_c j_x$, where j_x is determined by Eq. (8) with the substitution $d\to d_0$. The lack of uniqueness and the change in sign of the Hall field do not arise.

The numerical estimates of the effects considered here reduce to estimates of the measurement units for **E**, **j**, and ω_c, the latter depending on the SL parameters n, d, Δ, and τ (the values of the corresponding quantities for a 1-SL can serve as a reference point[1,4]).

We are grateful to O. V. Yaltychenko for assistance in the numerical calculations.

[1] A. P. Silin, Usp. Fiz. Nauk **147**, 485 (1985) [Sov. Phys. Usp. **28**, 972 (1985)].
[2] A. I. Ansel'm, *Introduction to Semiconductor Theory*, Prentice-Hall, Englewood Cliffs, N. J., 1981.
[3] V. N. Bogomolov, A. I. Zadorzhniĭ, T. M. Pavlova, V. P. Petranovskiĭ, V. P. Podkhalyuzin, and A. L. Kholkin, JETP Lett. **31**, 378 (1980).
[4] F. G. Bass, A. A. Bulgakov, and A. P. Tetervov, *High-Frequency Properties of Semiconductors with Superlattices* [in Russian], Nauka, Moscow, 1989.
[5] É. M. Épshteĭn, Izv. Vyssh. Uchebn., Zaved. Radiofiz. **22**, 373 (1979).
[6] É. M. Épshteĭn, Fiz. Tverd. Tela (Leningrad) **25**, 354 (1991) [Sov. Phys. Solid State **25**, 1375 (1992)].
[7] G. M. Shmelev and É. M. Epshteĭn, Fiz. Tverd. Tela (St. Petersburg) **34**, 2565 (1992) [Phys. Solid State **34**, 1375 (1992)].
[8] M. Ashe, Z. S. Gribnikov, V. V. Mitin, and O. G. Sarbeĭ, *Hot Electrons in Multivalley Semiconductors* [in Russian], Naukova dumka, Kiev, 1989.
[9] V. L. Bonch-Bruevich, I. P. Zvyagin, and A. G. Mironov, *Domain Electrical Instability in Semiconductors* [in Russian], Nauka, Moscow, 1972.

Translated by M. E. Alferieff

Nonstationary thermoelectric power in multilayered structures with $p-n$ junctions

V. N. Agarev

Nizhegorod State University, 603600 Nizhniĭ Novgorod, Russia
(Submitted August 20, 1996; accepted for publication December 16, 1996)
Fiz. Tekh. Poluprovodn. **31**, 920–921 (August 1997)

It is shown that the nonstationary thermoelectric power with characteristic rise and fall times of the order of seconds in multilayered structures with p–n junctions can be several orders of magnitude greater than the stationary thermoelectric power in a homogeneous semiconductor. This effect can be observed in polycrystalline films and artificially produced multilayer structures with p–n junctions and thin layers. It can be used to produce ultrasensitive temperature sensors.
 [S1063-7826(97)00608-X]

Multilayered structures with p–n junctions (MSs), whose number of layers is on the order of 10^4 cm^{-1}, are convenient models of polycrystalline films which exhibit an anomalous photovoltage (APV).[1–3] In addition, MSs are also of interest for producing new semiconductor devices.

The memory effect specific to MSs, which was studied by Stafeev in Ref. 4, consists of the fact that after a high voltage on the MS is switched off and the structure is short-circuited, the charge on the barrier capacitances of the p–n junctions is redistributed in a manner so that all p–n junctions are oppositely connected. Further relaxation of the charge on the barrier capacitances proceeds under the action of thermally generated currents over times much longer than the lifetime of the minority charge carriers. If the currents of the neighboring p–n junctions are different (for example, under nonuniform illumination, as in the case of the APV effect in films), then a nonstationary voltage, arises on the MS. The maximum value of this voltage can exceed $m\varphi$,[5,6] where $2m$ is the number of layers in the MS, and φ is the contact potential difference between the p and n regions.

In the present paper we shall examine the nonstationary voltage arising in a MS with precharged barrier capacitances of p–n junctions with a constant temperature gradient across the layers (i.e., along the MS).

Let the MS consist of $2mp$ and n layers whose dimensions are much smaller than the diffusion length of the minority charge carriers. If the MS is produced on the basis of wide-gap semiconductors, then the thermally generated currents in the p–n junctions will be higher than the thermally generated currents in the quasineutral regions.

The charge relaxation occurring on the jth p–n junction as a result of thermal current generation in the space charge layer is

$$\frac{dQ_i}{dt}=-\frac{qn_0(L(U)_j-L_0)}{\tau_0}=-\frac{n_0}{N\tau_0}(2Q_2-Q_0), \tag{1}$$

where $N_a=N_d=N$ is the impurity density in the p and n regions, n_0 and τ_0 are the density and lifetime of the charge carriers in the semiconductor itself, $L(U)_j$ and Q_j are the thickness and charge in the p–n junction at zero voltage, $Q_0=qNL_0$ is the stationary charge of the ionized impurity in the p or n region, and q is the electron charge.

Solving Eq. (1), we obtain

$$Q_j(t)=\left(\frac{Q_0}{2}\right)\sqrt{1+\frac{U_j(t)}{\varphi}}=\left(Q(0)-\frac{Q_0}{2}\right)\exp\left(\frac{-t}{\tau_j}\right)+\frac{Q_0}{2}. \tag{2}$$

The relaxation time of the charge on the jth p–n junction is

$$\tau_j=\frac{\tau_0 N}{2n_0}=\frac{(\tau_n P_0+\tau_p N_c)N}{2n_0^2}, \tag{3}$$

where τ_n and τ_p are the electron and hole lifetimes, respectively, and P_v and N_c are the density of states in the valence and conduction bands, scaled to the recombination level. When a temperature gradient is present along the MS, the relaxation times on the jth and $(j+1)$st p–n junctions will be different. According to Eq. (2), the total thermal voltage on the MS, disregarding the edge effects, is

$$\begin{aligned}\Delta U(t)=m(U_j-U_{j+1})=m\varphi\left[\frac{2Q(0)}{Q_0}-1\right]^2\left[\exp\left(-\frac{2t}{\tau_j}\right)\right.\\ \left.-\exp\left(-\frac{2t}{\tau_{j+1}}\right)\right]+2m\varphi\left[\frac{2Q(0)}{Q_0}-1\right]\\ \times\left[\exp\left(-\frac{t}{\tau_j}\right)-\exp\left(-\frac{t}{\tau_{j+1}}\right)\right].\end{aligned} \tag{4}$$

If the temperature gradient along the MS is small, then $\Delta\tau=\tau_j-\tau_{j+1}\ll\tau_j=\tau$ and the total thermal voltage on the MS will be

$$\begin{aligned}\Delta U(t)=m\varphi\frac{2t}{\tau}\frac{\Delta\tau}{\tau}\left\{\left[\frac{2Q(0)}{Q_0}-1\right]^2\exp\left(-\frac{2t}{\tau_\tau}\right)\right.\\ \left.+\left[\frac{2Q(0)}{Q_0}-1\right]\exp\left(-\frac{t}{\tau_j}\right)\right\}.\end{aligned} \tag{5}$$

If the charge stored in the barrier capacitances is much greater than the equilibrium charge, $(2Q(0)/Q_0)\gg 1$, then $\Delta U(t)$ reaches a maximum at $t_{\max}\simeq\tau/2$:

$$\Delta U_{\max}\simeq m\varphi\frac{\Delta\tau}{\tau}\left(\frac{2Q(0)}{Q_0}\right)^2\frac{1}{e}. \tag{6}$$

According to Eq. (3), for small temperature gradients we obtain

$$\Delta\tau=\frac{\Delta T}{2mT}\left(-\frac{E_g-\Delta E}{kT}\right)\tau, \tag{7}$$

where ΔT is the temperature difference between the ends of the MS, and ΔE is the energy difference between the conduction-band bottom and the recombination level if $\tau_p N_c \geqslant \tau_n P_v$, or the energy difference between the recombination level and the valence-band top if the opposite relation holds.

We obtain the maximum value of the differential thermoelectric power by substituting the expression (7) into Eq. (6)

$$\frac{\Delta U_{\max}}{\Delta T} \simeq \left[\left(\frac{k}{q}\right)\frac{\Delta F}{kT}\right]\left\{\frac{q\varphi}{\Delta F}\left(-\frac{E_g-\Delta E}{kT}\right)\left(\frac{2Q(0)}{Q_0}\right)^2\frac{1}{2e}\right\}, \tag{8}$$

where ΔF is the distance from the Fermi level to the conduction-band bottom in a τ-nondegenerate semiconductor or from the Fermi level to the valence-band top for a p-type semiconductor. The first term in brackets in expression (8) is the thermoelectric power in a nondegenerate semiconductor. Let us estimate the second term in the braces in expression (8). For $q\varphi \simeq 10\Delta F$, $E_q - \Delta E \simeq 20kT$, and $[2Q(0)/Q_0]^2 \simeq 30$, which is the scale factor in the braces in Eq. (8), is of the order of 10^3. The characteristic rise time of the thermoelectric power at $\tau_0 = 10^{-7}$ s and $N = 10^7 n_0$ is $t_{\max} \simeq 1/2$ s.

In summary, a nonstationary thermoelectric power, which is several orders of magnitude greater than the stationary thermoelectric power in a homogeneous semiconductor and with characteristic rise and fall times of the order of seconds, can be observed in MS with precharged barrier capacitances of the $p-n$ junctions. This effect can be observed in polycrystalline APV films and artificially produced MSs with thin layers, and it can be used to produce ultrasensitive temperature sensors.

[1] É. I. Adirovich, V. M. Rubinov, and Yu. M. Yuabov, Dokl. Akad. Nauk SSSR **164**, 529 (1965) [Sov. Phys. Dokl. **10**, 844 (1966)].
[2] É. I. Adirovich, V. M. Rubinov, and Yu. M. Yuabov, Dokl. Akad. Nauk SSSR **174**, 545 (1967) [Sov. Phys. Dokl. **12**, 477 (1967)].
[3] É. I. Adirovich, É. M. Mastov, and Yu. M. Yuabov, Dokl. Akad. Nauk SSSR **188**, 1254 (1969) [Sov. Phys. Dokl. **14**, 994 (1970)].
[4] V. I. Stafeev, Fiz. Tekh. Poluprovodn. **6**, 2134 (1972) [Sov. Phys. Semicond. **6**, 1811 (1972)].
[5] V. N. Agarev, Pis'ma Zh. Tekh. Fiz. **3**(13), 626 (1977).
[6] V. N. Agarev, Fiz. Tekh. Poluprovodn. **14**, 1018 (1980) [Sov. Phys. Semicond. **14**, 607 (1980)].

Translated by M. E. Alferieff

$Si/Si_{1-x}Ge_x$ epitaxial layers and superlattices. Growth and structural characteristics

F. F. Sizov, V. P. Klad'ko, S. V. Plyatsko, and A. P. Shevlyakov

Institute of Semiconductor Physics, Ukrainian National Academy of Sciences, 262650 Kiev, Ukraine

Yu. N. Kozyrev and V. M. Ogenko

Institute of Surface Chemistry, National Ukrainian Academy of Sciences, Kiev, Ukraine
(Submitted April 3, 1996; accepted for publication December 25, 1996)
Fiz. Tekh. Poluprovodn. **31**, 922–925 (August 1997)

Si, Ge, and $Si_{1-x}Ge_x$ epitaxial layers and $Si/Si_{1-x}Ge_x$ superlattices have been obtained on (100) and (111) silicon substrates by molecular-beam epitaxy. The growth processes and the structural characteristics and chemical composition of the structures were studied by x-ray diffraction and Auger spectroscopy. It is shown that under the experimental conditions for obtaining $Si/Si_{1-x}Ge_x$ superlattices structurally perfect, strained superlattices with satellites up to ± 5 orders can be obtained. © *1997 American Institute of Physics.* [S1063-7826(97)00708-4]

Modern epitaxial methods for growing semiconductor layers make it possible to monitor growth processes at the atomic level. Structures (heterojunctions, quantum wells, superlattices) with controllable characteristics for micro- and optoelectronics can be produced by combining different types of semiconductors and epitaxial layers of different thickness. The most thoroughly studied structures to date are those based on group-III and group-V semiconductors, the most important of which crystallize in the zinc blende structure. In some cases, lattice-matched components can be chosen for the structures; this makes it possible to achieve controlled heteroepitaxy and to obtain high-quality structures. However, the most important structures for applications are still structures based on elementary semiconductors, especially Si — the principal material of semiconductor electronics.

The properties of bulk $Si_{1-x}Ge_x$ crystals have been investigated for many years (see, for example, Ref. 1). Depending on the chemical composition, the band gap in these compounds can range from 1.1 to 0.7 eV and, for example, $Si_{1-x}Ge_x$-based photodetectors can operate in the spectral range 0.5–1.8 μm, so that they can be used in fiber-optic communication lines. However, the large lattice mismatch ($\Delta a = 4.2\%$ at $T = 300$ K) in the case where $Si_{1-x}Ge_x$ layers are grown in silicon substrates results in a high mismatch-dislocation density at the interface.

Progress in the development and investigation of strained quantum-well structures and heterostructures based on silicon (see, for example, Refs. 2 and 3) promises development of fundamentally new devices for micro- and optoelectronics in the system $Si/Si_{1-x}Ge_x$.[4,5]

In the present study we investigated the structural characteristics of Si, Ge, and $Si_{1-x}Ge_x$ layers and superlattices in the $Si/Si_{1-x}Ge_x$ system, prepared by molecular beam epitaxy (MBE) on (100) and (111) silicon substrates.

One of the main problems in growing perfect quantum-well structures and heterostructures based on Si and Ge is to assure layerwise two-dimensional stepped growth at relatively low epitaxy temperatures ($T \leqslant 550$ °C) while avoiding three-dimensional growth with a high germanium content in the layers, since otherwise the surface morphology of the $Si_{1-x}Ge_x$ layers is disrupted and a high defect density arises in them.

In the heteroepitaxy of lattice-mismatched semiconductors, there exist critical thicknesses of epitaxial layers up to which the lattice mismatch is compensated for by stresses in the layers. In the case at hand, this results in a tetragonal distortion of the unit cell. The typical values of the critical thicknesses for $Si_{1-x}Ge_x$ layers on substrates with growth temperatures $T \simeq 500$ °C are 1000 Å for layers with $\Delta a = 1\%$ ($\sim 20\%$ Ge) and only 10 Å for $\Delta a = 4.2\%$ (pure germanium). When the critical thicknesses are exceeded, relaxation of mechanical stresses occurs in the layers and mismatch dislocations are formed.

Epitaxial layers of Si and $Si_{1-x}Ge_x$ were grown on (100) and (111) substrates by molecular-beam epitaxy in a Katun' system with substrate temperatures $T = 400-830$ °C in vacuum with a residual pressure not exceeding 5×10^{-8} Pa. A high-energy electron diffractometer built into the growth chamber made it possible to monitor within 3 Å the thickness of the layers being grown and the degree of their structural perfection according to the rearrangements of the structure of the growth surface directly during the growth process.

The pre-epitaxial preparation of the silicon substrates consisted in chemical etching away of the natural oxide and depositing a ~ 1-μm-thick passivating oxide film with the aim of later removing the film in a controllable manner in the growth chamber. During the heating of the silicon substrates in the growth chamber up to a temperature $T \simeq 850$ °C with residual vapor pressure $\leqslant 10^{-7}$ Pa, the interaction of the weak Si vapor flow ($F_{Si} \simeq 10^{15}$ cm^2/s) with the surface of the substrates according to the reaction

$$SiO_2 + Si \rightarrow SiO\uparrow \qquad (1)$$

produced in a time of 2–5 min an oxygen-free, atomically clean surface and resulted in the appearance of clear reflections of 7×7 and 2×1 structures for (111) and (100) orientations, respectively.

The minimum temperature at which epitaxial growth of the Si buffer layers could be achieved was equal to

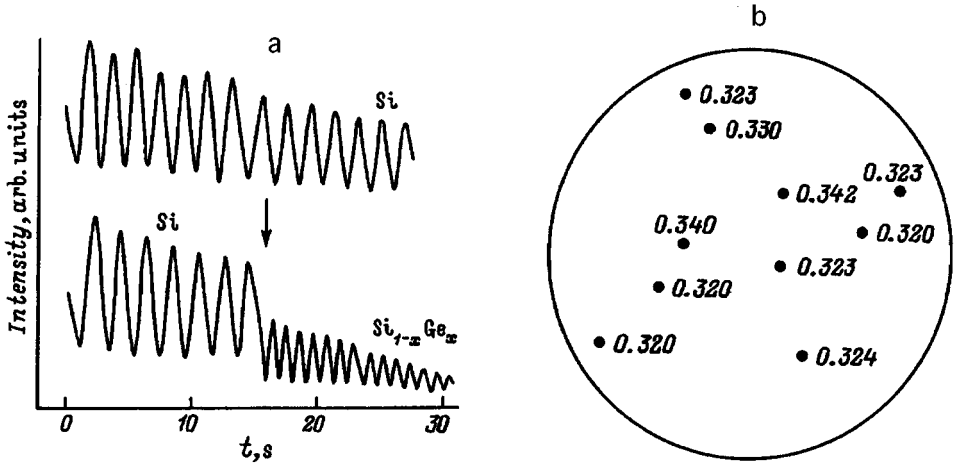

FIG. 1. a — Oscillations of the central HEED reflection at time t during growth of Si epitaxial films (top) and the change occurring in the oscillations when the Ge source (bottom, arrow) for growing $Si_{1-x}Ge_x$ epitaxial layers is switched on b — distribution of the chemical composition in the plane of a $Si_{1-x}Ge_x$ epitaxial layer with thickness $d \simeq 1$ μm, obtained by molecular-beam epitaxy on a Si (100) plate. The values of x are indicated.

~400 °C with a growth rate of 1.0−1.5 Å/s. The oscillations of the central HEED reflection (see Fig. 1a), according to which the epitaxial growth rate was determined, remained distinct and stable, indicating that the growth of the epitaxial layers was a two-dimensional process.

The conditions for obtaining epitaxial Ge and $Si_{1-x}Ge_x$ layers on Si (111) substrates were investigated. Specifically, the optimal growth parameters of epitaxial germanium films on silicon substrates with surface restructurings $(7\times7)\rightarrow(5\times5)\rightarrow(2\times8)\rightarrow(1\times1)$ were determined and studied in the temperature range $T=350-650$ °C. The epitaxial $Si_{1-x}Ge_x$ layers ranged in thickness from 50 Å to 1 μm and in Ge content $x\simeq0.07-0.70$. The growth conditions made it possible to obtain $Si_{1-x}Ge_x$ epitaxial layers on Si substrates, 60–76 mm in diameter, with a relative composition uniformity of $\pm1\%$.

Figure 1b shows the distribution of the Ge content in $Si_{1-x}Ge_x$ epitaxial layers for the regimes prescribed for obtaining layers with $x\simeq0.35$. It is obvious that the uniformity of the Ge distribution is relatively high, and that the composition matches well the prescribed growth conditions. Figure 2 shows diffraction-reflection curves for $Si/Si_{1-x}Ge_x$ heterosystems with different chemical compositions of the epitaxial layers.

The composition of the $Si_{1-x}Ge_x$ epitaxial layers was monitored according to the angular separation $\Delta\theta$ between the positions of the peaks in the x-ray diffraction reflection pattern assuming that Vegard's law holds [Vegard's law holds well in $Si_{1-x}Ge_x$ (the lattice constants are $a=5.431$ Å for Si and $a=5.657$ Å for Ge at $T=300$ K)], taking into account the corrections for the degree of relaxation of the strained layers. The error in measuring $\Delta\theta$ is $\pm1''$ (irrespective of the composition). This makes it possible to determine the composition of the layers with an absolute accuracy of $\pm0.3\%$. The elastic stresses existing in heterojunctions affect the determination of the chemical composition of the layers. However, as a result of the relatively large radii of curvature of the silicon plates with epitaxial layers, in determining the composition of the layers the corrections made so as to take into account the relaxation of the mechanical stresses in the heterostructure are small.

The intensity of the diffraction reflection peaks from the thin Si, Ge, and $Si_{1-x}Ge_x$ epitaxial layers and from the $Si/Si_{1-x}Ge_x$ superlattices is a fraction of a percent of the intensity of the reflection peak from the silicon substrate. However, these peaks are still intense enough to determine the thickness of the epitaxial layers with a relative accuracy of $\pm3\%$.

The profiles of the chemical composition distribution in the heterostructures and $Si/Si_{1-x}Ge_x$ superlattices were also investigated by layerwise analysis in a 09 IOS-005 Auger spectrometer. The surface of the samples was etched with argon ions at a constant rate in the energy range 2.0–3.5 keV and with ion-beam current densities 180–350 $\mu A/cm^2$ and ion-beam diameter ~0.75 μm. The intensity (number N of electrons) of the Ge Auger peak (energy $E=1146.8$ eV) was measured continuously. The typical dependence of the change in the intensity of the Ge Auger peak over the depth of the sample (the accumulation time t_a with a constant etch rate is proportional to the distance from the sample surface) is shown in Fig. 3. As one can see from Fig. 3, the periodicity and thickness of the separate Si and $Si_{1-x}Ge_x$ layers (70-Å SiGe and 90-Å Si) hold up quite well. The Ge molar

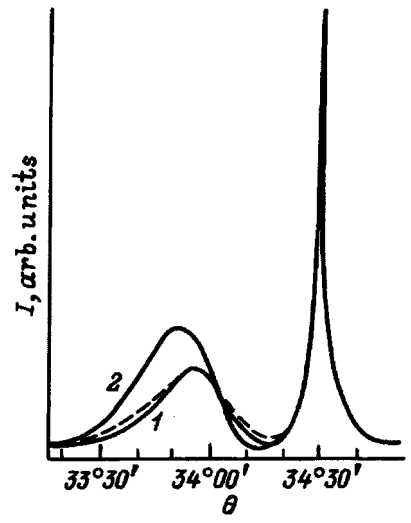

FIG. 2. Diffraction reflection curves for $Si_{1-x}Ge_x$ heterostructures on Si (100) substrates. x: *1* — 0.39, *2* — 0.44. The intensity I scale is logarithmic.

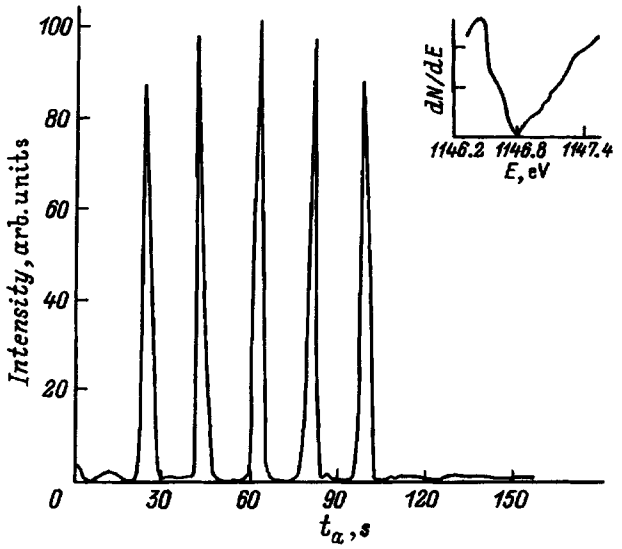

FIG. 3. Variation in the intensity of the Ge Auger peak $E=1146.8$ eV with layerwise etching of the surface of a strained $Si_{1-x}Ge_x$ superlattice by Ar ions. The ion energy is 2.8 keV, the current is $250\mu A/cm^2$, and the ion beam diameter is 0.75 μm. The period of the superlattice is 160 Å. Inset: Ge Auger peak.

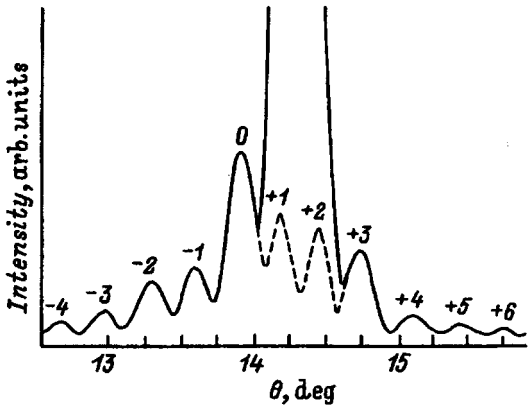

FIG. 4. X-Ray diffraction intensity versus diffraction angle for a five-period $Si_{1-x}Ge_x$ superlattice on a Si (111) substrate with a 0.2-μm-thick Si buffer layer. Measurement conditions: CuKα1 radiation line with wavelength $\lambda=1.54051$ Å, Si (100) monochromator, (400) reflection. Superlattice parameters: period 181 Å, SiGe layer thickness 72 Å, Si layer thickness 109 Å. The peaks of the negative $(-i)$ and positive $(+j)$ satellites for the superlattice are numbered. The dashed line represents the oscillations of the x-ray diffraction of the satellites which are masked by the intense diffraction reflection peak from the silicon substrate.

fraction in the $Si_{1-x}Ge_x$ layers, determined according to the ratio of the Ge and Si Auger peak intensities for heterostructures and $Si/Si_{1-x}Ge_x$ superlattices, correspond satisfactorily to the prescribed regimes of experimental growth of the structures.

The structural characteristics of the Si and $Si_{1-x}Ge_x$ buffer layers, as well as the periodic $Si_{1-x}Ge_x$ structures with period $d=100-300$ Å were investigated by the x-ray diffraction method in a DRON-3 diffractometer with a double-crystal scheme in the $(n,-n)$ geometry with a Si (100), (111) monochromator and a CuKα1 radiation line ($\lambda=1.54051$ Å). The x-ray diffraction method makes it possible to determine at the same time the stress distribution, the chemical composition, and the period of the superlattices. The mechanical stresses arising as a result of the lattice mismatch between the buffer layer and the substrate and between the buffer layer and the superlattice results in bending of the silicon plates; this bending can be determined according to the change in the angular position of the main diffraction peak. The average curvature of the silicon plates with the $Si_{1-y}Ge_y$ ($y\simeq 0.5x$) buffer layers was equal $R^{-1}\simeq 0.2\ m^{-1}$.

The period d of the $Si_{1-x}Ge_x$ superlattices was determined according to the angular separation $\Delta(2\theta)$ between the satellites in the x-ray diffraction spectra

$$d=\frac{\lambda}{\Delta(2\theta)}\cos\theta_s^{-1}, \qquad (2)$$

where θ_s is the Bragg angle of reflection from the substrate.

During the growth of $Si_{1-x}Ge_x$ superlattices the condition for pseudomorphic growth of the epitaxial layers was satisfied (strained superlattices), and satellites up to ± 5 orders were observed in the x-ray diffraction reflection spectra. The presence of numerous, regularly spaced, and well-defined x-ray satellites attests to the structural perfection of the superlattices[6] — the existence of sharp boundaries between the layers, uniformity of their chemical composition, etc.

The typical x-ray diffraction pattern of a five-period $Si_{1-x}Ge_x$ superlattice ($x\simeq 0.35$, period $d\simeq 181$ Å, SiGe layer thickness 72 Å, Si thickness 109 Å) on a silicon (111) substrate with a 0.2-μm-thick Si buffer layer is shown in Fig. 4. The main (wide at the base) peak at $\theta=14°13'$ is due to the (111) reflection from the silicon substrate and is a reference reflection in the present case. The intensity of the diffraction reflection peaks from the $Si/Si_{1-x}Ge_x$ superlattice equals fractions of a percent of the intensity of the reflection peak from the silicon substrate. Several relatively wide but well-separated negative $(-i)$ and positive $(+j)$ satellites, which attest to the good uniformity of the layers over thickness, can be seen in Fig. 4.

The free-carrier density in the Si, Ge, and $Si_{1-x}Ge_x$ epitaxial layers was equal to $10^{15}-10^{17}$ cm^{-3}. To control the electrical characteristics of the layers of the superlattices, the Si layers were doped with boron with a resulting density of $10^{17}-10^{19}$ cm^{-3}.

In summary, our investigations of the growth of Si, Ge, and $Si_{1-x}Ge_x$ layers and our study of their structural characteristics have shown that structurally perfect heterostructures and $Si/Si_{1-x}Ge_x$ superlattices with a large area and prescribed chemical composition can be obtained.

[1] S. C. Jain, J. R. Willis, and R. Bullough, Adv. Phys. **39**, 127 (1990).
[2] G. Abstreiter, ''Engineering the future of electronics,'' Physics World, 1992, p. 36.
[3] F. F. Sizov, in *Infrared Photon Detectors*, edited by A. Rogalski, SPIE Optical Engineering Press, Bellingham, Washington, 1995, p. 561.
[4] R. A. Metzger, Compound Semicond. **1**, N 3, 21 (1995).
[5] K. Eberl, W. Wegscheider, and G. Abstreiter, J. Cryst. Growth **111**, 882 (1991).
[6] B. M. Clemens and J. G. Gay, Phys. Rev. B **35**, 9337 (1987).

Translated by M. E. Alferieff

Simple method for reconstructing the doping fine structure in semiconductors from $C-V$ measurements in an electrolytic cell

V. I. Shashkin, I. R. Karetnikova, A. V. Murel', I. M. Nefedov, and I. A. Shereshevskiĭ

Institute of Microstructure Physics, Russian Academy of Sciences, 603600 Nizhniĭ Novgorod, Russia
(Submitted August 13, 1996; accepted for publication December 25, 1996)
Fiz. Tekh. Poluprovodn. **31**, 926–930 (August 1997)

A simple method is proposed for reconstructing the doping fine structure in semiconductors from capacitance-versus-voltage measurements with electrochemical etching. The method makes it possible to determine the doping profile directly from the semiconductor surface and provides resolution on scales of less than the Debye screening length. Numerical calculations confirm that the doping profile in semiconductors can be reconstructed with a resolution of several nanometers. © *1997 American Institute of Physics.* [S1063-7826(97)00808-9]

1. INTRODUCTION

A method based on measurements of the capacitance-versus-voltage ($C-V$) characteristics with a reverse bias applied to a Schottky barrier is widely used to determine the dopant concentration profile of semiconductor structures.[1] In the mid-1970s it was suggested that a barrier contact of a semiconductor sample with an electrolyte be used for this purpose (instead of depositing metal or mercury contacts).[2] The possibility of performing consecutively a measurement of the concentration and very precise electrolytic etching of a sample in an electrolytic cell made it possible in practice to remove the limit on the doping profiling depth. Thus, investigators were equipped with a convenient and efficient method for reconstructing a profile during electrochemical etching (ECP method).[3] While ECP method retains the fundamental principles of $C-V$ measurements, it also inherits the drawbacks:[1,4] 1) It is impossible to obtain information about the impurity distribution in the initial-depletion region near the surface and 2) there are errors and limits on the resolution of the fine structure of the doping profile on scales comparable to the Debye screening length. Both drawbacks arise from the fact that the analysis is performed on the basis of classical formulas which are obtained in the complete-depletion approximation. The concentration is determined at the boundary of the depletion region, where the approximation is very crude. A clear formulation of the problem of the accuracy of the doping profiling was given a long time ago[5] and the problem was subsequently discussed repeatedly (see, for example, Refs. 1 and 4). However, practical schemes for reconstructing sharp doping profiles on the basis of $C-V$ data have only recently been proposed.[6–8] These schemes are based on an iterative determination of the doping profile in a given class of functions by numerically minimizing the discrepancy between the measured and computed $C-V$ curves. Such information is obviously very important for the investigation of diverse semiconductor multilayer microstructures.

In the present paper we propose a simple method for reconstructing the doping fine structure in semiconductors on the basis of electrochemical $C-V$ measurements during electrochemical etching. The method provides a resolution of less than the Debye screening length and it reconstructs the doping profile in the region of initial depletion near the surface. The limits of applicability of the approach are discussed. Numerical modeling of experiments on ECP of test semiconductor structures shows that the doping profile can be reconstructed with nanometer resolution.

2. FORMULATION OF THE DIRECT PROBLEM FOR CALCULATING THE CAPACITANCE

Let us assume that an electrolyte is brought into contact with the flat surface of a *n*-type semiconductor possessing a nonuniform impurity distribution $N(x)$ near the surface. For a given bias V the current through the contact is weak; this corresponds to constant positions of the Fermi quasilevels in the semiconductor (E_{FS}) and electrolyte (E_{FE}).[9] The problem is assumed to be one-dimensional. For simplicity, let us assume that the impurities in the semiconductor are completely ionized, that there are no deep levels, that the contribution of the minority carriers is small, that the electrons satisfy Boltzmann's statistics, and that the voltage drop in the electrolyte can be ignored.

The electrostatic potential $\psi(x)$ satisfies the Poisson equation

$$\frac{\partial^2\psi}{\partial x^2}=\frac{4\pi e}{\varepsilon}[N_0\exp(e\psi/kT)-N(x)],\quad x\geqslant x_e \tag{1}$$

with the standard boundary conditions

$$\psi(x_e)=-V-\frac{\Phi-E_0}{e},\quad \psi(\infty)=0, \tag{2}$$

which are elucidated by the band scheme of the electrolyte–semiconductor contact shown in Fig. 1. Here Φ is the Galvani potential, and $E_c(x)$ denotes the position of the conduction-band bottom

$$E_c(x)=E_0-e\psi(x),\quad E_0=-kT\ln(N_0/N_c), \tag{3}$$

where N_c is the effective density of states in the conduction band. The notation has been introduced for the position of the etch front — x_e and for the boundary of the depletion region — x_d.

In writing the relations (1)–(3) it is actually assumed that at some x_0 the semiconductor becomes uniform, i.e., the density of the dopant remains constant,

 1063-7826/97/080789-04$10.00

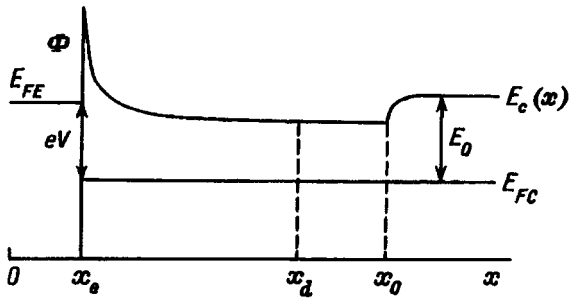

FIG. 1. Band diagram of electrolyte–semiconductor contact with $V \neq 0$.

$$N(x)=N_0, \quad x \geqslant x_0. \tag{4}$$

As noted in Ref. 10 , this assumption often corresponds to the real situation for an epitaxial structure grown on a semiconductor substrate or it can be justified by the fact that doping nonuniformities which are located sufficiently far away cannot greatly influence the space charge in the depletion region.

For a prescribed profile $N(x)$ the problem (1) and (2) has a solution that determines the integral characteristics — the charge per unit area

$$Q(x_e,V)=-\frac{\varepsilon}{4\pi}\frac{\partial\psi}{4\pi}\Big|_{x=x_e}$$

$$=e\int_{x_e}^{\infty}[N(x)-N_0\ \exp(e\psi/kT)]dx \tag{5}$$

and the specific capacitance

$$C(x_e,V)=\frac{\partial Q}{\partial V}, \tag{6}$$

which are functions of the two independent variables x_e and V.

3. APPROXIMATION OF COMPLETE DEPLETION OF THE NONUNIFORM-DOPING REGION

The complete-depletion approximation is based on the introduction of a sharp hypothetical boundary x_d which separates a region $x<x_d$ which is completely depleted of majority carriers from the neutral region $x \geqslant x_d$ (see, for example, Ref. 1). It is obvious that the complete-depletion approximation can be satisfactory if the nonuniformly doped part of the structure becomes depleted in the range of voltages V and etch steps x_e of interest, i.e.,

$$x_d(x_e,V)>x_0. \tag{7}$$

Then the solution of the problem is obvious

$$Q(x_e,V)=e\int_{x_e}^{x_d}N(x)dx, \tag{8}$$

$$\psi(x_d)-\psi(x_e)=V+\frac{\Phi-E_0}{e}=\frac{4\pi e}{\varepsilon}\int_{x_e}^{x_d}(x-x_e)N(x)dx, \tag{9}$$

and there are no doubts that the boundary condition $\psi(x_d)=0$ is admissible in Ref. 9 . Let the variables x_e and V be independent. Let us differentiate the expressions (8) and (9)

$$\frac{1}{e}dQ=N(x_d)\frac{\partial x_d}{\partial V}dV+\left[N(x_d)\frac{\partial x_d}{\partial x_e}-N(x_e)\right]dx_e, \tag{10}$$

$$\frac{\varepsilon}{4\pi e}=N(x_d)(x_d-x_e)\frac{\partial x_d}{\partial V}dV$$

$$+\left[N(x_d)(x_d-x_e)\frac{\partial x_d}{\partial x_e}-\frac{1}{e}Q\right]dx_e. \tag{11}$$

Using expression (6), we obtain the standard $C-V$ profiling formulas[1,4]

$$C=eN(x_d)\frac{\partial x_d}{\partial V}=\frac{\varepsilon}{4\pi(x_d-x_e)} \tag{12}$$

and

$$x_d=x_e+\frac{\varepsilon}{4\pi C}, \quad N(x_d)=\frac{8\pi}{\varepsilon e}\left[\frac{\partial(1/C^2)}{\partial V}\right]^{-1}, \tag{13}$$

which determine in parametric form the doping profile on the basis of the measured dependence $C(x_e,V)$. It is obvious that on the strength of the assumption (7) the calculations based on Eq. (13) give the trivial result $N(x_d)=N_0$.

4. SIMPLE METHOD FOR RECONSTRUCTING THE DOPING PROFILE

Expressions for $N(x_e)$ and Q, which are more important for the discussion below, follow from Eqs. (10) and (11):

$$N(x_e)=\frac{1}{e}\left(\frac{4\pi}{\varepsilon}QC-\frac{\partial Q}{\partial x_e}\right), \tag{14}$$

$$Q(x_e,V)=\left[1+\frac{\varepsilon}{4\pi}\frac{\partial(1/C)}{\partial x_e}\right]\left[\frac{\partial(1/C)}{\partial V}\right]^{-1}. \tag{15}$$

The relations presented above are the solution of the inverse problem and make it possible to determine on the basis of the measured voltage dependences of the capacitance $C(x_e,V)$ the dopant concentration profile at each etch step, starting directly from the semiconductor surface.

Other methods of finding the concentration profile, which could be convenient from the experimental standpoint, follow from Eqs. (10) and (11). For example, measurements can be performed with the position of the boundary of the depletion region held constant for several etching steps. Setting $dx_d=0$ in Eqs. (10) and (11), we find

$$N(x_e)=\frac{\varepsilon}{4\pi e}\frac{d^2V}{dx_e^2} \tag{16}$$

provided that

$$x_e+\frac{\varepsilon}{4\pi C(x_e,V)}=\text{const}. \tag{17}$$

In this case the doping profile is reconstructed as follows. Voltage increments ΔV satisfying the condition (17) are se-

lected for several successive etch steps and a numerical differentiation scheme is used to calculate $N(x_e)$ from Eq. (16).

The main difference between the standard approach based on Eq. (13) and the proposed approach based on Eqs. (14) and (16) for reconstructing the doping profile is that in the latter case the change in the capacitance characteristics of the semiconductor is attributed to the charge present in the surface layer and is removed by electrolytic etching. Therefore the characteristic features of the distribution of mobile charge carriers at the depletion boundary do not greatly influence the accuracy and resolution of the doping profiling. For this reason, resolution limits on scales of the Debye screening length, which are inherent in the standard approach, do not arise in the calculations based on Eqs. (14) and (16).[5] It is obvious that the validity of the expressions (16) and (17) can be substantiated if the assumptions of Sec. 3 are not made. Indeed, Eq. (16) is the Poisson equation (1) written for the surface part of the structure, where $-\psi \gg kT/e$ and the contribution of mobile charge carriers can be neglected. The condition (17) gives the change in the applied voltage (2) on etch steps x_e and x_e' that maintains a constant potential corresponding to the exact equation (1) in the bulk of the semiconductor, $\psi(x_e,V,x)=\psi(x_e',V',x)$ for $x>x_e'>x_e$. Solving Poisson's equation in the interval (x_e,x_e'), it is easy to establish the required relation between the capacitances:

$$\frac{1}{C(x_e',V')}=\frac{1}{C(x_e,V)}-\frac{\varepsilon}{4\pi(x_e'-x_e)}, \tag{18}$$

which is equivalent to Eq. (17). Therefore, in contrast to the approach based on Eq. (14), the only condition on the applicability of Eq. (16) for doping profiling is the requirement that the depletion must be strong near the surface of the semiconductor: $-\psi \gg kT/e$.

5. RESULTS OF NUMERICAL MODELING

To assess the possiblity of reconstructing doping profiles on the basis of Eqs. (14) and (16), numerical modeling of the ECP process was performed for different profiles $N(x)$. To find the voltage dependence of the capacitance at each etch step, be solved numerically the direct boundary value problem (1) and (2), which was reduced to a Cauchy problem by the method described in detail in Ref. 10. Furthermore, to avoid errors arising from the numerical differentiation in calculating the capacitance (6), we differentiated with respect to V the Poisson equation and the boundary conditions. The system of two second-order equations obtained was solved by the fourth-order Runge–Kutta method with automatic selection of the step size. The function $C(x_e,V)$ calculated in this manner was used to reconstruct the doping profile in the variant A — according to Eq. (14) and in the variant B — according to Eq. (16), interpolating C as a function of V in order to find the required increments ΔV.

Piecewise constant profiles $N(x)$ were chosen as test profiles. The typical parameters for the ECP method were used in the modeling:[4,11] etch step is 1 nm, $\Phi-E_0=1.7$ eV, and voltage range is from 0 to 0.2 V.

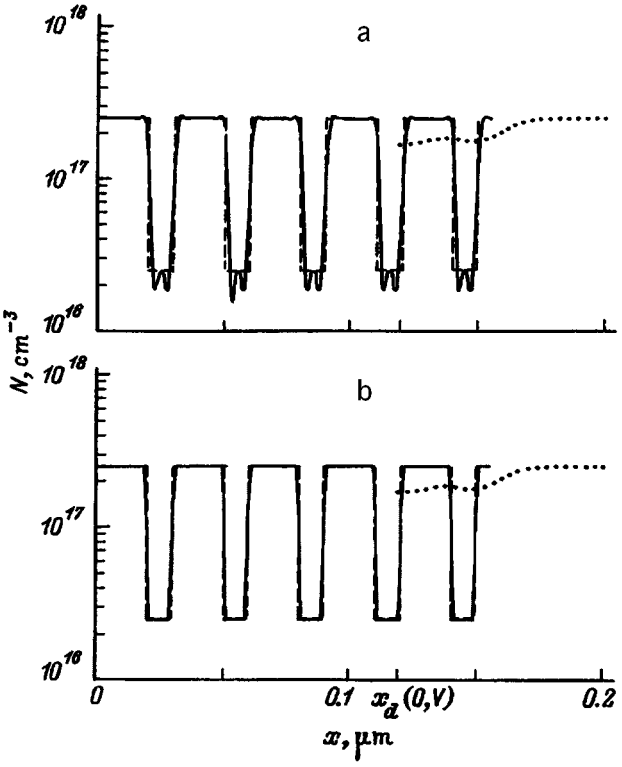

FIG. 2. Results of a numerical calculation of the doping profile (solid line) in the variants A (a) and B (b), as well as calculations on the basis of the standard equation (13) (dotted line). Dashed line — given profile.

The form of $N(x)$ and the computational results are presented in Figs. 2 and 3. The dashed line shows the initial profile and the dotted line shows the doping profile obtained with the standard approach (13). The position of the boundary of the depleted region, which is reached at the first etch step $x_e=0$, is marked in the figures. For the doping profile shown in Fig. 2, the nonuniform part of the structure is initially depleted. It is evident from the figures that to within the etch step the profiles computed in the variants A and B are identical to the given variant. The additional peaks in Figs. 2a and 3a are related to the numerical-differentiation errors, which were found to be greatest near the jumps in $N(x)$. For the structure shown in Fig. 3 with wider regions of constant density, the condition (7) breaks down; nonetheless, both profiling variants again give good agreement with the initial profile. In general, when the condition (7) is violated, the calculations in variant A lead to appreciable errors. In this case the standard calculation represented by the dots in Fig. 3 essentially does not show the structure of the impurity distribution.

The numerical calculations performed for different parameters of the problem show that the main difficulty in using the proposed Eqs. (15) and (16) arises due to the necessity of calculating high-order derivatives. This imposes stringent requirements on the accuracy of the initial data. Specifically, to use Eq. (15) the value of the capacitance must be known with a higher degree of accuracy than when Eq. (16) is used. On the other hand, Eq. (16) requires $C-V$ curves in a wider and more thoroughly computed voltage range.

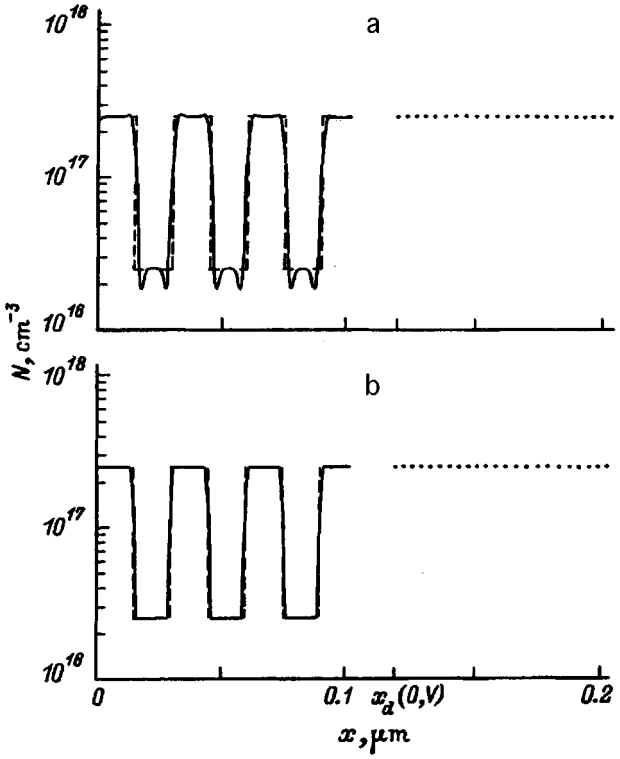

FIG. 3. Same as Fig. 2 but for a structure with wider regions of constant density.

6. CONCLUSIONS

A simple method has been proposed for reconstructing the doping fine structure by electrochemical $C-V$ profiling. The method makes it possible to reconstruct the doping profile directly from the semiconductor surface with a high spatial resolution on scales less than the Debye screening length. The resolution is formally limited by the size of the etch step, which can be equal to several nanometers.[4] The proposed approach can obviously be extended for analysis of more complicated semiconductor structures (for example, anisotropic structures, structures with degenerate statistics, and others).

This method has the drawback that numerical differentiation of the experimental data is required. This imposes stringent requirements on the accuracy of measurements and requires that the known experimental errors in the ECP procedure be reduced to a minimum.[4] The method can be implemented on the basis of known electrochemical profilometer schemes, for example, profilometers based on an automated digital system, as described in Ref. 11. The results of the profiling of real semiconductor structures will be published.

This work was sponsored by the Russian Fund for Fundamental Research under Project No. 95-02-05870a.

[1] E. H. Rhoderick and R. H. Williams, *Metal-Semiconductor Contacts* (1988).
[2] M. M. Faktor, T. Ambridge, and E. G. Bremner, *Apparatus and Method for Measuring Carrier Concentration in Semiconductor Materials*, U. K. Patent Specification No. 1482929 (1975).
[3] M. M. Faktor, T. Ambridge, C. R. Elliot, and J. C. Regnault, *Current Topics in Material Science*, edited by E. Kuldis, 1980, Vol. 6, p. 1.
[4] P. Blood, Semicond. Sci. Technol. **1**, 7 (1986).
[5] W. C. Johnson and P. T. Panousis, IEEE Trans. Electron. Dev. **ED-18**, 965 (1971).
[6] G. J. L. Ouwerling, Solid–State Electron. **33**, 757 (1990).
[7] K. Iniewski and C. A. T. Salama, Solid–State Electron. **34**, 309 (1991).
[8] M. F. Kokorev, N. A. Maleev, V. M. Ustinov, A. Yu. Egorov, and A. F. Zhukov, in *Abstracts of Reports at the Intern. Symp. on Nanostructures: Physics and Technology*, St. Petersburg, 1996, p. 161.
[9] V. A. Myamlin and Yu. V. Pleskov, *Electrochemistry of Semiconductors* [in Russian], Nauka, Moscow, 1965.
[10] L. H. Holway, IEEE Trans. Electron. Dev. **ED-37**, 1104 (1990).
[11] I. V. Irin and A. V. Murel', Prib. Tekh. Eksp., No. 6, 150 (1993).

Translated by M. E. Alferieff

Effect of pulsed laser irradiation on the optical characteristics and photoconductivity of the solid solutions CdHgTe

L. A. Golovan', P. K. Kashkarov, and V. Yu. Timoshenko[a)]

M. V. Lomonosov Moscow State University, 119899 Moscow, Russia

V. M. Lakeenkov

State Scientific-Research Institute of Rare Metals, Moscow, Russia

(Submitted September 23, 1996; accepted for publication December 25, 1996)
Fiz. Tekh. Poluprovodn. **31**, 931–935 (August 1997)

The melting threshold of $Cd_{0.2}Hg_{0.8}Te$ has been determined by numerical modeling of the irradiation of the material with nanosecond ruby-laser radiation pulses: $W_n = 40-50$ mJ/cm^2 with initial crystal temperature $T_0 = 100$ K and $W_m = 30-40$ mJ/cm^2 at $T_0 = 300$ K. Laser-induced modification of the surface of the sample under irradiation with energy density $W < W_m$ was found; it was manifested as a quenching of the stationary photoconductivity and an increase in the reflection coefficient. For laser irradiation with W above the melting threshold, the reflection coefficient increases further in the region up to $W \gtrsim 100$ mJ/cm^2 and decreases for $W > 110$ mJ/cm^2. For above-threshold irradiation, the photoconductivity signal was found to decrease monotonically with increasing energy density in the laser pulse; this can be explained by defect formation caused by laser-induced variation of the composition in the surface region. © *1997 American Institute of Physics.* [S1063-7826(97)00908-3]

The solid solutions $Cd_xHg_{1-x}Te$ find application in modern optoelectronics and are widely used in the fabrication of infrared radiation detectors. It is important to develop new methods of directed modification of the electrical and optical properties of this compound. They include pulsed laser irradiation (PLI), which is distinguished by the local nature and short duration of the action on a semiconductor.[1] Auger spectroscopy,[2,3] Rutherford backscattering,[3–5] and optical[6–8] investigations of laser-induced modifications of the structural, compositional, and recombination properties of CdHgTe have revealed a number of PLI-induced processes, including mercury depletion of the CdHgTe surface[4] and the appearance of a nonmonotonic distribution of the concentrations of the components.[3]

However, in the literature there is no general consensus concerning a number of questions regarding the PLI of CdHgTe. This refers primarily to the energy density W_m at which the CdHgTe surface melts during PLI. It is very important to know the value of W_m in order to clarify the question of the mechanisms of laser-induced modification of a semiconductor.[9] We note that there are no direct experimental measurements of W_m. The published computed values and the data obtained from indirect observations are very inconsistent. For example, in Refs. 2 and 6 the melting threshold for irradiation with nanosecond YAG:Nd-laser pulses is estimated to be 30–40 mJ/cm^2. In Ref. 8 the melting threshold for PLI of CdHgTe by ruby-laser radiation is taken to be 160 mJ/cm^2. The calculations performed in Ref. 10 for the case of irradiation with nanosecond ruby-laser pulses gave the value $W_m = 180$ mJ/cm^2. The latter values are very high, since CdHgTe is distinguished by low thermal conductivity and a low melting point.

Data on the variation of the electronic properties of CdHgTe under PLI are sparse and inconsistent. For example, in Ref. 7 a PLI-induced decrease of the photoconductivity (PC) signal was observed. In Ref. 8, in contrast, it was reported that irradiation with below- and above-threshold (from the standpoint of the authors) pulses increased the PC signal substantially. These inconsistencies could be due to the lack of accurate information about the melting threshold, as well as information about the laser-induced variation of the reflection coefficient. Laser-induced modification of the reflection coefficient could change the recorded PC signal.

In the present work we performed calculations of the temperature profiles in $Cd_{0.2}Hg_{0.8}Te$ in order to determine the melting threshold of a surface irradiated with nanosecond ruby-laser pulses. The PLI-induced changes in the reflection coefficient were investigated experimentally. The stationary PC signal from CdHgTe before and after laser action were measured.

1. NUMERICAL MODELING OF PULSED LASER IRRADIATION OF CdHgTe

The action of nanosecond ruby laser pulses on $Cd_xHg_{1-x}Te$ ($x = 0.2$) single crystals with initial surface temperatures $T_0 = 300$ and 100 K was studied. The latter value of the surface temperature was chosen because the PC measurements were performed at this temperature. The one-dimensional heat-conduction equation was solved[1]

$$\rho C(T)\frac{\partial T(x,t)}{\partial t} = \frac{\partial}{\partial x}\left[K(T)\frac{\partial T(x,t)}{\partial x}\right] + P(x,t)$$

with the boundary conditions

$$\left.\frac{\partial T}{\partial x}\right|_{x=0} = 0, \quad T|_{x\to\infty} = T_0,$$

where ρ is the density, $C(T)$ is the specific heat, $K(T)$ is the thermal conductivity, $P(x,t)$ is the heat generation function,

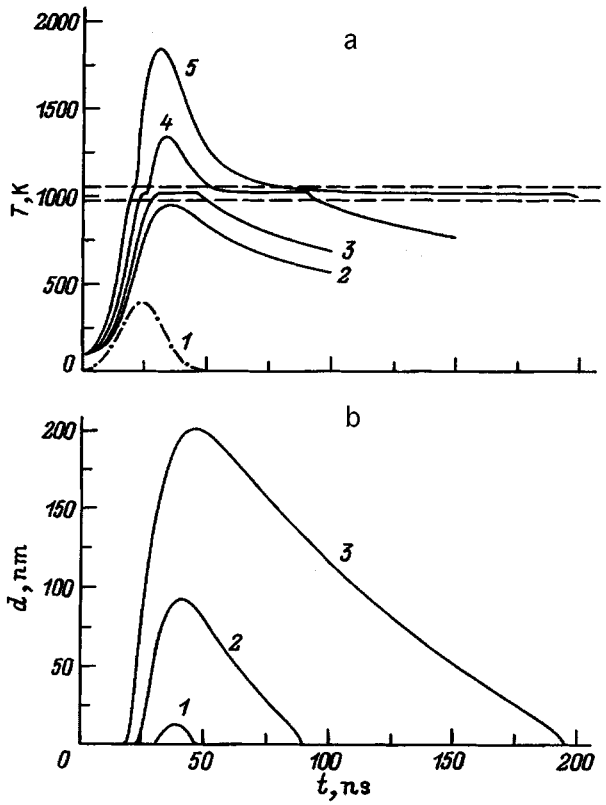

FIG. 1. a — Surface temperature (T) of $Cd_{0.23}Hg_{0.77}Te$ as a function of the irradiation time (t). W, mJ/cm^2: *2* — 40, *3* — 50, *4* — 70, *5* — 110; $T_0=100$ K; *1* — laser pulse. The dashed lines correspond to $T=975$ and 1050 K between which melting occurs. b — Thickness d of the melted layer as a function of irradiation time t with $W=50$ (*1*), 70 (*2*), 110 (*3*) mJ/cm^2 and $T_0=100$ K.

$$P(x,t)=(1-R)\alpha I(t)\exp(-\alpha x),$$

α is the absorption coefficient, R is the reflection coefficient, and $I(t)$ is the intensity of the laser pulse.

It was assumed that the laser pulse is a Gaussian with a 20-ns duration at half-maximum. In the calculations the functions $C(T)$ and $K(T)$ from Ref. 10 , extrapolated to low temperatures in the case of irradiation at $T_0=100$ K, were used. In accordance with the data of Ref. 11 , it was assumed that the absorption coefficient in the solid phase is $\alpha=1.3\times10^5$ cm^{-1} and the reflection coefficient is $R=0.35$ (α and R were assumed to be temperature-independent). The absorption coefficient of $Cd_{0.2}Hg_{0.8}Te$ in the liquid phase was chosen to be 5×10^5 cm^{-1} (Ref. 12), and the reflection coefficient was assumed to be constant since it changes very little on melting (see below). The melting temperature was chosen to be $T_m=1018$ K, i.e. it falls between the values 975 and 1063 K, which determine the temperature range of the solid–liquid phase transition in the solid solution $Cd_{0.2}Hg_{0.8}Te$.[13]

Figure 1a shows a curve of the temperature of the semiconductor surface (T) and Fig. 1b shows the thickness of the melted layer (d) for the case of irradiation at $T_0=100$ K. As one can see from Fig. 1, for $W\simeq50$ mJ/cm^2 the surface temperature reaches T_m, and the thickness of the melt is about 10 nm. Taking into account the range of melting temperatures for the solid solution CdHgTe, at $T_0=100$ K the melting threshold W_m lies in the range of energy densities 40–50 mJ/cm^2. As the energy density W increases, the surface temperature and thickness of the melted layer also increase, reaching 1850 K and 200 nm, respectively, for $W=110$ mJ/cm^2.

Similar calculations for an initial crystal temperature $T_0=300$ K give melting thresholds of 30–40 mJ/cm^2, in agreement with the value of W_m obtained in Ref. 2 on the basis of an analysis of compositional changes.

2. EXPERIMENTAL PROCEDURE

$Cd_{0.23}Hg_{0.77}Te$ single crystals with [111] orientation grown by a modified Bridgman method with the melt zone constantly replenished with a solid phase were used. Prior to the experiments the samples were treated in a solution of bromine in ethanol.

Irradiation was conducted with ruby laser pulses (wavelength $\lambda=694$ nm, pulse length $\tau=20$ ns) in vacuum at $T_0=100$ K. A quartz homogenizer was used to obtain uniform and unpolarized radiation.[9]

Both the static and dynamic variations of the reflection coefficient with a single PLI were measured. The intensity of the Ar^+-laser probe beam ($\lambda=488$ nm) reflected from the sample surface was recorded for this purpose. The temporal resolution of the recording system was no worse than 5 ns.

The measurement of the recombination properties with repeated irradiation by pulses of different energy densities was monitored by the method of stationary PC excited by continuous Ar^+ and He–Ne laser radiation with $\lambda=488$, 633, and 1150 nm at 100 K. The intensities of the radiation employed were approximately the same.

3. EXPERIMENTAL RESULTS

Figure 2 shows the time dependences of the reflection coefficient during irradiation with different energy densities. Even at $W=28$ mJ/cm^2 the variations of the reflection coefficient ΔR become appreciable, and they increase with W. For $W>30$ mJ/cm^2 the reflection coefficient does not return to its initial value R_0. Indeed, as one can see from Fig. 3, the stationary reflection coefficient increases under PLI with $W=30-100$ mJ/cm^2. Laser action with energy densities $W>100$ mJ/cm^2 decreases the reflection coefficient, as one can see from Fig. 2 (curve *6*) and Fig. 3. An increase in the diffuse scattering of light from the sample surface was observed at the same time. Measurements of the spectral dependence of the reflection coefficient of CdHgTe samples showed that large changes in the form of the spectrum in the range 0.4–1 μm do not occur after PLI with the energy densities employed.

The dependence of the stationary PC I_{PC} on the energy density is shown in Fig. 4. One can see that the PC signal starts to decrease at $W=27$ mJ/cm^2. The magnitude of the change in the PC increases with the PLI energy density and approaches a stationary value. The degree of quenching of the PC increases with decreasing wavelength of the exciting light.

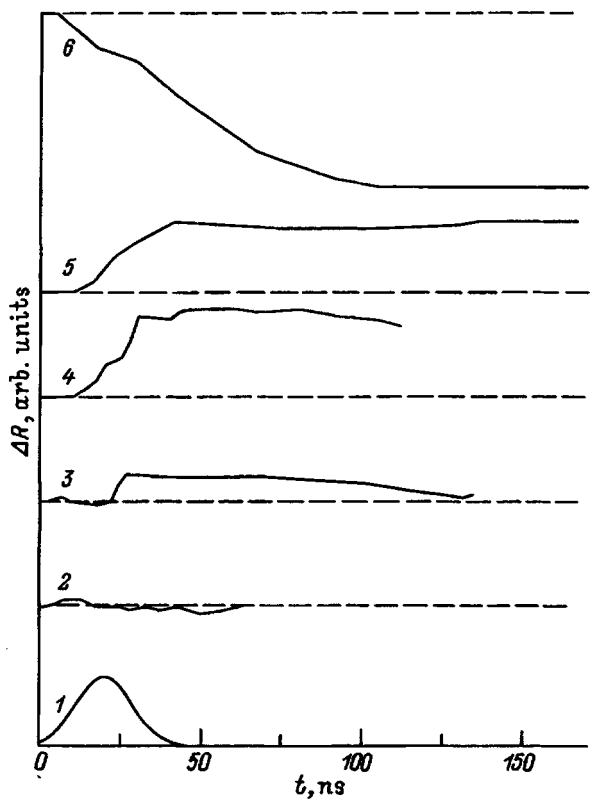

FIG. 2. Dynamics of the change ΔR in the reflection coefficient of $Cd_{0.23}Hg_{0.77}Te$ under irradiation. w, mJ/cm^2: *2* — 19, *3* — 28, *4* —32, *5* — 77, *6* — 123; $T_0=100$ K. *1* — Laser pulse.

4. DISCUSSION

Laser-induced changes in the reflection coefficient and PC start at $W\simeq 30$ mJ/cm^2. This figure is less than the value determined in the calculations of the melting threshold, $W_m=40-50$ mJ/cm^2. This probably indicates that subthreshold processes can occur during PLI of CdHgTe. A possible subthreshold process is the sublimination of the components during heating. For example, mercury, characterized by saturated vapor pressure $p_s\simeq 30$ atm at $T=970$ K (Ref. 14), can effectively evaporate before melting starts. This agrees with the data obtained in Ref. 15 with pulsed thermal annealing of CdHgTe. In interpreting the changes in the reflection coefficient and the PC, the possibility of other subthreshold mechanisms of laser-induced defect formation in the surface region, for example, the electronic-deformation-thermal mechanism,[9] also cannot be ruled out.

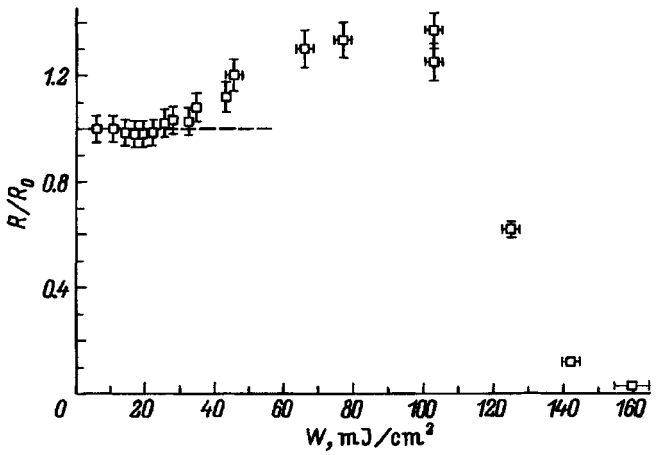

FIG. 3. Stationary reflection coefficient of $Cd_{0.23}Hg_{0.77}Te$ versus the energy density in the laser pulse. $T_0=100$ K.

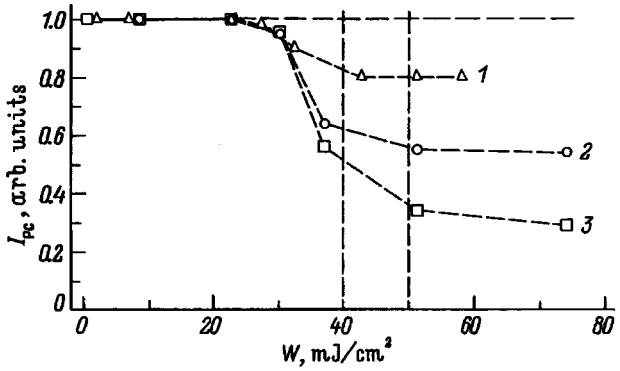

FIG. 4. Stationary photoconductivity I_{PC} of $Cd_{0.23}Hg_{0.77}Te$, normalized to the initial value, versus the PLI energy density. Wavelength of the exciting light λ, μm: *1* — 1.15, *2* — 0.633, *3* — 0.488. The vertical lines indicate the energy-density interval containing the melting threshold. $T_0=100$ K.

Let us now discuss the changes occurring in the properties of CdHgTe under irradiation with energies $W\geqslant W_m$. The maximum PLI-induced increase in the reflection coefficients (Fig. 3) reaches 30% ($R\simeq 0.45$), which corresponds to the magnitude of the change in the reflection coefficient of CdTe under PLI[16] but is less than the analogous variations under laser irradiation of IV and III–V materials.[17] We note, however, that the dynamics of the PLI-induced variation of the reflection coefficient of CdHgTe differs substantially from the dynamics of variation of the reflection coefficient of CdTe and IV and III–V materials, for which a nonmonotonic variation of $R(t)$ during laser irradiation was recorded. This difference could be due to the more complicated PLI-induced compositional changes occurring in CdHgTe.

The PLI-induced increase in the reflection coefficient for $30<W<100$ mJ/cm^2 can be explained by the change in the crystal structure of the surface layer. Another reason could be a separation of a high-reflection phase (for example, a Hg- or Te-enriched phase) in a layer near the surface. The annealing, observed in Ref. 4, of ion-implanted $Cd_xHg_{1-x}Te$ by ruby laser pulses attests to the first assumption. The second assumption — the separation of a Hg-enriched phase on the surface — was advanced in Ref. 6. In Ref. 2 the mercury concentration at a depth of 5–10 nm was observed to increase. Although an increase in the Hg concentration was not observed in other investigations of PLI-induced changes in the composition of CdHgTe,[3,4] in Ref. 18, where the experimental results of Ref. 3 are explained on the basis of evaporation, diffusion, and segregation of Hg in the melt, it was shown that a thin mercury-enriched layer can form. The possibility that a thin Te-enriched layer forms on the surface of samples after laser action, with which the observed increase in the reflection coefficient could be associated, also cannot be ruled out. However, we know of no direct experimental

evidence of the segregation of tellurium in CdHgTe after PLI.

The PLI-induced decrease in the reflection coefficient for $W>110$ mJ/cm^2 is due primarily, in our view, to the intense evaporation and boiling of the melted layer, which result in substantial damage to the surface. This conclusion is confirmed by the fact that electron-microscopic investigations of CdHgTe samples subjected to PLI with $W=100-150$ mJ/cm^2 show an appreciable change in surface morphology.[2,8]

Let us now discuss the data on the effect of above-threshold PLI on the PC. The magnitude of the laser-induced quenching of PC cannot be explained by a change in the reflection coefficient in view of the small variations and constancy of the shape of the spectrum of the reflection coefficient after PLI. Consequently, it can be concluded that the lifetime of the minority charge carriers decreases as a result of defect formation. The high degree of quenching of PC excited by shorter wavelength radiation is explained by surface localization of the defects which are produced. The PC reaches a stationary value probably as a result of the contribution of charge carriers which had been differentiated into the bulk. Indeed, the diffusion length of charge carriers in CdHgTe is 10 μm,[19] while for $W=70$ mJ/cm^2 the thickness of the fused layer does not exceed the value 100 nm (see Fig. 1b) and the thickness of the defect layer formed as a result of laser action with the same energy density, determined by the Rutherford backscattering method, is 40 nm. A change in the composition of the surface region can be suggested as a possible mechanism of defect formation. The latter mechanism is confirmed by variations of the reflection coefficient after PLI. The character of the possible PLI-induced composition modifications (profiles of the distribution of the components) requires further investigation.

In summary, we calculated the temperature profiles in $Cd_{0.2}Hg_{0.8}Te$. The melting threshold of this material was determined by the nanosecond ruby laser pulses. It was found to be $W_m=40-50$ mJ/cm^2 with initial crystal temperature $T_0=100$ K and $W_m=30-40$ mJ/cm^2 at $T_0=300$ K. We observed laser-induced formation of defects as a result of irradiation with $W<W_m$. It manifested itself as a quenching of the stationary PC and an increase in the reflection coefficient. Laser action with $W\geqslant W_m$ results in a nonmonotonic dependence of the reflection coefficient on the energy density: An increase for $W<100$ mJ/cm^2 and a decrease for $W>110$ mJ/cm^2. The PC signal decreases under above-threshold irradiation; this can be explained by laser-induced defect formation due to, for example, a PLI-induced change in the composition of the damaged region. Photoconductivity measurements performed at different wavelengths attest to the surface nature of the laser-induced defects.

[a)]e-mail: vtim@ofme.phys.msu.su

[1] A. V. Dvurechenskiĭ, G. A. Kachurin, E. V. Nidaev, and L. S. Smirnov, *Pulsed Annealing of Semiconductor Materials* [in Russian], Nauka, Moscow, 1982.
[2] P. V. Goloshikhin, K. E. Mironov, and A. Ya. Polyakov, Poverkhnost'. Fizika, Khimiya, Mekhanika, No. 12, 12 (1991).
[3] C. N. Afonso, M. Alonso, J. L. N. Neira, A. D. Sequeira, M. F. da Silva, and J. C. Soares, J. Vac. Sci. Technol. A **7**, 3258 (1989).
[4] G. Bahir and R. Kalish, Appl. Phys. Lett. **39**, 730 (1981).
[5] L. A. Golovan', A. Perez Navarro, P. K. Kashkarov, V. S. Kulikauskas, V. Yu. Timoshenko, and N. G. Chechenin, Poverkhnost'. Fizika, Khimiya, Mekhanika [in press].
[6] G. G. Gromov, S. V. Seregin, S. V. Zhuk, and V. B. Ufimtsev, Fiz. Khim. Obrab. Materialov, No. 4, 19 (1990).
[7] I. S. Virt, A. S. Lyubchenko, P. E. Mozol', and V. A. Gnatyuk, Fiz. Tekh. Poluprovodn. **23**, 1386 (1986) [Sov. Phys. Semicond. **23**, 862 (1986)].
[8] P. E. Mozol, V. V. Borsch, V. A. Gnatyuk, E. P. Kopishynskaya, and A. I. Vlasenko, Semicond. Sci. Technol. **10**, 61 (1995).
[9] P. K. Kashkarov and V. Yu. Timoshenko, Pverkhnost'. Fizika, Khimiya, Mekhanika, No. 6, 5 (1995).
[10] M. M. Jevtić and M. J. Šćepanović, Appl. Phys. A **53**, 332 (1991).
[11] L. Vi na, C. Umbach, M. Cardona, and L. Vodopyanov, Phys. Rev. B **29**, 6752 (1984).
[12] R. O. Bell, M. Toulemonde, and P. Siffert, Appl. Phys. **9**, 313 (1979).
[13] J. C. Brice, P. Capper, and C. L. Jones, J. Cryst. Growth **75**, 395 (1986).
[14] D. Long and J. L. Schmidt, *Semiconductors and Semimetals*, 1970, Vol. 5, p. 185.
[15] K. C. Demiduk, W. G. Opyd, J. F. Gibbons, T. W. Sigmon, T. J. Magee, and R. D. Ormond, J. Vac. Sci. Technol. A, *1*, 1661 (1983).
[16] L. A. Golovan', P. K. Kashkarov, and V. Yu. Timoshenko, Pis'ma Zh. Tekh. Fiz. **21**(23), 26 (1995) [Tech. Phys. Lett. **21**, 251 (1995)].
[17] P. K. Kashkarov, V. Yu. Timoshenko, N. G. Chechenin, and A. N. Obraztsov, Laser Physics **2**, 790 (1992).
[18] M. Šcepanović and M. Jevtić, Phys. Status Solidi A **147**, 379 (1995).
[19] N. S. Baryshev, B. L. Gel'mont, and M. I. Ibragimov, Fiz. Tekh. Poluprovodn. **24**, 209 (1990) [Sov. Phys. Semicond. **24**, 127 (1990)].

Translated by M. E. Alferieff

Effect of an electric field on the relaxation of photoconductivity in n-$Hg_{0.8}Cd_{0.2}Te$ crystals

I. S. Virt

I. Franko State Pedagogical Institute, 293720 Drogobych, Ukraine
(Submitted April 24, 1996; accepted for publication December 25, 1996)
Fiz. Tekh. Poluprovodn. **31**, 936–938 (August 1997)

The effect of a pulling electric field on the relaxation curves of the photoconductivity of n-$Hg_{0.8}Cd_{0.2}Te$ crystals has been investigated. It is shown that as the field intensity increases, the relaxation time of the slow component increases and that of the fast component decreases. The contribution of the slow component also decreases. This behavior of photoconductivity relaxation is due to the change in the energy-band bending near macrodefects in the presence of an electric field and to a change in the feeding of nonequilibrium charge carriers to the macrodefects. © *1997 American Institute of Physics.* [S1063-7826(97)01007-7]

The most widely used method of measuring nonequilibrium charge carrier (NCC) lifetimes is photoconductivity relaxation (nonstationary photoconductivity), which makes it possible to determine this characteristic directly. In combination with the stationary photoconductivity method, it is also possible to determine the presence of recombination centers (trapping centers) and attachment centers.[1] The pulling electric field, which is used for measuring the lifetime of NCCs, in $Hg_{1-x}Cd_xTe$ crystals can change the course of photoprocesses. For example, extraction of NCCs from crystals is observed for high values of the electric field.[2]

In most cases the photoconductivity (PC) relaxation curves which are ordinarily used to determine the NCC lifetime consist of several (at least two) exponentials.[3] For example, in the case of NCC recombination with the participation of local centers (Shockley–Read recombination), when the lifetime τ_n of the nonequilibrium electrons is much shorter than the lifetime τ_p of nonequilibrium holes, i.e., $\tau_n \ll \tau_p$, a fast electronic component, which is replaced by a slow hole component, is observed on the PC relaxation curve for short observation times.

1. EXPERIMENTAL PART

In this work the PC relaxation curves were investigated as a function of the electric field intensity. Samples with electronic-type conductivity, electron density $n=3\times10^{14}$ cm^{-3}, and electron mobility $\mu_n=8\times10^4$ (sample 1) and 2×10^5 $cm^2/(V\cdot s)$ (sample 2) were employed. The dimensions of the samples were $5\times1\times0.3$ mm. The photoconductivity was measured under the action of CO_2-laser radiation pulses with wavelength $\lambda=10.6$ μm and duration $\Delta t\simeq100$ ns. Filters were used to obtain low and high levels of photocarrier generation.

The PC relaxation curves (with an electric field $E=0.1$ V/cm in the sample) are shown in Fig. 1. It follows from Fig. 1 that the shape of the relaxation curve is determined not only by the excitation level but also by the characteristics of the samples. Two exponentials are seen in the relaxation curves constructed in semilogarithmic coordinates (Figs. 2) — fast and slow. The temperature dependences of the NCC (holes) lifetime, estimated according to the slow PC relaxation component, show that the activational character that is characteristic of the Shockley–Read NCC recombination mechanism is absent in the extrinsic conductivity region. This indicates that in this region an Auger mechanism, for which $\tau_n=\tau_p$, is the dominant NCC recombination process. It is obvious that the fast PC component is due not to the predominant electronic recombination but probably due to the participation of other competing channels, in which macrodefects can play a role (surface, block boundaries, composition inhomogeneities, and etc.); in addition to the volume NCC recombination channel. For example, in the sample with the lower value of μ_n (sample 1), evidently the PC is characterized by two exponential relaxation sections because of the high density of scattering centers.

Curves of the characteristic relaxation time versus the electric field strength with a low excitation level are shown in Fig. 3. The relative contribution of each component A_s/A_f (where A_s and A_f are, respectively, the amplitudes of the slow and fast PC components), are also shown. As the electric field increases, the characteristic time of the fast component decreases and that of the slow component increases. The weight of the slow component decreases. The relaxation times remain nearly constant for electric fields $E\leqslant1$ V/cm. In a more homogeneous sample with low biases, the PC contains one component that splits into two components as the electric field increases. The amplitude of the slow component decreases as a function of the field more rapidly in the homogeneous than in the inhomogeneous samples.

Similar changes also occur with a high excitation level. In this case the curve $\tau(E)$ for the fast and slow components of the inhomogeneous sample passes through a maximum. The ratio A_s/A_f as a function of the field does not vary as much with a high excitation level as with a low excitation level.

2. DISCUSSION

The complicated character of the PC relaxation curves and the variation in these curves under the action of an electric field in the case of an Auger NCC recombination mechanism can be explained by the presence of nonuniformities in

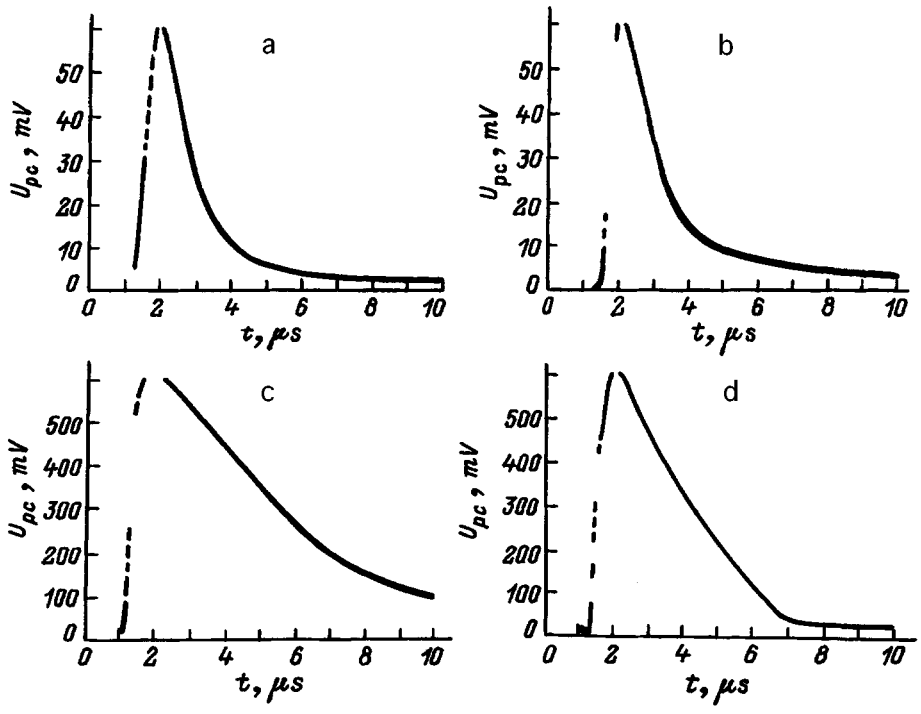

FIG. 1. Photoconductivity relaxation curves of samples *1* (a, c) and *2* (b, d) with low (a, b) and high (c, d) excitation levels. The pulling electric field $E=0.1$ V/cm.

the crystals of the solid solutions $Hg_{1-x}Cd_xTe$. The internal macrodefects, especially their surface, are a natural sink for NCCs[4] whose recombination rate is higher that in the bulk. Therefore, the change of the photoconductivity signal $U_{pc}(t)$ in time t is determined by two channels[3] — recombination of NCCs in the bulk and feeding of NCCs to macrodefects with subsequent recombination on them:[5]

$$U_{pc}(t)=A\ \exp(-t/\tau_v)+B\ \exp(-t/\tau_s), \tag{1}$$

where τ_v and τ_s are the volume and surface NCC lifetimes.

In the case where the difference in the recombination rates of NCCs in the bulk and on macrodefects is small, so that the NCC recombination rate on the surface of macrodefects (s) can be regarded as low, the surface lifetime τ_s is determined by the diffusion (feeding) of macrodefects to the boundaries and in the simplest case (a flat surface of a macrodefect) depends on their density:

$$\tau_s=d^2/\pi D_p, \tag{2}$$

where D_p is the diffusion coefficient of nonequilibrium holes, and d is the distance between macrodefects. The fast PC component is determined by the shorter time — τ_s.

The electric field accelerates the feeding of NCCs to macrodefects, and the characteristic time of the fast PC relaxation component is given by

$$\tau_{s\ \mathrm{eff}}=\frac{\tau_s}{1+(\tau_s/d)\mu_a E}, \tag{3}$$

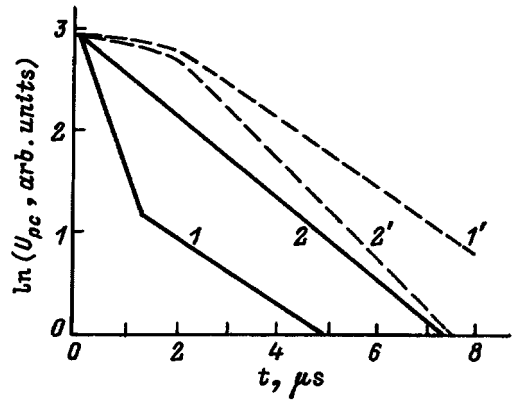

FIG. 2. Photoconductivity relaxation curves of samples 1 (*1*, *1′*) and 2 (*2′*, *2′*) with low (1, 2) and high (*1′*, *2′*) excitation levels. The pulling electric field $E=0.1$ V/cm.

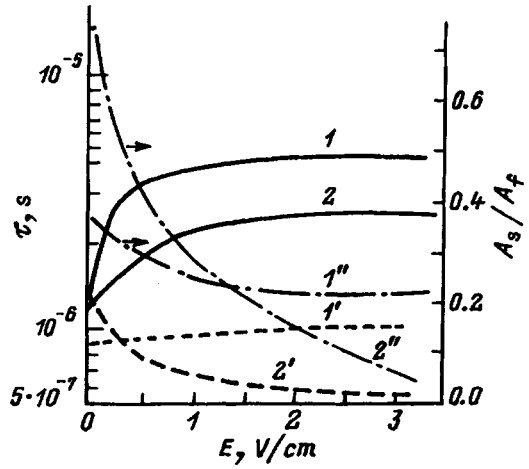

FIG. 3. Field dependences of the characteristic relaxation times of the slow (*1*, *2*) and fast (*1′*, *2′*) components with a low excitation level and also the ratio A_s/A_f (*1″*, *2″*) for samples 1 and 2, respectively.

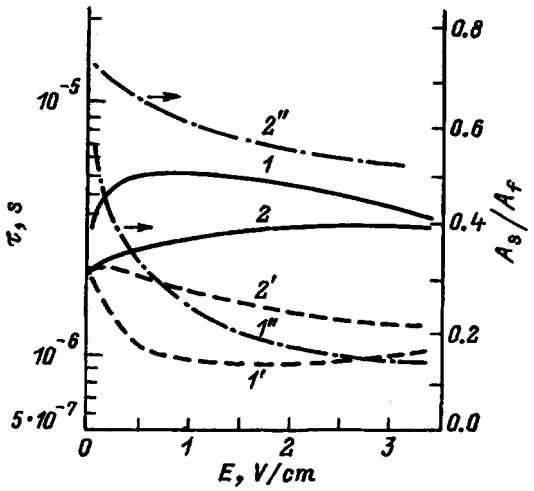

FIG. 4. Field dependences of the characteristic relaxation time of the slow and fast photoconductivity components with a high excitation level as well as the ratio A_s/A_f. The labeling of the curves is the same as in Fig. 3.

where μ_a is the ambipolar mobility of NCCs. Therefore, the characteristic relaxation time of the fast component decreases as the field increases (Fig. 4). The characteristic time of the slow component increases because of the decrease in energy barriers (band fluctuations) inside the crystal matrix. For high electric field strengths, NCC extraction is superimposed on the dependence $\tau_\nu(E)$. This is more strongly manifested in an inhomogeneous sample. In this case, the electric field decreases the measured lifetime $\tau_{\nu\,\mathrm{eff}}$ according to the expression

$$\tau_{\nu\,\mathrm{eff}}=\frac{\tau_\nu}{1+(\tau_\nu/l)\mu_a E}, \tag{4}$$

where l is the length of the sample.

As the field increases, the amplitude of the fast component also increases because of the dominant role of the NCC recombination on the surfaces of macrodefects. For high NCC excitation levels, the surface bending of energy bands at the interface of the crystal matrix and a macrodefect, which increases the surface recombination rate s, also changes. Judging from the dependence of A_s/A_f on E, this decreases the contribution of the fast PC component.

In summary, the effect of an electric field on PC relaxation in $Hg_{1-x}Cd_xTe$ crystals is due to a change in the rate at which NCCs are fed to recombination macrodefects and to a change in the energy-band bending at an interface with macrodefects.

[1] S. M. Ryvkin, *Photoelectric Phenomena in Semiconductors* [in Russian], Fizmatgiz, Moscow, 1963.
[2] A. I. Vlasenko and A. V. Lyubchenko, Fiz. Tekh. Poluprovodn. **28**, 1219 (1994) [Semiconductors **28**, 695 (1994)].
[3] V. S. Lopes, A. J. Syllaios, and M. C. Chen, Semicond. Sci. Technol. **44**, 824 (1993).
[4] A. I. Elizarov, V. I. Ivanov-Omskiĭ, A. A. Kornniyash, and V. A. Petryakov, Fiz. Tekh. Poluprovodn. **18**, 201 (1984) [Sov. Phys. Semicond. **18**, 125 (1984)].
[5] V. N. Ovsyuk, *Electronic Processes in Semiconductors with a Space-Charge Region* [in Russian], Novosibirsk, Nauka, 1984.

Translated by M. E. Alferieff

Calculation of the size-quantization levels in strained ZnCdSe/ZnSe quantum wells

M. V. Maksimov, I. L. Krestnikov, S. V. Ivanov, N. N. Ledentsov, and S. V. Sorokin

A. F. Ioffe Physicotechnical Institute, Russian Academy of Sciences, 194021 St. Petersburg, Russia
(Submitted December 16, 1996; accepted for publication December 25, 1996)
Fiz. Tekh. Poluprovodn. **31**, 939–943 (August 1997)

The ZnSe and CdSe parameters required to calculate levels in ZnCdSe/ZnSe quantum wells are determined by fitting to published data. The model is shown to be adequate for the example of structures with a collection of quantum wells whose thickness and composition were determined by independent methods. © *1997 American Institute of Physics.* [S1063-7826(97)01108-3]

1. INTRODUCTION

A great deal of attention has been directed in recent years to the development of optical blue-green-range II–VI semiconductor lasers. Since the active region in these devices is a ZnCdSe quantum well (QW) or a collection of quantum wells in a ZnSe matrix, it is of interest to calculate the interband optical transition energies. This problem has long been solved for the system GaAs/AlGaAs, and the solution is used, specifically, for determining the thickness of a QW according to the transition energy. However, the system ZnCdSe/ZnSe has been studied not nearly as extensively, indicating a need for further investigations.

In the present paper we generalize the published data on the optical transition energies and use them to determine some physical parameters of ZnSe and CdSe which are required for calculations. In addition, we grew structures with a collection of ZnCdSe QWs, in which the QW thicknesses and composition were determined by transmission electron microscopy (TEM) and by growth gauging, respectively. The calculation of the transition energies on the basis of the parameters determined from published data gave good agreement with experiment, indicating that our model is adequate.

2. EXPERIMENTAL

Epitaxial structures were grown in a molecular beam epitaxy system (EP-1203) on GaAs (100) substrates.[1] Elemental Zn(6*N*), Se(6*N*), and Cd(6*N*) were used as molecular-beam sources. A cryostat, in which the sample was located in a helium gas flow at a temperature of 80 K was used for investigations of the photoluminescence (PL). A halogen lamp, whose light was passed through a monochromator, was used as the excitation source. A MDR-23 monochromator and a cooled photomultiplier operating in the photon-counting mode were used as a recording system.

3. COMPUTATIONAL MODEL

In contrast to the GaAs/AlGaAs system mentioned above, the ZnSe lattice parameter is different from that of CdSe. As a result, the structure with a ZnCdSe QW in a ZnSe matrix is strained. The elastic stresses change the width of the band gap in the deformed material and therefore also the potential barrier in the QW. In the case of pseudomorphous growth, i.e., when the lattice parameter of the QW is ''inherited'' from the matrix, the deformation can be represented as a superposition of a hydrostatic deformation and a shear deformation.[2] The hydrostatic stress due to the hydrostatic deformation changes the difference of the valence- and conduction-band centers of gravity by the amount

$$\Delta E^{hy}=2a\left(1-\frac{C_{12}}{C_{11}}\right)\left(\frac{a_0^b}{a_0}-1\right), \tag{1}$$

where a_0 and a_0^b are, respectively, the lattice parameters of the unstrained well material and matrix, C_{11} and C_{12} are the elastic constants of the well material, and a is the hydrostatic deformation potential for the bandgap. Shear stress, in contrast to hydrostatic stress, affects only the valence band. Here the change in the energy position of the heavy- and light-hole bands is different as a result of the difference in their symmetry properties. This effect leads to an additional splitting of the heavy- and light-hole levels compared to the quantum-well effect. For some ZnCdSe compositions, the edge of the light-hole band can lie at a lower energy in the QW than in the barrier; i.e., a type-II QW for the light hole can occur. In this case there is no localizing potential for the light hole and transitions occur from electronic levels into a state of the barrier. The changes in the energy position of the heavy-hole band (ΔE_h^{sh}) and the light-hole band (ΔE_l^{sh}) relative to the degenerate position are determined by

$$\Delta E_h^{sh}=\delta E^{sh}, \tag{2}$$

$$\Delta E_l^{sh}=\frac{1}{2}\left[\Delta_0-\frac{1}{2}\,\delta E^{sh}-\sqrt{(\Delta_0+\delta E^{sh})^2+8(\delta E^{sh})^2}\right], \tag{3}$$

where Δ_0 is the spin-orbit splitting and

$$\delta E^{sh}=-b\left(1+2\frac{C_{12}}{C_{11}}\right)\left(\frac{a^b}{a_0}-1\right), \tag{4}$$

Here b is the shear deformation potential. Then the effective band gap in the well for the heavy ($E_{g,w}^{\mathrm{eff},h}$) and light ($E_{g,w}^{\mathrm{eff},l}$) holes and the band offset are

$$E_{g,w}^{\mathrm{eff},h(l)}=E_{g,w}+\Delta E^{hy}+\Delta E_{h(l)}^{sh}, \tag{5}$$

$$U_e=(1-Q)(E_{g,b}-E_{g,w}^{\mathrm{eff},h}), \tag{6}$$

$$U_h=Q(E_{g,b}-E_{g,w}^{\mathrm{eff},h}), \tag{7}$$

$$U_l=E_{g,b}-E_{g,w}^{\mathrm{eff},l}-U_e, \tag{8}$$

where $E_{g,b}$ and $E_{g,w}$ are the band gaps of the unstrained barrier and QW materials, respectively, and Q is the relative valence-band offset for the heavy hole. The quantity U_l can

TABLE I. Physical parameters of ZnSe and CdSe employed in the calculations.

	References		Calculation	
	ZnSe	CdSe[a]	ZnSe	CdSe[a]
a_0, Å	5.65 (Ref. 2), 5.6676 (Refs. 3,4)	6.077 (Ref. 3), 6.052 (Ref. 4)	5.6676	6.077
E_g, eV	2.83[b] (Ref. 2), 2.82[b] (Refs. 3,5,6,7)	1.9[b] (Ref. 4), 1.77[b] (Ref. 5), 1.765[b] (Refs. 3,6), 1.8[b] (Ref. 7)	2.81[c]	1.79[c,d]
Δ_0, eV	0.43 (Ref. 2)	0.42 (Ref. 2)	0.43	0.42
C_{11}, 10^{10} N/m^2	8.26 (Refs. 2,3,5,6), 8.59 (Ref. 4)	7.49 (Ref. 5), 6.67 (Refs. 3,4,6)	8.26	6.67
C_{12}, 10^{10} N/m^2	4.98 (Refs. 2,3,5,6), 5.06 (Ref. 4)	4.61 (Ref. 5), 4.63 (Refs. 3,4,6)	4.98	4.63
a, eV	−5.82 (Refs. 2,5), −5.4 (Ref. 4), −4.25 (Ref. 6)	−3.45 (Ref. 4), −3.664 (Ref. 6)	−4.7[d]	−2.6[d]
b, eV	−1.2 (Refs. 2,3,4,5,6)	−1.1 (Ref. 5), −0.8 (Refs. 3,4,6)	−1.2	−0.8
m_{el}/m_0	0.16 (Refs. 3,5,6), 0.14 (Ref. 4)	0.13 (Refs. 3,5,6), 0.11 (Ref. 4)	0.16	0.13
m_{hh}/m_0	0.6 (Refs. 3,6), 1.4 (Ref. 5), 0.49 (Ref. 4)	1.23 (Ref. 5), 0.45 (Refs. 3,4,6)	0.6	0.45
m_{lh}/m_0	0.145 (Refs. 3,4), 0.15 (Ref. 5)	0.145 (Ref. 4)	0.15	0.145
B, eV	0.35 (Ref. 4), 0.75 (Ref. 5), 0.26 (Ref. 5), 0.51 (Ref. 7)		0.45[d]	
Q	0.25 (Ref. 4)		0.20[d]	

Note: [a]For the cubic modification. [b]For 5 K. [c]For 77 K. [d]Fitted parameter.

take on negative values, which corresponds to a type-II QW. The parameters for a solid solution in a $Zn_{1-x}Cd_xSe$ well with composition x are determined in a quadratic approximation for E_g and a linear approximation for all other parameters (B is the coefficient of the quadratic nonlinearity):

$$E_{g,w}=x\cdot E_{g,\mathrm{CdSe}}+(1-x)\cdot E_{g,\mathrm{ZnSe}}-x(1-x)B, \tag{9}$$

$$par=x\cdot par_{\mathrm{CdSe}}+(1-x)par_{\mathrm{ZnSe}}, \tag{10}$$

where par is any parameter except E_g.

The energy levels ε in the potential wells are determined from the transcendental equation

$$\pm\left(\sqrt{\frac{m_w}{m_b}(U-\varepsilon)}\right)^{\pm 1}=\tan\left(\sqrt{\frac{m_w\varepsilon}{2}}\frac{L}{\hbar}\right), \tag{11}$$

where the plus sign corresponds to odd levels and the minus sign corresponds to even levels; m_b and m_w are the effective masses of particles in the barrier and QW, respectively (we disregarded the spatial anisotropy of the masses), U is the height of the potential barrier, and L is the thickness of the QW. The optical transition energy can then be written

$$\hbar\omega=E_{g,w}^{\mathrm{eff}}+\varepsilon_e+\varepsilon_{h(l)}-E_x, \tag{12}$$

where E_x is the exciton binding energy. In the case of a type-II QW it is pointless to talk about a light-hole quantum-well level, and $\varepsilon_l=0$ since transitions occur into a state of the barrier. In our model we ignored the dependence of the exciton binding energy on the QW composition and thickness (E_x can vary from 21 meV for bulk material up to ~40 meV for a QW less than 50 Å thick[4]). However, we employed different binding energies for heavy- and light-hole excitons: For the ''heavy'' exciton $E_x=30$ meV and the value is lower ($E_x=20$ meV) for the ''light'' exciton because the reduced mass is smaller and because type-II QWs can be realized for light holes, which also lowers the exciton binding energy.

4. RESULTS AND DISCUSSION

In order to use the above-described model for calculations, it is necessary to know the numerical values of the physical parameters of ZnSe and CdSe. They are summarized in Table I. Some parameters are known with an adequate degree of reliability, but for others the published data differ substantially. We attempted in this connection to systematize the published data on optical transition energies in ZnCdSe/ZnSe QWs (published data on the thickness and composition of QWs are presented in Table II) and to choose on the basis of these data the parameter values that give the best agreement between the calculations and the experimental data. The results of the fitting process are presented in Table I (the varied parameters are distinguished by large type). The average disagreement between calculation and experiment is ~15 meV (see Table II) and in some case reaches 70 meV. Such a large discrepancy could be due to the fact that the error in determining the percentage content of CdSe in the QW can be 1–2 mole %, especially for the case of high CdSe content. As one can see from Fig. 1, even a small change in the composition results in a large change in the transition energy, while the dependence of the transition energy on the thickness of the QW is weaker. Accordingly, we fitted the compositions in the QWs, keeping the thickness constant to reduce the diagreement between calculation and experiment to a minimum in each case (see Table II, the column labeled ''calculation for a different composition''). The change in the CdSe content did not exceed 1.5 mole % in all cases except for samples 19–22, where we had to change the composition by 7 mole %, indicating a possible systematic error in the experimental data. In the case of the fitted compositions the discrepancy is ~5 meV, which is adequate accuracy.

To check the computational model, we grew a structure with a collection of QWs, whose thicknesses were in the ratio 1:2:3:4:5 (structure A) and a structure with a collection of QWs with the same thickness which were separated by barriers whose thicknesses were 15% less than that of the QW (structure B). Photographs obtained for these structures by the TEM method are shown in Fig. 2. The thicknesses of the QWs were determined from these photographs: (24 ± 2):(48 ± 2):(72 ± 2):(96 ± 2):(120 ± 2) Å for structure A and 70 ± 2 Å for structure B. The Cd content was determined according to the growth calibrations and was equal to 22 ± 2% in the case of structure A and 13 ± 1% in

TABLE II. Published data and calculation of the energies of optical transitions in $Zn_{1-x}Cd_xSe$ quantum wells.

			$e1 - hh1$, eV			$el - hl1$, eV			
Sample No.	L, Å	x, %	Experiment	Calculations	Calculations for different compositions	Experiment	Calculations	Calculations for different compositions	References
1	28	10	2.703	2.721					8
2	30	10	2.747	2.717	2.747	2.766	2.740	2.766	9
3	30	26	2.580	2.560	2.585	2.646	2.614	2.636	9
4	60	14	2.650	2.631	2.653				6
5	90	14	2.639	2.613	2.636				6
6	120	14	2.629	2.606	2.628				6
7	30	11	2.718	2.708	2.718	2.737	2.733	2.743	3
8	30	16	2.685	2.660	2.687	2.720	2.695	2.718	3
9	70	11	2.658	2.660	2.655	2.685	2.695	2.693	3
10	30	23	2.580	2.590	2.582	2.640	2.6382	.633	3
11	200	11	2.670	2.636	2.665	2.692	2.675	2.701	3
12	70	11	2.640	2.660	2.46	2.695	2.695	2.685	7
13	70	14	2.627	2.623	2.627	2.672	2.665	2.670	7
14	70	17	2.581	2.587	2.582	2.637	2.636	2.634	7
15	70	22	2.514	2.526	2.519	2.594	2.587	2.584	7
16	30	10	2.737	2.717	2.740	2.761	2.740	2.761	4
17	40	10	2.728	2.700	2.726	2.749	2.727	2.749	4
18	50	10	2.717	2.688	2.715	2.743	2.717	2.740	4
19	20	31	2.646	2.575	2.644	2.679	2.626	2.683	4
20	30	31	2.591	2.509	2.590	2.663	2.573	2.640	4
21	40	31	2.536	2.470	2.546	2.604	2.542	2.605	4
22	50	31	2.512	2.446	2.524	2.590	2.523	2.588	4

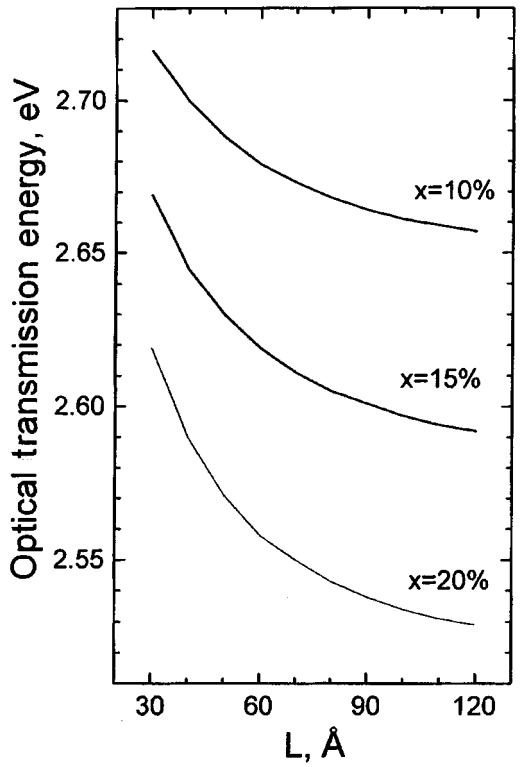

FIG. 1. Computed energies of optical transitions with the participation of heavy holes as a function of the quantum-well thickness for different compositions.

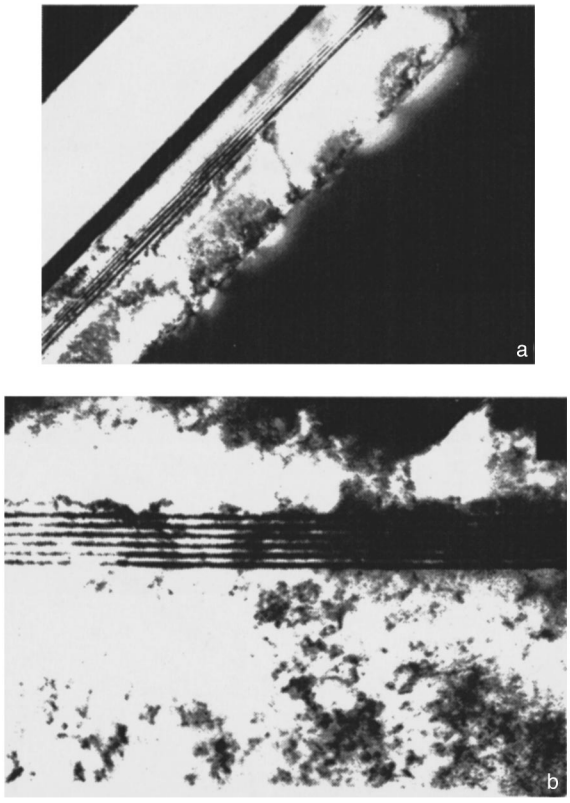

FIG. 2. Photographs obtained by transmission electron microscopy of structures *A* (a) and *B* (b).

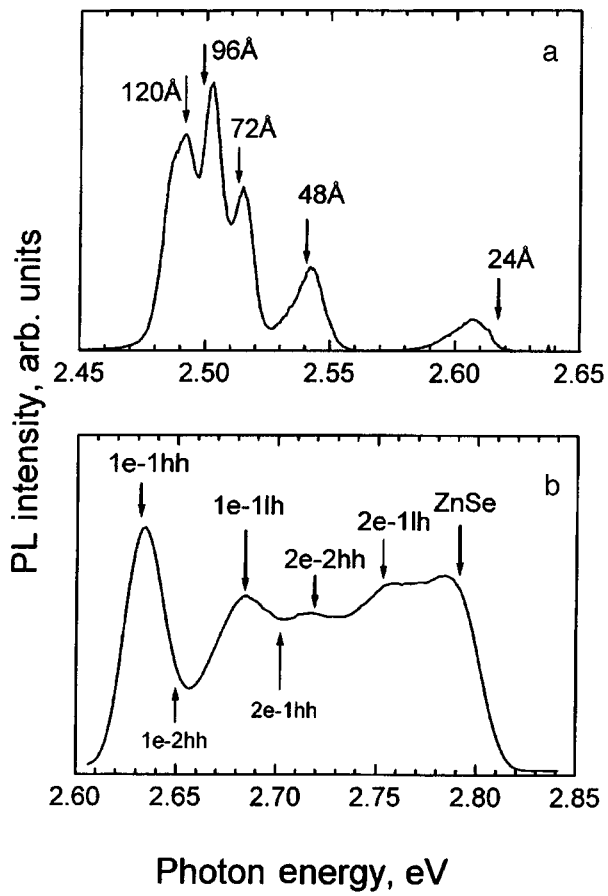

FIG. 3. Photoluminescence spectra from structure *A* (a) and photoluminescence excitation spectrum from structure *B* (b). The spectra were obtained at 77 K. The arrows mark the transition energies calculated for 23.8% CdSe and QW thicknesses 24:48:72:96:120 Å (structure *A*) and 13.8% and 70 Å (structure *B*), respectively.

the case of structure *B*. Figure 3 shows the luminescence spectra from structure *A* and the luminescence excitation spectra from structure *B*. The spectra obtained were obtained at 77 K. The arrows indicate the transition energies calculated for a CdSe content of 23% and QW thicknesses 24:48:72:96:120 Å (structure *A*) and CdSe content of 13.5% and QW thickness 70 Å (structure *B*), respectively. One can see from the figure that the computed transition energies are in good agreement with the experimental values (the large discrepancy in the case of a narrow QW (24 Å) can be explained by an increase in the exciton binding energy, whose dependence on the thickness of the QW we ignored). The degree of agreement shows that this model with the parameters from Table I can be used for calculations. However, the parameter Q is determined with a low accuracy, because the value of this parameter has virtually no effect on the energy of transitions in which the first few levels participate. Therefore, the excited states must be taken into account in making any further improvements to the model.

5. CONCLUSIONS

The published data on the optical transition energies in ZnCdSe/ZnSe QW were analyzed. On the basis of this analysis values giving the best agreement between the computational model and experiment were obtained for some physical parameters of ZnSe and CdSe. The model was also checked with use of structures, which we grew, with a collection of QWs whose thickness and composition were determined by independent methods.

We thank N. A. Bert for providing the TEM data.

This work was supported by INTAS under Grant INTAS-94-481 and the Russian Fund for Fundamental Research under Grant No. 95-02-04056.

[1] S. V. Ivanov, S. V. Sorokin, P. S. Pop'ev, J. R. Kim, H. D. Jung, and H. S. Park, J. Cryst. Growth **159**, (1996).
[2] Chris G Van de Walle. Phys. Rev. B **39**, 1871 (1989).
[3] R. Chingolani, P. Prete, D. Greco, P. V. Guigno, M. Lomascolo, R. Rimaldi, L. Calcagnile, L. Vanzetti, L. Sobra, and A. Franciosi, Phys. Rev. B **51**, 5176 (1995).
[4] V. Pellegrini, R. Atamasov, A. Tredicucci, F. Beltram, C. Amzulini, L. Sobra, L. Vanzetti, and A. Francioso, Phys. Rev. B **51**, 5171 (1995).
[5] Y. Wu, K. Ichino, Y. Kawakami, and S. Fujita, Jpn. J. Appl. Phys. **31**, 1737 (1992).
[6] H. J. Lozykowski and V. K. Shastri, J. Appl. Phys. **69**, 3235 (1991).
[7] F. Liaci, P. Bigenwald, O. Briot, B. Gil, N. Briot, T. Cloitre, and R. L. Aulombard, Phys. Rev. B **51**, 4699 (1995).
[8] R. Chingolani, R. Rimaldi, L. Calcagnile, P. Prete, P. Sciacovelli, L. Tapfer, L. Vanzetti, G. Mula, F. Bassani, L. Sobra, and A. Franciosi, Phys. Rev. B **49**, 16 769 (1994).
[9] R. Chingolani, M. Di Duo, M. Lomascolo, R. Rimaldi, P. Prete, L. Vasanelli, L. Vanzetti, F. Bonanni, L. Sobra, and A. Franciosi, Phys. Rev. B **50**, 12 179 (1994).

Translated by M. E. Alferieff

Calculation of the trapping of hot electrons by repulsive centers under the conditions of a needle-type distribution function

Kh. Z. Kachlishvili, Z. S. Kachlishvili, and F. G. Chumburidze

Tbilisi University, Georgia
(Submitted June 17, 1996; accepted for publication January 15, 1997)
Fiz. Tekh. Poluprovodn. **31**, 944–946 (August 1997)

The trapping coefficient of hot electrons repelled by a Coulomb center is calculated explicitly for a needle-shaped electron distribution function under conditions where the effective trapping cross section, along with the Sommerfeld factor, depends exponentially on the energy of the electron which has tunneled through the barrier. The criteria under which the effective Bonch–Bruevich cross section is valid are obtained. © *1997 American Institute of Physics.* [S1063-7826(97)01308-2]

The recombination of hot charge carriers on like-charge centers has been studied extensively (see, Refs. 1 –4). In all these studies an expression was employed for the trapping probability that was first obtained by Bonch–Bruevich.[1] However, the development and improvement of the existing theories have induced us to revisit this problem.

In Ref. 5 it was shown that in the case of an electron trapped by a repulsive center the trapping probability with the Sommerfeld factor should depend exponentially on the energy of the electron which has tunneled through the barrier. In Ref. 5, just as in Ref. 1, in a calculation of the trapping coefficient in the electron-temperature approximation it is shown that taking this dependence into account changes the electronic temperature to an effective electronic temperature. The latter temperature contains a parameter of the center which is of the order of the reciprocal of the phonon energy. In the case where the electronic temperature is much lower than this energy, the result of Ref. 5 is identical to the the result obtained by Bonch–Bruevich.[1]

In Ref. 6, the trapping coefficient is calculated under the conditions of transverse runaway (TR) of hot electrons, taking into account the dependence mentioned above. According to the results obtained in Ref. 6, near the threshold for TR the exponential factor plays an important role in the effective trapping cross section, while far from the TR threshold the effective cross section obtained by Bonch–Bruevich is a good approximation.

In Ref. 3 the trapping coefficient was calculated for a hot-electron distribution with the maximum anisotropy. Naturally, this raises the question of how the result obtained in Ref. 3 changes when the aforementioned dependence is taken into account. In the present paper we investigate this question.

A needle-shaped distribution of hot charge carriers is obtained when the following inequality is satisfied:

$$T_0 \gg T, \quad \frac{p_0}{eE\tau_0} \gg 1, \quad \frac{p_0}{eE\tau} \ll 1, \quad \tau_0 \ll \tau, \tag{1}$$

where $T_0=\hbar\omega_0/k$ is the excitation temperature of optical phonons, T is the temperature of the crystal, p_0 is the momentum of an electron with energy $\hbar\omega_0$, τ_0 is the characteristic emission time of optical phonons, τ is the relaxation time due to an elastic-scattering mechanism, and E is the electric-field intensity.[7] The fourth inequality in Eq. (1) should hold in the ''active'' energy region (i.e., for electron energy $w>w_0\equiv\hbar\omega_0$) and the third inequality should hold in the ''passive'' region $w<w_0$.

As is well known, the hot-electron distribution function normalized to the hot-electron density n is given in this case by the expression[7]

$$f(\mathbf{p})=2\varphi(w)\,\delta(\cos\,\theta-1), \tag{2}$$

where θ is the angle between the electron momentum $\mathbf{p}$ and the applied electric field.

Taking into account that electrons only arrive in the ''passive'' region and only leave the ''active'' region, and solving Boltzmann's equation, we obtain the following expression for the distribution function $\varphi(w)$:[3]

$$\varphi=N\begin{cases} w^{-1}, & w<\hbar\omega_0, \\ w^{-1}\,\exp\left[\dfrac{\Phi(y)}{\nu}\right], & w>\hbar\omega_0, \end{cases} \tag{3}$$

where N is a normalization constant, $\nu=\dfrac{eEp_0\tau_0}{m\hbar\omega_0}$, and the function $\Phi(y)$ is given by the expression

$$\Phi(y)=\sqrt{y(y-1)}-\ln(\sqrt{y}+\sqrt{y-1}), \quad y=\frac{w}{w_0}. \tag{4}$$

The trapping coefficient is

$$C_n=\frac{1}{n}\int d\mathbf{p} f(\mathbf{p})\frac{p}{m}\sigma(w), \tag{5}$$

where $\sigma(w)$ is the effective trapping cross section. Using the results obtained in Refs. 1 and 6, we can represent σ in the form

$$\sigma(w)=w^{\nu_c-1}\Psi(w)\left[\exp\left(\frac{2\pi ze^2}{\varepsilon\hbar\nu}\right)-1\right]^{-1}\exp\left(-\frac{\tau_1 m\nu^2}{\hbar}\right), \tag{6}$$

where ν_0 is a parameter of order unity, $\Psi(w)$ is a slowly varying function of energy, z is the charge of the repulsive center in units of the electron charge, $\nu=p/m$ is the electron velocity, ε is the permittivity, and τ_1 is the tunneling time.[5]

In accordance with what we have said above, $\sigma(w)$ contains, in addition to the Sommerfeld factor, an exponential factor that depends on the energy of the tunneled electron.

Using Eqs. (3) and (6), we can represent Eq. (5) the form

$$C_n=\frac{2m}{n}w_0^{\nu_0}N(C_1+C_2), \tag{7}$$

where

$$C_1=\int_0^1 y^{\nu_0-1}\Psi(w_0y)\frac{\exp(-\gamma_0y)}{\exp(\gamma/\sqrt{y})-1}dy, \tag{8}$$

$$C_2=\int_1^\infty y^{\nu_0-1}\Psi(w_0y)\frac{\exp[-\gamma_0y-\Phi(y)/\nu]}{\exp(\gamma/\sqrt{y})-1}dy, \tag{9}$$

$\gamma=\dfrac{2\pi ze^2}{\varepsilon\hbar\nu_0}$, $\gamma_0=2\tau_1w_0/\hbar$, and ν_0 is the velocity of an electron with energy w_0.

It is obvious that $\nu\ll 1$ [the second inequality in Eqs. (1)] and that $\gamma\gg 1$. We then obtain for the normalization factor and C_1 the expressions

$$N=\frac{(2\pi\hbar)^3n}{2w_0^{1/2}(2m)^{3/2}}\left[1+\frac{\Gamma(5/3)}{2}\left(\frac{3\nu}{2}\right)^{2/3}\right]^{-1}, \tag{10}$$

$$C_1\simeq 2\Psi(w_0)\gamma^{-1}\exp[-(\gamma+\gamma_0)]. \tag{11}$$

We shall calculate C_2 by the steepest-descent method. Of the different possible ratios of the parameters, the realizable cases are: $\gamma\gg 1$, $\nu\ll 1$, so that the inequality $\nu\gamma/2\ll 1$ would hold. When these inequalities are satisfied, in order to find an approximate solution of the transcendental equation $f_1'(y_0)=0$ near the boundary of the active region $y\gtrsim 1$, where

$$f_1(y)=\gamma_0y+\frac{\Phi(y)}{y}+\ln\left[\exp\left(\frac{\gamma}{\sqrt{y}}\right)-1\right],$$

the inequality $\gamma_0\nu\ll 1$ must also be satisfied. Under these conditions, for the fields $E<E_0$ we obtain

$$y_0\simeq 1+\nu^2\left(\frac{\gamma}{2}-\gamma_0\right)^2=1+\left(\frac{E}{E_0}\right)^2\left(1-2\frac{\gamma_0}{\gamma}\right)^2,$$

where $E_0\equiv(2\hbar\omega_0)/(e\nu_0\tau_0\gamma)$, and for C_2 we have

$$C_2\simeq 4\sqrt{\pi}\Psi(\hbar\omega_0)\sqrt{\left|\frac{\gamma}{2}-\gamma_0\right|}\,\frac{\exp[-(\gamma+\gamma_0)]}{\gamma}\,\frac{E}{E_0}\times\exp\left[\frac{4}{3\gamma^2}\left(\frac{E}{E_0}\right)^2\left(\left|\frac{\gamma}{2}-\gamma_0\right|^3\right)\right]. \tag{12}$$

Substituting the expressions (10)–(12) into Eq. (7), we obtain the following expression for the trapping coefficient:

$$C_n=C_0\left[1+\frac{\Gamma\left(\frac{5}{3}\right)}{2}\left(\frac{3}{\gamma}\right)^{2/3}\left(\frac{E}{E_0}\right)^{2/3}\right]^{-1}\times\left\{1+2\sqrt{\pi}\sqrt{\left|\frac{\gamma}{2}-\gamma_0\right|}\frac{E}{E_0}\times\exp\left[\frac{4}{3\gamma^2}\left(\frac{E}{E_0}\right)^2\left(\left|\frac{\gamma}{2}-\gamma_0\right|^3\right)\right]\right\}, \tag{13}$$

where

$$C_0\equiv\frac{(2\pi\hbar)^3}{(2m)^{1/2}}(\hbar\omega_0)^{\nu_0-1/2}\Psi(\hbar\omega_0)\frac{\exp[-(\gamma+\gamma_0)]}{\gamma}. \tag{14}$$

In the case when $\gamma_0\ll\dfrac{\gamma}{2}$, the expressions (13) and (14) are identical to the results of Ref. 3.

We shall now make some speculative estimates so as to clarify the conditions under which the last factor in the expression (6) can be disregarded. Accordingly, we rewrite the inequality in the form

$$T_1\gg\frac{T_0^{3/2}}{\pi T_B^{1/2}}, \tag{15}$$

where

$$T_B=\frac{E_B}{k}=\frac{z^2}{k}\frac{me^4}{2\hbar^2\varepsilon^2},\quad T_1=\frac{\hbar}{2\tau_1k}.$$

In the case of *n*-Ge the inequality (15) assumes the form $T_1\gg 260$ K for a singly-charged center and $T_1\gg 130$ K for a doubly charged center. In the case of *n*-Si we have $T_1\gg 340$ K and $T_1\gg 170$ K for singly and doubly charged centers, respectively.

In summary, as the charge multiplicity of the trapping center increases, the dependence of the effective trapping cross section on the energy of the electron which has tunneled through the barrier becomes weaker. If $T_1\sim 10^3$ K (Ref. 6), we clearly see that for Ge and Si with $z=2$ the effective Bonch-Bruevich trapping cross section is a good approximation.

The results presented in the present paper, just as the results in Ref. 3 , can be realized at $T=20$ K in the range of fields

$$200\text{ V/cm}<E<400\text{ V/cm}.$$

[1] V. L. Bonch-Bruevich, Fiz. Tverd. Tela (Leningrad) **6**, 2047 (1964) [Sov. Phys. Solid State **6**, 1615 (1964)].
[2] V. L. Bonch-Bruevich and S. G. Kalashnikov, Fiz. Tverd. Tela (Leningrad) **7**, 750 (1965) [Sov. Phys. Solid State **7**, 599 (1965)].
[3] V. L. Bonch-Bruevich, Z. S. Kachlishvili, Vestn. MGU. Fiz., Astron., No. 5, 580 (1974).
[4] Kh. Z. Kachlishvili and M. G. Mironov, Tr. Tbil. gos. un.-ta **291** (28), 37 (1989).
[5] V. N. Abakumov, V. Karpus, V. I. Perel', and I. N. Yassievich, Fiz. Tekh. Poluprovodn. **22**, 262 (1988) [Sov. Phys. Semicond. **22**, 159 (1988)].
[6] Z. S. Kachlishvili, Kh. Z. Kachlishvili, and F. G. Chumburidze, Fiz. Tekh. Poluprovodn. **30**, 74 (1996) [Semiconductors **30**, 141 (1996)].
[7] I. I. Vasilyus and I. B. Levinson, Zh. Éksp. Teor. Fiz. **50**, 1660 (1966) [*sic*].

Translated by M. E. Alferieff

Properties of tellurium-doped gallium antimonide single crystals grown from nonstoichiometric melt

A. E. Kunitsyn and V. V. Chaldyshev

A. F. Ioffe Physicotechnical Institute, Russian Academy of Sciences, 194021 St. Petersburg, Russia

A. G. Mil'vidskaya and M. G. Mil'vidskiĭ

State Institute of the Rare-Metals Industry, 109017 Moscow, Russia

(Submitted December 27, 1996; accepted for publication January 17, 1997)
Fiz. Tekh. Poluprovodn. **31**, 947–949 (August 1997)

The electric and luminescence properties of tellurium-doped gallium antimonide single crystals grown from gallium-enriched melt by Czochralski's method have been investigated. It was determined that the crystals possess *n*-type conductivity and are strongly compensated. It was found that toward the end of the ingot the concentration of the impurity tellurium increases more rapidly than that of the compensating acceptors. The possibilities of obtaining the properties of GaSb single crystals by growing the crystals from nonstoichiometric melts followed by heat treatment of the material are discussed. © *1997 American Institute of Physics.* [S1063-7826(97)01408-7]

Moving away from stoichiometry in growing single crystals and epitaxial films of III–V compounds is an effective method for controlling the properties of the material, since then it is possible to control the dopant distribution factors and to form composition- and concentration-optimized ensembles of intrinsic point defects. For gallium antimonide, such effects have been studied in greatest detail in the case of layers grown by liquid-phase epitaxy. It was determined that switching from the standard gallium solvent to fluxed solutions based on the isovalent impurity Bi (with Ga and Sb present in the stoichiometric proportion)[1,2] and to antimony-enriched fluxed solutions substantially changes the electrical parameters of the epitaxial layers.[3,4] In particular, even the type of conductivity was found to change in tin-doped GaSb films.[2]

The admissible deviations of the composition of the liquid phase from stoichiometry are much smaller when growing GaSb single crystals than in the case of liquid-phase epitaxy. Changes in the properties of the crystals grown are nonetheless possible even in this case. In particular, it can be expected that when growing tellurium-doped single crystals, the distribution factor of the donor substitution impurity Te_{Sb} will increase when the melt is enriched with gallium. Other conditions remaining the same, this should result in a higher charge carrier density in the doped ingot. The electrical parameters of the crystal grown can also be influenced by the changes which are produced in the densities of the intrinsic point defects of the lattice as a result of a deviation from stoichiometry. Furthermore, the possibility that the excess component will precipitate,[5,6] which can also affect the properties of the material, must also be taken into account.

In the present study we investigated the effect of a deviation from stoichiometry (excess gallium in the melt) on the electrical properties and photoluminescence of tellurium-doped GaSb single crystals grown by the Czochralski method.

Two tellurium-doped GaSb crystals 60 mm in diameter were grown. One crystal (the control crystal) was grown by the standard technology with a stoichiometric melt. The second crystal was grown from melt with a gallium excess of 1 at. %. The tellurium content in the melt was same in both cases. Growth was conducted in the crystallographic direction $\langle 100 \rangle$ on a seed crystal with dislocation density not exceeding 2×10^2 cm^{-2}.

The electrical parameters were investigated by the van-der-Pauw method at 77 and 300 K on a series of plates cut from different parts of the ingot. The photoluminescence (PL) of the same plates at a temperature of 4.2 K was also investigated. An Ar^+ laser, a grating monochromator, and a germanium photodetector were used for the PL investigations. The spectra were recorded with a resolution of no worse than 5 meV.

The structural perfection of the crystal was checked by means of selective etching and transmission electron microscopy. These investigations did not show any large precipitates which could be observed in the crystals grown with a large excess of gallium in the melt.[6] Only single clusters, several nanometers in size, were observed. The dislocation density in the crystals investigated did not exceed 5×10^3 cm^{-2}.

The GaSb:Te crystals possessed *n*-type conductivity. The electron mobility and density in different parts of the ingot at 300 and 77 K are given in Table I. It is seen that the electron density increases toward the end of the ingot. This type of variation of the electron density along the ingot is due to an increase in the tellurium concentration in the single crystals, since the distribution factor of this impurity in GaSb $K_{Te}<1$. Figure 1 shows comparative data on the electron density distribution along the control crystal and the crystal grown from gallium-enriched melt. The electron density is obviously lower in the latter case. In both crystals the electron density increases toward the end of the ingot, but the increase is much stronger in the crystal grown from nonstoichiometric melt than in the control crystal.

Figure 2 shows the PL spectra for different parts of these crystals. A single wide line is observed in all spectra. The

TABLE I. Mobility and electron density in different parts of a GaSb:Te single crystal.

No.	Distant from the start of the ingot, mm	Electron density, cm^{-3}		Electron mobility, $cm^2/(V\cdot s)$	
		77 K	300 K	77 K	300 K
1	15	4.0×10^{17}	2.0×10^{17}	4.2×10^{3}	3.0×10^{3}
2	45	3.8×10^{17}	2.1×10^{17}	4.7×10^{3}	3.3×10^{3}
3	70	5.0×10^{17}	2.8×10^{17}	5.3×10^{3}	3.3×10^{3}
4	110	8.2×10^{17}	5.0×10^{17}	6.1×10^{3}	3.1×10^{3}

maximum of this line is strongly displaced into the region of lower energies relative to the band gap E_g in undoped GaSb. This form of the PL spectrum is characteristic of strongly doped, compensated semiconductors and is due to radiative transitions of carriers from the conduction band into the valence-band tail and transitions between band tails. The shift of the PL line relative to E_g is greatest in the spectra of samples cut from the initial and middle sections of both crystals and reaches $\Delta\sim80$ meV. Such a large value of Δ shows that the control and experimental GaSb:Te crystals are not only strongly doped but also strongly compensated.

In the spectra of samples cut from the end portions of the ingots, Δ decreases but the PL is also broadened some more. This shows that the density of Te donors and compensating acceptors increases. The increase in the tellurium density toward the end of the ingot, as noted above, is due to the low value of the distribution factor of this impurity in GaSb. The chief acceptor in gallium antimonide is a so-called ''natural'' acceptor — an isolated antistructural defect Ga_{Sb} or a more complicated complex that includes Ga_{Sb}.[1,7] It was shown in Ref. 6 that when GaSb single crystals are grown from melts enriched with gallium, the density of this acceptor increases toward the end of the ingot as a result of the accumulation of excess gallium in the melt. However, the acceptor density increases more slowly than the Te donor density. This is indicated by measurements of the electron density (see Table I and Fig. 1) and by the shift in the PL line into the short-wavelength region, probably because of the shift of the Fermi level into the conduction band. The decrease in compensation is indicated by the increase in the electron mobility, which occurs simultaneously with an increase in the electron density (see Table I).

In summary, our investigations have shown that *n*-type GaSb crystals grown by the Czochralski method and doped with tellurium up to the level $n=3\times10^{17}-1\times10^{18}$ cm^{-3} are strongly compensated. The gallium excess in the initial melt (1 at. %) results in a higher density of compensating acceptors, and in the experimental density range this effect predominates over an increase in the density of the Te donor impurity in the crystal. Appreciable precipitation of excess gallium was not observed.

The fact that the degree of compensation decreases at the end of the crystal apparently indicates that a compensating acceptor center forms in the ingot during post-crystallization cooling of the ingot in a definite temperature interval. When growth has stopped, the end of the crystal cools most rapidly, which strongly suppresses the formation of a ''natural'' acceptor in this part of the ingot. This acceptor center is probably due not to an isolated intrinsic point defect but rather a complex of which it is a constituent. The degree of compensation of strongly doped *n*-type GaSb crystals can be effectively influenced and the maximum achievable electron density and electron mobility can be increased by regulating the post-growth cooling rate of the crystal or by subjecting the ingot or the plates cut from it to subsequent heat treatment.

We thank N. A. Bert and A. A. Kalinin for performing the electron-microscopic investigations. This work was spon-

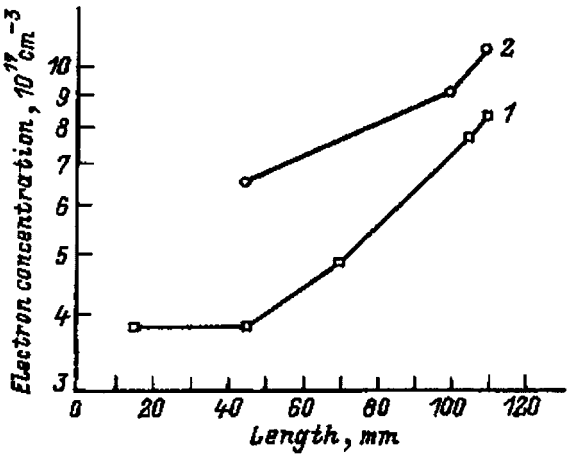

FIG. 1. Free-electron density distribution along a tellurium-doped GaSb single crystal grown from gallium-enriched melt (*1*) and in a control crystal grown by the standard technology (*2*).

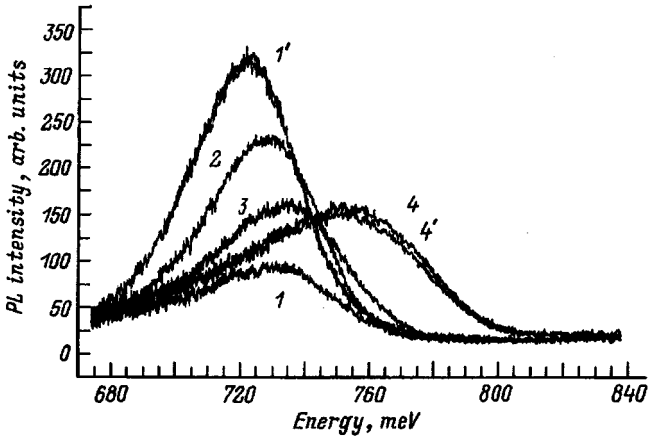

FIG. 2. Photoluminescence spectra at 4.2 K for samples cut from different parts of a tellurium-doped GaSb single crystal grown from gallium-enriched melt (*1–4*). The numbers of the spectra correspond to the numbers of the samples in Table I. *1′*, *4′* — PL spectra of samples cut from the corresponding parts of the control single crystal.

sored by the State Committee on Science and Technologies (the programs ''Fullerenes and atomic clusters'' and ''Physics of solid-state nanostructures'') and the Russian Fund for Fundamental Research.

[1] V. P. Germogenov, Ya. I. Otman, V. V. Chaldyshev, Yu. V. Shmartsev, and L. E. Épiktetova, Fiz. Tekh. Poluprovodn. **24**, 1095 (1990) [Sov. Phys. Semicond. **24**, 689 (1990)].
[2] R. Kh. Akchurin, V. A. Zhegalin, and V. V. Chaldyshev, Fiz. Tekh. Poluprovodn. **26**, 1409 (1992) [Sov. Phys. Semicond. **26**, 790 (1992)].
[3] C. Woelk and K. W. Benz, J. Cryst. Growth **27**, 177 (1974).
[4] N. T. Bagraev, A. N. Baranov, T. I. Voronina, Yu. N. Tolparov, and Yu. P. Yakovlev, Pis'ma Zh. Tekh. Fiz. **11**, 117 (1985) [Sov. Tech. Phys. Lett. **11**, 47 (1985)].
[5] V. M. Smirnov, A. A. Kalinin, B. T. Bublik, A. G. Braginskaya, G. P. Kolchina, A. N. Morozov, V. B. Osvenskiĭ, Kristallografiya **31**, 615 (1986) [Sov. Phys. Crystallogr. **31**, 816 (1986)].
[6] N. A. Bert, A. E. Kunitsyn, A. G. Mil'vidskiĭ, M. G. Mil'vidskiĭ, and V. V. Chaldyshev, Fiz. Tekh. Poluprovodn. **29**, 1116 (1995) [Semiconductors **29**, 578 (1995)].
[7] D. Effer and P. J. Etter, J. Phys. Chem Solids **25**, 451 (1964).

Translated by M. E. Alferieff

Dependence of the resonant conductivity of symmetric double-barrier structures on the amplitude of rf field

E. I. Golant[a)] and A. B. Pashkovskiĭ

Scientific-Research Institute ''Istok'', 141120 Fryazino, Russia
(Submitted March 5, 1996; accepted for publication January 20, 1997)
Fiz. Tekh. Poluprovodn. **31**, 950–953 (August 1997)

An analytical expression for the rf amplitude dependence of the conductivity in a symmetric double-barrier resonance-tunneling structure with high, thin barriers under conditions of collisionless electron transport is found on the basis of the solution of a nonstationary Schrödinger equation describing the resonance interaction of electrons with the rf field. It is shown that under the action of a rf field with frequency ω and amplitude approximately corresponding to triple the width of the resonance level, up to half of the electrons passing through this level can be transferred, emitting or absorbing a quantum of energy $\hbar\omega$, into a neighboring level. © *1997 American Institute of Physics.* [S1063-7826(97)01508-1]

The study of electron transmission through quantum-well structures in rf electric fields of infinitesimal[1] and finite[2] amplitudes is very important from the theoretical standpoint and for applications. Starting with the basic study[3] and the discovery of the high oscillator strengths of intersubband transitions in double-barrier resonance-tunneling structures (DBRTS)[4], many suggestions have been made for using such transitions for infrared-range lasing.[5,6] However, this idea has been realized only comparatively recently in the so-called quantum cascade laser,[7] whose rapid improvement[8] makes it a very promising radiation source.

The calculation of devices operating on intersubband transitions is ordinarily based on the assumption of successive tunneling of the carriers of a phonon-assisted current.[5] At the same time, as shown in Ref. 9 , intersubband transitions in a coherent-tunneling regime, where the lifetime of electrons in each level of a quantum well is determined not by phonon scattering but rather by tunneling through a barrier which should be quite thin in this case, could have interesting device applications. The characteristic features of the resonance interaction of electrons with an rf field in DBRTS with high and thin barriers have been investigated in Ref. 10 in the low-signal approximation. Simple analytical expressions were obtained for the width of a resonance level and the monoenergetic resonance conductivity of a symmetric DBRTS as a function of the size of the quantum well, the barrier thickness, and the frequency of the field. At the same time, it is very important to find the dependence of the intensity of the resonance interaction on the amplitude of the rf field itself. This makes it possible to determine the quantum efficiency of the transitions. The well-known methods for calculating electron transport in DBRTS in a finite-amplitude rf electric field[2,11] are based on numerical algorithms and suffer from a lack of physical clarity. For this reason, it is of interest to obtain simple analytical expressions for the wave functions of electrons in a DBRTS, as done in Ref. 10 , as a function of the amplitude of the rf field. It should be noted that it is only rarely that a quantum-mechanical problem of this kind can be solved analytically in a closed form.

Let us consider a symmetric double-barrier structure of width a with thin (δ-like) barriers of thickness b and height φ_b. Let us assume that a uniform electric field, which varies in time as $\mathcal{E}\cos\omega t = E(e^{i\omega t}+e^{-i\omega t})$, where $\mathcal{E}=2E$, is applied to the structure. For definiteness, let the electrons move from left to right. Taking into account the assumptions made above, we can then write the nonstationary Schrödinger equation in the form

$$i\hbar\frac{\partial\psi}{\partial t} = -\frac{\hbar^2}{2m^*}\frac{\partial^2\psi}{\partial x^2} + \alpha\delta(x)\psi + \alpha\delta(x-a)\psi + H(x,t)\psi, \tag{1}$$

$$H(x,t) = -qE\{x[\theta(x)-\theta(x-a)] + a\theta(x-a)\}(e^{i\omega t} + e^{-i\omega t}).$$

Here q and m^* are the electron charge and mass, $\alpha=\varepsilon_b b$, and $\theta(x)$ is the unit step function.

It is well known that the transmission coefficient of a DBRTS has a distinct resonance character, and that for symmetric structures with thin barriers the magnitude of the wave vector, which determines the resonance levels on which the transmission coefficient equals, 1 is found from the solution of the transcendental equation[12]

$$\tan ka = -\frac{k\hbar^2}{\alpha m^*} = -\frac{2k}{y}. \tag{2}$$

Here we have introduced, for convenience, the notation $y=2m^*\alpha/\hbar^2$. Let the electrons pass through the Nth resonance level (for definiteness, we call it the ground state). The unperturbed electron wave function ψ_0, normalized to one electron, will then have the form

$$\psi_0(x) = \begin{cases} \exp ikx + D_0\exp(-ikx), & x<0; \\ A_0\sin kx + B_0\cos kx, & 0<x<a; \\ C_0\exp ik(x-a), & x>a. \end{cases} \tag{3}$$

Here $k=(2m^*\varepsilon/\hbar^2)^{1/2}$ is the wave vector of the electrons with energy ε, which are incident on the structure, and all other parameters are

$$A_0 = y/k + i, \quad B_0 = 1, \quad C_0 \approx (-1)^{N+1}, \quad D_0 = 0. \tag{4}$$

Then, as shown in Ref. 10 , if the frequency of the rf field corresponds to transitions to the Lth level, then a resonant interaction of electrons with the rf field will be observed. Assuming the amplitude of the field to be small, we seek the solution in the form of a perturbation series.

In first-order perturbation theory the correction ψ_1 to the wave function of the ground state[13] is

$$\psi_1=\psi_{1+}(x)e^{-i(\omega_0+\omega)t}+\psi_{1-}(x)e^{-i(\omega_0-\omega)t},$$

where $\omega_0=\varepsilon/\hbar$. The functions $\psi_\pm$ for this problem have the form

$$\psi_{1\pm}(x)=\begin{cases} D_{1\pm}\exp(-ik_\pm x), & x<0;\\ A_{1\pm}\sin k_\pm x+B_{1\pm}\cos k_\pm x+\chi_{1\pm}(x), & 0<x<a;\\ C_{1\pm}\exp ik_\pm(x-a)+P_{1\pm}\exp ik(x-a), & x>a,\end{cases} \tag{5}$$

where

$$k_\pm=[2m^*(\omega_0\pm\omega)/\hbar^2]^{1/2},\quad P_\pm=\pm\frac{qEa}{\hbar\omega}\varphi_0(a),$$

$$\chi_{1\pm}(x)=\mp qEx\psi_0(x)/\hbar\omega+qE\psi_0'(x)/m^*\omega^2$$

are partial solutions of the corresponding equations for $\psi_\pm$,[10,13] and the system of equations for determining the coefficients $A_{1\pm}$, $B_{1\pm}$, $C_{1\pm}$, and $D_{1\pm}$ has the form[10]

$$\begin{pmatrix} 1 & 0 & -1 & 0\\ ik_\pm-y & k_\pm & 0 & 0\\ 0 & \sin k_\pm a & \cos k_\pm a & -1\\ 0 & -k_\pm\cos k_\pm a & k_\pm\sin k_\pm a & ik_\pm-y\end{pmatrix}\times\begin{pmatrix} D_{1\pm}\\ A_{1\pm}\\ B_{1\pm}\\ C_{1\pm}\end{pmatrix}=\begin{pmatrix} f_1\\ f_2\\ f_3\\ f_4\end{pmatrix}, \tag{6}$$

where

$$f_1=\chi_\pm(0),\quad f_2=-\chi_\pm'(0),$$

$$f_3=P_\pm-\chi_\pm(a),\quad f_4=(y-ik)P_\pm+\chi_\pm'(a).$$

For sufficiently strong barriers ($y\gg k_\pm$) and a wave vector corresponding to a resonance level the determinant of the system (6) becomes small: $\Delta\approx 2ik_\pm^2(-1)^{L+1}$, and in the case of transitions to a nonresonance level it is $\Delta\approx k_\pm y$. Therefore, the probability of transitions only between two levels is substantial for narrow resonance levels. For this reason, in what follows, we shall study transitions only between the ground state and the upper resonance level (the plus sign $+$) or the ground state and and a lower (the minus sign $-$) resonance level.

For $y\ll k_\pm$, using only of the terms with the maximum powers of y, we find, from the system (6), for the coefficients of the wave function (5) the expression

$$B_{1\pm}\approx D_{1\pm}\approx(-1)^{L+1}C_{1\pm}\approx\frac{qEy^2}{im^*\omega^2k_\pm},$$

$$A_{1\pm}\approx\frac{qEy^3}{im^*\omega^2k_\pm^2}, \tag{7}$$

if $N-L$ is odd, and these coefficients are small if $N-L$ is even (see Ref. 10 for a more detailed account).

Inside the structure ($0<x<a$) the first-order correction to the wave function has the form

$$\psi_{1\pm}(x)\approx\frac{qEy^2}{im^*\omega^2k_\pm}\left(\frac{y}{k_\pm}\sin k_\pm a+\cos k_\pm a\right). \tag{8}$$

Here the fact that since $y\gg k_\pm$ and $\chi_{1\pm}(x)$ contains terms with powers of the ratio $y/k_\pm$ no higher than 1, the contribution of $\chi_{1\pm}(x)$ to the correction to the first-order wave function, just as the contribution of $\chi_{1\pm}(x)$ to the partial solution of the equation for the second-order correction (see Ref. 14), is small. Moreover, since $|C_{1\pm}|\gg|P_{1\pm}|$ and the function f_4, which contains $P_{1\pm}$, does not make a large contribution to $\psi_{1\pm}$, here and below the terms of the type $P_\pm\exp[k(x-a)]$ will be neglected. Since $A_0\approx y/k$, it is obvious that inside the structure the first-order correction to the ground-state wave function has the same form as the ground-state wave function. Therefore, repeating the above-described procedure for finding the corrections to the wave function and taking into account the fact that only the function $\psi_{1-}(x)$ contributes to the second-order correction (if the ground-state level lies above the resonance level into which the electron passes) or $\psi_{1+}(x)$ (if the ground state level lies below the resonance level) and all other components are small, we obtain

$$\psi_2(x)\approx\begin{cases} D_2\exp(-ikx), & x<0;\\ A_2\sin kx+B_2\cos kx, & 0<x<a;\\ C_2\exp[ik(x-a)], & x>a,\end{cases} \tag{9}$$

where

$$B_2\approx D_2\approx(-1)^{L+1}C_2\approx-\left(\frac{qE}{m^*\omega^2}\right)^2\frac{y^4}{kk_-},$$

$$A_2\approx-\left(\frac{qE}{m^*\omega^2}\right)^2\frac{y^5}{k^2k_-}. \tag{10}$$

Here, just as in the preceding case, only terms containing the maximum powers of the parameter y/k are taken into account. One can see that inside the structure the second-order correction to the wave function of the ground state also has the same form as the ground-state wave function. Hence we obtain immediately

$$B_{3\pm}\approx D_{3\pm}\approx(-1)^{L+1}C_{3\pm}\approx-\frac{qEy^2}{im^*\omega^2k_\pm}\left(\frac{qE}{m^*\omega^2}\right)^2\frac{y^4}{kk_\pm},$$

$$A_{3\pm}\approx-\frac{qEy^3}{im^*\omega^2k_\pm^2}\left(\frac{qE}{m^*\omega^2}\right)^2\frac{y^4}{kk_\pm}. \tag{11}$$

Comparing Eqs. (4), (7), (10), and (11), it is easy to see that if the procedure described above for obtaining corrections to the wave function is continued and the corrections are summed, then the coefficients of the wave function on each of the resonance levels can be represented as a constant and as a sign-alternating series

$$1-z+z^2-z^3+\ \ldots\ +(-1)^{n+1}z^n,$$

where

$$z=\left(\frac{qE}{m^*\omega^2}\right)^2\frac{y^4}{kk_\pm}, \tag{12}$$

which in the region of convergence $|z|<1$ represents the expansion of the function $1/(1+z)$ in powers of z. Therefore, the electron wave function for the present problem has the form

$$\psi\approx\psi_N(x)e^{-i\omega_0 t}+\psi_L(x)e^{-i(\omega_0\pm\omega)t}, \tag{13}$$

where

$$\psi_N(x)=\frac{1}{1+z}\times\begin{cases}(1+z)\exp(ikx)-z\ \exp(-ikx), & x<0;\\ A_0\ \sin kx+B_0\ \cos kx, & 0<x<a;\\ C_0\ \exp[ik(x-a)], & x>a;\end{cases} \tag{14}$$

$$\psi_L(x)=\frac{1}{1+z}\times\begin{cases}D_{1\pm}\ \exp(-ik_\pm x), & x<0;\\ A_{1\pm}\ \sin k_\pm+B_{1\pm}\ \cos k_\pm x, & 0<x<a;\\ C_{1\pm}\ \exp[ik_\pm(x-a)], & x>a.\end{cases} \tag{15}$$

For wave functions of the form (13) the dynamic conductivity at the frequency ω is determined by the difference in the fluxes of electrons, which have absorbed and emitted a quantum of energy $\hbar\omega$ and which have left the DBRTS:[13]

$$\sigma=\frac{\hbar^2\omega}{2aE^2m^*}[k_+(|C_+|^2+|D_+|^2)-k_-(|C_-|^2+|D_-|^2)]. \tag{16}$$

In Ref. 10 it was shown that for monoenergetic electrons with density n and transitions between resonance levels a wave function of the form (5) leads to the following expression for the weak-signal active conductivity of a DBRTS

$$\sigma_M\approx\pm\frac{8q^2m^*\alpha^4n}{\pi L\hbar^6\omega^3}[1-(-1)^{N-L}]. \tag{17}$$

From the relations (15) we can therefore write the following expression for the dependence of the conductivity on the amplitude $\mathcal{E}=2E$ of the rf field, since there is no difference between transitions from the upper level to the lower level and vice versa:

$$\sigma\approx\pm\frac{8q^2m^*\alpha^4n}{\pi L\hbar^6\omega^3}\left(\frac{1}{1+z}\right)^2[1-(-1)^{N-L}], \tag{18}$$

where z is expressed in terms of the amplitude of the field and the barrier strength as

$$z=\left(\frac{qE}{m^*\omega^2}\right)^2\frac{4(m^*)^4\alpha^4a^2}{\hbar^8\pi^2LN}. \tag{19}$$

The expression is valid for $z<1$ or for a field amplitude below the critical value

$$\mathcal{E}<\mathcal{E}_K=\frac{\hbar^4\omega^2\pi(LN)^{1/2}}{2qm^*\alpha^2a}. \tag{20}$$

Let us rewrite the expression for z in the form

$$z=\left(\frac{qEa}{\hbar\omega}\right)^2\left(\frac{y^2}{k_Nk_L}\right)^2\frac{LN}{\pi^2(N^2-L^2)^2}$$

$$=\frac{(qEa)^2}{\Gamma_N\Gamma_L}\frac{64L^2N^2}{\pi^4(N^2-L^2)^4}, \tag{21}$$

where Γ_N and Γ_L are the widths of the resonance levels.[3] The critical rf voltage $u=q\varepsilon a$ applied to the DBRTS, which corresponds to $z=1$, is found from expression (21) as

$$u=(\Gamma_N\Gamma_L)^{1/2}\pi^2\frac{(N^2-L^2)^2}{8LN}. \tag{22}$$

Hence the following criterion for the applicability of Eq. (18) can be given for neighboring resonance levels with large numbers, when $\Gamma_N\approx\Gamma_L=\Gamma$:

$$q\varepsilon a<\pi^2\Gamma/2.$$

The parameter $(y/k)^2$ shows by what factor the squared wave function at a level is greater than the squared wave function of the electrons which are incident on the DBRTS and — for a unit (symmetric structure!) static transmission coefficient — electrons which have passed through the DBRTS. Therefore, the average number P_N of collisions an electron makes with the barriers in the level N before leaving the structure can be estimated as $P_N\approx(y/k)^2/2$, so that the maximum admissable value $z=1$ [in accordance with Eq. (21)] is attained at

$$u(P_NP_L)^{1/2}=\pi\hbar\omega|N^2-L^2|/2(NL)^{1/2}.$$

For the neighboring resonance levels $N=L+1$, so that

$$u(P_NP_L)^{1/2}\approx\pi\hbar\omega.$$

This means that the series (12) converges when the classical interaction energy of the electrons interacting with an alternating field over a distance equal to the average geometric tranvel distances of electrons along resonance levels does not exceed the spacing between the levels by more than a factor of 3.

It is obvious that the amplitude u is very small for narrow levels, and that this calculation is applicable only for narrow levels. However, as one can see from Eq. (14), at this amplitude the reflection coefficient of the DBRTS is $z^2/(1+z)^2=0.25$ and the transmission coefficient is $1/(1+z)^2=0.25$, so that the field transfers exactly half of the electrons in the incident flux to a different energy level; the fraction of the transferred electrons is equal to $1-(1+z^2)/(1+z)^2$. It is maximum exactly at $z=1$ and it starts to decrease for field amplitudes greater than the critical amplitude (20). The latter assertion is valid on the strength of the fact that the solution (13)–(15) can be continued analytically beyond the convergence radius of the series (12).

At $z=1$ we obtain the most interesting region, from the practical point of view, in which the maximum number of electrons effectively interacts with the rf field. Although the active conductivity decreases to one-fourth the maximum value in this case, it remains sufficiently high, say, for efficient operation of a laser with collisionless transport of electrons through DBRTS, as suggested in Ref. 9 .

It is interesting to note that as the amplitude of the field increases, an increasingly larger number of electrons is reflected from the structure with no change in energy. This fact can be explained qualitatively by the modulation of the position of a level relative to the monoenergetic electron flux incident on the DBRTS. In the weak-signal regime this modulation is weak and all electrons occupy the center of the level, where the static reflection coefficient has its lowest value — in our symmetric case zero — so that all electrons pass straight through the DBRTS. As the energy of the modulating field increases to values comparable to or exceeding the level width, the electron flux irradiates the structure increasingly shorter times in the region with nonzero transmission coefficient and therefore increasingly fewer electrons pass through the DBRTS.

This work is supported by the Russian Fund for Fundamental Research under project No. 94-02-04449 and the Scientific Council on the program ''Physics of solid-state nanostructures'' under project No. 1-050.

[a)]e-mail: golant@fod.fian.msk.su

[1] M. Buttiker and R. Landauer, Phys. Rev. Lett. **49**, 1739 (1982).
[2] M. J. Hagman, J. Appl. Phys. **78**, 25 (1995).
[3] R. F. Kazarinov and R. A. Suris, Fiz. Tekh. Poluprovodn. **5**, 797 (1971) [Sov. Phys. Semicond. **5**, 707 (1971)].
[4] L. C. West and S. J. Eglash, Appl. Phys. Lett. **46**, 1156 (1985).
[5] A. Kastalsky, V. J. Goldman, and J. H. Abeles, Appl. Phys. Lett. **59**, 2636 (1991).
[6] M. Helm in *Intersubband Transitions in Quantum Wells*, edited by E. Rosencher *et al.*, Plenum Press, N. Y., 1992.
[7] J. Faist, F. Capasso, D. L. Sivco, C. Sirtori, A. L. Hutchinson, and A. Y. Cho, Science **264**, 553 (1994).
[8] J. Faist, F. Capasso, C. Sirtori, D. L. Sivco, J. N. Baillargeon, A. L. Hutchinson, S.-N. G. Chy, and A. Y. Cho, Appl. Phys. Lett. **68**, 3680 (1996).
[9] E. I. Golant, A. B. Pashkovskiĭ, and A. S. Tager, Pis'ma Zh. Tekh. Fiz. **20**, 74 (1994) [Tech. Phys. Lett. **20**, 886 (1994)].
[10] I. V. Belyaeva, E. I. Golant, and A. B. Pashkovskiĭ, Fiz. Tekh. Poluprovodn. **31**, 137 (1997) [Semiconductors **31**, 103 (1997)].
[11] W. R. Frensley, Rev. Mod. Phys. **62**, 745 (1990).
[12] V. M. Galitskiĭ, B. M. Karnakov, and V. I. Kogan, *Problems in Quantum Mechanics* [in Russian], Nauka, Moscow, 1981.
[13] A. B. Pashkovskiĭ, Fiz. Tekh. Poluprovodn. **29**, 1712 (1995) [Semiconductors **29**, 893 (1995)].
[14] A. B. Pashkovskiĭ, Pis'ma Zh. Tekh. Fiz. **21**, 28 (1995) [Tech. Phys. Lett. **21**, 290 (1995)].

Translated by M. E. Alferieff

Temperature dependence of the electrical properties of polycrystalline silicon in the dark and in sunlight

K. M. Doshchanov

Physicotechnical Institute Science and Industrial Union ''Physics–Sun,'' Uzbekistan Academy of Sciences, 700084 Tashkent, Uzbekistan

(Submitted July 8, 1996; accepted for publication January 20, 1997)
Fiz. Tekh. Poluprovodn. **31**, 954–956 (August 1997)

The electric resistance and effective carrier mobility in polycrystalline silicon are calculated as functions of temperature and the photoexcitation level. The theoretical results are in agreement with existing experimental data. © *1997 American Institute of Physics.* [S1063-7826(97)01608-6]

Interest in the photoelectric properties of polycrystalline silicon (polysilicon) has recently increased because of the increasing use of this material for solar cells (see the bibliography in Refs. 1 and 2 and the detailed critical analysis of this problem). A new theory of recombination and charge transfer in photoexcited polycrystalline semiconductors has recently been proposed.[3] In the present paper we show that this theory is in agreement with the experimental results of Ref. 4 , where the first investigations of the temperature dependence of the electrical characteristics of polysilicon in the dark and in sunlight were performed.

Just as in Refs. 1–3, we shall examine a model polycrystal consisting of identical cubic grains doped with a shallow donor impurity with density N_d. Acceptor-type boundary states (BSs) distributed over energy E with surface density $N(E)$ are present at the grain boundaries. Trapping of electrons from inside the grains into boundary states results in the formation of intercrystallite potential barriers, which limit electron transfer from one grain into another and they also function as recombination barriers in the photoexcitation of the polycrystal. We shall model the electron scattering directly by the grain boundary itself using the square potential barrier of height V_n and width δ (δ is the ''thickness'' of a grain boundary).[2,3,5] In Ref. 2 , to obtain agreement between the theoretical dependences and the experimental data of Ref. 4 , it was suggested that V_n depends on the temperature of the sample. This assumption is superfluous in the theory which we are examining here.

In the equilibrium state we have

$$n_{s0}=\int_{E_\nu}^{E_c} N(E)f(E-F_s)dE, \tag{1}$$

where n_{s0} is the equilibrium density of electrons trapped in BSs, $f(E-F_s)$ is the Fermi–Dirac distribution function, $F_s=E_c-V_{s0}-kT\ln(N_c/N_d)$ is the position of the Fermi level at the grain boundaries, and, $V_{s0}=e^2n_{s0}^2/8\varepsilon_0\varepsilon N_d$ is the equilibrium height of the intercrystallite barriers. All other notation is standard.

The trapping of holes in BSs during photoexcitation of a polycrystal results in a lower density n_s of electrons localized at grain boundaries. The dependence of n_s on the photoexcitation level can be determined from the equation[3]

$$N_d\left[\exp\left(-\frac{V_s}{kT}\right)-\exp\left(-\frac{V_{s0}}{kT}\right)\right]=G\tau_n, \tag{2}$$

where the left-hand side determines the increase in the electron density at the tops of the intercrystallite barriers (at the current-flow level), $V_s=e^2n_s^2/8\varepsilon_0\varepsilon N_d$ is the height of the intercrystallite barriers during photoexcitation, G is the rate of photogeneration of electron-hole pairs, and τ_n is the lifetime of nonequilibrium electrons at the tops of the intercrystallite barriers. If the condition $L_p\gg n_s/N_d$ is satisfied, where L_p is the diffusion length of the minority carriers in the volume of the grains, we have[3]

$$\tau_n=\frac{L_p^2}{\nu_nS_n(N_s-n_s)}\left[l+\frac{D_p}{\nu_pS_pn_s}\exp\left(-\frac{V_s}{kT}\right)\right]^{-1}, \tag{3}$$

where $\nu_n(\nu_p)$ is the average thermal velocity of the electrons (holes), $S_n(S_p)$ is the cross section for trapping an electron (hole) in a BS, N_s is the total density of BSs, $l=L_p(a+1)/(a-1)+4L_p^2/d$; here $a=\exp(d/L_p)$ and d is the grain size; and D_p is the hole diffusion coefficient.

The estimates show that for $N_d>10^{15}$ cm^{-3} and photoexcitation levels $G\lesssim 1$ sun (1 sun = 10^{20} cm$^{-3}\cdot$s^{-1}; Refs. 1 and 2), the contribution of the minority carriers to charge transfer is negligible. According to Ref. 3, the resistivity ρ of a polycrystal is determined by the expressions

$$\rho=\frac{1}{e\mu_nN_d}+\frac{1}{\sigma_c}, \tag{4}$$

$$\sigma_c=\frac{c^2\nu_nf^*d}{2kT}[2\overline{D_n}+S_n(N_s-n_s)]\times\left[G\tau_n+N_d\exp\left(-\frac{V_{s0}}{kT}\right)\right]. \tag{5}$$

Here μ_n is the electron mobility in the volume of the grains, f is a modeling factor,[5,6] and $\overline{D_n}$ is the integrated transmittance of the grain boundary for electrons. The temperature dependence of $\overline{D_n}$ is determined by the expression

$$\overline{D_n}=\frac{V_n}{kT}\int_0^1\exp\left[-\alpha\sqrt{1-\xi}-\frac{V_n}{kT}\xi\right]d\xi-\exp\left(-\frac{V_n}{kT}\right), \tag{6}$$

where $\alpha=4\pi\delta\sqrt{2m^*V_n}/h$, m^* is the electron effective mass, and h is Planck's constant. The first term in Eq. (6)

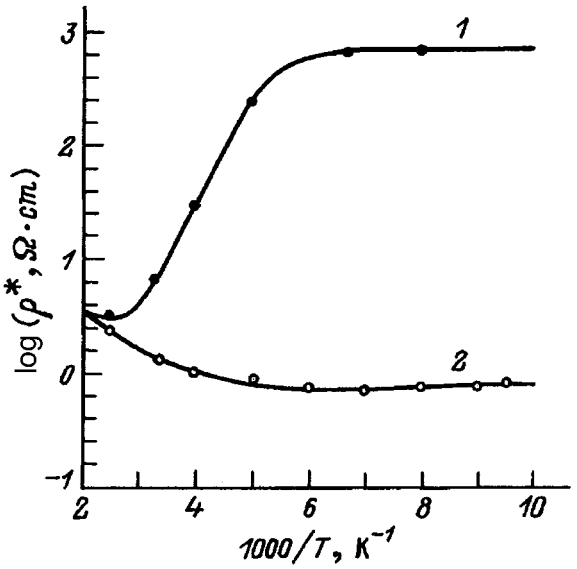

FIG. 1. Temperature dependence of the resistivity of polycrystalline silicon: *1* — in the dark ($G=0$), *2* — in sunlight ($G=1$ sun). Dots — experimental data of Ref. 4 .

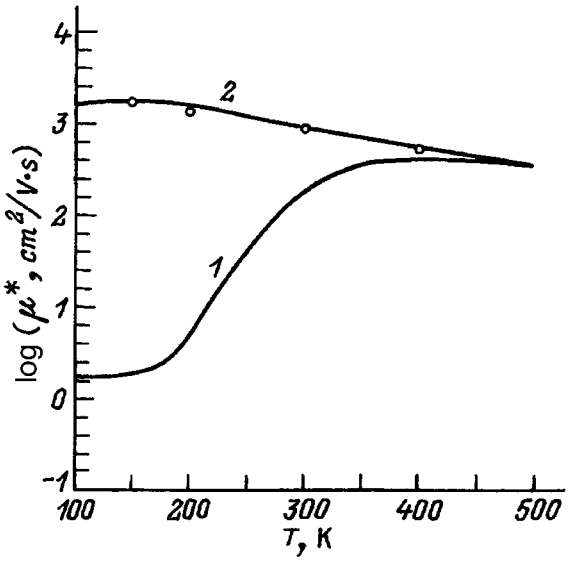

FIG. 2. Temperature dependence of the effective (Hall) mobility of electrons in polycrystalline silicon: *1* — in the dark ($G=0$), *2* — in sunlight ($G=1$ sun). Dots — experimental data of Ref. 4 .

determines the electron tunneling current through the scattering barrier of a grain boundary, and the second term determines the above-barrier current.

To describe the dark electrical conductivity of polysilicon at low temperatures, one other charge-transfer mechanism must be invoked: hopping electron transfer along intergrain defects.[2,6] The expression for the resistivity corresponding to this mechanism has the form[7,8]

$$\rho_h=\rho_0\sqrt{T}\,\exp(T_0/T)^{1/2}. \tag{7}$$

In polysilicon the values $\rho_0=10.15\ \Omega\cdot\mathrm{cm/K}^{1/2}$ and $T=1400$ K satisfy the experimental data.[6]

For the effective resistivity ρ^* and effective (Hall) carrier mobility μ_n^* we have

$$1/\rho^*=1/\rho+1/\rho_h, \tag{8}$$

$$\mu^*=1/e\rho^*N_d. \tag{9}$$

Figures 1 and 2 show the computational results for $\rho^*(T)$ and $\mu^*(T)$ in polysilicon for the following values of the parameters: $d=0.1$ cm, $N_d=5\times10^{15}\ \mathrm{cm}^{-3}$, $\mu_n=350(500\ \mathrm{K}/T)\ \mathrm{cm}^2/(\mathrm{V\cdot s})$ (Ref. 4); $E_c-E_\nu=1.12$ eV, $D_p=20\ \mathrm{cm}^2/\mathrm{s}$, $L_p=10^{-2}$ cm, $\nu_n=\nu_p=10^7\sqrt{T/300\ \mathrm{K}}$ cm/s (Ref. 2), $f^*=0.05$, $\alpha=5.1$, $V_n=0.06$ eV, $S_p=10^{-13}\ \mathrm{cm}^2$, and $S_n=7.7\times10^{-15}\ \mathrm{cm}^2$; the parameters of the Gaussian distribution of the boundary states are: $N_s=2.18\times10^{11}\ \mathrm{cm}^{-2}$, $E_s=E_\nu+0.37$ eV, and $\Delta E=0.05$ eV. The theoretical dependences are evidently in good agreement with the experimental data.

It should be noted that the interpretation proposed in Ref. 2 for the experimental results of Ref. 4 is doubtful. The dependence $V_n(T)$, proposed in Ref. 2, was obtained not from physical considerations but rather by comparing the theoretical dependence $\rho^*(T,G=1\ \mathrm{sun})$ with the experimental data [in other words, $V_n(T)$ is used as a fitted function]. This approach would be justified if it were shown at the same time that the function $\rho^*(T,G=0)$, calculated for the same function $V_n(T)$ and the same values of the parameters, agrees with the experimental data. However, the dark electric conductivity was not studied in Ref. 2. Other inaccuracies in the theory of Refs. 1 and 2 were also indicated previously in Ref. 3. It appears that the explanation presented in the present paper is the most convincing explanation of the experimental results of Ref. 4.

[1] D. P. Joshi, D. P. Blatt. IEEE Trans. Electron. Dev. **37**, 237 (1990).
[2] D. P. Bhatt, D. P. Joshi. J. Appl. Phys. **68**, 2338 (1990).
[3] K. M. Doshchanov, Fiz. Tekh. Poluprovodn. **30**, 558 (1996) [Semiconductors **30**, 305 (1996)].
[4] H. Paul Maruska, A. K. Ghosh, A. Rose, T. Feng. Appl. Phys. Lett. **36**, 381 (1980).
[5] N. C. C. Lu, L. Gergberg, C. Y. Lu, J. D. Meindl, IEEE Trans. Electron. Dev. **30**, 137 (1983).
[6] B. P. Tyagi, K. Sen. Phys. Status Solidi A **90**, 709 (1985).
[7] D. K. Paul, S. S. Mitra, Phys. Rev. Lett. **31**, 1000 (1973).
[8] P. C. Mathur, R. P. Sharma, R. Srivastrava, P. Saxena, and R. K. Kotnala, J. Appl. Phys. **54**, 3913 (1983).

Translated by M. E. Alferieff

Total external x-ray reflection and infrared spectroscopy study of porous silicon and its aging

L.A. Balagurov, V.F. Pavlov, E.A. Petrova, and G.P. Boronina

State Institute of Rare Metals, 109017 Moscow, Russia
(Submitted October 20, 1996; accepted for publication January 22, 1997)
Fiz. Tekh. Poluprovodn. **31**, 957–960 (August 1997)

Study of *p*-type porous silicon has been carried out by x-ray reflectometry for the first time. Its critical total-external-reflection angle and its reflection coefficient in the subcritical angle range are much smaller than for *c*-Si, which was grown by the Czochralski method. The critical angle decreases with increase of the porosity. The critical angle and the reflection coefficient increase with aging. These results are attributable to the much smaller electron density of porous silicon in comparison with *c*-Si, to the microgeometry of its surface, and to changes in both of these factors attendant to aging due to an increase in the concentration of atmospheric constituents observed in the infrared absorption spectra. As the porosity increases, the concentration of atmosmopheric impurities also increases, and in high-porosity material in addition to chemically adsorbed oxygen, carbon and water seem to contribute appreciably. [S1063-7826(97)01708-0]

1. INTRODUCTION

In recent years there has been a phenomenal growth of interest in porous silicon (PS) as a promising basic material in the fabrication of opto-electronic devices.[1,2] This interest is based on its huge specific surface area (more than 10^2 m^2/cm^3) and the very small size of its crystallites, which together are the reason for the high sensitivity of its properties to the surrounding medium.[3]

In this paper we report the results of a first-of-its-kind study of porous silicon and its aging by the method of x-ray reflexometry based on the effect of total external reflection (TER) of x rays,[4] and also infrared (IR) spectroscopy.

2. EXPERIMENTAL TECHNIQUE

Porous-silicon layers were obtained by anodic etching in a single-chamber cell with clamped contact and a platinum grid as the opposite electrode in the galvanostatic regime on KDB-1 (111) Si wafers with chemically-mechanically processed working surfaces. An ohmic contact was created on the back side of the wafer by sputtering-on aluminum with subsequent brazing-in at 550 °C for 15 min. The area of the layers was roughly 2 cm^2. Two series of layers of porous silicon were obtained in electrolyte mixtures $HF : C_2H_5OH$ with different proportions of the components. In each series in the preparation of the layers the total charge that passed through the system remained unchanged while the current density i was varied. The regimes in which the layers were fabricated are listed in Table I. The thickness of the porous-silicon layers $d = 4-14$ μm was measured on a cleavage of the layer with a ''Reichert'' Me-F2 optical microscope.

Measurements of the x-ray reflection coefficient R as a function of grazing angle θ were carried out on a ''Rigaku'' two-crystal topographical setup with an RU-200 CuKα x-radiation generator on a goniometric head having micrometric axial rotation with a scale division of $\sim 0.5'$. To lower the error in determining θ, we monochromatized the CuKα radiation ($\lambda = 1.54$ Å) with the help of a silicon crystal monochromator with (220) reflection. Comparison of the experimentally obtained values of $R(\theta)$ for a single-crystal silicon substrate (Fig. 1, curve *1*) with the values calculated theoretically according to the Fresnel formula allowing for absorption by a nonideal silicon surface showed that the error in the experimental values of R relative to the calculated values amounted to $2-3\%$ at angles less than the critical TER angle, reaching 5% in the region of the critical angle. We also monitored crystallographic bending of the porous-silicon films, which was not large (the radius of bending varied between 80 and 100 m) and could not affect the results of the TER measurements.

We also measured the infrared transmission spectra in the region $400-4000$ cm^{-1} on a ''Perkin-Elmer 983G'' spectrometer.

3. RESULTS AND DISCUSSION

Infrared transmission spectra of a porous-silicon layer (sample No. 1), measured directly after fabrication and after keeping it in air at room temperature for six months, are shown in Fig. 2. From the positions of the interference maxima we determined the values of the index of refraction of porous silicon n. From these values we found the density of the porous-silicon layers in the effective-medium approximation, in which a mixture of phases is treated as a homogeneous material with some mean polarizability.[5] The silicon volume fraction in the porous silicon, f_{Si}, was found from an expression given in Ref. 6, which assumes that porous silicon is a mixture of only two phases: *c*-Si and voids:

$$f_{Si}=[(1-n^2)(n_{Si}^2+2n^2)]/[3n^2(1-n_{Si}^2)], \quad (1)$$

where $n_{Si}=3.43$. The mean porosity over the thickness of a porous-silicon layer is $P_0=1-f_{Si}$. The values of n in the samples were found to lie within the limits 1.35–1.75 and during aging, within the limits of measurement error remained unchanged, apparently because of the similar values of the refractive indices of porous silicon and the natural

 1063-7826/97/080815-04$10.00

TABLE I.

Sample	Anodization regimes: Composition of solution $HF:C_2H_5OH$	Anodization regimes: i, mA/cm^2	Anodization regimes: t, min	Measurement results: P_0	P'_m	θ'_c, min	P_r	R''_m	θ''_c, min
c-Si					1	13			
1	2 : 1	130	2.5	0.66	0.62	5.4	0.84	1	8
2	2 : 1	180	1.8	0.69	0.78	4.5	0.88	0.9	8.5
3	3 : 5	6.5	14	0.62	0.72	6	0.79	1	7.5
4	3 : 5	13	7	0.72	0.78	5.5	0.83	0.87	8.5
5	3 : 5	26	3.5	0.78	0.78	4.7	0.87	0.8	8

Note: R'_m, θ'_c — initial measurments; R''_m, θ''_c — measurements after holding the samples in air for six months.

oxide, which agrees with the data of Ref. 3. The P_0 values which we obtained are listed in Table I. It can be seen that in both series of samples, obtained for different composition of the electrolyte, the porosity increased with growth of the anode current.

In the spectra of just the porous-silicon layers (Fig. 2, curve *1*) we observed absorption bands associated with vibrations of the Si–H_x groups (2115, 2090, 906, 662 624 cm^{-1}) and, probably, Si–F (815 cm^{-1}).[7,8] During aging, absorption bands associated with vibrations of the Si–O (1055−1150, 880, and 450 cm^{-1}), O–H (3450 cm^{-1}), and Si–C groups (2960 and 2930 cm^{-1}) appeared and grew (Fig. 2, curve *1a*).[7,8] From the absorption band of the stretching vibrations of the Si–O groups (1055−1150 cm^{-1}) we estimated the concentration of the silicon-bound oxygen (N_O) using the equation

$$N_O = A \int \alpha d\alpha.$$

We calculated the absorption coefficient α using the equation for the case of an absorbing layer on a transparent substrate.[9] For definition we used the value $A = 0.156$ at. %·cm/eV for α-Si from Ref. 10, which to within 5% coincides with the corresponding value for c-Si, obtained from the coefficient of proportionality between the maximum of the absorption peak and the oxygen concentration for c-Si (Ref. 11) allowing for the integral $\int \alpha d\alpha$.

The reflexometric measurements of the porous-silicon layers were performed about two weeks after preparation of the layers and after six months. In the case of one of the samples there were no noticeable changes in the measurement results during the two weeks after preparation of the samples. Curves of the reflection coefficient as a function of the x-ray grazing angle $R(\theta)$ are shown in Fig. 1. Table I lists the critical TER angle θ_c for each sample, where as the angle we took the angle corresponding to the intersection point of the extrapolated straight-line segments of $R(\theta)$. Table I also lists the reflection coefficient in the TER region, R_m, calculated as the arithmetic mean of the values R in the region $\theta < \theta_c$. It is evident that for all the samples the value of R_m is significantly smaller than for silicon, but the region of angles θ, in which the TER effect completely disappears, is substantially shifted toward angles smaller than for silicon. For relatively fresh layers, as the porosity is increased θ_c is observed to decrease and R_m exhibits a tendency to grow. All the samples are characterized by growth of R_m and θ_c as a result of aging.

In general, the form of the functional dependence $R(\theta)$ is determined by the electron density, by absorption, and by the microrelief of the near-surface layer whose thickness in the small angle region is (10−15)λ (where λ is the wavelength of the x radiation), i.e., in our case ~20 Å, and rarely grows in the region of disappearance of the TER effect.[3,12–14]

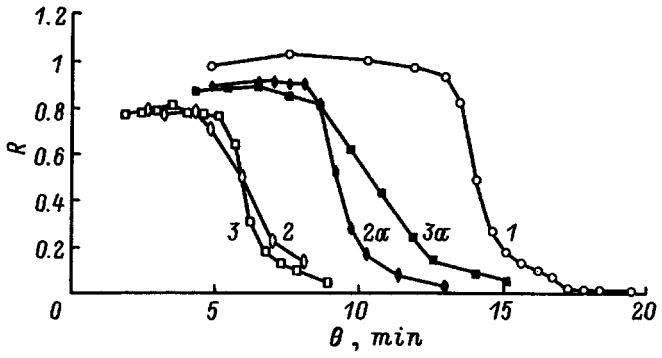

FIG. 1. Reflection coefficient R plotted versus grazing angle θ of the x-radiation incident on the surface for c-Si (*1*) and porous silicon. *2, 3* — initial measurements; *2a, 3a* — after holding in air for six months. Sets of data points *2, 2a* — for sample No. 2; *3, 3a* — for sample No. 4 (see Table I).

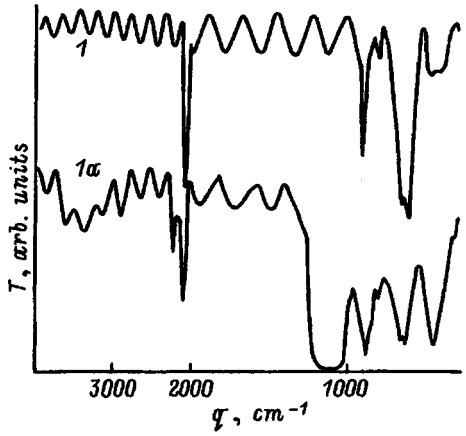

FIG. 2. Transmission spectra for a layer of porous silicon in the infrared for sample No. 1 (see Table I): *1* — initial measurements, *1a* — after holding in air for six months.

For $\theta \simeq \theta_c$ it is increased by roughly an order of magnitude. In the case of a silicon single crystal, absorption does not strongly alter the form of the dependence $R(\theta)$, calculated without allowance for absorption. For porous silicon, by virtue of its high porosity the effect is apparently weaker and can be disregarded. The decrease of θ_c with increasing porosity can be estimated from the relation[4]

$$\theta_c = (\lambda^2 e^2 n_e / \pi m c^2)^{1/2}, \quad (2)$$

where m is the electron mass, n_e is the electron density, and c is the speed of light in vacuum. The porosity P_r in the surface layer of thickness ~ 100 Å, estimated according to the formula

$$P_r = (\theta_{1c}^2 - \theta_c^2)/\theta_{1c}^2,$$

where θ_{1c} is the critical TER angle for c-Si, is systematically higher than the layer thickness-averaged values obtained from the optical measurements. This apparently indicates an enhanced porosity in the skin layer, in accordance with the data of Ref. 15.

The changes in the $R(\theta)$ curves during aging are obviously due to changes in the electron density of the porous-silicon layers and in their microgeometry due to an accumulation of atmospheric constituents in the porous silicon samples, which is what we observed from the infrared absorption spectra (Fig. 2). We assumed that for extended storage of samples in air the main contribution to the change in the electronic structure comes from oxygen and to a lesser degree carbon.[3] Since the number of electrons in the oxygen atom differs only slightly from the number of electrons in the carbon atom, we estimated from Eq. (2) the total amount of these impurities needed to obtain the shift in $R(\theta)$ toward larger θ observed experimentally during aging.

Figure 3 plots the dependence of the total concentration of oxygen and carbon (from the TER data) and oxygen located in the form of Si–O groups (from the infrared spectroscopy data) on the porosity for samples held in air for six months. It is apparent that the concentration of atmospheric impurities increases with increasing porosity. From these values it is not hard to estimate the ratio of the concentration of atmospheric impurities of silicon in the layers, which relative to less porous material (<0.8) does not exceed 1:1, and for more porous material grows to (2–3):1. The similar values of the concentration of oxygen found in the form of Si–O groups and the total impurity concentration obtained for relatively less porous material indicates that the main impurity in the less porous material is oxygen found in a chemically adsorbed state. It would appear that the substantial extent (see Fig. 3) by which the limiting concentration of the silicon-bound oxygen corresponding to the formation of SiO_2 (*1*) exceeds the total impurity concentration (*2*) must be attributed to the accumulation in the porous-silicon samples of water and carbon. It is also apparent because of its higher porosity in comparison with the volume-average that the skin layer is enriched with atmospheric impurities.

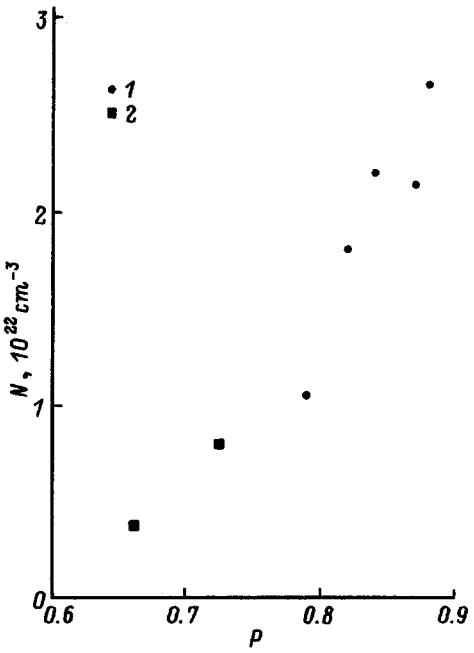

FIG. 3. Concentration of atmospheric impurities in porous silicon plotted as a function of porosity: *1* — total concentration of oxygen and carbon (from the total external reflection data); *2* — concentration of the oxygen present in the form of Si–O groups (from the infrared spectroscopy data).

4. CONCLUSIONS

In summary, the present study represents a first-of-its-kind investigation of porous silicon by x-ray reflexometry. We have shown that for porous silicon the critical angle θ_c and the reflection coefficient R_m in the subcritical angle range are significantly less than their values for c-Si. The critical angle decreases with increase of the porosity. R_m and θ_c were observed to increase during aging. The results presented here are explained by a significantly lower electron density of porous silicon in comparison with silicon and by the microgeometry of its surface, and also by changes in these parameters brought about by aging caused by an increase in the concentration of atmospheric constituents—oxygen, carbon, and water–in the porous silicon layers.

An increase in the total concentration of atmospheric impurities is observed with growth of porosity, where in strongly porous material, in addition to chemically absorbed oxygen, carbon and water contribute substantially.

The surface layer of porous silicon of thickness ~ 100 Å has a higher porosity than the total volume, and by virtue of this circumstance is enriched by atmospheric impurities.

The author is grateful to M.G. Mil'vidskiĭ, V.T. Bublik, and S.I. Zheludevaya for helpful discussions of the results of this work.

[1] W. Lang, P. Steiner, and F. Kozlowski, J. Lumin. **57**, 341 (1993).
[2] J. P. Zheng, K. L. Jiao, W. P. Shen, W. A. Anderson, and H. S. Kwok, Appl. Phys. Lett. **61**, 459 (1992).
[3] L. T. Canham, M. R. Houlton, W. Y. Leong, C. Pickering, and J. M. Keen, J. Appl. Phys. **70**, 422 (1991).
[4] R. W. James, *The Optical Principles of the Diffraction of X-Rays*, revised edition. (Bell, London, 1962).
[5] D. E. Aspnes and J. B. Theeten. J. Appl. Phys. **50**, 4928 (1979).
[6] C. Pickering, M. I. J. Beale, D. J. Robbins, P. J. Pearson, and R. Greef, J. Phys. C: Solid State Phys. **17**, 6535 (1984).

[7] A. Borghesi, A. Sassella, B. Pivac, and L. Pavesi, Solid State Commun. **87**, 1 (1993).
[8] K. H. Beckman, Surf. Sci. **3**, 314 (1965).
[9] E. C. Freeman and W. Paul, Phys. Rev. B **20**, 716 (1979).
[10] G. Lucovsky, S. S. Chao, J. Yang, J. E. Tyler, and W. Czubatyj, Phys. Rev. B **28**, 3225 (1983).
[11] *Handbook of Semiconductor Silicon Technology*, edited by W. C. O'Mara, R. B. Herring, and L. P. Hunt (Noyes Publications, Park Ridge, New Jersey, 1990).
[12] M. A. Andreeva, S. F. Borisova, and S. A. Stepanov, Poverkhnost', No. 4, 5 (1985).
[13] V. M. Sinaĭskiĭ and V. I. Sidenko, Instr. Exp. Tech. No. 6, 5 (1974).
[14] L. A. Smirnov and S. B. Anokhin, Opt. Spektrosk. **48**, 574 (1980) [Opt. Spectrosc. **48**, 319 (1980)].
[15] Y. Morin, L. Saviot, B. Champagnon, C. Esnouf, and A. Halimaout, Thin Solid Films **255**, 188 (1995).

Translated by Paul F. Schippnick

Calculation of $2p$ levels for thermal double donors in silicon

L. F. Makarenko

Belorussian State University, 220050 Minsk, Belarus[a)]

(Submitted May 11, 1996; accepted for publication January 28, 1997)
Fiz. Tekh. Poluprovodn. **31**, 961–965 (August 1997)

A two-center model is developed to explain the electronic structure of thermal double donors (TDD) in silicon. Calculations of $2p$ levels of singly ionized TDD's are performed in the effective mass approximation. From a comparison of the calculated results with the experimental data, the internuclear distance between the two electrically active atoms is evaluated as 0.75–0.95 nm for the TDD1–TDD3 and 1.35–1.75 nm for the next four species: TDD4–TDD7. © *1997 American Institute of Physics.* [S1063-7826(97)02008-5]

1. INTRODUCTION

The interpretation of infrared absorption spectra associated with electronic transitions between the levels of hydrogen-like impurities in semiconductors is based on effective-mass theory (EMT).[1] This theory very accurately predicts differences between the energies of the excited states of shallow substitution donors.[1–3] Its application has also proved to be successful in the description of the electronic structure of such complex defect complexes as, for example, thermal double donors (TDD) in silicon.[4] These defects constitute an entire family of successively formed donor centers. At least twelve types of donor centers are well known,[4,5] which we will denote, following the notation of Ref. 5, as TDD0, TDD1,...TDD11. Their optical characteristics and the electronic structure of a configuration with shallow donors have been described in detail in Refs. 4, 5, and 7.

Earlier works also report deviations of the properties of the given complexes from those predicted by the standard effective-mass theory considered in Refs. 1–3. One such deviation is the two-valley structure of the TDD ground state, discovered in Ref. 6 and confirmed by the data of Ref. 7. According to effective-mass theory, the wave function (WF) of the shallow donor in the semiconductor in silicon-like semiconductors is represented as a sum:

$$\psi(\mathbf{r}) = N\sum_{i=1}^{\nu} c_i F_i(\mathbf{r}) u(\mathbf{k}_{0i}, \mathbf{r}), \tag{1}$$

where ν is the number of valleys, N is a normalization factor, and $F(\mathbf{r})$ is the Bloch envelope wave function of the ith valley of the conduction band $u(\mathbf{k}_{0i}, \mathbf{r})$. While for an ordinary shallow donor (e.g., phosphorus in silicon) all the coefficients $c_i = 1$, for a TDD four of them are equal to zero.[4–7].

Another peculiarity of the electronic structure of thermal donors is splitting of the $2p_{\pm}$ state. Here the energy of one of the two new states $2p_{\pm h}$, like the ground-state energy, increases with the index of the thermal donor (n), and the energy of the other state $2p_{\pm l}$ decreases.[4] In this same work it was found that some of the characteristics of thermal donors vary discontinuously with growth of n. For example, a clear difference is observed between the properties of TDD3 and TDD4 (Ref. 4).

An understanding of the reasons for such deviations has not yet been achieved. Thus, for example, in Refs. 4, 6, and 7 the two-valley structure was explained as a result of a local uniaxial deformation of the lattice. Another explanation is connected with the model of a two-center core.[8,9] According to this model, the thermal donor core consists of two point donors located along the [110] axis of the defect. Thus, as a result of the anisotropy of the effective mass, the energies of states constructed from the wave functions of two valleys elongated along the perpendicular to this axis (Fig. 1) are lower than the energies of any other combinations of type (1). This hypothesis about the atomic structure of the considered defects at once gives the correct electronic structure of the TDD ground state in Ge (Ref. 10).

The variation in the energy with growth of the index of the TDD was explained in Ref. 9 within the framework of the two-center core model by a variation in the distance between the atoms responsible for the electrical activity of these complexes. The aim of the present paper is to develop these ideas further in order to achieve a consistent explanation of the observed peculiarities of the electronic structure of the excited $2p$ states of the entire family of TDD's and to be able to estimate the distance between the nuclei of the electrically active atoms.

2. CALCULATIONS

Of greatest interest would be a calculation of the $2p$ levels of singly ionized TDD's since it is for such TDD's that detailed spectroscopic data are available.[4,6,7] For the calculations we chose the arrangement of the axes of the Cartesian coordinate system shown in Fig. 1. In this case the effective-mass equation for the envelope wave function can be written in the form

$$\left[-\Delta + (1-\gamma)\frac{\partial^2}{\partial y^2} - \frac{2}{r_a} - \frac{2}{r_b}\right] F(\mathbf{r}) = EF(\mathbf{r}). \tag{2}$$

Equation (2) is written for the effective Bohr radius $a^* = 4\pi\varepsilon\varepsilon_0 \hbar^2/(m_t e^2) = 3.166$ nm as the unit of length and the effective Rydberg energy $\mathrm{Ry}^* = m_t e^4/[2\hbar^2(4\pi\varepsilon\varepsilon_0)^2] = 19.94$ meV as the unit of energy. Numerical values of all the constants were chosen following Ref. 3. The quantities r_a and r_b are distances measured from the atoms a and b, respectively (Fig. 1). For convenience in the

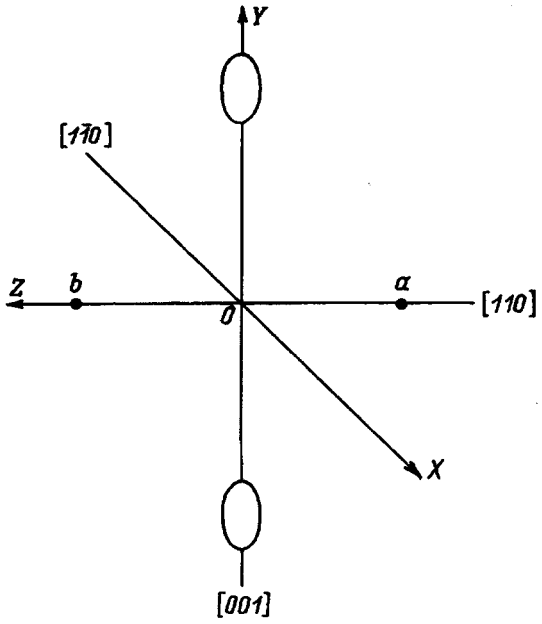

FIG. 1. Arrangement of the axes of the Cartesian coordinate system relative to the crystallographic axes of the crystalline lattice of silicon. The pair of electrically active atoms a and b is located on the z axis and has coordinates $z_a = R/2$ and $z_b = -R/2$. The y axis is aligned with the long axis of the ellipsoids of rotation of the constant-energy surface of those valleys of the conduction band, from Bloch wave functions of which the ground state of the thermal donors is ''constructed.''

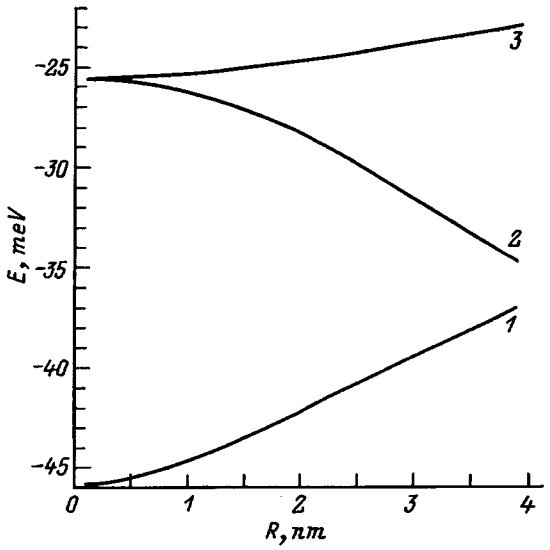

FIG. 2. The energy (E) of the states $2p\pi_x$ (*1*), $2p\sigma_z$ (*2*), and $2p\pi_y$ (*3*) of a pair of shallow donors, calculated in the effective-mass approximation, plotted versus the distance between donor nuclei (R). The orientation of the axes is shown in Fig. 1. The energy is reckoned from the bottom of the conduction band.

representation of the test functions $F(\mathbf{r})$, we transform to the deformed coordinate system $\tilde{x}=x$, $\tilde{y}=y$, $\tilde{z}=\beta z$. The factor β is a variational parameter.

In this coordinate system we can introduce elliptical coordinates

$$\tilde{\varepsilon}=(\tilde{r}_a+\tilde{r}_b)/\tilde{R}, \quad \tilde{\eta}=(\tilde{r}_a-\tilde{r}_b)/\tilde{R}$$

and construct simple approximate molecular orbitals, which will allow us to calculate the energies of the $2p$ states with high accuracy. These orbitals were constructed on the basis of Refs. 11 and 12 and are given in Table I. Calculation shows that the error in calculating the energy levels of a molecular hydrogen ion using the given orbitals does not exceed 0.1% for $R<1.3a_B$, where a_B is the Bohr radius. Table I also gives the test functions $F(\mathbf{r})$ for calculating the $2p$ states of a point donor in a semiconductor of the type Si and Ge.[2] Using these functions to calculate the energies of the corresponding states for silicon leads to errors no greater than 0.1% (Ref. 3).

All the calculations were performed numerically. For the $2p\pi$ orbitals the variational parameters were α and β, and for the $2p\sigma$ orbitals they were α, β, and p. The results of these calculations are plotted in Fig. 2.

3. DISCUSSION

As can be seen from Fig. 2, splitting of the $2p_\pm$ state of the thermal donors is explained in the two-center model as the result of the difference in energy of the $2p\pi$ and $2p\sigma$ states of the molecular hydrogen ion. While the ground-state energy increases with growth of the TDD index, the energy of the $2p\sigma$ state decreases with increasing distance between the nuclei of the atoms responsible for the donor action of the complex. Thus, all the noted peculiarities find a consistent explanation within the framework of the standard theory of the molecular hydrogen ion.[13] However, the energy levels of the analog of the molecular hydrogen ion, calculated in the effective-mass approximation, differ from their experimental values.[4] Let us consider in more detail the reasons for these differences.

According to Ref. 4, the binding energy of the $2p_0$ states of the single ionized TDD's TDD1–TDD7 decreases with growth of the center index from 50.4 to 47.7 meV. These

TABLE I. Test functions (approximate molecular orbitals) for calculating the energy levels of the $2p$ states of the thermal donors and the corresponding test functions at $R=0$ for calculating the levels of a shallow donor in a Si-type semiconductor.[2,3]

Designation of the molecular orbital	Approximate molecular orbital	Test wave function for $R=0$	Designation of states of the shallow donor
$2p\pi_x$	$N\tilde{x}\exp(-\alpha\tilde{\mu})$	$N\tilde{x}\exp(-\alpha\tilde{r})$	$2p_\pm$
$2p\pi_y$	$N\tilde{y}\exp(-\alpha\tilde{\mu})$	$N\tilde{y}\exp(-\alpha\tilde{r})$	$2p_0$
$2p\sigma_z$	$N(p+\alpha R\tilde{\mu})\exp(-\alpha\tilde{\mu})$	$N\tilde{x}\exp(-\alpha\tilde{r})$	$2p_\pm$

Note: N is a normalization factor.

values exceed those calculated within the framework of the effective-mass theory (Fig. 2). Such a relationship between the theoretically predicted and experimentally observed energies of the $2p$ states was observed for donors bound with interstitial magnesium[14] and aluminum[15] atoms. In Ref. 14 it was suggested that such a deep position of the $2p_0$-state is due to corrections to the local field arising from the interstitial position of the donor atom. Thus, we may conclude that the electrically active atoms of the thermal donors occupy interstitial positions in the silicon lattice. This conclusion accords with current ideas about the atomic structure of the thermal donors.[16]

The deviations from the effective-mass theory for the $2p_+$ states Mg_i and Al_i are smaller than for the $2p_0$ levels.[14,15] In addition, the $2p_\pm$ level of Mg_i splits in two. The reason for this split is unclear. It may have to do with the chemical nature of the donor atom.

Proceeding from these arguments, we write the energy of the $2p$ levels of the TDD in the form

$$E_n^{(i)} = E_{\mathrm{EMT},n}^{(i)} + E_{\mathrm{LFC},n}^{(i)}, \quad i = 1, 2, 3, \tag{3}$$

where $n = 0, 1, 2, \ldots$ is the TDD index, $i = 1$ corresponds to the $2p_0$ state, $i = 2$ corresponds to the lower $2p_\pm$ state denoted in Ref. 4 as $2p_{\pm l}$, and $i = 3$ corresponds to the upper $2p_\pm$-state denoted in Ref. 4 as $2p_{\pm h}$. The quantity $E_{\mathrm{EMT},n} = E_{\mathrm{EMT}}(R_n)$ is the energy calculated in the effective-mass theory, which depends on the distance between the nuclei of the electrically active atoms R_n. The quantity $E_{\mathrm{LFC},n} = E_{\mathrm{LFC}}(\mathbf{r}_n, R_n)$ is the correction for the EMT energy, which is associated with the local field and which depends on the coordinates of the donor atom in the unit cell $\mathbf{r}_n$ and, possibly, on the lattice distortion which is different for different R_n. Because of the presence of the $E_{\mathrm{LFC},n}$ term, direct comparison of the results of calculation with experiment is impossible. However, such a comparison is more justified for differences of the form

$$\delta_n = E_n^{(3)} - E_n^{(2)},$$

$$\Delta_n = E_n^{(3)} - E_n^{(1)}.$$

In the comparison of the calculated and experimental values δ_n and Δ_n it is necessary to bear in mind that the correction to the local field E_{LFC} for the $2p_0$ states of the interstitial donor is significantly greater than for the $2p_\pm$ states.[14] Therefore, if $\Delta = 20.4$ meV for a point EMT-donor with $Z = 2$ for $E(+/++) = E_c - 0.125$ meV, then for Mg_i^+ $\Delta = 21.8$ meV for $E(+/++) = E_c - 0.26$ meV (Ref. 14); and for Al_i^+ $\Delta = 22.8$ meV for $E(+/++) = E_c - 0.96$ meV (Ref. 15). Consequently, the calculated curves $\delta(\Delta)$ are shifted relative to the experimental curves along the abscissa. Since the quantity Δ_{LFC} is unknown for the thermal donors and may be different for defects with different index, it makes sense to augment the calculated values of $\Delta(R)$ by some mean correction to the local field, which we choose to be equal to 4 meV. Comparing the positions of the experimental points and the trend of the so-corrected theoretical curve (Fig. 3), we may conclude that the calculated data as a whole faithfully reflect the correlation between the quantities δ_n and Δ_n for the various

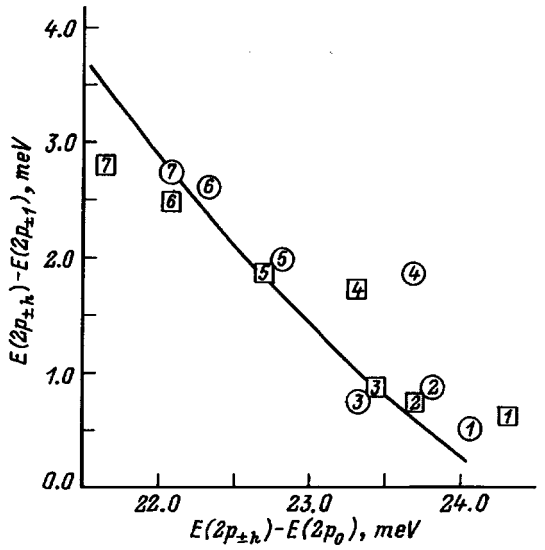

FIG. 3. Comparison of energy differences $\Delta = E(2p_{\pm h}) - E(2p_0)$ and $\delta = E(2p_{\pm h}) - E(2p_{\pm l})$, obtained for different types of thermal donors (labeled on the curve) from the infrared-spectroscopy data in Ref. 4 (circles) and Ref. 15 (squares), and the differences $\Delta = E(2p\pi_x) - E(2p\pi_y) + 4$ meV and $\delta = E(2p\pi_x) - E(2p\sigma_z)$, calculated in the present work (solid line).

TDD's. The experimental data were taken from Refs. 4 and 15. The data on the $2p_\pm$ levels of TDDn with $n > 7$ are indeterminate due to the superposition of bands belonging to the various centers.

The corrections for the local field for the $2p_-$ levels are significantly smaller. Thus, for Mg_i^+ we have $\delta = 0.23$ meV (Ref. 14) and for Al_i^+ $\delta = 0$. Let us initially assume that for all the thermal donors, just as for Al_i^+, $\delta_{\mathrm{LFC}} = 0$. With this assumption, we estimate the distance between the nuclei of the atoms of the pair from a comparison of the experimental values of δ_n with the calculated values (Fig. 4). Such a comparison leads to the value $R = 0.75 - 0.95$ nm for the first

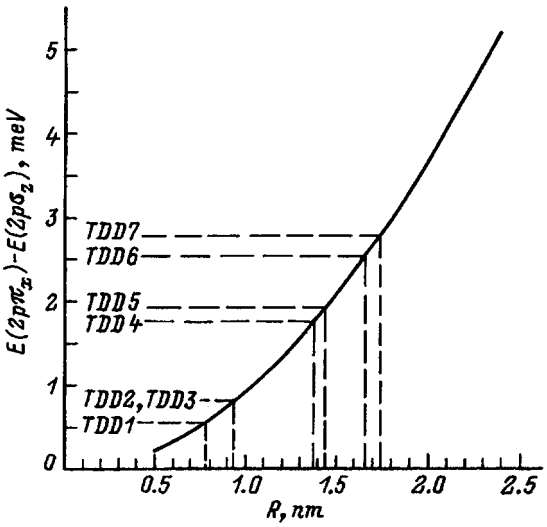

FIG. 4. Calculated dependence of splitting of the $2p_+$ level of a pair of shallow donors on the distance between them. The experimental values of $\delta = E(2p_{\pm h}) - E(2p_{\pm 1})$ are indicated for thermal donors of different types, taken as the arithmetic means of the data.[4,15]

group of centers with indices $n=1-3$ and $R=1.35-1.75$ nm for the second group with indices $n=4-7$. It should be noted that the error of determining the internuclear distance decreases with increasing thermal donor index. If, proceeding from the data for Mg_i^+, we take the indeterminacy for δ_n to be ± 0.23 meV, then we are led to an error in the determination of R_7 of only ± 0.07 nm.

The large break between the TDD3 and TDD4 parameters, also noted in Ref. 4 for other spectroscopic characteristics of these two defects, stands out. Its appearance may be explained on the basis of the values obtained for the internuclear distances of the pair of electrically active atoms entering into the makeup of defects with different indices n. All the R_n are grouped near the values mR^*, where $m=1, 2$ and $R^*=\sqrt{2}a_0=0.768$ nm is the distance between two tetrahedral interstitial sites which are nearest neighbors in the [110] direction, and a_0 is the lattice constant of silicon. Given this, if the donor atoms of the pair for TDD3 are found in two neighboring unit cells ($m=1$), then in the transformation from TDD3 to TDD4 one of these atoms will be shifted to the following cell, i.e., TDD4 now occupies not two but three neighboring unit cells in the [110] direction ($m=2$). As a result of such a transformation, not only the value of $E_{\mathrm{EMT},n}$, but also of $E_{\mathrm{LFC},n}$, is radically altered since the coordinates $\mathbf{r}_n$ of both donors of the pair will be different in their own unit cells. Thus, the considered defects can be divided into two groups. To the first group we may assign TDD1–TDD3 and apparently TDD0, which is not observable by infrared spectroscopy. The second group includes the four defects TDD4–TDD7.

The appearance of these two groups may be connected with the character of the arrangement of the interstitial oxygen atoms entering into the makeup of the defect. Because of the Coulomb repulsion forces between the nuclei, the donor pair deforms the lattice, which leads to the appearance of tensile stresses in the direction perpendicular to the pair axis. Evidence of such anisotropic stresses is provided by the data of Ref. 7. The deformation field so arising attracts the oxygen atoms which are built into the lattice between the atoms of the pair. The addition of a new oxygen atom, in turn, alters the local lattice stresses and, consequently, the distance between the donor centers. The addition of each fifth oxygen atom causes a transformation of the defect, which is accompanied by a transition of one of the atoms of the pair to a more remote interstitial site.

The nature of the atoms of the pair is still unclear. They may be intrinsic interstitial silicon atoms, which would explain the small value of $\delta_{\mathrm{LFC},n}$. At the same time, it cannot be ruled out that a pair of oxygen atoms may be electrically active. However, on the basis of only the infrared spectroscopy data it is apparently impossible to provide an answer this question.

4. CONCLUSIONS

The $2p$ levels of the singly ionized state of thermal double donors in silicon have been calculated in the effective-mass approximation on the assumption that the core of the given defects consists of a pair of shallow donor centers arrayed along the [110] axis. The calculated results have been compared with the available infrared spectroscopy data. As follows from the experimental data, the first seven thermal donors may be divided into two groups: TDD1–TDD3 and TDD4–TDD7. It is assumed that the electrically active atoms of the pair for the first group are found at interstitial sites located in neighboring unit cells in the [110] direction, and separated by one unit cell for the second group.

I would like to express my gratitude to Ya.I. Latushko for numerous helpful discussions.

[a)]Fax:0172/265-940; E-mail: root@fpm.bsu.minsk.by

[1] F. K. Ramdas and S. Rodriguez, Rep. Progr. Phys. **44**, 1297 (1981).
[2] W. Kohn and J. M. Luttinger, Phys. Rev. **98**, 915 (1955); W. Kohn, in *Solid State Physics*, edited by F. Seitz and D. Turnbull (Academic Press, New York, 1957). Vol. 5.
[3] R. A. Faulkner, Phys. Rev. **184**, 713 (1969).
[4] P. Wagner and J. Hage, Appl. Phys. A **49**, 123 (1989).
[5] G. D. Watkins, Rev. Solid State Phys. **4**, 279 (1990).
[6] M. Stavola, K. M. Lee, J. C. Nabity, P. E. Freeland, and L. C. Kimerling, Phys. Rev. Lett. **54**, 2639 (1985).
[7] P. Wagner, H. Gottschalk, J. M. Trombetta, and G. D. Watkins, J. Appl. Phys. **61**, 346 (1987).
[8] L. F. Makarenko, Fiz. Tekh. Poluprovodn. **28**, 1434 (1994) [Semiconductors **28**, 806 (1994)].
[9] L. F. Makarenko, Dokl. Akad. Nauk Belarus. **39**, 44 (1995).
[10] P. Clauws, F. Callens, F. Maes, Y. Vennik, and E. Boesmaa, Phys. Rev. B **44**, 3665 (1991).
[11] A. Dolgarno amd G. Poots, Proc. Phys. Soc., London, Sect. A **67**, 343 (1954).
[12] B. L. Moiseiwitsch and A. L. Stewart, Proc. Phys. Soc., London, Sect. A **67**, 457 (1954).
[13] J. C. Slater, *Electronic Structure of Molecules* (McGraw-Hill, New York, 1963).
[14] A. Thilderkvist, M. Kleverman, and H. G. Grimmeiss, Phys. Rev. B **49**, 16 338 (1994).
[15] Ya. I. Latushko, *Abstract of Candidate's Dissertation* (Belorussian State University, Minsk, 1988).
[16] P. Deák, L. C. Snyder, and J. W. Corbett, Phys. Rev. B **45**, 11 612 (1992).

Translated by Paul F. Schippnick

Conductivity stimulated by temperature oscillations in dissociated cadmium telluride and cadmium sulfide solid solutions

A. P. Belyaev, V. P. Rubets, and I. P. Kalinkin

St. Petersburg Technological Institute, 198013 St. Petersburg, Russia
(Submitted October 7, 1996; accepted for publication January 28, 1997)
Fiz. Tekh. Poluprovodn. **31**, 966–968 (August 1997)

The relaxation properties of films of dissociated cadmium sulfide and cadmium telluride solid solutions have been investigated. Conductivity stimulated by temperature oscillations was observed. The relaxations caused by a change in the external electric field and temperature were studied. It was determined that residual conductivity and increasing current relaxations are characteristic of the experimental samples. The results are interpreted in a model of an inhomogeneous semiconductor. © *1997 American Institute of Physics.*
[S1063-7826(97)02108-X]

In Ref. 1 , relaxational processes in CdS_xTe_{1-x} layers at low temperatures were reported. In the present study we investigated of the characteristic features of processes occurring at higher temperatures — above 300 K. The long-time relaxation processes initiated in CdS_xTe_{1-x} layers, subjected to thermally activated dissociation, by a change in temperature, illumination, and external voltage were investigated.

A sharp increase in voltage produced a rapid increase in the current to a maximum value, after which the current decreased monotonically to a minimum value and then again increased to a steady-state value. The characteristic current rise time (of the order of 1 min at 400 K) was many times longer than the decay time and depended exponentially on the temperature. Short-circuiting the current after a stationary current was established gave rise to a monotonic decrease of the current. The relaxation time of the ''residual conductivity'' depended on the temperature. It could be decreased substantially by light with photon energy $\hbar\omega > 1.1$ eV. Current relaxation increased sharply as a result of irradiation.

Figure 1 shows the results of an investigation of the relaxation properties arising as a result of temperature variations. Curves *1* and *2*, obtained by heating at a constant rate, contain sections of a rapid increase in conductivity. Increasing the heating rate shifted the onset of rapid growth to higher temperatures.

A nontrivial phenomenon was also found — conductivity stimulated by temperature oscillations (CSTO), i.e., temperature oscillations gave rise to a substantial increase in the conductivity of the samples. The magnitude of the additional conductivity (CSTO amplitude) was temperature-dependent (curves *3* and *4*). Holding a sample at a constant temperature, even for a much longer period of time, had virtually no effect on its conductivity. The effect was reversible.

In order for electronic equilibrium to be established in an inhomogeneous semiconductor, potential barriers must be overcome. This factor accounts for the long equilibration time and its exponential temperature dependence.[2–4] When a system in equilibrium is heated continuously, its conductivity will assume a new equilibrium value only when the characteristic heating time t_+ equals the characteristic equilibration time τ between the impurity levels and the conduction band.[4] At lower temperatures the effect of impurities is seemingly ''switched off.'' When the equality between t_+ and τ is reached, the impurities are ''switched on'' and the free current through the system increases sharply. An increase in the rate of heating decreases t_+ ; a higher temperature is therefore required to switch on the impurities, which accounts for the shift in the region of sharp current growth.

Proceeding from $t_+ = \tau$ and using the results of Ref. 4

$$\tau = \tau_0 \exp(E_r/kT),$$

$$t_+ = \Delta\rho / \left|(d\rho_0/dT)(dT/dt)\right|, \tag{1}$$

we obtain the approximate equality

$$E_r \approx \frac{kT_1T_2}{T_2 - T_1} \ln\left\{\frac{(dT/dt)_2 T_1^2}{(dT/dt)_1 T_2^2}\right\} \tag{2}$$

where $\Delta\rho$ is the sensitivity of the apparatus, and ρ_0 is the quantity measured by the apparatus.

To determine E_r it is sufficient to know the temperatures at which the impurities are activated, T_i, for different rates of heating $(dT/dt)_i$. The value $E_r \approx 0.4$ eV was obtained from Eq. (2) for the sample corresponding to Fig. 1. According to Ref. 3 , this quantity determines the energy required for electrons to be transferred from high-resistance regions (HRR) of an inhomogeneous system into low-resistance regions (LRR). In the case of the experimental samples, the HRR and LRR evidently correspond to switching on of a dissociated solid solution with a large and small quasigap, respectively. Surface states (SSs) with energy ε_s, which contribute to the formation of the potential well of the bands, are present directly at the boundaries of these regions. The energy diagram of the system can therefore be represented as shown in Fig. 2. An external field applied to such a system (Fig. 2b), because of the high inhomogeneity of the system, distorts the potential well.[1,5] An external field is rapidly screened in LRR and vice versa in HRR. As a result, equilibrium between the electrons in the conduction band and the impurity levels ε_i in the bulk and the surface states ε_s breaks down. Near the boundaries of the LRR, oriented toward the positive pole, the free-carrier density increases and conditions are created for trapping of carriers in ε_s, which gives rise to an increase in the intercrystallite barriers and therefore

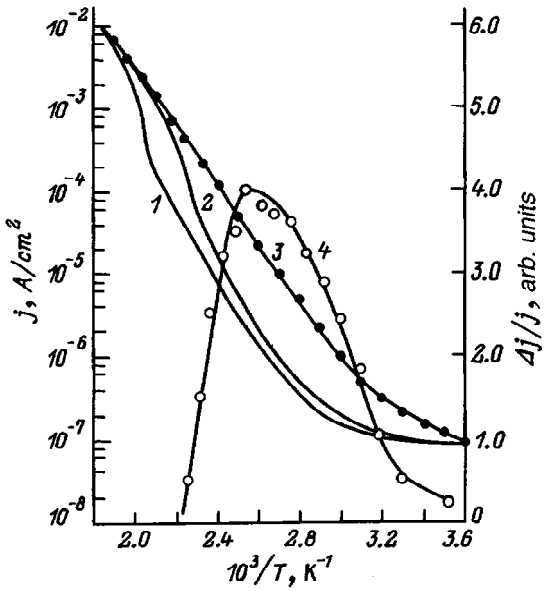

FIG. 1. Temperature dependences of the current density j with monotonic heating of the sample at a constant rate $dT/dt=0.2$ (*1*) and 0.07 K/s (*2*) and in the presence of temperature oscillations (*3*) as well as the amplitude $\Delta j/j$ of the conductivity stimulated by temperature oscillations (*4*).

a decrease of the through current. On the other side of the LRR the electron density decreases. Conditions arise for ionization of ε_s. This process decreases the intercrystallite barriers and increases the conductivity. If ε_s is greater than the amplitude of the potential well of the conduction band, then the rate of the second process will be lower. Equilibration after an external voltage is switched on abruptly will then be characterized by a current which initially decreases and then increases, consistent with our experiment. On this basis, the energy calculated from the slope angle of the temperature dependence of the characteristic time of the relaxation current increase can be interpreted as an ionization energy $\varepsilon_s \sim 0.95$ eV. This result agrees with Ref. 6 .

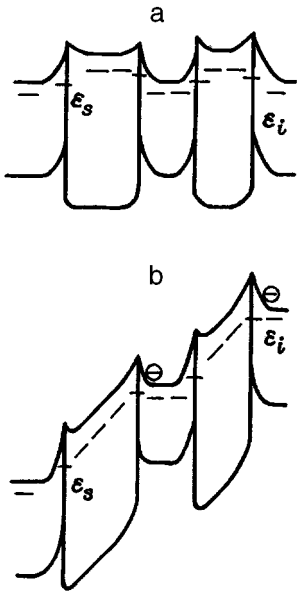

FIG. 2. Schematic representation of a band diagram of a decomposed solid solution of cadmium sulfide and telluride without (a) and with (b) the action of an external electric field.

The investigations of the relaxations of the ''residual conductivity'' confirm the model. Removing the external field again changes the potential well and again the equilibrium between the band and the levels is disrupted. The localized charges which are generated by an external field and which screen the quasidipoles set up the potential difference at the electrodes. We thus obtain the relaxation current with characteristic time determined by emptying of the traps.

The observed acceleration of the relaxation of residual conductivity by light with $\hbar\omega > 1.1$ eV, i.e., with energies close to the experimental value $E_r \approx 0.95$ eV (ionization of the BS level ε_s), provides additional support for the model.

Let us examine the processes accompanying the temperature oscillations. A temperature change destroys the LRR–HRR equilibrium. Restoration of equilibrium requires an anomalously long time. Extrapolation of the experimental temperature dependence of the characteristic time of the increasing relaxations shows that for the experimental samples at $T=300$ K the characteristic time τ will equal tens of hours. The large value of τ explains the apparent stability of the current at relatively low temperatures. However, a long time is required for the nonequilibrium carriers to be transferred from HRR to LRR via an activational path, but a different, faster path is possible by hopping along impurity levels. The hopping relaxation mechanism is all the more likely because II–VI layers synthesized by vacuum condensation characteristically have a high density of states in the quasigap.[7]

On the strength of the large magnitude of the potential well of the system, the electron hops must occur as multiphonon processes. A necessary condition for such hops are thermal fluctuations which level the wells between which hops occur.[8] Temperature oscillations promote fluctuations. Evidently, this is what causes the acceleration of the relaxation processes, which is manifested in the form of the CSTO.

The tunneling CSTO mechanism agrees with the experimental temperature dependence of the CSTO amplitude (Fig. 1, curve *4*). Indeed, the experimentally recorded conductivity can be conventionally divided into two components: 1) conductivity after establishment of quasiequilibrium in the band (established rapidly) and 2) additional conductivity arising after equilibrium is established between the conduction band and the levels (this equilibrium is established slowly). Since the position of the Fermi level is a nonlinear function of the temperature, the contribution of the additional conductivity increases with temperature. Therefore, the CSTO amplitude should also increase. However, while the contribution of the additional conductivity increases, its rise time decreases exponentially. Hence, even at the first oscillation, the experimentally recorded conductivity will contain a part in the additional conductivity that increases with temperature. This gives rise to a corresponding decrease in the CSTO amplitude. The competition between the processes is responsible for the maximum in the temperature curve of the CSTO amplitude.

In closing, we wish to make two remarks. The first one concerns the increasing-relaxation processes. The proposed model is close to the one obtained from a numerical analysis of transient currents in a semiconductor with barrier contacts.[9] The only difference is in the barrier-lowering mechanism. In Ref. 9 it is assumed that only a field acts on the barriers, which is amplified by charge redistribution; the boundary states are neglected. In the model considered here, the field action is followed by a change in the barriers as a result of a change in the charge occupying the BSs. It seems to us that in the systems investigated the mechanism of Ref. 9 could have occurred on each reverse-biased heterojunction, but since BSs are undoubtedly present in polycrystals, the field effect on the barriers should, as a rule, give rise to the mechanism described above.

The second remark concerns the experimental observation of CSTO. As shown above, samples not only with a unique potential well, but also with a high density of states in the quasigap are required for experimental observation. Evidently, this is why the phenomenon described above is rarely observed.

This work was sponsored by the All-Russia Fund for Fundamental Research under contract No. 96-02-19138.

[1] A. P. Belyaev, V. P. Rubets, and I. P. Kalinkin, Fiz. Tekh. Poluprovodn. **31**, 286 (1997) [Semiconductors **31**, 177 (1997)].
[2] A. Ya. Shik, Zh. Éksp. Teor. Fiz. **71**, 1159 (1976) [Sov. Phys. JETP **44**, 606 (1976)].
[3] A. Ya. Shik and A. Ya. Vul', Fiz. Tekh. Poluprovodn. **8**, 1675 (1974) [Sov. Phys. Semicond. **8**, 1085 (1974)].
[4] A. Ya. Vul', Sh. I. Nabiev, and P. ya. Shik, Fiz. Tekh. Poluprovodn. **11**, 506 (1977) [Sov. Phys. Semicond. **11**, 292 (1977)].
[5] B. I. Shklovskiĭ, Fiz. Tekh. Poluprovodn. **13**, 93 (1979) [Sov. Phys. Semicond. **13**, 53 (1979)].
[6] V. A. Smentyna, *Author's Abstract of Doctoral Dissertation* [in Russian], Semiconductors Institute of the Ukrainian Academy of Sciences, Kiev, 1988.
[7] A. P. Belyaev, V. P. Rubets, and I. P. Kalinkin, Thin Sol. Films, **158**, 25 (1988).
[8] N. Mott and E. Davis, *Electronic Processes in Non-Crystalline Materials*, Oxford University Press, N. Y., 1979 [Russian trans., Mir, Moscow, 1982].
[9] B. A. Bobylev and É. G. Kostsov, Fiz. Tekh. Poluprovodn. **23**, 224 (1989) [Sov. Phys. Semicond. **23**, 139 (1989)].

Translated by M. E. Alferieff

Intrinsic photoconductivity in chromium disilicide epitaxial thin films

N. G. Galkin, A. V. Konchenko, and A. M. Maslov

Institute of Automation and Control Processes, Far-Eastern Branch of the Russian Academy of Sciences, 690041 Vladivostok, Russia

(Submitted December 3, 1996; accepted for publication January 28, 1997)
Fiz. Tekh. Poluprovodn. **31**, 969–972 (August 1997)

Spectral and integrated photoconductivities in chromium-disilicide epitaxial films grown on single-layer silicon substrates have been studied in the photon energy range 0.5−1.6 eV. The region of the photoconductivity maximum observed at 1.23 eV corresponds to the third direct interband transition in chromium disilicide at 0.9−0.95 eV. Possible reasons for the weak photoconductivity signal in the region of the fundamental absorption edge are analyzed.
 [S1063-7826(97)02208-4]

Transition-metal disilicides possessing semiconductor properties ($CrSi_2$, β-$FeSi_2$, $MnSi_{1.73}$, $ReSi_2$) have aroused interest as promising materials for silicon planar technology. Much attention has been devoted to questions of heteroepitaxy on silicon,[1,2] and the electrical[3,4] and optical properties of such films.[4–7] However, the photoelectric properties of such films were investigated only for polycrystalline thin films of iron disilicide.[5]

In the present paper we report the first results of a study of the intrinsic photoconductivity in epitaxial thin films of chromium disilicide ($CrSi_2$) of *A*-type on silicon (111) substrates and establishes an interconnection between the energy band structure of $CrSi_2$, found from first-principles theoretical calculations, and the experimental energy dependence of the absorption coefficient obtained from calculations of the absorption and reflection spectra of the system ⟨$CrSi_2$ epitaxial film⟩–⟨Si substrate⟩.

$CrSi_2$ (0001) epitaxial films of *A*-type on Si (111) were grown by the seed layer method[2] with finishing by molecular-beam epitaxy from two sources in vacuum at a residual pressure of 3×10^{-9} Torr (Ref. 4). The spectral dependence of the photoconductivity and the integrated photoconductivity of epitaxial layers of $CrSi_2$ were recorded at room temperature on test structures with two current contacts and two potential ohmic contacts using a halogen lamp, an MDR-3 monochromator with an illumination system and a system for modulation and synchronization of the light beams, Ge and Si photodiodes, an interference filter and a silicon filter, a synchronized amplified with detector, and an x–y plotter.

The spectral dependence of the intrinsic photoconductivity σ_{ph} of a $CrSi_2$ epitaxial film of *A*-type and thickness 1000 Å is shown in Fig. 1a (curve *1*). The photoconductivity starts to grow at photon energies above 1.0 eV, passes through two maxima (a weak one at 1.1 eV and a strong one at 1.23 eV) and then decreases at photon energies above 1.3 eV. Efforts to spectrally resolve the photoconductivity signal at energies less than 1.0 eV were not successful. However, the total photoconductivity in the energy range 0.50−0.83 eV (the transparency region of the interference light filter) has been found for epitaxial films of chromium disilicide of thicknesses 300−2000 Å. As the incandescence current (J_L) of the halogen lamp is increased, the photocurrent (I_{ph}) grows nonlinearly (Fig. 1b). Since the thickness of the films was small, part of the photon flux with energies in the range 0.9−1.1 eV passed into the silicon substrate (Fig. 2a, curve *4*), which could have caused photoconduction in silicon. To control the possible contribution of silicon to the photoconductivity signal of the system $CrSi_2$/Si, the photoconductivity signal of the clean silicon substrate was also recorded (Fig. 1a, curve *2*). Since the shapes of the curves for silicon and the system $CrSi_2$/Si are quite similar, we carried out additional experiments. The spectral dependence of the photoconductivity of silicon and of chromium-disilicide epitaxial film on silicon was recorded using a clean, high-resistance ($150\ \Omega\cdot$cm) silicon wafer as the light filter in front of the samples (Fig. 2a, curves *1* and *2*). A shift of the photosensitivity maxima of Si and the $CrSi_2$ film on silicon is clearly observed. The transmittance (T) of the silicon light filter is also shown in Fig. 2a (curve *4*). The photoconductivity maximum of silicon in such a recording scheme is located at a photon energy of 1.07 eV, where the transmittance of the light filter is down by only 5% from maximum (Fig. 2a, curves *2* and *4*). The photoconductivity maximum of the $CrSi_2$ epitaxial film on Si is observed at 1.14 eV, where the transmittance of the silicon light filter is down by 29% from maximum (Fig. 2a, curves *1* and *4*). Consequently, the spectral photosensitivity of $CrSi_2$ epitaxial film is higher at higher energies in comparison with the photosensitivity of the clean silicon substrate. The absorption of the silicon light filter (Fig. 2a, curve *4*) is significantly lower than the absorption of the $CrSi_2$ film deposited on Si (Fig. 2a, curve *3*) at the same energies (1.0−1.2 eV), calculated from the transmission and reflection spectra. Therefore, the intensity of the light reaching the silicon substrate after passing through the $CrSi_2$ film is also small. Thus, the contribution of the silicon substrate to the photoconductivity signal in the system $CrSi_2$/Si is a very small quantity and may be noticeable only at photon energies below 1.07 eV. Consequently, the observed spectral dependence of the photoconductivity of the system $CrSi_2$/Si (Fig. 1a, curve *1*) is determined mainly by the contribution of the $CrSi_2$ epitaxial film.

The spectral dependence of the absorption coefficient of the $CrSi_2$ epitaxial film, calculated using the two-layer model,[8] is plotted in Fig. 2b. One feature of the energy band structure of $CrSi_2$ epitaxial films is the presence of three

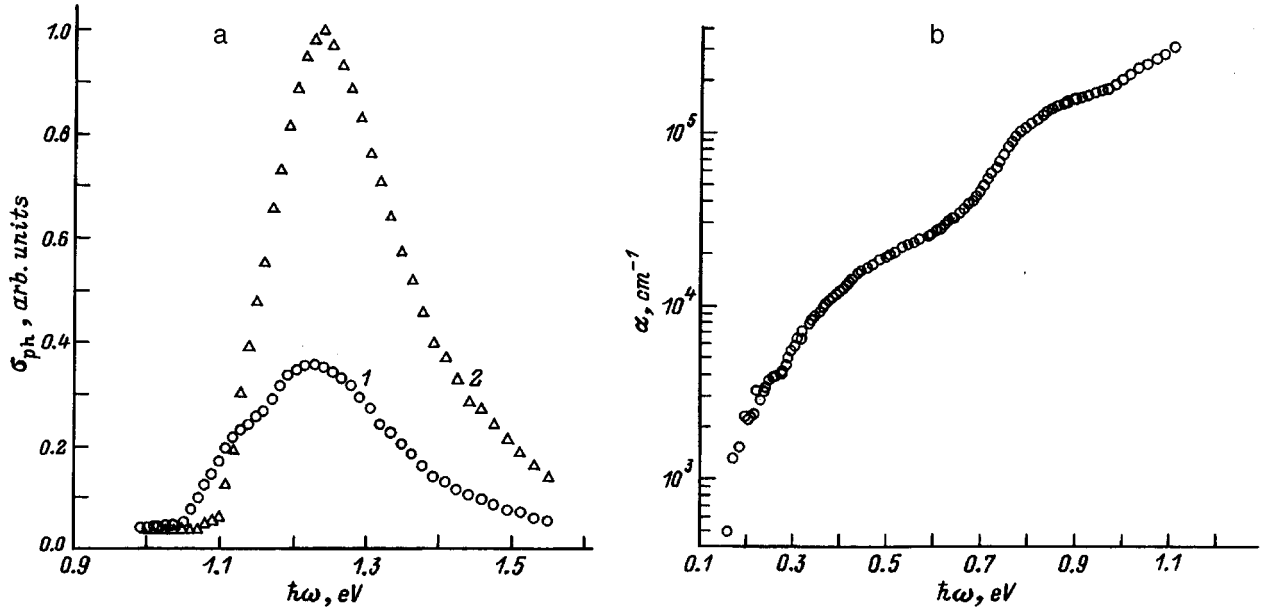

FIG. 1. a — photoconductivity spectra σ_{ph} of a chromium-disilicide epitaxial film deposited on silicon (*1*) and the high-resistance silicon substrate (*2*) at room temperature; b — total photocurrent (I_{ph}) of the epitaxial film of chromium disilicide on silicon in the energy range $0.50-0.83$ eV plotted versus the incandescence current of the halogen lamp (J_L).

direct interband transitions at 0.34, 0.7, and 0.9 eV,[4,8] which is not usually observed in semiconductors of the groups IV, III–V, and II–VI.[9] $CrSi_2$ epitaxial films of *A*-type are characterized by a combined density of states in the fundamental absorption region that is depressed in comparison with the density of states contributing to the interband transitions at 0.7 and 0.9 eV (Ref. 8) and a narrow energy region ($0.3-1.3$ eV) of the transition from the minimal combined density of states to the maximal are characteristic.[7,8]

Theoretical calculations of the energy band structure of $CrSi_2$ from first principles in various approximations have predicted the formation of an indirect fundamental interband transition with large spread of energies $E_g=0.21-0.38$ eV and a second direct interband transition in the energy range $E_2=0.39-0.47$ eV.[7,10,11]

In addition, according to the results of first-principles theoretical calculations of one of the papers in Refs. 12 a direct interband transition should be observed in $CrSi_2$ at $0.25-0.26$ eV and a second direct transition at $E_2=0.48-0.49$ eV. However, the reflection spectrum of $CrSi_2$, calculated from the results of theoretical calculations,[7] differs strongly from the reflection spectra of $CrSi_2$ single

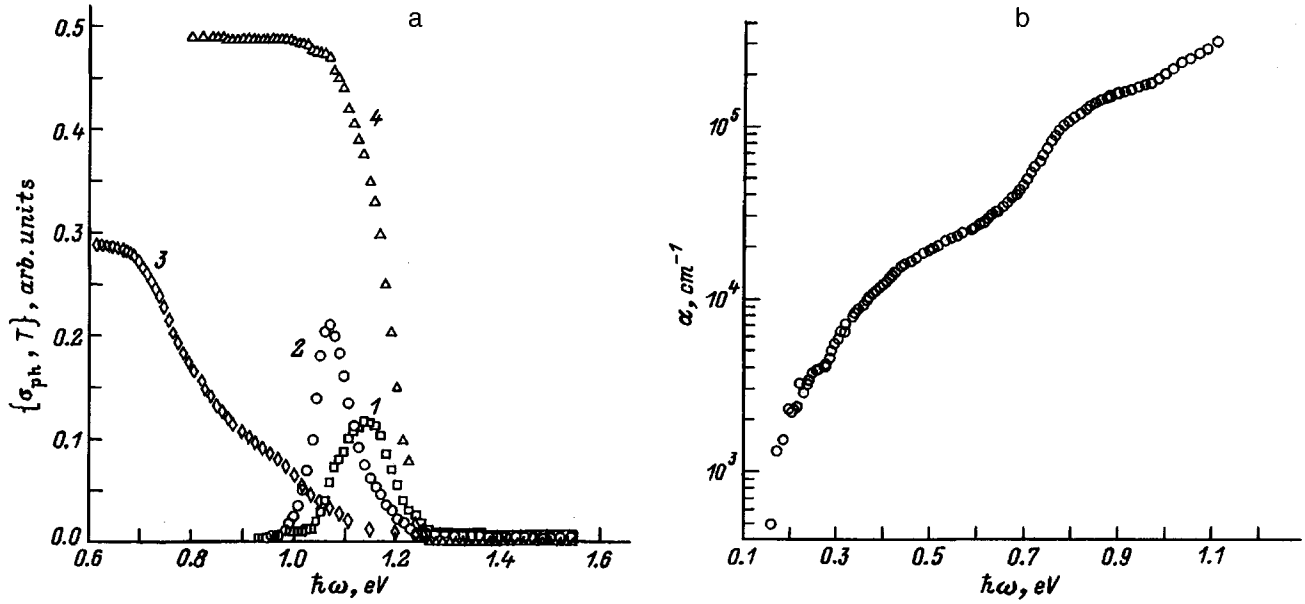

FIG. 2. a — Photoconductivity spectra σ_{ph} (*1,2*) transmission spectra T (*3,4*) of a chromium-disilicide film deposited on silicon (*1,3*) and the high-resistance silicon substrate (*2,4*) using a silicon light filter; b — spectral dependence of the absorption coefficient α of the chromium-disilicide epitaxial film.

crystals[7] and polycrystalline[6,7] and epitaxial[8] films. Consequently, at present theoretical calculations from first principles give quite contradictory results on the main interband transitions in the energy band structure of $CrSi_2$ and cannot be reliably used in the interpretation of the spectral dependence of the photoconductivity.

For small thickness of the $CrSi_2$ films and rapid growth of the combined density of states in the range of transition energies $0.34-1.3$ eV,[7,8] one might expect a shift of the photosensitivity maxima toward higher energies.[13] Such a picture has been observed for the spectral dependence of the photoconductivity in polycrystalline thin films of β-$FeSi_2$ on Si (Ref. 5), where the long-wavelength edge of the photoconductivity was found to lie at 1.0 eV, and the photoconductivity maximum—at 1.35 eV. Here the width of the band gap of β-$FeSi_2$ is equal to 0.87 eV (Ref. 5), and the long-wavelength edge of the photoconductivity corresponds to the absorption coefficient equal to $\alpha=1\times10^5\text{cm}^{-1}$. For $CrSi_2$ epitaxial films the maximum of the spectral sensitivity is found at 1.23 eV, which corresponds to the absorption coefficient equal to $\alpha\approx4\times10^5\text{cm}^{-1}$ (Fig. 2b). For the $CrSi_2$ film thickness $d=1000$ Å (or 1×10^{-5} cm) the quantity $\alpha d=4$, which does not contradict the condition for the observation of photoconductivity maxima for semiconductors $\alpha d\geqslant1$ (Ref. 9). The integrated photoconductivity of $CrSi_2$ epitaxial film in the energy range $0.50-0.83$ eV (Fig. 1b) supports the appearance of a weak photoconductivity signal in the region of energies close to the edge of the intrinsic absorption ($E_g=0.34$ eV). As the thickness of the epitaxial films of $CrSi_2$ on Si is increased to $(1-3)\times10^{-4}$ cm, one might expect to see a shift of the maximum of the spectral photosensitivity into the energy range $0.6-0.8$ eV. In preliminary experiments on $CrSi_2$ epitaxial films with thickness from 2000 to 8000 Å the main photoconductivity maximum was found to shift into the energy range $1.18-1.12$ eV.

In summary, the spectral range of the intrinsic photoconductivity of $CrSi_2$ epitaxial films of A-type on Si (111) with thickness 1000 Å includes the range of photon energies 0.5–1.6 eV, and the first three direct interband transitions with energies 0.34, 0.7, and 0.9 eV participate in the formation of the photoconductivity signal and correspond to a gradual rise in the combined density of states.[8] The observed shift of the photosensitivity maximum into the energy region of the third interband transition can be explained by the small thickness of the investigated films and peculiarities of the spectral dependence of the density of combined states in epitaxial films of chromium disilicide. Taking into account the participation of direct interband transitions in the photoconduction process, we can assume that radiative transitions in chromium-disilicide epitaxial films can be realized.

This work was carried out with the support of the Russian Fund for Fundamental Research (Grant No. 96-02-16038-a).

[1] J. M. Gay, P. Stocker, and F. Rethore, J. Appl. Phys. **73**, 8169 (1993).
[2] N. I. Plusnin, N. G. Galkin, and V. G. Lifshits, Surf. Rev. Lett. **2**, 439 (1995).
[3] F. Nava, T. Tien, and K. N. Tu, J. Appl. Phys. **57**, 2018 (1985).
[4] N. G. Galkin, T. V. Velitchko, S. V. Skripka, and A. B. Khrustalev, Thin Solid Films **280**, 211 (1996).
[5] M. C. Bost and J. E. Mahan, J. Vac. Sci. Technol. B **4**, 1336(1986).
[6] M. C. Bost and J. E. Mahan, J. Appl. Phys. **63**, 839 (1988).
[7] V. Bellani, G. Guizzetti, F. Marabelli, A. Piaggi, A. Borghesi, F. Nava, V. N. Antonov, Vl. N. Antonov, O. Jepsen, O. K. Andersen, and V. V. Nemoshkalenko, Phys. Rev. B **46**, 9380 (1992).
[8] N. G. Galkin, A. M. Maslov, and A. V. Konchenko, Thin Solid Films (1997) (to be published).
[9] T. S. Moss, G. J. Burrell, and B. Ellis, *Semiconductor Opto-Electronics* (Butterworths, London, 1973).
[10] L.F. Matheiss, Phys. Rev. B **43**, 1863 (1991).
[11] M.P.C. Krijn and R. Eppenda, Phys. Rev. B **44**, 9042 (1991).
[12] V. E. Borisenko, L. I. Ivanenko, and S. Yu. Nikitin, Mikroélektronika **21**, 69 (1992).
[13] J. N. Humphrey, Appl. Optics, **4**, 665 (1965).

Translated by Paul F. Schippnick

Enhancement of the photovoltaic effect in a two-dimensionally disordered medium

M. V. Énti[a)]

Institute of Semiconductor Physics, Siberian Branch of the Russian Academy of Sciences, 630090 Novosibirsk, Russia

(Submitted January 17, 1997; accepted for publication January 28, 1997)
Fiz. Tekh. Poluprovodn. **31**, 973–975 (August 1997)

The photogalvanic effect in a two-dimensional, weakly absorbing Dykhne medium without an inversion center is studied. It is shown that a giant enhancement of the effective photovoltaic coefficient occurs as a result of the divergence of the mean-square modulus of the electric field. © *1997 American Institute of Physics.* [S1063-7826(97)02308-9]

It has been shown in a number of recent works[1–6] that local electric fields in randomly inhomogeneous macroscopic media consisting of nonabsorbing microscropic parts are intensified as a result of the excitation of local plasmons. As a result, the averages of the even powers of the modulus of the electric field diverge in such a medium. These quantities are determining factors for different nonlinear responses of the system, which should result in an enhancement of these responses.

We studied a special case of such effects — the photovoltaic effect arising in a medium without an inversion center. Let a high-frequency polarization $\mathbf{D}^{\omega}$ and the local stationary current density $\mathbf{j}^0$ in the medium be described by the expressions

$$D_i^{\omega}=\varepsilon^{\omega}(\mathbf{r})E_i^{\omega}, \tag{1}$$

$$j_i^0=\sigma^0(\mathbf{r})E_i^0+\alpha_{ijk}E_j^{\omega}E_k^{-\omega}+\text{c.c.}, \tag{2}$$

where $E_k^{-\omega}=(E_k^{\omega})^*$. The first term describes the high-frequency part of the polarization of the medium at optical frequencies ω and the second term describes the low-frequency photovoltaic current. Both quantities satisfy Maxwell's equations

$$\nabla\cdot\mathbf{j}^0=0, \quad \nabla\times\mathbf{E}^0=0, \tag{3}$$

$$\nabla\cdot\mathbf{D}^{\omega}=0 \quad \nabla\times\mathbf{E}^{\omega}=0. \tag{4}$$

Let high-frequency permittivity $\varepsilon^{\omega}(\mathbf{r})$ and the zero-frequency conductivity $\sigma^0(\mathbf{r})$ be random functions of the coordinates.

An effective photovoltaic coefficient $a_{ijk,\text{eff}}$ can be introduced by analogy with the effective conductivity as

$$\langle j_k\rangle=\alpha_{ijk}\langle E_j^{\omega}(E_k^{\omega})^*\rangle=\alpha_{ijk,\text{eff}}\langle E_j^{\omega}\rangle\langle(E_k^{\omega})^*\rangle. \tag{5}$$

In Eq. (5) the average is a spatial average. In general, not only the directly photovoltaic current, but also the static response associated with the redistribution of the static field, described by the first term in Eq. (2), contributes to the average current. However, the average of this term vanishes if $\sigma^0(\mathbf{r})$ and $\varepsilon^{\omega}(\mathbf{r})$ [and therefore $\mathbf{E}^{\omega}(\mathbf{r})$] are independent random quantities or the conductivity is completely independent of the coordinates. In this case the expression for the effective photovoltaic coefficient $\alpha_{ijk,\text{eff}}$ is determined by averaging the second term in Eq. (1) and therefore reduces to the average $\langle E_j^{\omega}(E_k^{\omega})^*\rangle$.

Let an electromagnetic wave be incident on the sample in a direction perpendicular to the (x,y) plane of the sample, and let the medium be macroscopically isotropic and possess a two-dimensional inhomogeneity $\varepsilon^{\omega}(\mathbf{r})=\varepsilon^{\omega}(x,y)$. Then there will be no distinguished directions in the plane and for the components $(i,j)=(x,y)$ the tensor of the averages can be expressed in terms of the mean-square modulus of the field $\langle E_j^{\omega}(E_k^{\omega})^*\rangle=(1/2)\,\delta_{ij}\langle|\mathbf{E}^{\omega}|^2\rangle$. Let us consider a Dykhne medium[7] — a two-phase statistically equivalent mixture of media with permittivities $\varepsilon_1>0$ and $\varepsilon_2<0$ — as a model of the high-frequency permittivity ε. Specifically, it can be assumed that the permittivity of the initial media is determined by free carriers in the Drude–Lorentz model

$$\varepsilon_{1,2}=1-\frac{\omega_{p(1,2)}^2}{\omega(\omega+i/\tau_{1,2})} \tag{6}$$

and the light frequency ω falls between the close plasma frequencies $\omega_{p(1,2)}$. In this limit the low-frequency conductivity is virtually coordinate-independent while the high-frequency permittivity has different signs at different points. At high frequencies $\omega\tau\gg1$ and $\varepsilon_{1,2}=\varepsilon'_{1,2}+i\varepsilon''_{1,2}=1-\omega_{p(1,2)}^2/\omega^2+i\omega_{p(1,2)}^2/(\omega^3\tau)$, where $\varepsilon''_{1,2}\ll\varepsilon'_{1,2}$.

Examples of the objects under study are semiconductor–semiconductor, metal–insulator, and metal–metal composite materials, consisting of components with close properties in the frequency range where the imaginary part of the permittivity is less than the real part and the signs of the local values of $\varepsilon'_{1,2}$ are different. In semiconductors, this is possible near the free-carrier plasma resonance, near a polariton resonance, and near frequencies far above the optical absorption edge.

In the case of a Dykhne medium, an exact expression can be found for the average $\langle|\mathbf{E}^{\omega}|^2\rangle$. It follows from the energy conservation law that

$$\varepsilon''_{\text{eff}}|\langle\mathbf{E}^{\omega}\rangle|^2=\langle\varepsilon''|\mathbf{E}^{\omega}|\rangle. \tag{7}$$

Carrying out the Dykhne transformation for the induction $\mathbf{D}^{\omega}=\varepsilon\mathbf{E}^{\omega}$ and for the field in both media

$$\begin{aligned}&\mathbf{E}^{\omega\prime}=(1/\varepsilon_{\text{eff}})[\mathbf{n}\times\mathbf{D}^{\omega}], \quad x\to y,\\ &\mathbf{D}^{\omega\prime}=\varepsilon_{\text{eff}}[\mathbf{n}\times\mathbf{E}^{\omega}], \quad y\to -x,\end{aligned} \tag{8}$$

which preserves the form of Maxwell's equations (4) for them

$$\nabla\cdot\mathbf{D}^{\omega\prime}=0, \quad \nabla\times\mathbf{E}^{\omega\prime}=0 \tag{9}$$

 1063-7826/97/080829-02$10.00

and transforms medium 1 into medium 2 and vice versa and the expression for the induction $\mathbf{D}^{\omega}=\varepsilon\mathbf{E}^{\omega}$ into $\mathbf{D}^{\omega\prime}=(\varepsilon/\varepsilon_{\text{eff}})\mathbf{E}^{\omega\prime}$, we find

$$|\varepsilon_1|\langle|\mathbf{E}^{\omega}|^2\rangle_1=|\varepsilon_2|\langle|\mathbf{E}^{\omega}|^2\rangle_2. \tag{10}$$

The subscripts 1 and 2 mean averaging over the first and second media, respectively. Combining the expressions (7) and (10), we obtain

$$\langle|\mathbf{E}^{\omega}|^2\rangle_{1,2}=\langle|\mathbf{E}^{\omega}|^2\rangle\frac{2|\varepsilon_{2,1}|\mathrm{Im}(\sqrt{\varepsilon_1\varepsilon_2})}{\varepsilon_1''|\varepsilon_2|+\varepsilon_2''|\varepsilon_1|}, \tag{11}$$

$$\langle|\mathbf{E}^{\omega}|^2\rangle=\frac{(|\varepsilon_1|+|\varepsilon_2|)\mathrm{Im}(\sqrt{\varepsilon_1\varepsilon_2})}{\varepsilon_1''|\varepsilon_2|+\varepsilon_2''|\varepsilon_1|}|\langle\mathbf{E}^{\omega}\rangle|^2. \tag{12}$$

As a result, we obtain for the average photovoltaic current

$$\langle j_i\rangle=2\,\mathrm{Im}(\sqrt{\varepsilon_2\varepsilon_2})\frac{\alpha_{i,1}|\varepsilon_2|+\alpha_{i,2}|\varepsilon_1|}{\varepsilon_1''|\varepsilon_2|+\varepsilon_2''|\varepsilon_1|}|\langle\mathbf{E}^{\omega}\rangle|^2, \tag{13}$$

where $\alpha_{i,(1,2)}=(1/2)(\alpha_{ixx,(1,2)}+\alpha_{iyy,(1,2)})$.

In the particular case when $\alpha_{1,2}$ are identical we have

$$\langle j_i\rangle=\alpha_i\frac{(|\varepsilon_1|+|\varepsilon_2|)\mathrm{Im}(\sqrt{(\varepsilon_1\varepsilon_2)})}{\varepsilon_1''|\varepsilon_2|+\varepsilon_2''|\varepsilon_1|}|\langle\mathbf{E}^{\omega}\rangle|^2=\alpha_{\text{eff},i}|\langle\mathbf{E}^{\omega}\rangle|^2. \tag{14}$$

According to Eqs. (13) and (14), in the region of weak local absorption ($\varepsilon_{1,2}''\to 0$) the denominator approaches zero while the numerator remains finite if $\varepsilon_1\varepsilon_2<0$; i.e., the photovoltaic tensor is intensified. In a weakly absorbing medium the imaginary part of the effective permittivity remains finite under these conditions. The reason is that a local electric field is excited. The squared modulus of the electric field is determined, according to Eq. (7), by the balance of the macroscopic absorption and the rate of local losses, which are determined by ε''. In the transmission region of the medium $\varepsilon_1\varepsilon_2>0$ the effective photovoltaic tensor is of the same order of magnitude as the local tensor.

As an example, consider a noncentrosymmetric GaAs crystal without an inversion center, in which symmetry permits a volume photovoltaic effect. Let us assume that a bulk sample consists of alternating strongly and weakly doped ''columns'' oriented along the $z=\langle 111\rangle$ axis, which is oriented in a direction along the normal to the surfaces of the sample, with statistically identical properties. Specifically, this can be the checkerboard distribution of the properties. The photovoltaic effect is enhanced near frequencies between the free-electron plasma frequencies. In a bulk GaAs sample the components of the photovoltaic tensor are all equal and of the type α_{123}. Assuming that the orientation of axes is $x=\langle 01\overline{1}\rangle$ and $y=\langle\overline{2}11\rangle$, we find that $j_x=0$ and $j_y=\sqrt{2/3}\alpha_{\text{eff}}|\langle\mathbf{E}^{\omega}\rangle|^2$.

Let us now discuss the results. First, we note that the approximation which assumes that the fluctuations of the static conductivity are small does not affect the order of magnitude of the response as long as these fluctuations do not exceed the average conductivity: $\ln(\sigma/\langle\sigma\rangle)\lesssim 1$. This happens because the enhancement of the photovoltaic effect is due not to the closeness to the percolation threshold but rather to the possibility of absorption of the field in a medium with no local losses.

In the limit of a low light frequency the enhancement of $\langle\mathbf{E}\rangle^2$ appears in a metal–insulator mixture, where the ratio $h=\sigma_1/\sigma_2$ of the static conductivities, which determines the closeness to the percolation threshold, is small. In a percolation system the mean-square field diverges. Indeed, it follows from Ref. 7 that in a system with conductivities $\sigma_1$and σ_2

$$\langle\mathbf{E}^2\rangle=\frac{\sigma_1+\sigma_2}{\sqrt{\sigma_1\sigma_2}}\langle\mathbf{E}\rangle^2. \tag{15}$$

If one of the quantities $\sigma_{1,2}$ approaches 0 and the other remains bounded, then $\langle\mathbf{E}^2\rangle\to\infty$. However, in this limit, in contrast to the high-frequency case, to find the average current it is not enough to average the magnitude of the current. It is also necessary to solve an equation for the static field to second-order in the alternating field, and it is impossible to conclude on the basis of the expression (15) that the effective photovoltaic coefficient diverges.

I thank É. M. Baskin for fruitful discussions.

This work was supported, in part, by the Russian Fund for Fundamental Research under grants Nos. 95-0204432 and 96-0219353 and Volkswagen–Stiftung.

[a]e-mail: entin@isp.nsc.ru

[1] F. Brouers, S. Blacher, and A. K. Sarychev in *Fractal Reviews in the Natural and Applied Sciences*, 1995, p. 237.
[2] F. Brouers, S. Blacher, N. Henrioulle, and A. K. Sarychev in *Electrical Transport and Optical Properties of Inhomogeneous Media*, Scientific Center for Applied Problems of Electrodynamics, Moscow, 1996, p. 46.
[3] A. N. Lagarkov, K. N. Rosanov, A. K. Sarychev, and N. A. Simonov; submitted to J. Phys. A (1996).
[4] J. P. Clerc, G. Giraud, J. M. Laugier, and J. M. Luck, Adv. Phys. **39**, 191 (1990).
[5] M. V. Éntin and G. M. Éntin, JETP Lett. **64**, 467 (1996).
[6] É. M. Baskin, M. V. Éntin, A. K. Sarychev, and A. A. Snarskiĭ, Physica A (in press).
[7] A. M. Dykhne, Zh. Éksp. Teor. Fiz. **59**, 110 (1970) [Sov. Phys. JETP **32**, 63 (1971)].

Translated by M. E. Alferieff

InAsSb/InAsSbP diode lasers with separate electrical and optical confinement, emitting at 3–4 μm

T. N. Danilova, A. P. Danilova, O. G. Ershov, A. H. Imenkov, N. M. Kolchanova, M. V. Stepanov, V. V. Sherstnev, and Yu. P. Yakovlev

A. F. Ioffe Physicotechnical Institute, Russian Academy of Sciences, 194021 St. Petersburg, Russia
(Submitted January 20, 1997; accepted for publication January 28, 1997)
Fiz. Tekh. Poluprovodn. **31**, 976–979 (August 1997)

Diode lasers based on InAsSb/InAsSbP with separate electrical and optical confinement, emitting in the wavelength interval 3–4 μm, are investigated. The lasers attain a higher operating temperature when electrical confinement is created by means of type-II heterojunctions. Interface Auger recombination is suppressed in lasers of this type, and the experimental current density is close to the theoretically calculated value for the case of predominant volume Auger recombination at a temperature of 180–220 K. © *1997 American Institute of Physics.* [S1063-7826(97)02408-3]

1. Lasers emitting in the mid-infrared range are attracting considerable attention for their potential applications, specifically in optical communications utilizing fluorite glasses, in molecular spectroscopy with the capability for precision testing and control in high-technology industries, and also in medicine. The main problem for lasers based on III–IV compounds and emitting in the range 3–5 μm is their low operating temperature. The only cases reported in the literature to date are the operation of quantum-cascade lasers based on GaInAs/AlInAs at a temperature of 320 K and emitting at a wavelength $\sim$5 μm (Ref. 1) and type-II quantum-well lasers with four constituents in each period (InAs–$Ga_{0.7}In_{0.3}Sb$–InAs–AlSb) operating at temperatures up to 350 K with pulsed optical pumping and emitting at a wavelength $\sim$3 μm at 300 K (Ref. 2). The same group of authors (see Ref. 2) has constructed InAs–$Ga_{1-x}In_xSb$–InAs–AlSb lasers emitting in the interval 3.9–4.1 μm with pulsed optical pumping up to 285 K (Ref. 3). In diode heterolasers emitting at wavelengths greater than 3 μm a room-temperature operating level is not attained. For InAsSb/InAlAsSb diode heterolasers having several quantum wells in the active region and emitting at wavelengths of 3.2–3.55 μm a maximum operating temperature of 225 K is attained in the pulsed regime.[4] We have previously investigated diode double laser heterostructures based on InAsSb/InAsSbP (Refs. 5–9), which attained an operating temperature $\sim$180 K in the pulsed regime.

In the present article we have set the objective of investigating diode laser structures having separate electrical and optical confinement and an InAsSb-based active region. For this purpose we have fabricated lasers with type-I and type-II heterojunctions between the active region and the electrical confinement layers. The type-II heterojunctions had the optimal ratio of valence-band to conduction-band discontinuities as determined theoretically in Ref. 10.

2. The laser structures were fabricated by liquid-phase epitaxy on an InAs substrate oriented in the (100) plane. Figure 1 shows the schematic arrangement of the layers in the laser structure and the energy diagrams in the lasing regime for structures with a type-I heterojunction (Fig. 1a) and with a type-II heterojunction as the electrical confinement (Fig. 1b), which we identify from now on as type-I and type-II structures, respectively.

The active region was identical for both types of structures, having the composition $InAs_{0.95}Sb_{0.05}$ and a band gap of width $E_g \approx 0.376$ eV, which corresponds to an emission wavelength $\lambda \approx 3.3$ μm. The wide-gap optical confinement layers were also identical for both types of structures, having the composition $InAs_{0.5}Sb_{0.16}P_{0.34}$ and $E_g \approx 0.593$ eV. The electrical confinement layers in the laser structure with a type- II heterojunction consisted of InAs with $E_g \approx 0.413$ eV and at the boundary with the active region had discontinuities of the valence band $\Delta E_v \approx 0.052$ eV and the conduction band $\Delta E_c \approx 0.015$ eV, so that the ratio $\Delta E_v/\Delta E_c \approx 3.4$. The electrical confinement layers in the type-I laser structure had the composition $InAs_{0.85}Sb_{0.05}Sb_{0.05}P_{0.1}$ with $E_g \approx 0.464$ eV and band discontinuities at the boundary with the active region $\Delta E_v \approx 0.038$ eV and $\Delta E_c \approx 0.050$ eV. These values of the band gaps and the band discontinuities were calculated for a temperature of 77 K.

The active region was not specially doped, and it had *n*-type conductivity with a density of electrons $\sim 10^{16}$ cm^{-3}. The wide-gap *p*-type InAsSbP layers were doped with Zn to a hole density $\sim 2\times 10^{18}$ cm^{-3}, and the *n*-InAsSbP was doped with Sn to an electron density $\sim 10^{18}$ cm^{-3}. The doping level of the electrical confinement layers was approximately half these values. The thicknesses of the layers of the active region and the electrical confinement region fell within the interval 0.65–0.8 μm, and the thicknesses of the optical confinement layers were 2.5–3 μm. The lasers had a mesa-stripe configuration with a stripe width of 15–55 μm and a cavity length of 255–350 μm.

The lasers were investigated in the pulsed regime with a pulse duration of 100 ns and a repetition rate of 10^5 Hz in the temperature interval from 77 K to the maximum operating temperature.

3. We now discuss the experimental results.

Figure 2 shows the current-voltage (*I–V*) characteristics of the laser structures of type I (S221-2 No. 2 laser) (curve *1*) and type II (V1133-3 laser) (curve *2*) at a temperature of 77 K. Both *I–V* characteristics have cutoffs on the voltage axis at $\sim$0.36 V. At currents $J > 0.5$ A the *I–V* characteristic of

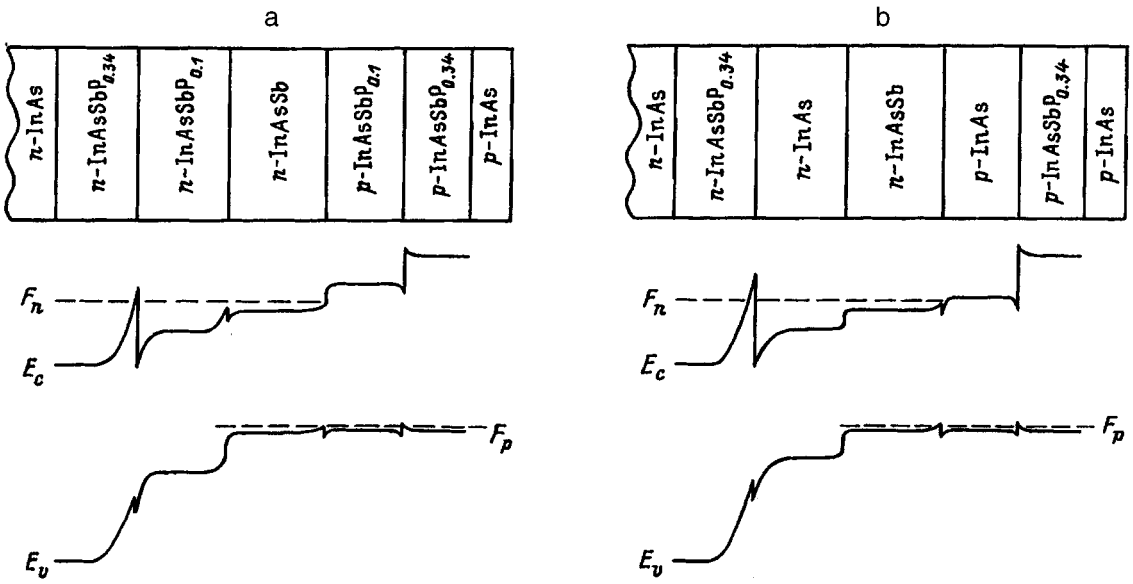

FIG. 1. Configuration of layers and lasing energy diagram in type-I (a) and type-II (b) laser structures.

the type-II structure becomes linear with a series resistance $\sim 0.45\ \Omega$. The I–V characteristic of the type I structure becomes linear at currents $J > 1$ A with a series resistance $\sim 0.55\ \Omega$. The I–V characteristics change very little as the temperature is increased.

The threshold current densities of the investigated lasers at a temperature of 77 K have values $j_{th} \approx 800$ A/cm^2 for the best type-I samples and $j_{th} \approx 1000$ A/cm^2 for type-II samples. Temperature curves of j_{th} are shown in Fig. 3 for a type-I (S286) laser (curve *1*) and a type-II (V1133-3 No. 1) laser (curve *2*). The characteristic temperatures for type-I and type- II lasers are $T_0 \approx 35$ K and 22 K, and the maximum operating temperatures are ~ 203 K and ~ 145 K, respectively. Also shown in this figure are the calculated temperature curves of j_{th} when volume recombination is predominant, taking into account radiative recombination alone (curve *3*), Auger recombination due to CHCC and CHHS transitions alone (see Ref. 11) (curve *4*), or total recombination (curve *5*). The calculations are based on the theory set forth in Ref. 11.

Since the maximum operating temperature is determined not only by the temperature dependence of the threshold current density of the laser, but also by the optical losses, which increase with increasing temperature, we compare the tem-

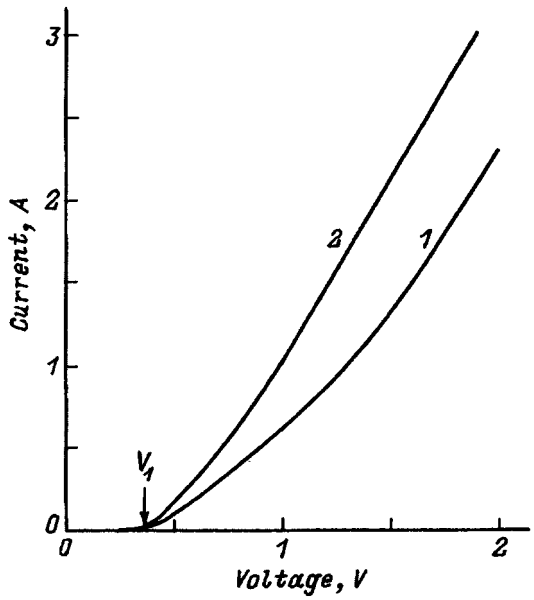

FIG. 2. Current-voltage characteristics at $T = 77$ K. *1*) Type-I laser S221-2 No. 2; *2*) type-II laser V1133-3.

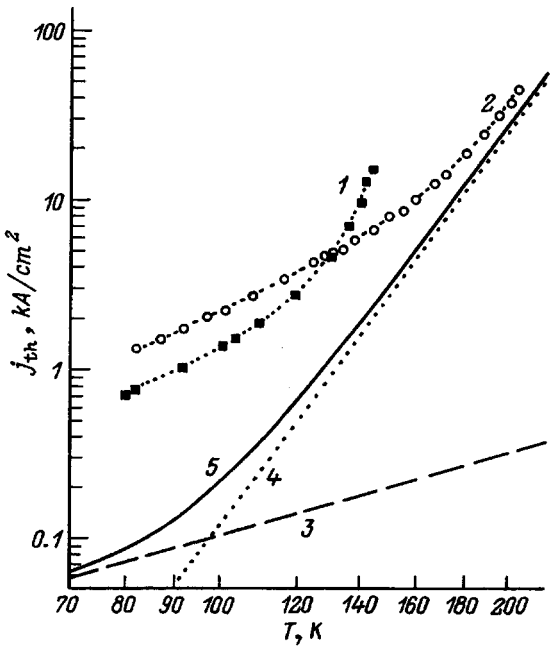

FIG. 3. Threshold current density (j_{th}) versus temperature (T). *1*) Type-I laser S286; *2*) type-II laser V1133-3 No. 1; *3*) calculated for predominant volume radiative recombination; *4*) calculated for predominant Auger recombination due to CHCC and CHHS transitions; *5*) total theoretical recombination curve.

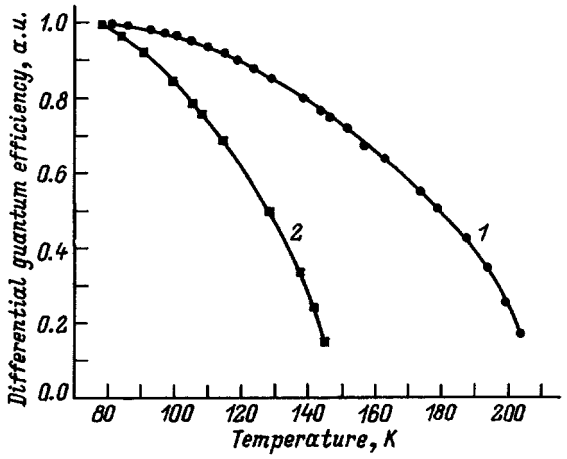

FIG. 4. Differential quantum efficiency versus temperature. *1*) Type-I laser S286; *2*) type-II laser V1133-3.

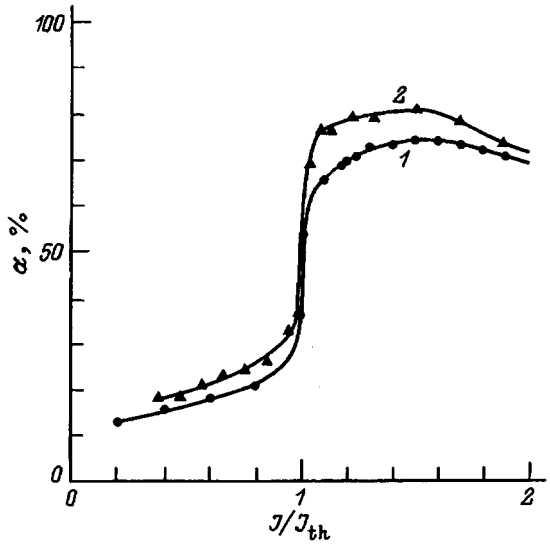

FIG. 5. Degree of polarization of radiation versus the ratio of the current to the threshold current J/J_{th}. *1*) Type-I laser S286; *2*) type-II laser V1133-3.

perature curves of the differential quantum efficiencies of type-I and type-II lasers (Fig. 4). It is evident that the differential quantum efficiency of type-I lasers (S286 laser, curve *1*) and type-II lasers (V1133-3 laser, curve *2*) decreases as the temperature rises, the slopes of the curves increasing at a certain temperature $\sim$120 K for type-I lasers and $\sim$150 K for type-II lasers.

To compare the influence of type-I and type-II heterojunctions on the coherent radiation of the lasers, we have investigated the current dependence of the degree of polarization of the laser beams $\alpha=(F_{\text{TM}}-F_{\text{TE}})/(F_{\text{TM}}+F_{\text{TE}})$, where F_{TM} and F_{TE} are the radiation intensities of TM- and TE-polarized light, respectively. The type-I and type-II lasers have a high degree of TM polarization, for which the electric field vector **E** of the light wave is perpendicular to the plane of the *p–n* junction. The maximum value of α is observed at a current $J\sim 1.5j_{\text{th}}$ and is equal to $\sim$80% for type-II and $\sim$73% for type-I lasers.

4. Here we discuss the results of the investigation.

It is evident from a comparison of the energy diagrams for the type-I and type-II lasers (Fig. 1) that the *I-V* characteristics of the laser diodes should not differ appreciably, and this conclusion is corroborated by measurements. The cutoffs of the *I–V* characteristics V_1, corresponding to the minimum width of the band gap, i.e., E_g in the active region, indicate that the main resistance in either type of laser is the *p–n* junction and not isotypic junctions. The curvature of the *I–V* characteristics indicates that the resistance of isotypic junctions varies as the current is increased.

In analyzing the temperature dependence of the threshold current density, we take only volume recombination into account, because the band discontinuities at the heterojunctions of the active region are commensurate with kT and merely create qualitative trends.

The threshold current density j_{th} with predominantly volume radiative recombination must increase with the temperature T according to the law $j_{\text{th}}\sim T^{3/2}$ (Fig. 3, curve *3*). When Auger recombination due to CHCC and CHHS transitions is predominant, we have $j_{\text{th}}\sim T^7$ (Fig. 3, curve *4*). The calculated radiative and nonradiative volume recombination are identical at a temperature of approximately 100 K. The total current density (Fig. 3, curve *5*) is expressed by the relations $j_{\text{th}}\sim T^{2.5}$ at $T=77$–90 K and $j_{\text{th}}\sim T^7$ at $T=180$–200 K. We note that the current density calculated according to this theory in lasers with a narrow-gap InGaAsSb layer ($E_g=0.62$ eV) of large thickness (2 μm) and GaAlAsSb confinement layers agrees with the experimental value.[11]

The threshold current density in the lasers investigated here is almost an order of magnitude higher than the calculated value at $T=77$–90 K, but its increase with the temperature has the same slope. The small slope indicates the predominance of radiative recombination, but the latter is most likely the interface type. It is higher in type-II lasers than in type-I lasers. Interface Auger recombination is probably suppressed in type-II lasers,[10] because the experimental current density is close to the theoretically calculated value for the case of predominant volume Auger recombination at a temperature of 180–220 K. Interface Auger recombination should be significant in type-I lasers, because over the entire temperature range the experimental current density is almost an order of magnitude higher than the theoretical value calculated with allowance for volume Auger recombination.

The fact that the maximum operating temperature is determined not only by the excess of the current above the threshold level, but also by the sharp drop of the differential quantum efficiency with increasing temperature (Fig. 4), implies that the radiation losses increase with the temperature as a result of absorption by free carriers. Since the two compared types of lasers have identical active regions, the higher absorption losses of the type-I lasers probably takes place either in the electrical confinement layers or at their heterojunctions.

The significant influence of the heterojunctions on the emission of radiation is indicative of the nature of the radiation polarization (Fig. 5). The radiation from type-I and type-II lasers is predominantly TM-polarized. It has been shown[8] that indirect radiative transitions associated with interaction

between carriers and a heterojunction are predominantly TM-polarized. Since the degree of TM polarization of type-II lasers is higher, the interaction between carriers and the heterojunction is stronger in them. We recall that the predominant emission of radiation at heterjunctions also follows from the excess of the threshold current density above the theoretical value at $T=77-90$ K, when radiation recombination is predominant.

Consequently, our investigation of InAsSb-based lasers with separate optical and electrical confinement has shown that such laser configurations are capable of achieving a higher operating temperature if electrical confinement is created by means of a type-II heterjunction.

This work has been supported, in part, by the United States Air Force European Office of Aerospace Research and Development (US EOARD), Contract F 6170894C0011, and by the Ministry of the Russian Federation Project ''Laser Physics and Optics,'' No. 4.14.

[1] J. Faist, F. Capasso, C. Sirtori, D. L. Sivco, J. N. Baillargeon, S. L. Hutchinson, S.-N. G. Chu, and A. Y. Cho, Appl. Phys. Lett. **68**, 3680 (1996).
[2] J. I. Malin, C. L. Felix, J. R. Meyer, S. A. Hoffman, F. F. Pinto, C.-H. Lin, P. C. Chang, S. J. Murry, and S.-S. Pei, Electron. Lett. **32**, 1593 (1996).
[3] J. I. Malin, J. R. Meyer, C. I. Felix, J. R. Lindle, L. Goldberg, C. A. Hoffman, F. J. Bartoli, C.-H. Lin, P. C. Chang, S. J. Murry, R. Q. Yang, and S.-S. Pei, Appl. Phys. Lett. **68**, 2976 (1996).
[4] H. K. Choi, G. W. Turner, J. J. Manfra, and M. K. Cannors, Appl. Phys. Lett. **68**, 2936 (1996).
[5] A. H. Baranov, T. N. Danilova, O. G. Ershov, A. N. Imenkov, V. V. Sherstnev, and Yu. P. Yakovlev, Pis'ma Zh. Tekh. Fiz. **18**, 6 (1992) [Sov. Tech. Phys. Lett. **18**, 725 (1992)].
[6] A. H. Baranov, T. N. Danilova, O. G. Ershov, A. N. Imenkov, V. V. Sherstnev, and Yu. P. Yakovlev, Pis'ma Zh. Tekh. Fiz. **19**, 30 (1993) [Tech. Phys. Lett. **19**, 543 (1993)].
[7] A. N. Baranov, A. N. Imenkov, V. V. Sherstnev, and Yu. P. Yakovlev, Appl. Phys. Lett. **64**, 2480 (1994).
[8] T. N. Danilova, O. G. Ershov, G. G. Zegrya, A. N. Imenkov, M. V. Stepanov, V. V. Sherstnev, and Yu. P. Yakovlev, Fiz. Tekh. Poluprovodn. **29**, 1604 (1995) [Semiconductors **29**, 834 (1995)].
[9] T. N. Danilova, O. G. Ershov, A. N. Imenkov, M. V. Stepanov, V. V. Sherstnev, and Yu. P. Yakovlev, Fiz. Tekh. Poluprovodn. **30**, 1265 (1996) [Semiconductors **30**, 667 (1996)].
[10] G. G. Zegrya and A. D. Andreev, Zh. Éksp. Teor. Fiz. **109**, 615 (1995) [J. Exp. Theor. Phys. **82**, 328 (1995)].
[11] A. A. Andaspaeva, A. N. Baranov, B. L. Gel'mont, B. B. Dzhurtanov, G. G. Zegrya, A. N. Imenkov, Yu. P. Yakovlev, and S. G. Yastrebov, Fiz. Tekh. Poluprovodn. **25**, 394 (1991) [Sov. Phys. Semicond. **25**, 240 (1991)].

Translated by James S. Wood

Electron-probe microanalysis of doped PbTe and $Pb_{0.8}Sn_{0.2}Te$ single crystals

M. V. Bestaev, A. I. Gorelik, V. A. Moshnikov, and Yu. M. Tairov

St. Petersburg State Electrical Engineering University, 197376 St. Petersburg, Russia
(Submitted January 22, 1997; accepted for publication January 28, 1997)
Fiz. Tekh. Poluprovodn. **31**, 980–982 (August 1997)

The distribution of the elements in naturally faceted PbTe and $Pb_{0.8}Sn_{0.2}Te$ single crystals doped with zinc and cadmium is analyzed. The results show the formation of a multilayer structure with an outer layer of ZnTe (CdTe) on top of a metallic sublayer. © *1997 American Institute of Physics.* [S1063-7826(97)02508-8]

Lead-tin chalcogenides enjoy broad applications in infrared optoelectronics.[1] As a rule, device fabrication involves doping. This practice has stimulated intensive research on diffusion processes in PbTe, $Pb_{1-x}Sn_xTe$, PbSe, $Pb_{1-x}Se_xTe$, and other chalcogenides. Group-II and group-III elements are the most commonly used dopants. Chalcogenides doped with these impurities have a number of unique new properties.[2]

The diffusion parameters are usually calculated from concentration profiles obtained by grinding off successive layers (radioisotope assay, thermal probing, and other techniques were used[3]). The trend here is to describe the experimental results on the basis of conventional diffusion models employing one or more diffusion models.

We have previously shown that during the diffusion of indium, tin, lead, and germanium in PbTe and PbSnTe the tellurium vapor pressure of the crystal itself, being dependent on the deviation of its composition from stoichiometry, plays a vital role in mass transfer through the gaseous phase.[4,5] On the other hand, the segregation of lead is known to be observed when lead telluride is doped with zinc or cadmium.[6] We have proposed[7] a model whereby a multilayer structure is formed on the surface of lead telluride. The outer layer has a ZnTe or CdTe composition and rests on top of a lead sublayer.

To confirm the proposed model experimentally, it is necessary to conduct investigations of high-quality, naturally faceted single crystals. When the structural integrity of the

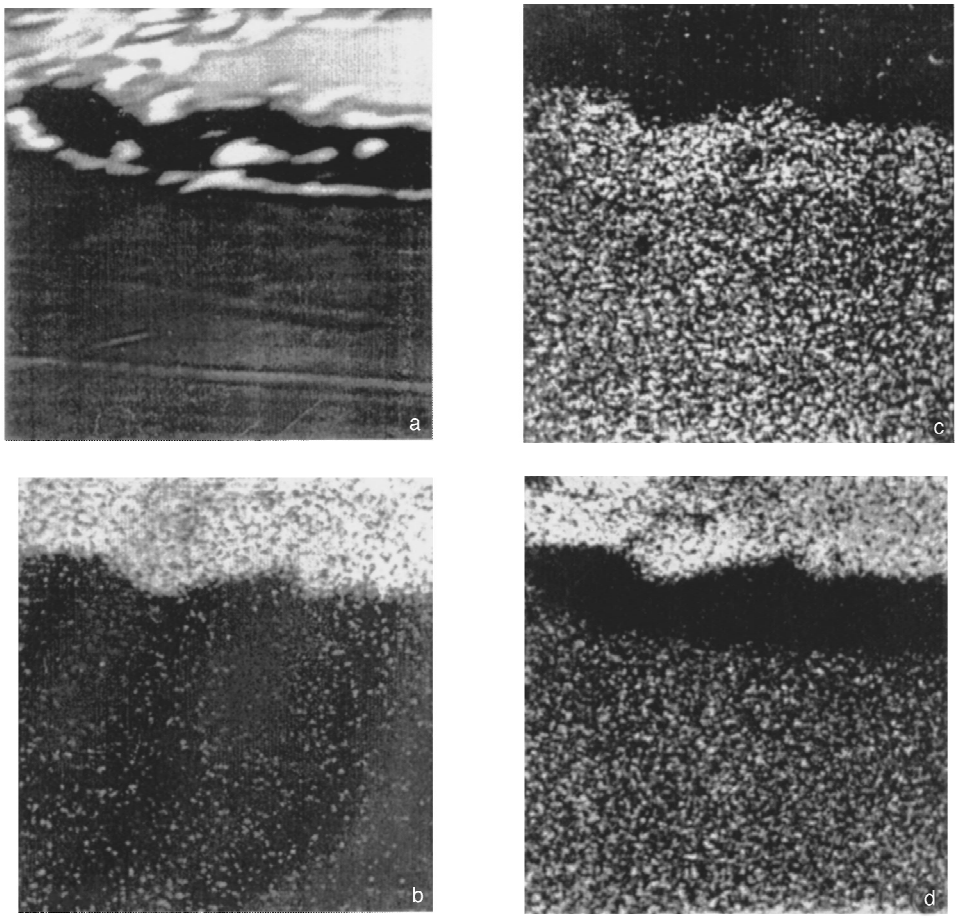

FIG. 1. Qualitative distribution pattern of elements in the surface layer of a PbTe single crystal doped with zinc by diffusion annealing from the gaseous phase for 10 h at 973 K. a) Electron-absorption image ($100\times100\ \mu m^2$); b) x-ray image in Kα1Zn emission; c) x-ray image in Lα1Pb emission; d) x-ray image in Lα1Te emission.

 1063-7826/97/080835-03$10.00

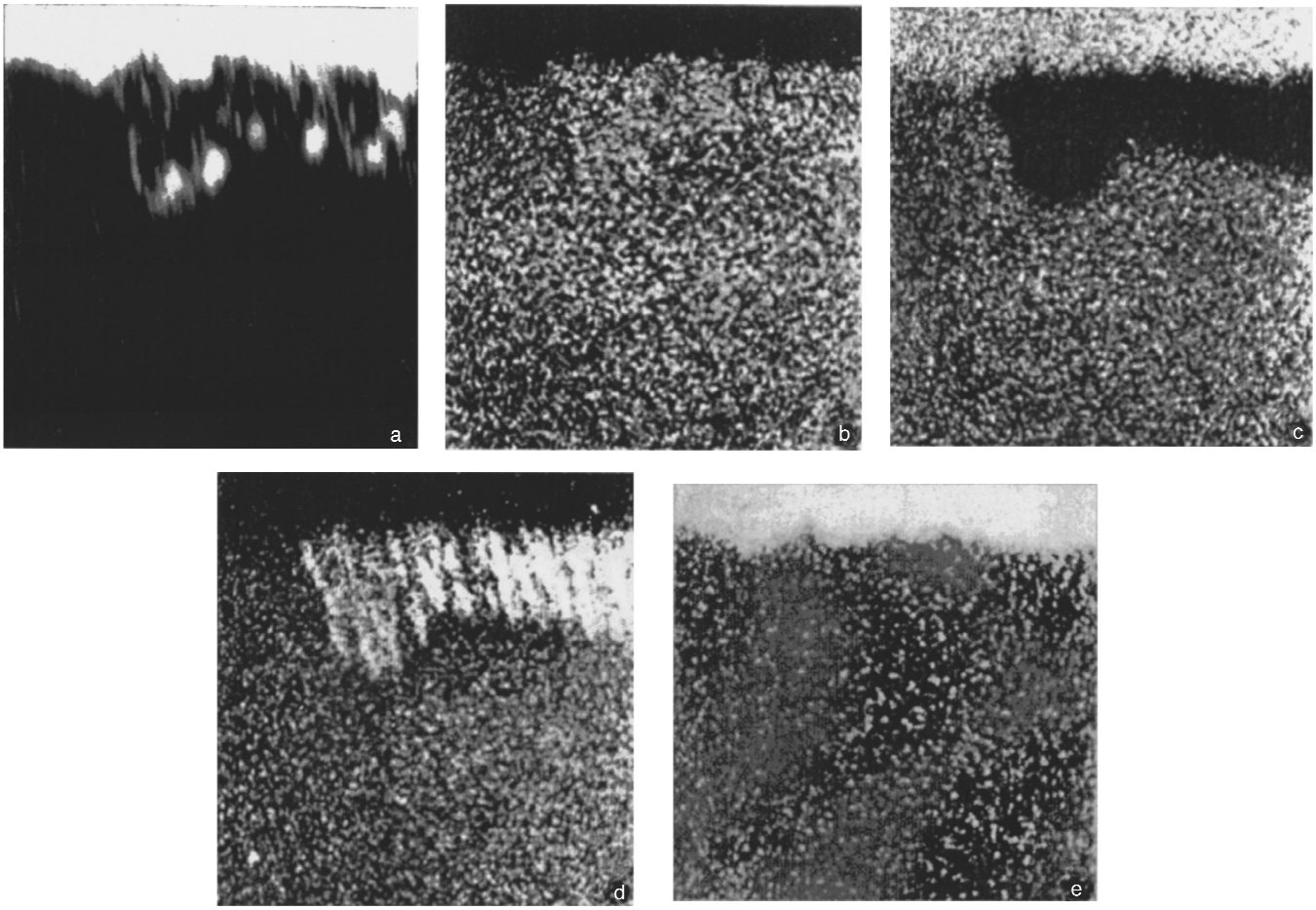

FIG. 2. Qualitative distribution pattern of elements in the surface layer of a $Pb_{0.8}Sn_{0.2}Te$ single crystal doped with zinc by diffusion annealing from the gaseous phase for 5 h at 973 K. a) Electron-absorption image (200×200 μm^2); b) x-ray image in $L_{\alpha1}$Pb emission; c) x-ray image in $L_{\alpha1}$Te emission; d) x-ray image in $L_{\alpha1}$Sn emission; e) x-ray image in Kα1Zn emission.

surface of a single crystal is disturbed, useful information is lost through head-on diffusion fluxes. The objective of the present study is to investigate the diffusion of zinc and cadmium on PbTe and $Pb_{0.8}Sn_{0.2}Te$ single crystals.

The PbTe and $Pb_{0.8}Sn_{0.2}Te$ single crystals were prepared by a technique described in Ref. 8. The crystals had dimensions $5\times3\times2$ mm and were faceted along (100) planes; the density of charge carriers had values of 5×10^{17}–5×10^{18} cm $^{-3}$ for PbTe and $Pb_{0.8}Sn_{0.2}Te$. Diffusion annealing was performed from the gaseous phase in evacuated and sealed capsules. The concentration distribution after diffusion annealing was determined by electron-probe microanalysis on the surface of a slice cleaved perpendicular to the direction of diffusion.

As examples, Figs. 1 and 2 show the results of analyzing the distribution of the elements in zinc-doped PeTe and $Pb_{0.8}Sn_{0.2}Te$ single crystals. It is evident from the figure that the outer layer contains zinc and tellurium in both cases. Beneath it is a layer that does not contain any zinc or tellurium. During the diffusion annealing of PbTe the second layer has essentially a pure lead composition, and in the case of $Pb_{0.8}Sn_{0.2}Te$ its composition corresponds to a mixture of lead and tin. The mass concentrations of tin are much higher in this case than in the as-prepared (untreated) crystal. It follows from the electron-absorption image that pore consolidation is observed at the boundary of the second layer with the untreated single crystal. This phenomenon is attributable to the uncompensated loss of tellurium. The difference in the configurations of the intermediate layer in the investigated samples is dictated by the higher degree of perfection of the PbTe single crystals. A similar pattern of segregation of lead and tin was observed in doping with cadmium. It follows from the reported investigations that diffusion models with traditional boundary conditions cannot be used in determining the diffusion parameters of cadmium and zinc in lead-tin chalcogenides.

[1] N. Kh. Abrikosov and L. E. Shelimova, *Semiconductor Materials from IV–VI Compounds* [in Russian], Nauka, Moscow (1975).
[2] V. I. Kaĭdanov, S. A. Nemov, and Yu. I. Ravich, Fiz. Tekh. Poluprovodn. **28**, 369 (1994) [Semiconductors **28**, 223 (1994)].
[3] B. I. Boltaks, *Diffusion and Point Defects in Semiconductors* [in Russian], Nauka, Leningrad (1972).
[4] M. V. Bestaev, T. T. Dedegkaev, and V. A. Moshnikov, Fiz. Tverd. Tela (Leningrad) **27**, 1868 (1985) [Sov. Phys. Solid State **27**, 1122 (1985)].
[5] M. V. Bestaev, T. T. Dedegkaev, and V. A. Moshnikov, Fiz. Tverd. Tela (Leningrad) **26**, 2200 (1984) [Sov. Phys. Solid State **26**, 1335 (1984)].
[6] A. V. Novoselova, V. P. Zlomanov, A. M. Gas'kov, L. I. Ryabova, and M. A. Lazarenko, Vestn. Mosk. Univ. Khim. **22**, 3 (1982).

[7] M. V. Bestaev, T. T. Dedegkaev, T. B. Zhukova, and H. V. Siukaev, in *Proceedings of the Fourth All-Union Conference on the Kinetics and Mechanism of Chemical Reactions in the Solid State* [in Russian], Inst. Khim. Fiz. Akad. Nauk SSSR, Chernogolovka (1986).

[8] M. V. Bestaev, A. I. Gorelik, and V. V. Tomaev, Izv. SP Gos. Élektrotekh. Univ., No. 495, 41 (1996).

Translated by James S. Wood

Steady-state lux-ampere characteristics of compensated crystals at various excitation intensities

A. A. Lebedev

A. F. Ioffe Physicotechnical Institute, Russian Academy of Sciences, 194021 St. Petersburg, Russia
(Submitted January 24, 1997; accepted for publication January 28, 1997)
Fiz. Tekh. Poluprovodn. **31**, 983–986 (August 1997)

Equations are derived in parametric form for calculating the steady-state lux-ampere characteristics of photoresistors with an arbitrary concentration of deep levels at arbitrary excitation intensity. The conditions underlying the formation of the sublinear and superlinear segments of the lux-ampere curve as a function of the excitation intensity and the concentration and parameters of the deep levels can be determined from calculations according to the derived equations. © *1997 American Institute of Physics.* [S1063-7826(97)02608-2]

Difficulties are encountered in calculating the photoexcitation curves, or so-called lux-ampere characteristics (LCCs), in general form for photoresistors made from compensated crystals in the presence of a high concentration of deep levels, because the nonequilibrium carrier lifetime is not constant in this case, but depends on the deep-level filling factor. As a rule, only the limiting cases of a low concentration of deep levels and weak or strong excitation are considered.[1] In this article a simple method is proposed for calculating the LCC for an arbitrary concentration of deep levels and an arbitrary excitation level.[2]

THE MODEL

Here we investigate crystals that contain shallow levels and are compensated by a single type of simple deep-level centers. For definiteness we consider crystals doped with shallow donors at a concentration N_d and with deep acceptors at a concentration M. All levels in the crystal are assumed to be uniformly distributed throughout the volume. The temperature is assumed to be such that shallow donors are fully ionized, and thermal exchange by electrons between the deep levels and allowed bands can be disregarded. We also assume that the generation of electron-hole pairs takes place uniformly throughout the entire volume of the sample, i.e., that the photon energy of the incident radiation is close to the width of the band gap of the crystal, and the absorption coefficient is small in comparison with the reciprocal of the sample thickness. We assume that recombination through surface states and other types of deep levels in the volume is negligible. The generation of electron-hole pairs is also possible in the presence of injection from a p–n junction. In this case we assume that the thickness of the sample is much smaller than the diffusion length of nonequilibrium carriers.

Under these assumptions the excitation intensity (generation rate) G is related to the recombination of electrons and holes by the equation

$$G=\alpha_n(M-m)n=\alpha_p p m, \tag{1}$$

where m is the concentration of electron-populated deep levels, $\alpha_{n(p)}=v_T S_{n(p)}$, v_T is the thermal velocity, $S_{n(p)}$ is the electron (hole) capture cross section of the deep levels, and n and p are the densities of free electrons and holes, respectively. The neutrality condition under the stated assumptions has the form

$$n+m=N_d+p. \tag{2}$$

Combining Eqs. (1) and (2), we obtain the following expression for the rate of generation of electron-hole pairs in dimensionless units:

$$G'=\frac{G}{\alpha_n M^2}=\frac{m'(1-m')(N_d'-m')}{m'-\theta(1-m')}>0, \tag{3}$$

where $m'=m/M$, $N_d'=N_d/M$, and $\theta=\alpha_n/\alpha_p$.

The nonequilibrium conductivity of the crystal (for $N_d<M$) is

$$\sigma=q\mu_n n+q\mu_p p.$$

Making use of Eqs. (1) and (3), in dimensionless units we can write

$$\sigma'=\frac{\sigma}{q\mu_p M}=G'\left(\frac{b}{1-m'}+\frac{\theta}{m'}\right). \tag{4}$$

Here q is the electron charge, μ_n and μ_p are the electron and hole mobilities, respectively, and $b=\mu_n/\mu_p$.

Equations (3) and (4) are parametric equations for calculating the LCC by varying m' at arbitrary concentrations of shallow and deep levels and any excitation intensity.

CALCULATION RESULTS

At very high excitation intensities ($G\to\infty$) such that $n\approx p$, it follows from Eq. (1) that the maximum filling of deep levels is given by the equation $m'=\theta/(1+\theta)$. Substituting this value of m' into Eq. (4), we obtain

$$\sigma'=G'(b+1)(\theta+1), \tag{5}$$

i.e., at a high excitation level the LCC is always linear, and σ' is essentially independent of θ for $\theta\ll 1$.

Equations (3) and (4) are simplified for a narrow excitation level under the conditions $N_d=M$ (exact compensation), $\theta\gg 1$, and $m'\lesssim 1$:

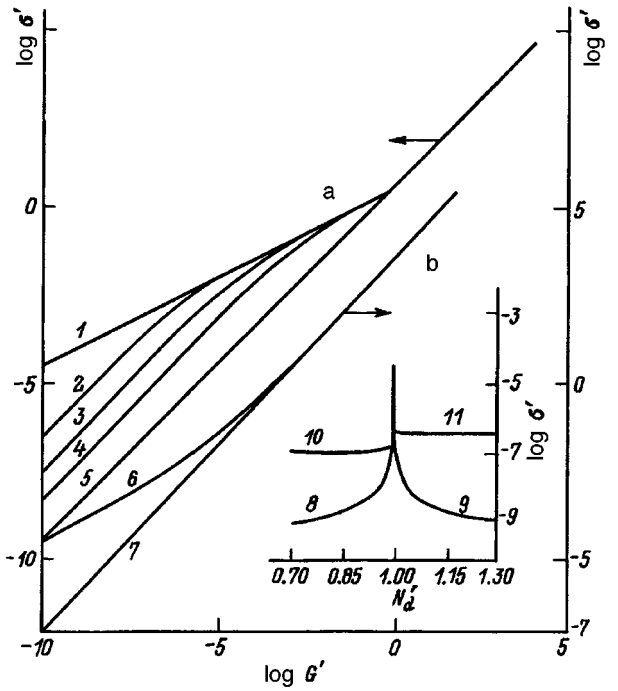

FIG. 1. Dimensionless conductivity σ' versus dimensionless excitation intensity G' for $b=3$. Left scale (a), $\theta=10^{-3}$: *1*) $N_d'=1$; *2*) 0.999; *3*) 0.99; *4*) 0.95; *5*) 0.1. Right scale (b), $\theta=10^{3}$: *6*) $N_d'=1$; *7*) 0.99. Inset: σ' versus N_d' for $G'=10^{-10}$: *8, 9*) $\theta=10^{-3}$; *10, 11*) $\theta=10^{3}$.

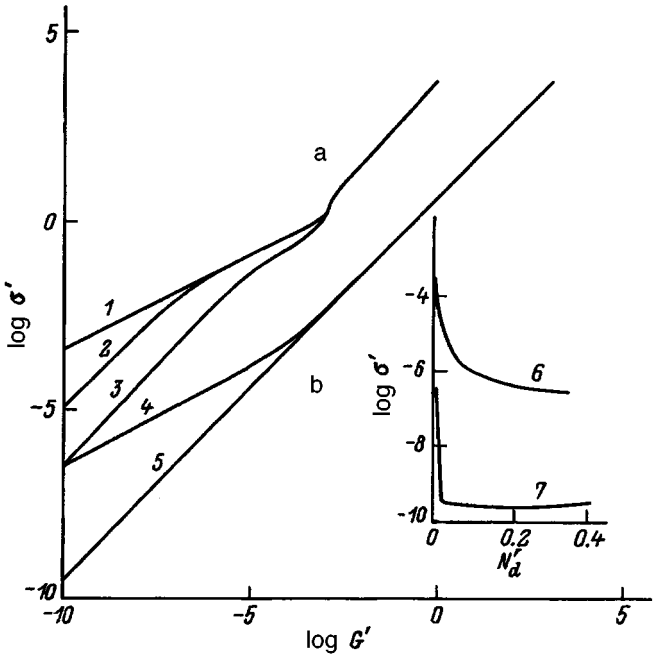

FIG. 2. Dimensionless conductivity σ' versus dimensionless excitation intensity G' for $b=3$. a) $\theta=10^{3}$: *1*) $N_d'=0$; *2*) 0.01; *3*) 0.3. b) $\theta=10^{-3}$: *4*) $N_d'=0$; *5*) 0.01. Inset: Graph of σ' vs. N_d': *6*) $\theta=10^{3}$; *7*) $\theta=10^{-3}$.

$$G'\approx(1-m')^2, \quad \sigma'\approx\frac{bG'}{1-m'}=b\sqrt{G'}, \tag{6}$$

i.e., the LCC is practically independent of θ and at a low excitation level is sublinear (Fig. 1a, curve *1*). It becomes linear as G' increases.

In crystals with inexact compensation ($N_d<M$) the LCC is linear at low excitation intensities. As G' increases, the deep levels empty, then beginning with a certain value of G', the LCC becomes sublinear (Fig. 1a, curves *2–4*), and with a further increase in G' it once again becomes linear. In the high-G' range it follows from Eq. (5) that the LCCs for different N_d' merge. In the case of inexact deep-level compensation, therefore, the LCC acquires two linear segments at low and high excitation intensities and a sublinear segment in between. Such LCCs can serve as a measure of inexact deep-level compensation. If the degree of compensation is close to the maximum filling of deep levels as $G'\to\infty$, the LCC is practically linear over the entire range of G' (Fig. 1a, curve *5*).

The inset in Figu. 1c (curves *8* and *9*) shows plots of $\sigma'=f(N_d')$ for $G'=10^{-10}$. For $N_d>M$ shows the behavior of $\Delta\sigma'$ due to nonequilibrium carriers. In the previous notation it is given by

$$\Delta\sigma'=G'\left(\frac{b}{1-m'}+\frac{\theta}{m'}\right)-b(N_d-1). \tag{7}$$

It is evident from the inset in Fig. 1c that the $\Delta\sigma'(N_d')$ curve is symmetric about the maximum at $N_d=M$, and a 1% deviation of N_d' from unity causes σ' to decrease by three orders of magnitude.

For $N_d'=1$, $\theta\gg1$, and weak excitation ($m'\approx1$), when the condition $m'\gg\theta(1-m')$ holds, Eq. (6) is valid, and the LCC is sublinear (Fig. 1b, curve *6*). The sublinear LCC eventually becomes linear as G' increases. The LCCs essentially merge after a deviation from exact compensation ($N_d\neq M$) (Fig. 1b, curve *7*). Calculations have shown that the slightest deviation from exact compensation ($\gtrsim1\%$) causes G' to drop by several orders of magnitude and become almost independent of N_d' (see the inset to Fig. 1, curves *10* and *11*).

We now consider another limiting case, when $N_d\gtrsim0$, i.e., when shallow donors are nonexistent or have a very low concentration. For $N_d=0$, $0\gg1$, and weak excitation ($m'\approx0$), and $m'\ll\theta(1-m')$ we have

$$G'\approx\frac{(m')^2}{\theta}, \quad \sigma'=\frac{G\theta}{m'}\approx\sqrt{\theta G'}, \tag{8}$$

i.e., the LCCs are sublinear and depend on θ. As G' increases, the LCCs become linear in accordance with (5) (Fig. 2a, curve *1*). However, in contrast with the preceding case, the sublinear and linear segments of the LCC are separated by a superlinear segment. It is attributable to the fact that the deep levels fill up with electrons ($m'\approx1$), and more mobile electrons begin to prevail in the conductivity. But if $\theta\ll1$, this segment disappears from the LCC (Fig. 2b, curve *4*).

If the deep levels are partially filled with electrons ($N_d'>0$), the LCC is linear in weak excitation, but as G' increases, it becomes successively sublinear, then superlinear, and finally linear (Fig. 2a, curve *2*). The conductivity σ' drops by several orders of magnitude as N_d' increases. The $\sigma'=f(N_d')$ curve is comparatively smooth for $\theta\gg1$ (see

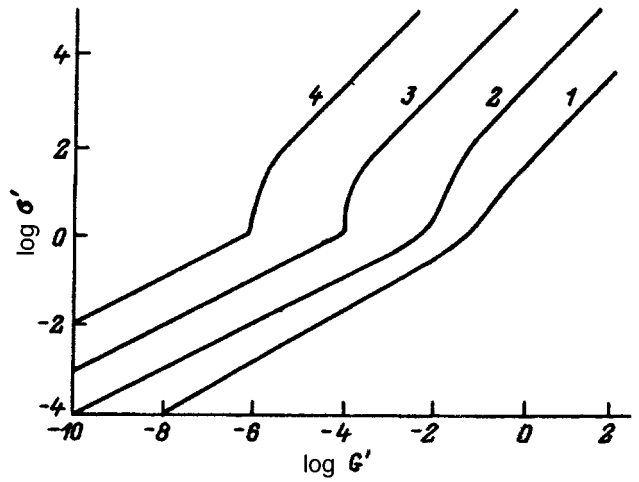

FIG. 3. Graph of σ' vs. G' for $N_d'=0$, $b=15$. *1)* $\theta=1$; *2)* 10^2; *3)* 10^4; *4)* 10^6.

the inset to Fig. 2, curve *6*). If $\theta \ll 1$, we observe a sharp decrease of σ' at $N_d' \approx 0.01$, after which σ' remains almost constant (inset to Fig. 2, curve *5*).

The calculations whose results are shown in Fig. 2 are based on a comparatively small difference in the mobilities of electrons and holes: $b=3$. In some semiconductors the ratio b attains a value of 100 (Refs. 3 and 4). The superlinear segment of the LCC is far more pronounced in such materials. Figure 3 shows the results of calculations for $b=15$, $N_d=0$, and several values of $\theta \geqslant 1$. It is evident from the figure that σ' increases by one or two orders of magnitude on the superlinear segment. It follows from Eq. (5) that the linear segment shifts toward lower G' as θ increases. Consequently, in the presence of a certain ambient illumination the sensitivity of photoresistors made from crystals having a low hole mobility and doped with high-θ impurities increases considerably.

These results are readily extended to compensated crystals with hole conductivity.

We now estimate the results of the calculations in dimensionless units. The volume-averaged generation rate is related to the intensity I of radiation incident on the sample surface by the equation

$$G = I(1-R)[1-\exp(-\eta d)]/d,$$

where R and η are the reflection and absorption coefficients, respectively, and d is the thickness of the sample. Under the condition $\eta d \ll 1$ we have

$$I \approx \frac{\alpha_n M^2}{(1-R)\eta} G'.$$

The power of the incident radiation for a photon energy $h\nu$ is given by $W = qh\nu I$.

These equations can be used to estimate I and W for any value of G'. For estimation we assume that $v_T = 1.5\times 10^7$ cm/s, $S_n = 1\times 10^{-15}$ cm^2, $M = 1\times 10^{13}$ cm^{-3}, $R=0.3$, and $\eta = 10$ cm^{-1}. It is evident from Fig. 1a that the transition from the sublinear to the linear LCC takes place at $G'=1$. We then have $W \approx 0.5$ W/cm^2 for $h\nu = 2$ eV. The transition from the sublinear to the superlinear LCC for $\theta = 10^4$ takes place at $G' \approx 10^{-4}$ (Fig. 3, curve *3*), i.e., for $W \approx 5\times 10^{-5}$ W/cm^2.

These estimates are very approximate, since the excitation intensity is not uniform throughout the volume, particularly for large values of ηd, and the LCCs become even more dependent on the carrier diffusion length.

CONCLUSIONS

The above-described simple model is suitable for explaining both the sublinear and superlinear behavior of the nonequilibrium conductivity of crystals doped with deep levels of only one type. It is not necessary to invoke the model of deep levels with distributed ionization energies[5] in order to account for the superlinear LCC. This model can also be used to estimate the influence of deviation from exact compensation on the photosensitivity of crystals. In comparing the results of the calculations with the lux-ampere characteristics of real structures, it must be borne in mind that the given model disregards recombination through other kinds of centers in the volume and on the surface, the volume-nonuniform concentration of shallow and deep centers, excitation intensities, and other characteristics specific to real experimental conditions.

It is proposed in the future to extend the model, taking into account the thermal and optical excitation of carriers with deep levels.

[1] S. M. Ryvkin, *Photoelectric Effects in Semiconductors* Consultants Bureau, New York (1964) [Russian original, Fizmatgiz, Leningrad (1963)].
[2] A. A. Lebedev, in *Photoelectric Effects in Semiconductors (Conference Proceedings)* [in Russian], Ylym, Ashkhabad (1991).
[3] R. A. Smith, *Semiconductors*, Cambridge Univ. Press, Cambridge, 2nd ed. (1978) [Russian trans., Mir, Moscow (1982)].
[4] V. L. Bonch-Bruevich and S. G. Kalashnikov, *Physics of Semiconductors* [in Russian], Nauka, Moscow (1990).
[5] A. Rose, *Concepts in Photoconductivity and Allied Problems*, Interscience, New York (1963) [Russian trans., Mir, Moscow (1966)].

Translated by James S. Wood

Evolution of static negative differential conductivity in $Ga_{1-x}Al_xAs$ as a function of the transverse magnetic field and the composition of the solid solution

G. É. Dzamukashvili, Z. S. Kachlishvili, and N. K. Metreveli

Tbilisi State University, 380028 Tbilisi, Georgia

(Submitted January 18, 1996; accepted for publication January 30, 1997)
Fiz. Tekh. Poluprovodn. **31**, 987–988 (August 1997)

The authors investigate the behavior of the current-voltage characteristic of electrons under conditions of dynamic intervalley transfer in strong $\mathbf{E}\perp\mathbf{H}$ fields in a solid solution $Ga_{1-x}Al_xAs$ as the energy gap $\Delta\varepsilon$ between the lower and upper valleys is gradually diminished. It is shown that the static negative differential conductivity is particularly sensitive to variation of the magnetic field H for small gaps $\Delta\varepsilon$. Increasing H suppresses the static negative differential conductivity in this case. This technique can be used to eliminate low-frequency Gunn oscillations while simultaneously preserving the dynamic negative differential conductivity, which is suppressed in the submillimeter spectral range. © *1997 American Institute of Physics.* [S1063-7826(97)02708-7]

1. We have previously demonstrated[1] the onset of dynamic negative differential conductivity (NDC) in $Ga_{1-x}Al_xAs$ in crossed $\mathbf{E}\perp\mathbf{H}$ fields — in the cyclotron resonance effect. The resonance is more pronounced, the smaller the energy gap $\Delta\varepsilon$ between the Γ and X valleys. However, the experimental observation of dynamic NDC is obscured by the possible onset of low-frequency oscillations associated with static negative differential conductivity, which is responsible for the Gunn effect. The difficulties encountered in attempting to eliminate static NDC are well known. One technique involves the application of a magnetic field to the sample. For example, it has been shown[2] that as the magnetic field is increased in short GaAs samples, the modulus of the NDC decreases, and the maximum of the current-voltage (I–V characteristic) shifts toward higher electric fields. A second way to eliminate static NDC is to decrease the gap $\Delta\varepsilon$. We generally prefer this approach, because the cyclotron resonance discussed in Ref. 1 is more pronounced. Consequently, the simultaneous application of a magnetic field and a reduction of $\Delta\varepsilon$ should establish highly favorable conditions for the experimental implementation of dynamic NDC. To the best of our knowledge the problem has never been studied in this aspect.

In this report we give the results of an investigation of the I–V characteristics in the presence of dynamic intervalley electron transfer in strong $\mathbf{E}\perp\mathbf{H}$ fields in $Ga_{1-x}Al_xAs$ as the gap $\Delta\varepsilon$ is gradually diminished. We show how the static NDC and the critical field for its onset vary under these conditions. The investigations have been carried out on short samples ($L/d\ll 1$, where L and d are the length and a characteristic transverse dimension of the sample), so that the Hall voltage is shorted. The current in the sample runs in the same direction as the external field $\mathbf{E}$.

2. We assume that the temperature and the electric field are such that they validate the conditions $\tau_E<\tau_{op}$ and $k_0T\ll\hbar\omega^*$. Here τ_E is the warmup time of electrons in the Γ valley to the energy of initiation of intervalley transfer $e_0=\Delta\varepsilon+\hbar\omega^*$ ($\hbar\omega^*$ is the intervalley phonon energy). Because of the large effective mass of electrons in X valleys, the conditions $\varepsilon^X<\hbar\omega$ and $\varepsilon^X\ll\varepsilon_0$ are readily satisfied (ε^X is the average electron energy in X valleys), so that after $X\rightarrow\Gamma$ scattering, electrons transfer to a circular strip of width ε^X along the constant-energy surface $\varepsilon_1=\Delta\varepsilon-\hbar\omega^*$, and in this case the Γ valley contains two clearly distinguishable groups of electrons in the Γ valley, A and B (see Fig. 1), that initiate motion in momentum space from the half-disks $\varepsilon_1=\text{const}$, $P_z<0$ and $\varepsilon_1=\text{const}$, $P_z>0$, respectively. They provide different contributions to the formation of the distribution function.[3,4] The centers of the electron phase trajectories are situated on the segment $(P_x,P_c,0)-P_1<P_x<P_1$, where

$$P_1=\sqrt{2m_\Gamma^*\varepsilon_1},\quad P_c=c_0m_\Gamma^*E/H,$$

m_Γ^* is the effective electron mass in the Γ valley, and c_0 is the speed of light. In the case

$$P_1'<P_c<\frac{P_1'+P_0'}{2} \tag{1}$$

C-type trajectories appear in phase space (see Fig. 1b), where P_1' and P_0' are the radii of the disks formed by the intersection of the yz plane with the surfaces $\varepsilon_1=\text{const}$ and $\varepsilon_0=\text{const}$, respectively:

$$P_1'=\sqrt{P_1^2-P_x^2},\quad P_0'=\sqrt{P_0^2-P_x^2}\ \ (P_0=\sqrt{2m_\Gamma^*\varepsilon_0}).$$

The transfer of electrons from open trajectories to C trajectories is achieved only through transfers in the upper valleys (C trajectories intersect the surface $\varepsilon_1=\text{const}$). The transfer of electrons from C trajectories to open trajectories takes place by virtue of the finite quantity $\nu_{op}=\tau_{op}^{-1}$. The degree of redistribution of electrons between closed and open trajectories for fixed values of $\Delta\varepsilon$ and E is characterized by the parameter ν_{op}/ω_c, where $\omega_c=eH/c_0m_\Gamma^*$ is the cyclotron frequency. We assume for simplicity that ν_{op} is independent of the energy. In the case

$$P_c>\frac{P_0+P_1}{2}\equiv P_c^* \tag{2}$$

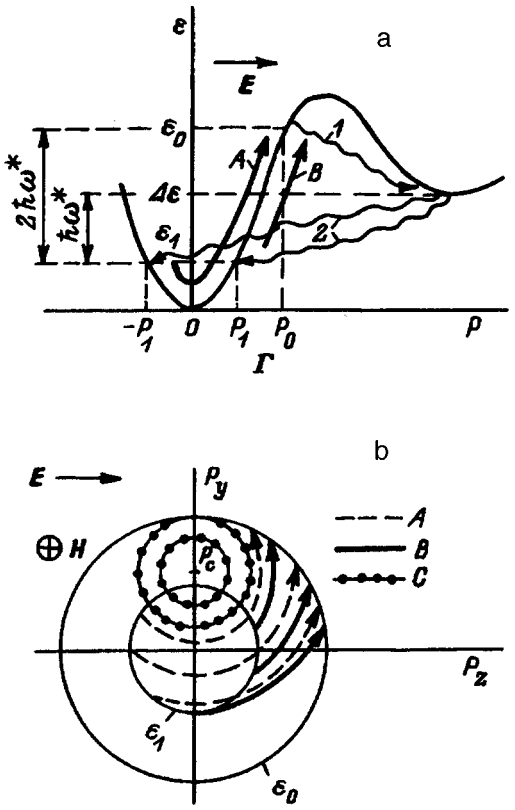

FIG. 1. Diagram of intervalley electron transfers (a) and the distribution of electrons in momentum space of the Γ valley (b) in the two-valley conduction band model. Here Γ is a light valley, and *X* is a heavy valley. *1)* Γ→*X* transfers; *2)* *X*→Γ transfers. The arrows indicate the free motion of *A* and *B* electrons; *C* electrons are closed in the magnetic trap.

all trajectories are open. We denote by E^* the minimum value of the electric field at which condition (2) holds for given H. The kinetic equation for the electron distribution function in the Γ valley f_Γ in homogeneous static electric and magnetic fields with configurations $e\mathbf{E}\|\mathbf{z}$ and $\mathbf{H}\|\mathbf{x}$ has the form

$$eE\frac{\partial f_\Gamma}{\partial P_z}+\omega_c\left(P_z\frac{\partial f_\Gamma}{\partial P_y}-P_y\frac{\partial f_\Gamma}{\partial P_z}\right)$$
$$=\frac{N_X\nu_1}{2\pi P_1}\delta(P^2-P_1^2)-\nu_{op}f_\Gamma, \qquad (3)$$

where the quantity

$$\nu_1=D_{\Gamma X}^2(m_\Gamma^*)^{3/2}\sqrt{\varepsilon_1}/\sqrt{2}\pi\hbar^3\rho\omega^*$$

is a characteristic frequency of the $X\to\Gamma$ transition, $D_{\Gamma X}$ is the deformation potential of intervalley scattering, ρ is the density of the sample, N_x is the density of electrons in the X valley, and the δ-function is introduced because of the small width of the source in the Γ valley. The coefficient of the δ-function is a normalization factor. The term $-\nu_{op}f_\Gamma$ in Eq. (3) appears only on C trajectories. In the case $E<E^*$ those closed trajectories which do not intersect the surface $\varepsilon=\varepsilon_1$ appear in the energy range $\varepsilon<\varepsilon_0$. The electron distribution on these trajectories is symmetric about the *xy* plane. Consequently, the current generated along the field **E** by these electrons is equal to zero.

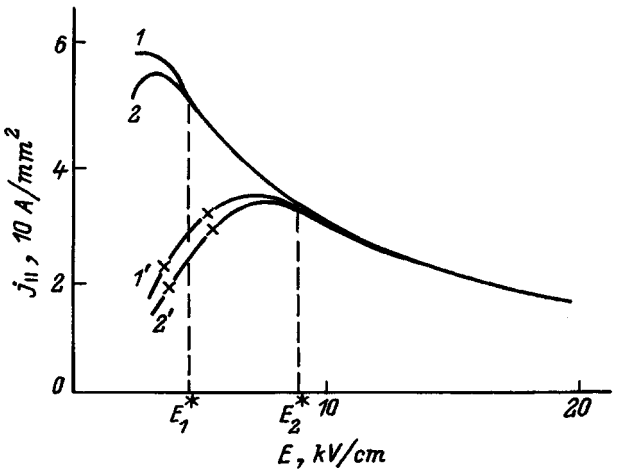

FIG. 2. Current density j versus electric field E for a $Ga_{0.7}Al_{0.3}As$ structure, $\Delta\varepsilon=4.5\hbar\omega^*$. *1,1′)* $\nu_{op}=1.2\times10^{12}$ s^{-1}; *2,2′)* 6×10^{11} s^{-1}; *1,2)* $H=10$ kOe, $\omega_c=1.9\times10^{12}$ s^{-1}, $E_1^*=7.5$ kV/cm; *1′,2′)* $H=20$ kOe, $\omega_c=3.8\times10^{12}$ s^{-1}, $E_2^*=15$ kV/cm.

3. The triple integrals in the current equation have been evaluated by the Monte Carlo method. Figures 2 and 3 show some of the results of our investigation of the *I–V* characteristics. As expected, the modulus of the NDC decreases as $\Delta\varepsilon$ decreases and as the magnetic field is increased. In the latter case, as in Ref. 2, the maximum of the *I–V* characteristic shifts toward higher electric fields. The total conductivity in the Γ valley decreases as ν_{op} decreases. Each of these results is physically obvious.

In fact, the decrease in the modulus of the NDC with decreasing $\Delta\varepsilon$ is attributable mainly to a decrease in the energy interval $0<\varepsilon<\Delta\varepsilon-\hbar\omega^*$ in which the distribution function is inverted. The NDC associated with this inversion is particularly sensitive to a variation of H for small gaps $\Delta\varepsilon$. An increase in H drastically undermines the inversion condition. Consequently, the modulus of the static NDC is

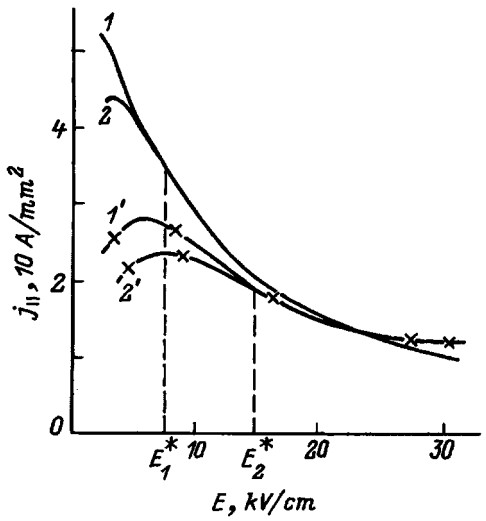

FIG. 3. Current density j versus electric field E for a $Ga_{0.63}Al_{0.37}As$ structure, $\Delta\varepsilon=1.7\hbar\omega^*$. *1,1′)* $\nu_{op}=1.2\times10^{12}$ s^{-1}; *2,2′)* 6×10^{11} s^{-1}; *1,2)* $H=10$ kOe, $\omega_c=1.8\times10^{12}$ s^{-1}, $E_1^*=4.5$ kV/cm; *1′,2′)* $H=20$ kOe, $\omega_c=3.6\times10^{12}$ s^{-1}, $E_2^*=9$ kV/cm.

easily diminished for such values of $\Delta\varepsilon$. For example, if $\Delta\varepsilon=(4-5)\hbar\omega^*$ at $H=40$ kOe, the NDC is so low that it is not sufficient to bring on instability in a static electric field. Moreover, for fixed values of $\Delta\varepsilon$ and E the current decreases as H increases. Indeed, with an increase in H, the residence time of electrons in the Γ valley increases, as does the number of electrons held in the magnetic ''trap,'' and the current therefore decreases.

A gradual increase in E at fixed H causes electrons to jump from closed trajectories to open trajectories, and their fraction in the conductivity increases. Upon application of a strong magnetic field, the current again drops for the well-known reason. This accounts for the shift of the maximum of the *I-V* characteristic toward higher values of E as H is increased.

The above-described quantitative dependence of the $I-V$ characteristic on the parameter ν_{op} (which is taken into account only for electrons moving on closed trajectories) is purely a model representation. It indicates the role of intravalley scattering in the range of electric fields $E<E^*$. Two different values are given for the parameter ν_{op}; they are the values most often used by various authors. It is obvious that for $E>E^*$ the $I-V$ characteristic must coincide exactly with the $I-V$ characteristic plotted for the case of zero scattering on open trajectories. The curves plotted for different values of ν_{op} therefore merge into a single curve at $E=E^*$.

The results of detailed investigations and similar reasoning show that the modulus of the static negative differential conductivity becomes positive for $\Delta\varepsilon\approx\hbar\omega^*$. This fact is also confirmed by calculations of the frequency dependence of the differential conductivity in a high-frequency field.[1]

[1] G. É. Dzamukashvili, Z. S. Kachlishvili, and N. K. Metreveli, Pis'ma Zh. Éksp. Teor. Fiz. **62**, 220 (1995) [JETP Lett. **62**, 234 (1995)].
[2] V. B. Gorfinkel', M. E. Levinshteĭ, and D. M. Mashovets, Fiz. Tekh. Poluprovodn. **13**, 563 (1979) [Sov. Phys. Semicond. **13**, 331 (1979)].
[3] A. A. Andronov and G. É. Dzamukashvili, Fiz. Tekh. Poluprovodn. **19**, 1810 (1985) [Sov. Phys. Semicond. **19**, 1111 (1985)].
[4] A. A. Andronov, V. A. Valov, V. A. Kozlov, and L. S. Mazov, Pis'ma Zh. Éksp. Teor. Fiz. **32**, 628 (1980) [JETP Lett. **32**, 615 (1980)].

Translated by James S. Wood

Inversion of the conduction type of epitaxial films of PbSnTe solid solutions under the influence of laser irradiation at subthreshold power

Yu. B. Grekov and T. A. Shlyakhov

Omsk State University, 644077 Omsk, Russia

N. A. Semikolenova

Institute of Sensor Microelectronics, Siberian Branch, Russian Academy of Sciences, 644077 Omsk, Russia
(Submitted January 14, 1997; accepted for publication February 4, 1997)
Fiz. Tekh. Poluprovodn. **31**, 990–992 (August 1997)

Conduction type inversion processes in $Pb_{1-x}Sn_xTe$ epitaxial films irradiated by a CO_2 laser ($\lambda = 10.6\mu$m) at subthreshold power is investigated. It is hypothesized that the stable inverted state is a result of the formation of neutral metal and chalcogen divacancies. © *1997 American Institute of Physics.* [S1063-7826(97)02808-1]

INTRODUCTION

For the fabrication of active elements of optical integrated circuits utilizing semiconductor solid solutions $Pb_{1-x}Sn_xTe$ it is necessary to vary the density of charge carriers in epitaxial structures over a wide range, from 10^{15} cm^{-3} for photodetectors to 10^{18} cm^{-3} for optical lasers.

It is generally known that the irradiation of *n*-type PbSnTe by a laser beam at wavelengths of 0.694 μm and 1.0 μm (photon energy greater than the width of the band gap $\hbar\omega > E_g$) with energy density above the recrystallization threshold leads to inversion of the conduction type, and the hole density increases by more than an order of magnitude in *p*-type single crystals.[1,2]

In the present study *p*-$Pb_{0.8}Sn_{0.2}Te$ films prepared by hot-wall epitaxy on a ⟨111⟩-oriented BaF_2 substrate have been subjected to laser irradiation. A source of composition $Pb_{0.8}Sn_{0.2})_{1.01}Te_{0.99}$ was synthesized from Pb(99.9999), Sn(99.9999), and Te(T-V4). Prior to the start of epitaxy the space containing the reaction chamber was evacuated to a pressure of $\sim 2\times10^{-6}$ Torr. The substrate temperature was 240 °C. The source was heated to 550 °C, and the wall temperature was ten degrees higher. A secondary tellurium source was introduced to vary the hole density in the samples.[3] The investigated epitaxial layers were in the form of squares with a side of 5 μm, and the film thicknesses were 10–40 μm. The epitaxial films were laser-annealed in an evacuated chamber. A continuous-wave CO_2 laser emitting at the wavelength $\lambda = 10.6$ μm was used for irradiation. The power density of the radiation was below the recrystallization threshold. In every case the width of the bad gap of the films $E_g = (0.21–0.22)$ eV satisfied the condition $E_g > \hbar\omega$.

EXPERIMENTAL RESULTS

Figure 1 shows the temperature dependence of the Hall coefficient R in the interval $T = 77–400$ K for a series of samples with different hole densities. The dependence of the Hall mobility μ on the hole density at 300 K is shown in Fig. 2. The functional dependences $R(T)$ and $\mu(T)$ for all the investigated samples are consistent with published experimental data. Figure 3 shows the temperature dependence of the Hall coefficient for a film with the maximum hole density ($p = 7\times10^{18}$ cm^{-3}) after laser irradiation at various power densities. The hole density decreases as the power density of the laser beam is increased (curves *1–4*), and conduction type inversion is observed at a power density $P_{inv} \approx 30$ W/cm^2 (Fig. 3, curve *5*). The inverted state is stable up to room temperatures. The variation of the Hall coefficient of this sample as the laser power density is varied at temperatures of 297 K and 77 K is shown in Fig. 4.

At radiation intensity $P < P_{inv}$, inversion states, which are unstable, also arise. The relaxation processes return the sample to *p*-type conductivity state in a time of 240–260h, as observed at room temperature and liquid-nitrogen temperatures. Additional irradiation can be used to obtain stable invserse states.

DISCUSSION OF THE RESULTS

As mentioned in Ref. 4, crystals of $Pb_{1-x}Sn_xTe$ solid solutions prepared from stoichiometric melts are character-

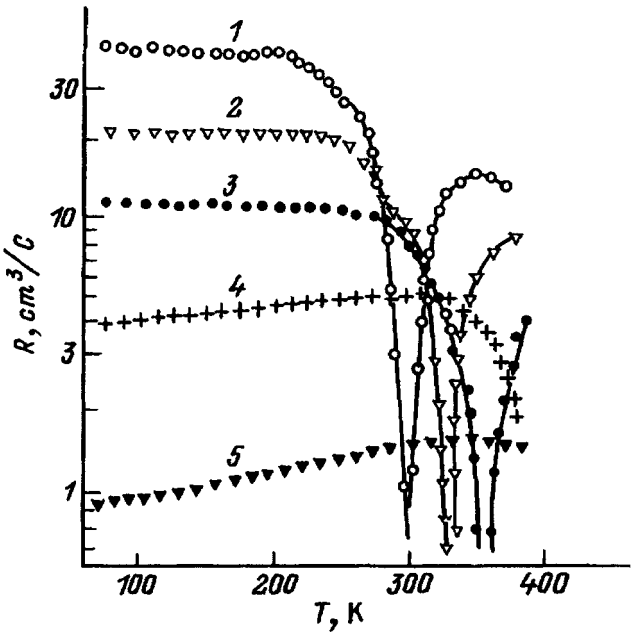

FIG. 1. Hall coefficient R versus temperature T for $Pb_{0.8}Sn_{0.2}Te$ epitaxial films with various hole densities *p*. *1*) $p = 1.3\times10^{17}$ cm^{-3}; *2*) 2.9×10^{17} cm^{-3}; *3*) 5.8×10^{17} cm^{-3}; *4*) 14×10^{17} cm^{-3}; *5*) 70×10^{17} cm^{-3}.

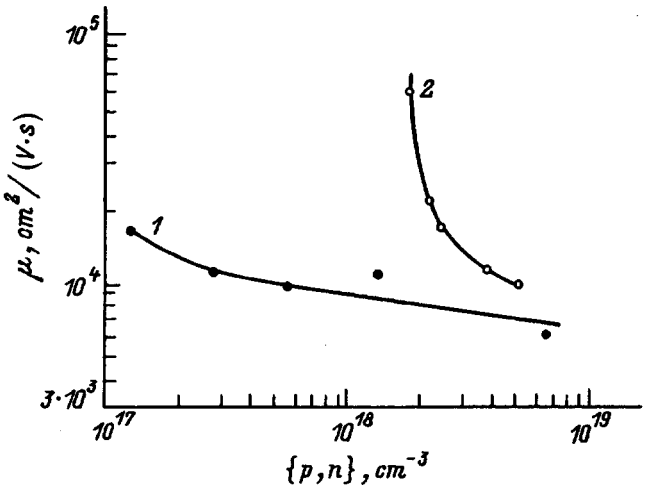

FIG. 2. Carrier mobility μ versus: *1*) hole density p before irradiation; *2*) electron density n after irradiation.

ized by large concentrations of defects — metal vacancies and chalcogen vacancies — which are electrically active. Moreover, as a result of concentration subcooling, the $Pb_{1-x}Sn_xTe$ crystals are characterized by the presence of zones enriched with metal and tellurium, irrespective of the contents of the components in the melt.[5,6] In all probability, under certain growth conditions the metal- and tellurium-enriched zones can also exist in epitaxial films grown by the hot-wall technique. The diffusion of metal atoms from such zones can induce a change from hole-type to electron-type conduction, because every time metal atom fills a vacancy in the metal sublattice, it liquidates two holes from that vacancy. On the other hand, metal ions situated in the interstices are singly charged donors.[7] This process takes place in the thermal annealing of *p*-type PbTe in a neutral atmosphere

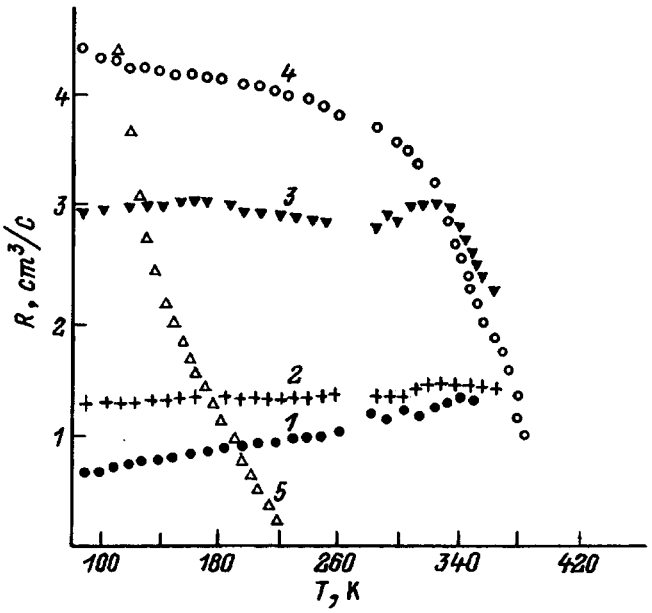

FIG. 3. Hall coefficient versus temperature for epitaxial film $Pb_{0.8}Sn_{0.2}Te$ with a hole density $p=7\times10^{18}$ cm^{-3}. Graphs *1–5* correspond to successive increments of the laser power density.

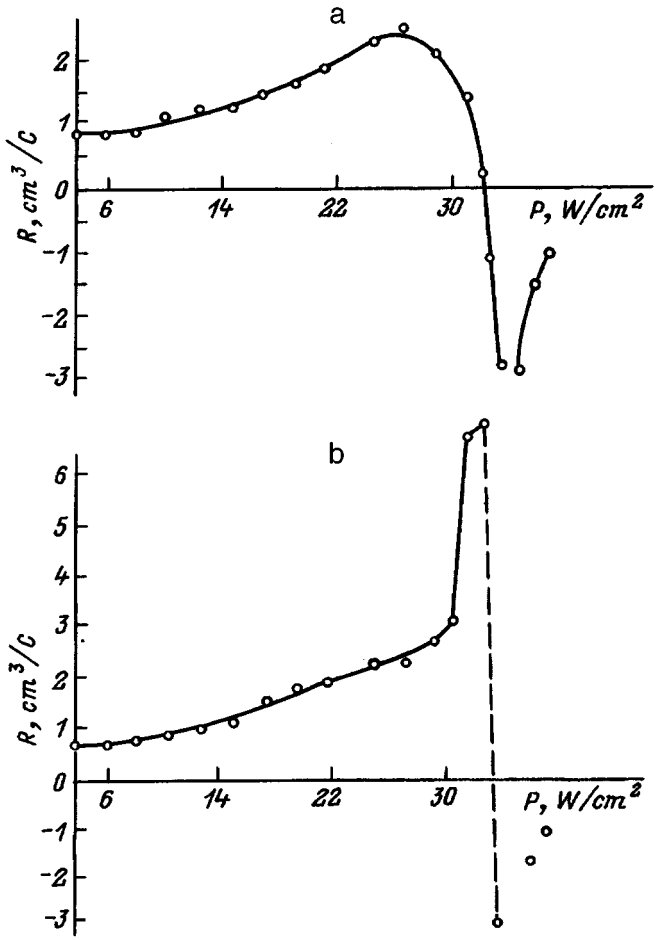

FIG. 4. Hall density versus laser power density for epitaxial film $Pb_{0.8}Sn_{0.2}Te$ with a hole density $p=7\times10^{18}$ cm^{-3} at different temperatures. a) $T=297$ K; b) $T=77$ K.

at $T=400$ °C, where conduction-type inversion is obtained without the use of doping impurities or an excess of metallic-component vapors.[6]

It has been shown[8] that the effect of laser irradiation under the condition $\hbar\omega<E_g$ is not associated with thermal annealing, but is attributable to the multiphoton excitation of interstitial atoms in the strong electromagnetic field of the CO_2 laser in zones of lattice distortion by clusters of atoms and their subsequent diffusion from such zones. The breakdown of microzones enriched with metallic components causes the conduction type of the sample to change, and the carrier mobility increases at the same time (Fig. 2). On the other hand, the dependence of the conduction type inversion on the laser power suggests that the thermal effect and multiphoton excitation act in concert. At a certain power level the temperature attains a value that together with multiphoton excitation leads to inversion of the conduction type.

In this case the inverted state is unstable and is accompanied by a relaxation process, which brings the sample back to *p*-type conduction. The electron density decreases after several days and then, after reinversion of the conduction type, returns to approximately the initial value. The relaxation processes can be associated with the return of Te atoms to the chalcogen sublattice from the interstices occupied as a

result of multiphoton excitation. In subsequent irradiations some of the Te atoms escape from the sample into the surrounding vacuum, and the *n*-type conduction becomes stable.

The possibility of multiphoton excitation of atoms is evinced by metastable states that emerge at various laser power densities. The stable inverted state is possibly associated with the formation of neutral metal and chalcogen divacancies, which break down above room temperature.[7,9]

[1] K. D. Tovstyuk, G. V. Plyatsko, V. B. Orletskiĭ *et al.*, Ukr. Fiz. Zh. **21**, 531 (1976).
[2] E. A. Gorin, I. A. Berezhnaya, D. A. Generalova, S. N. Emelin, and G. I. Yanko, Fiz. Tekh. Poluprovodn. **16**, 1687 (1982) [Sov. Phys. Semicond. **16**, 1078 (1982)].
[3] O. M. Savenko, Yu. B. Grekov, and A. S. Semikolenov, in *All-Union Conference on the Physicochemical Foundations of Ferroelectric and Related Materials Technology* [in Russian], Zvenigorod (1993), p. 190.
[4] V. I. Kaĭdanov and Yu. I. Ravich, Usp. Fiz. Nauk **145**, 51 (1985) [Sov. Phys. Usp. **28**, 31 (1985)].
[5] T. T. Dedegkaev, V. A. Moshnikov, D. B. Chesnokova, and D. A. Yas'kov, Pis'ma Zh. Tekh. Fiz. **6**, 1030 (1980) [Sov. Tech. Phys. Lett. **6**, 443 (1980)].
[6] R. Breshi, A. Camansi, and V. Fano, J. Cryst. Growth **5**, 399 (1982).
[7] H. Heinrich, in *Lecture Notes in Physics 133*, Springer-Verlag, Berlin-New York (1979), p. 407.
[8] S. V. Plyatsko, Yu. S. Gromovoĭ, and F. F. Sizov, Kvantovaya Élektron. (Kiev), No. 29, 93 (1985).
[9] Sh. Sh. Bashkirov, A. B. Liberman, S. S. Tsarevskiĭ, and R. A. Nasybullin, Fiz. Tverd. Tela (Leningrad) **30**, 281 (1988) [Sov. Phys. Solid State **30**, 161 (1988)].

Translated by James S. Wood

Nature of $E_c-0.37$ eV centers and the formation of high-resistivity layers in *n*-type silicon

O. V. Naumova, L. S. Smirnov, and V. F. Stas'

Institute of Semiconductor Physics, Siberian Branch of the Russian Academy of Sciences, 630090 Novosibirsk, Russia

(Submitted December 20, 1996; accepted for publication February 4, 1997)
Fiz. Tekh. Poluprovodn. **31**, 993–997 (August 1997)

The DLTS and Van der Pauw methods are used to investigate the production of $E_c-0.37$ eV centers responsible for the formation of high-resistivity layers in *n*-type Si irradiated with electrons and annealed in the temperature range 80–320 °C. An analysis of the experimental data leads to a conclusion as to the composition of the $E_c-0.37$ eV centers ([*V*–O–C]) and to the conclusion that their formation is stimulated by a flux of interstitial atoms away from the interface into the interior of the semiconductor during annealing accompanied by the reactions: 1) $I+C_s\rightarrow C_i, C_i+[V\text{–}O]\rightarrow[V\text{–}O\text{–}C]$ (dominant reaction); 2) $I+V_2\rightarrow V, V+[C\text{–}O]\rightarrow[V\text{–}O\text{–}C]$. © *1997 American Institute of Physics.* [S1063-7826(97)02908-6]

Defect-impurity reactions in the vicinity of the surface of silicon have distinctive features governed by the characteristics of the material, the mechanical and chemical operations performed on it, and the thermal and radiation conditions under which it is treated. Investigations of these reactions have been reported in many papers (see, e.g., Refs. 1–3). As an example, the formation of a high-resistivity surface layer has been observed during anneals of electron-irradiated silicon in the temperature range 180–300 °C (Ref. 2). It has been established that this phenomenon is observed only in oxygen-containing (grown by the Czochralski process) silicon and that centers with an energy level $E_c-0.37$ eV are responsible for the formation of the high-resistivity layer. It has been observed[4] that the γ-irradiation of silicon establishes a correlation between the formation of $E_c-0.37$ eV centers and the annealing of vacancy-oxygen complexes (A centers). The surprising aspect of the high-resistivity layer phenomenon, apart from the low temperatures at which the reactions take place, is the fact that it keeps resurfacing in peel-etching, provided only that the anneal temperatures and times do not exceed those required for the complete eradication of A centers.[2] Even though the phenomenon has been studied in detail and has been known for some time, the nature and mechanism of the formation of the high-resistivity layers in the low-temperature ($\lesssim$900 °C) treatments of irradiated silicon have yet to be established.

According to electron spin resonance (ESR) and infrared spectroscopy data, the annealing of vacancy-oxygen complexes in bulk silicon material is associated with the formation of [C–O–V_2] (Ref. 5), [*V*–O_2] (Refs. 6 and 7), [*V*–O–C] (Ref. 7), and V_3O (Ref. 8) centers. This evidence has prompted several authors to speculate that the defects responsible for the formation of the high-resistivity layers near interfaces are [C–O–V_2] (Ref. 9), [*V*–O_2] (Ref. 10), V_2O, and V_3O (Ref. 11) complexes. The mechanism of the formation of these complexes has been attributed to the following scenario. Near the interfaces, under the influence of stress fields, vacancy complexes anneal at lower temperatures than in the interior volume of the semiconductor. As a result: 1) the liberated vacancies are trapped by [C–O] complexes already present in the interior;[9] vacancy-oxygen complexes that are mobile near the surface interact with oxygen;[10] 3) during annealing, divacancies are formed near the surface, from which they then diffuse into the volume and interact with oxygen or with yet-unannealed A centers.[11]

The involvement of oxygen in the complex-forming process has been corroborated by the fact that an $E_c-0.37$ eV center is observed in silicon grown by the Czochralski process, but does not show up in ''oxygen-free'' (with oxygen concentration $N_O\leqslant 10^{16}$ cm^{-3}) silicon (note that the involvement of oxygen is a necessary but not sufficient condition, as indeed the formation of high-resistivity layers is not observed in certain samples with oxygen concentrations as high as 10^{18} cm^{-3}). To confirm whether $E_c-0.37$ eV complexes are monovacancy or multivacancy types and whether their composition contains carbon, experimental data are needed on: 1) the behavior of radiation defects containing vacancies during annealing; 2) the dependence of the phenomenon on the carbon concentration (an impurity highly prone to reactions with vacancies and oxygen[7] and usually present in silicon in large concentrations: $N_C\simeq 5\times 10^{16}$–$10^{17}$ cm^{-3}). The objective of the present study, therefore, is to investigate experimentally in greater detail the behavior of $E_c-0.37$ eV centers in comparison with other vacancy-containing complexes in silicon with a monitored carbon content.

The materials used for the investigation were of mark KÉF-1, KÉF-4.5, BKÉF-4.5 (''oxygen-free'' silicon with $N_O\leqslant 10^{16}$ cm^{-3}). The raw KÉF-1 and KÉF-4.5 samples had an oxygen concentration $N_O\simeq 10^{18}$ cm^{-3} and carbon concentrations $N_C<3\times 10^{15}$ and $\sim 5\times 10^{16}$ cm^{-3}, respectively. Some of the KÉF-1 samples were subjected to carbon or nitrogen ion implantation (ion energy $E=200$ keV, doses $\Phi_1=10^{13}$ cm^{-2}, $\Phi_2=5\times 10^{13}$ cm^{-2}) and a 30-min anneal at a temperature $T_a=900$ °C. All the samples were irradiated with electrons of energy $E=3.5$ MeV on a Mikrotron pulsed accelerator in the following regime: pulse repetition rate $\omega=100$ Hz, single-pulse duration $t_i=3$ μs, irradiation temperature $T_{\text{irr}}=300$ K. After irradiation and anneals (isother-

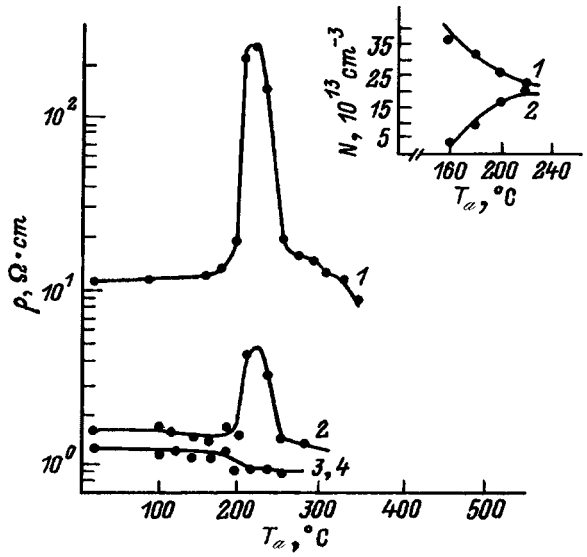

FIG. 1. Resistivity versus temperature in an isochronous anneal of silicon. *1* — KÉF-4.5, $N_C \approx 5\times10^{16}$ cm^{-3}, $\Phi_e = 1\times10^{16}$ cm^{-2}; *2–4* — KÉF-1, $N_C < 3\times10^{15}$ cm^{-3}, $\Phi_e = 3\times10^{16}$ cm^{-2}. Carbon irradiation flux: *1, 4* — $\Phi_C = 0$; *2* — $\Phi_C = 5\times10^{13}$ cm^{-2}; *3* — $\Phi_C = 1\times10^{13}$ cm^{-2}. Inset: Concentration N of A centers (graph 1) and $E_c - 0.37$ eV centers (graph 2) versus anneal temperature at a distance $x = 1.5$ μm from the interface of the p^+- and n-regions.

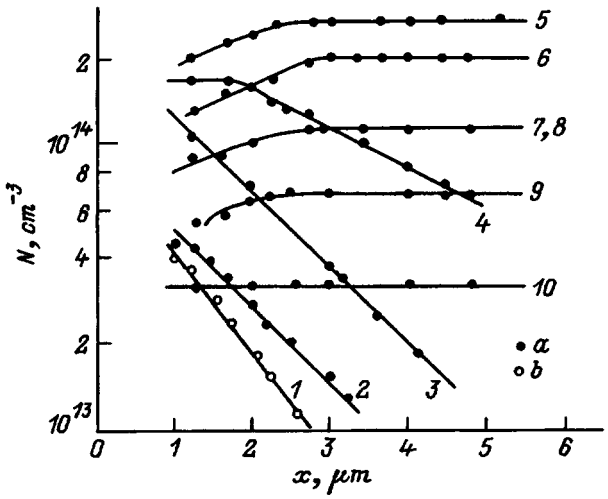

FIG. 2. Spatial distribution of the concentration N of $E_c - 0.37$ eV centers along the depth x of p^+–n structures during an isochronous anneal. Temperature increment $\Delta T_a = 20$ °C, anneal time $t_a = 20$ min. *1* — $T_a = 120$ °C; *2* — 160 °C; *3* — 180 °C; *4* — 200 °C; *5* — 220 °C; *6* — 240 °C; *7* — 260 °C; *8* — 280 °C; *9* — 300 °C; *10* — 320 °C; a — $U = 0$ V; b — $U = 20$ V. $\Phi_e = 3\times10^{15}$ cm^{-2}.

mal or isochronous in the interval 80–320 °C in steps $\Delta T_a = 20°$) the resistivity ρ was measured by the Van der Pauw method, and the spatial distribution of the concentration of radiation defects along the depth of the structures was measured by deep-level transient spectroscopy (DLTS; Ref. 12); for the DLTS measurements Schottky barriers were formed by gold-film evaporation, or p^+–n structures were created beforehand by boron diffusion to a depth of 2–3 μm.

EXPERIMENTAL RESULTS AND DISCUSSION

Figure 1 shows the results of isochronous annealing of silicon with various carbon contents.

As should be expected, for KÉF-4.5 with $N_C \simeq 5\times10^{16}$ cm^{-3} in the interval 180–220 °C the resistivity ρ was observed to increase with the anneal temperature (the formation of an high-resistivity layer did not occur in the case of the BKÉF-4.5 material). The DLTS measurements showed (Fig. 1) that the growth of ρ in the investigated material does in fact correlate with the anneal of A centers and an increase in the concentration of $E_c - 0.37$ eV centers. The variation of the concentration of $E_c - 0.37$ eV centers corresponds to the variation of the concentration of A centers within the measurement error limits (see also Refs. 2 and 4).

The phenomenon was not observed at all in the case of samples with $N_C < 3\times10^{15}$ cm^{-3} (Fig. 1, curve *4*). Only after carbon ion implantation was the formation of a high-resistivity layer observed on carbon-free samples (curves *2* and *3*). We note that under the given irradiation and activation anneal conditions the concentration of implanted carbon was $\sim 4\times10^{16}$ cm^{-3} and $\sim 2\times10^{17}$ cm^{-3} at the respective fluxes Φ_1 and Φ_2 ($N_C = \Phi_i/d$, where, according to secondary-ion mass spectrometry (SIMS) data, $d \sim 2.5\mu$m under the given experimental conditions). Consequently, a high-resistivity layer is formed in the presence of the typical carbon concentration of a material growth by the Czochralski process ($\sim 5\times10^{16}$–10^{17} cm^{-3}).

As a control measure, the oxygen-free samples were irradiated with nitrogen in the same flux range. The resistivity ρ did not increase. In addition, the following operations were performed on KÉF-1 samples irradiated with carbon at $\Phi_2 = 5\times10^{13}$ cm^{-2}: 1) 30-min anneal at 400 °C to remove radiation defects; 2) etching in SR-4 with peeling of a ~ 10 μm; 3) repeated irradiation with electrons at $\Phi_e = 10^{16}$ cm^{-2}; 4) isochronous anneal. An increase of ρ with increasing temperature was not observed, but the same operations performed on the KÉF-4.5 material resulted in the repeated formation of a high-resistivity layer. In our opinion, this evidence indicates the participation of carbon in the formation of $E_c - 0.37$ eV centers.

A question arises as to the depth distribution of the concentration of vacancy complexes and $E_c - 0.37$ eV centers in the structures. Figure 2 shows DLTS data on the depth distribution of the concentration of $E_c - 0.37$ eV centers in p^+–n structures. We infer from the nature of the distribution of centers in the initial stage of annealing (at $T_a < 220$ °C) that their formation is a diffusion process.

An analysis of the profiles of the depth distribution of the concentration of $E_c - 0.37$ eV centers in the structures after isothermal anneals at $T_a < 220$ °C shows that they conform to a Gaussian distribution function. It is therefore logical to assume that the formation of $E_c - 0.37$ eV centers is associated with diffusion of a certain component from the interface into the volume of the semiconductor, where this component either enters directly into the composition of the centers or stimulates their formation in interaction with other defects.

Figure 3 shows graphs of the relative variation of the concentration of A centers, E centers (vacancy-phosphor

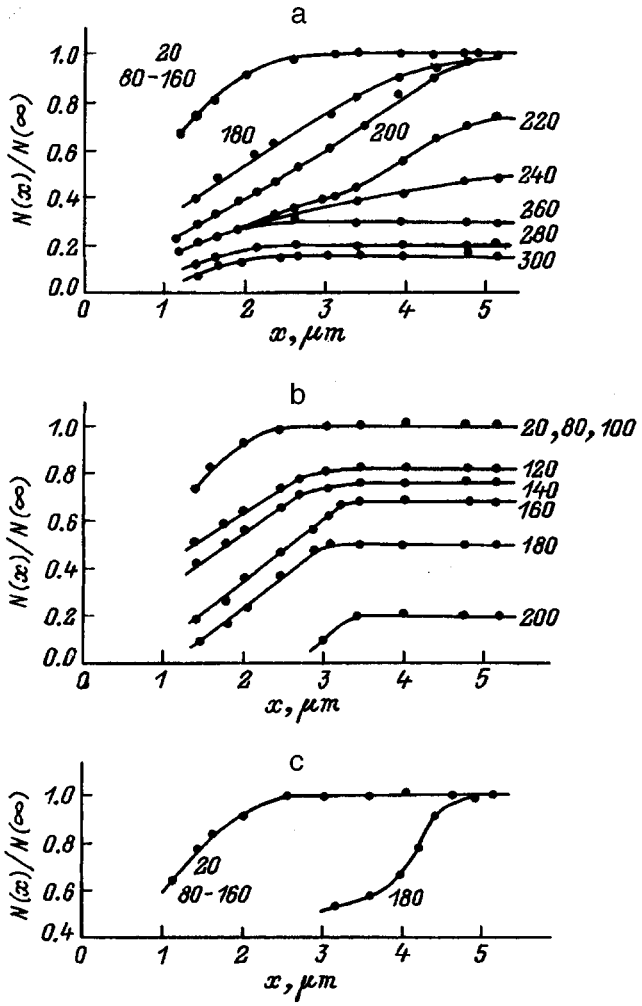

FIG. 3. Relative variations of the concentration N of various defects in the base of p^+–n structures during an isochronous anneal. a) A centers, $N(\infty)=1.7\times10^{14}$ cm^{-3}; b) E centers, $N(\infty)=1.1\times10^{13}$ cm^{-3}; c) divacancies V_2, $N(\infty)=0.3\times10^{14}$ cm^{-3}. Anneal temperature increment $\Delta T_a=20°$, anneal time $t_a=20$ min. The values of T_a,°C are indicated, $\Phi_e=10^{15}$ cm^{-2}, and $N(\infty)$ denotes the concentration of radiation defects in the interior volume prior to annealing.

complexes), and divacancies V_2 along the depth of diode structure after isochronous anneal. We see that the formation of $E_c-0.37$ eV centers does not influence the annealing of vacancy-phosphor complexes; their annealing begins at 120 °C, and the concentration distribution profiles scarcely change with T_a. In addition to A centers, divacancies V_2 anneal more efficiently (beginning with $T_a=180$ °C) in layers adjacent to the boundary of the p^+–n junction. The following characteristics are worth noting: 1) The V_2 concentration gradient does not run from the surface into the interior as postulated in Ref. 11, but in the opposite direction, so that the formation of $E_c-0.37$ eV centers at depths in the tens of micrometers cannot be attributed to the diffusion of divacancies into the interior of the semiconductor; 2) the annealing of V–O, V_2 complex is observed, beginning with $T\approx180$ °C, not only in layers adjacent to the interface of the p- and n-regions, but also at depths $x\gg1$ μm, where there are no interface stress fields or electric fields. Under such conditions (for the bulk material), however, A centers in silicon are stable up to 300 °C, and divacancies are stable up to 250 °C (Ref. 14). This leaves no choice but to assume that A centers and V_2 are both annealed at the given temperatures, interacting with defects or impurity atoms diffusing away from the surface (taking into account the nature of the propagation of $E_c-0.37$ eV centers; see Fig. 2), but do not migrate as a unit before interacting with oxygen.[10,11] Also taking into account the correlation between variations of the concentrations of A centers and $E_c-0.37$ eV centers and the fact that the concentrations of other vacancy complexes are much lower than the concentration of vacancy-oxygen complexes, we conclude that: 1) the complexes responsible for the formation of high-resistivity layers are monovacancy types; 2) an A center does not act as a feeder of vacancies to a new complex, but enters into it as a unit whole.

Our experimental results, therefore, suggest, from our point of view, that the favored choice among the several possible complexes responsible for the formation of high-resistivity layers near the interface goes to [V–O–C] complexes. The formation of these complexes requires A centers and a flux of carbon atoms.

The source of mobile carbon (at $T\geqslant300$ K) in silicon is assumed to comprise the reactions $I+C_s\rightarrow C_i$ during irradiation, when native interstitial atoms I are generated in the interior, or during annealing of complexes containing interstitial atoms.[7] It is logical to assume, therefore, that annealing is accompanied by the diffusion of interstitial carbon atoms from the interface into the interior of the semiconductor with the following reactions taking place:

$$I+C_s\rightarrow C_i,\quad C_i+[V\text{–O}]\rightarrow[V\text{–O–C}]$$

(dominant reaction), (1)

$$I+V_2\rightarrow V,\quad V+[\text{C–O}]\rightarrow[V\text{–O–C}]. \tag{2}$$

Let us assume that the complexes of interstitial atoms introduced by irradiation dissociate near the interfaces during annealing, and that there is a diffusion of I (or of C_i by virtue of the reaction $I+C_s\rightarrow C_i$) into the interior of the semiconductor. It is easy to estimate whether the radiation-generated interstitial silicon atoms are sufficient for the formation of $E_c-0.37$ eV centers through the reaction (1).

If the electron flux is $\Phi_e=3\times10^{15}$ cm^{-2}, the rate of injection of interstitial atoms is ~4 cm^{-1}, and the ''survival quotient'' (after annihilation with vacancies) is $\sim10\%$, the total number of generated I is $\sim10^{15}$ cm^{-3}. Hence, even if all interstitial complexes dissociate completely in a layer of thickness 1 μm, $\sim10^{11}$ interstitial atoms diffuse into the interior. We infer from the experimental data in Fig. 2 that the formation of $E_c-0.37$ eV centers in a layer of thickness ~10 μm requires $\sim2.4\times10^{11}$ interstitial atoms I at $T_a=220$ °C. By no means does every radiation-induced interstitial atom enter into the reaction (1); bearing this fact in mind, we conclude that in addition interstitial atoms introduced by irradiation, there must be another source of I for the formation of $E_c-0.37$ eV centers by the reaction (1). One cannot rule out the possibility of silicon surface layers being enriched by interstitial atoms during anneals involving the formation of SiO_2 films. A well-known phenomenon is the injection of I and the formation of stacking faults in the

high-temperature ($T \geqslant 900$ °C) oxidation of silicon (see, e.g., Ref. 3). However, does this kind of phenomenon occur in the investigated temperature range of 180–300 °C? There is a need for experimental proofs and judicious experimental design.

We now consider a model involving the active behavior of carbon near an interface. We assume that the flux of carbon atoms is a consequence of their liberation from complexes or from an interface decoration cloud. The following arguments support the migration of interstitial carbon into the interior of the sample.

1. *According to sample concentration.* For $N_C = 5\times10^{16}$–2×10^{17} cm^{-3} (when the formation of $E_c - 0.37$ eV centers is observed in the sample) the carbon content in a layer of thickness $x < 1$ μm is $< 10^{13}$ atoms. This estimate is approximately an order of magnitude higher than is required for the formation of the observed concentration $E_c - 0.37$ eV centers, although it must be borne in mind that the formation of the latter can only involve mobile interstitial C_i atoms.

2. *According to the diffusion coefficient.* An analysis of the profiles of the concentration of $E_c - 0.37$ eV centers after isothermal anneals has shown that the distribution of the concentration of centers along the depth of the structures at $T_a < 220$ °C corresponds to a Gaussian distribution function with diffusion coefficient $D \approx 10^{-11}$ cm^2/s. If we use the standard approximation for the diffusion coefficient of interstitial carbon $D_{C_i}[\text{cm}^2/\text{s}] = 0.44\ \exp(-0.87/kT[\text{eV}])$ (Ref. 15) in the range $T = 160$–200 °C, we obtain a result close to the experimental value, $D_{C_i} \approx 10^{-10}$ cm^2/s.

3. *Indirect evidence.* The legitimacy of recruiting C_i to account for the formation of high-resistivity layers is supported by the dependence of the phenomenon on the type of masking coating: The presence of an SiO_2 film (coating deposited prior to electron irradiation) has scarcely any effect on the behavior of the resistivity of the sample, whereas the deposition of an Si_3N_4 film shifts the maximum to higher temperatures, but the increase in ρ is comparatively small.[2] According to data in Ref. 16, interstitial carbon effectively interacts with nitrogen, forming C_i–N_s complexes, i.e., Si_3N_4 (in contrast with SiO_2) films are capable of deactivating part of the interstitial carbon.

Which complexes provide the source of mobile interstitial carbon? The experimental reality, that a high-resistivity layer forms repeatedly after etch-anneal operations,[2] indicates that the culprits are centers formed at a temperature below 180 °C, and in the interior of the sample their anneal temperature is not lower than that of V–O complexes, i.e., >300 °C. Are the interface stress and voltage levels great enough to weaken the bonds between the components of the complexes and to release interstitial atoms? Estimates show that the stresses and voltages provide an energy gain of $\sim 10^{-3}$–10^{-2} eV. Consequently, if the dissociation of carbon-containing complexes is determined by the interface electric and stress fields, they must be complexes with a low binding energy.

It has been shown[17] that the uniaxial compression of Si during heating lowers the anneal temperature of A and E centers. We have performed experiments in which an external voltage was applied to structures during an isochronous anneal (80–140 °C) in such a way as to take the p^+–n junction into a reverse-biased state. The experiment showed (Fig. 2) that the application of an electric field lowers to 120 °C the anneal temperature of A centers and, accordingly, the temperature at which $E_c - 0.37$ eV complexes are formed.

If we assume that the concentration of mobile C_i near the interface obeys the law $N_C \sim \exp[-(E_d + \Delta U)/kT]$, where E_d is the energy of dissociation of carbon-containing complexes, and ΔU is the change in energy under the influence of an electric field E, and if we compare the $N(x,t)$ curves at $T_a = 160$ °C and 120 °C (Fig. 2), we obtain $E_d < 0.072$ eV for a dissociating complex of maximum size $x \simeq 10$ Å and for values of E at the maximum equal to 1.6×10^4 V/cm and 7.7×10^4 V/cm in the cases of structures unbiased and reverse-biased during annealing, respectively. This explains why such small increments of the voltage fields ($\sim 10^{-2}$ eV) influence the behavior of $E_c - 0.37$ eV centers. However, the electric field can exert influence by a different mechanism, specifically by changing the charge state of defects in a way similar to the action of electric fields in the annealing of E centers.[18] In this case a variation of the energy of activation of anneal of complexes in a field can amount to tenths of an electron-volt. In any case, however, the energy of activation of the formation of $E_c - 0.37$ eV centers according to isothermal anneal data, $E_a \simeq 1.3$ eV, includes: 1) the energy of dissociation of carbon-containing complexes E_d; 2) the energy associated exclusively with C_i migration energy, $E_m = 0.87$ eV (Ref. 15); 3) the energy E_k of formation of the complex $C_i + [V - O]$.

Not enough experimental data are available at the present time to give preference to any one of these processes. The first one requires experimental proof that the interface is enriched with interstitial atoms originating from something other than radiation during an anneal in the temperature range $T_a = 180$–300 °C. The second calls for an answer to the question of which complexes (or processes) are the source of mobile carbon near interfaces. In all probability, both processes are involved. We merely note that the mechanism involving a flux of interstitial silicon atoms explains both the formation of $E_c - 0.37$ eV centers and the more efficient annealing of divacancies near interfaces (Fig. 3).

CONCLUSIONS

The reported experimental data lead to the conclusions that: 1) one condition for the formation of $E_c - 0.37$ eV centers in electron-irradiated silicon is a carbon content $N_C \geqslant 5\times10^{16}$ cm^{-3}; 2) the preferred choice among the several kinds of complexes potentially responsible for the formation of $E_c - 0.37$ eV centers and, hence, the formation of high-resistivity layers near the interfaces of silicon structures should be $[V$–O–C$]$ complexes. The mechanism underlying the formation of $[V$–O–C$]$ complexes, in our opinion, is a multistage process involving the diffusion of interstitial atoms away from the interface together with the reactions

1) $I + C_s \rightarrow C_i$, $C_i + [V\text{–O}] \rightarrow [V\text{–O–C}]$ (dominant reaction);

2) $I + V_2 \rightarrow V$, $V + [\text{C–O}] \rightarrow [V\text{–O–C}]$.

As a result of heat treatments in the temperature range 180–300 °C, the surface is probably the source of interstitial silicon atoms of other than radiation origin. Electron bombardment and the formation of a system of vacancy-containing complexes create a situation in which the reactions with intersitial atoms are activated.

We wish to thank S. A. Sukhikh and G. N. Kamaev for irradiating the samples with ions and electrons.

[1] L. S. Smirnov and S. I. Romanov, Fiz. Tekh. Poluprovodn. **10**, 876 (1976) [Sov. Phys. Semicond. **10**, 519 (1976)].
[2] N. N. Gerasimenko, N. P. Kibalina, and V. F. Stas', in *Radiation Effects in Semiconductors* [in Russian], L. S. Smirnov (Ed.), Novosibirsk (1979), p. 78.
[3] A. L. Aseeva, L. I. Fedina, D. Hoehl, and H. Bartsch, *Clustering of Interstitial Atoms in Silicon and Germanium* [in Russian], Novosibirsk (1991).
[4] L. S. Berman and V. B. Shuman, Fiz. Tekh. Poluprovodn. **10**, 1755 (1976) [Sov. Phys. Semicond. **10**, 1043 (1976)].
[5] Y. H. Lee, J. W. Corbett, and K. L. Brower, Phys. Status Solidi A **41**, 637 (1977).
[6] B. G. Svenson, J. L. Lindstrom, and J. W. Corbett, Appl. Phys. Lett. **47**, 841 (1985).
[7] J. L. Lindstrom and B. G. Svenson, in *Materials Science Forum: Defects in Semiconductors*, Vols. 38–41 (1989), p. 45.
[8] Y. H. Lee and J. W. Corbett, Phys. Rev. B **13**, 2653 (1976).
[9] I. F. Lugakov, T. A. Lukashevich, and V. V. Shusha, Fiz. Tekh. Poluprovodn. **13**, 401 (1979) [Sov. Phys. Semicond. **13**, 237 (1979)].
[10] R. V. Tayke and V. J. Faraday, in *Symposium on Lattice Defects in Semiconductors*, Univ. Tokyo Press, Tokyo (1966), p. 170.
[11] É. G. Batyev, N. N. Gerasimenko, and A. V. Efanov, Fiz. Tekh. Poluprovodn. **15**, 1448 (1981) [Sov. Phys. Semicond. **15**, 838 (1981)].
[12] D. V. Lang, J. Appl. Phys. **45**, 3023 (1974).
[13] U. Gosel, Mater. Res. Soc. Symp. Proc. **59**, 149 (1989).
[14] L. S. Smirnov (ed.), *Aspects of Semiconductor Radiation Technology* [in Russian], Novosibirsk (1980).
[15] G. Davies, E. S. Lightowles, R. C. Newman, and A. S. Oates, Semicond. Sci. Technol. **2**, 524 (1987).
[16] A. Dornen, R. Sauer, and G. Pensl, Mater. Res. Soc. Symp. Proc. **59**, 545 (1989).
[17] L. S. Milevskiĭ, T. M. Tkacheva, and A. A. Zolotukhin, in *International Conference on the Radiation Physics of Semiconductors and Related Materials* [in Russian], Tbilisi (1980), p. 350.
[18] L. C. Kimerling, Solid State Commun. **16**, 171 (1975).

Translated by James S. Wood

Formation of oxygen precipitates in silicon

I. V. Antonova, V. P. Popov, and S. S. Shaĭmeev

Institute of Semiconductor Physics, Siberian Branch of the Russian Academy of Sciences, 630090 Novosibirsk, Russia

A. Misiuk

Institute of Electronic Technology, Warsaw, Poland

(Submitted July 18, 1996; accepted for publication February 6, 1997)
Fiz. Tekh. Poluprovodn. **31**, 998–1002 (August 1997)

The initial stage of formation of oxygen precipitates in silicon is investigated by deep-level transient spectroscopy, selective etching, and infrared spectrometry. It is established that the formation of oxygen precipitates at $T_a = 600$–960 °C is sustained by the emergence of local zones enriched with interstitial oxygen. As the anneal time is increased, these zones decrease in size, and the local oxygen concentration makes a transition to the SiO_2 phase. Hydrostatic pressure applied in the nucleation stage leads to the formation of finer precipitates and accelerates the transition to the SiO_2 phase. © *1997 American Institute of Physics.* [S1063-7826(97)03008-1]

The existence of a so-called precipitate delay time is a well-known phenomenon[1] in the formation of oxygen precipitates, i.e., the emergence of an oxygen precipitate as an inclusion of the SiO_2 phase in silicon is preceded by a nucleation stage. It is difficult to study the nucleation stage experimentally, because methodological errors or inadequate sensitivity (or both at once) make virtually all the customary procedures for the investigation of oxygen precipitates incapable of yielding information about this stage. At present, therefore, only theoretical descriptions of the nucleation stage exist for the most part, where both homogeneous[2–4] and heterogeneous[5–7] mechanisms are discussed. Oxygen precipitate nuclei are usually interpreted to be local clusters of oxygen atoms which include the SiO_2 phase and those which do not, depending on the model concepts (see, e.g., Ref. 1). The basic parameters used in theories describing the nucleation of oxygen precipitates are the degree of supersaturation of the solid solution of oxygen in silicon, the critical nuclear radius r_c that must be attained for further growth of the precipitate, and the time required for nuclei to form. These parameters differ strikingly from one another as obtained in different theories. For example, according to the model in Ref. 8, $r_c = 1$ nm, whereas data in Ref. 9 indicate that the minimum gauge of size is the volume of one SiO_2 molecule. In previously published papers it is assumed that the oxygen atoms are uniformly distributed throughout the solid solution and that local concentration fluctuations fit a normal distribution. The acquisition of experimental data for the nucleation stage could provide a basis of preference for one theoretical development or another and shed light on the process of nucleation of oxygen precipitates.

A technique has been proposed[10] for investigating the nature of the distribution of oxygen atoms in the neighborhoods of oxygen precipitates; it stipulates the preliminary formation of electrically active complexes involving an interstitial oxygen atom (A center), whereupon electrical measurements can be made, in particular, by means of deep-level transient spectroscopy (DLTS). This approach affords the possibility of determining the parameters of local clusters of deep-level centers.[11,12]

The objective of the present study is to investigate the initial stage of formation of oxygen precipitates and to elucidate the physical mechanisms responsible for the process.

EXPERIMENTAL PROCEDURE

The basic material was *n*-type silicon grown by the Czochralski method with a density of charge carriers $(7–15)\times10^{14}$ cm^{-3}. The oxygen concentration in the material was determined by infrared (IR) spectroscopy and was equal to $N_O = (6–17)\times10^{17}$ cm^{-3}. Oxygen precipitate nuclei were formed during long-term heat treatments at 600–900 °C (see Table I). The tool used to influence the oxygen precipitation processes was hydrostatic pressure, which had a maximum value of 1.0 GPa. The heat-treated crystals were irradiated with electrons having an energy of 2.5 MeV at a flux of 8×10^{14} cm^{-2}. The principal energy-active defects for the irradiated samples were A centers (vacancy-oxygen complexes) with the $E_c - 0.18$ eV level in the band gap. DLTS was used to investigate the uniformity of the distribution of the introduced A centers. The measurements were performed at a frequency of 10 MHz. The parameters of the time window t_1 and t_2 were varied in the intervals $(0.1–2.2)\times10^{-3}$ s and $(0.11–2.2)\times10^{-2}$ s, respectively, in such a way as to maintain a constant ratio t_1/t_2. The duration of the filling pulse was $\tau = 2\times10^{-4}$ s. The dependence of the concentration of A centers on the measurement temperature was extracted from a series of DLTS curves recorded for various time windows.

It has been shown[10–12] that the profile of the concentration of A centers N_a as a function of the temperature T can be used to draw a conclusion as to the presence of local clusters of A centers and, hence, interstitial oxygen in the crystal. The parameters of the oxygen clusters were calculated from the plot of $N_a(T)$ (Fig. 1), viz.: 1) the characteristic space scale of the clusters R; 2) the total oxygen concentration in a local cluster. Since the nature of the local

 1063-7826/97/080852-05$10.00

TABLE I. Oxygen concentration in untreated silicon and crystal heat-treatment regimes.

N_O, 10^{17} cm^{-3}	Heat-treatment regimes: temperature/time/pressure
6.5	600 °C/1h, 5 h, 10 h, 19 h, 96 h /10^{-4} GPa
	650 °C/10h/10^{-4}, 10^{-2}, 0.1, 0.6, 1.0 GPa
	600 °C/10h/10^{-4}, 1.0 GPa
	650 °C/96h/10^{-4} GPa
8	650 °C/96h+650 °C/5 h/10^{-4},10^{-2},1.0 GPa
	960 °C/5h/10^{-4}, 10^{-2}, 1.0 GPa
13	720 °C/8h
15	720 °C/8h
17	720 °C/8h

clusters of interstitial oxygen is unknown in the sense of whether they are the result of decomposition of the initial metastable oxygen agglomerates or of diffusion clustering at local lattice inhomogeneities, the choice of function is determined to within a numerical factor. As an initial approximation the distribution of oxygen atoms in a cluster was assumed to be spherically symmetric and described by a Gaussian function (with R as the parameter of the function), and the vacancy-oxygen interaction constant was assumed to be the same both in the host crystal and in the cluster of oxygen atoms. In addition, the dependence of the concentration of A centers on the duration of the filling pulse, whose amplitude was varied in the interval from 5×10^{-6} s to 1×10^{-3} s, was investigated experimentally. The concentration of already-formed oxygen precipitates was determined by the selective silicon-etching method. The initial concentration of dissolved interstitial oxygen in the crystals (N_O) was determined by IR spectrometry.

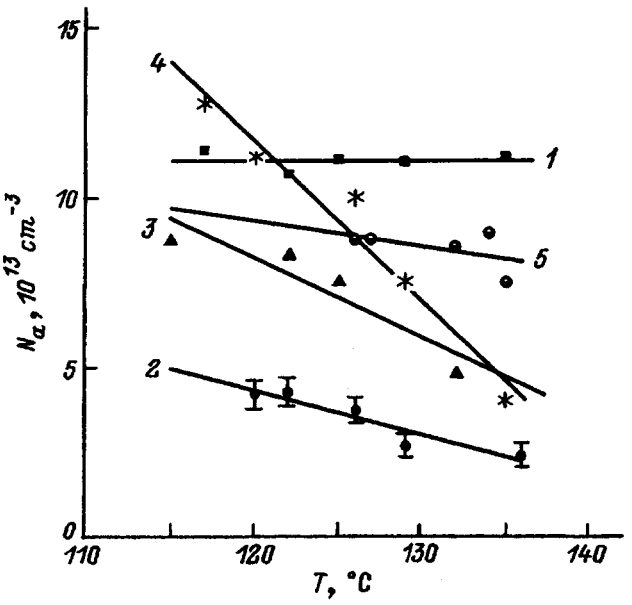

FIG. 1. Concentration of A centers versus temperature at which the corresponding DLTS is a peak for the untreated silicon (graph *1*) and for silicon annealed at 600 °C (graphs *2*–*5*). Anneal time: *2* — $t=1$ h; *3* — 5 h; *4* — 10 h; *5* — 19 h.

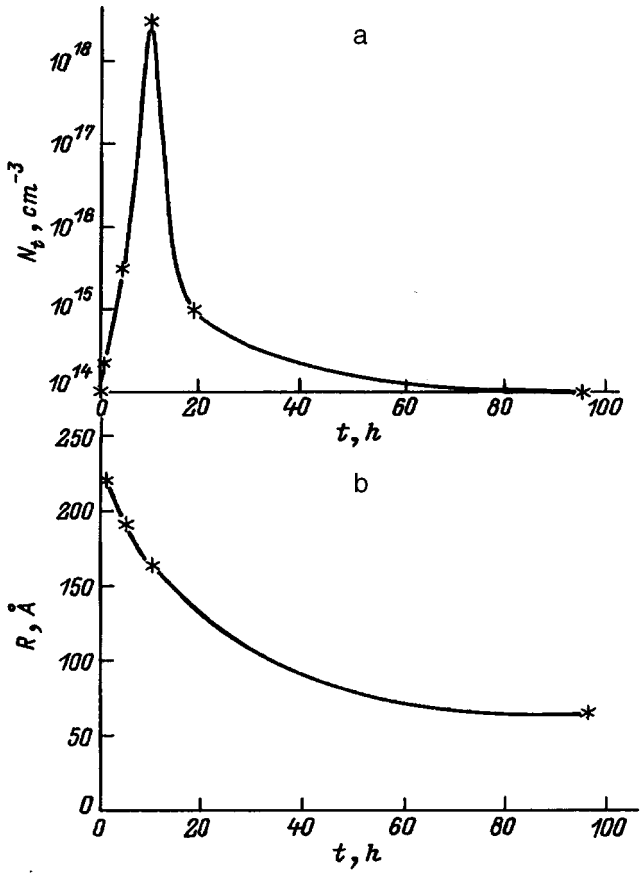

FIG. 2. Total concentration of A centers in a cluster N_t (a) and of the characteristic cluster radius dR (b) in the crystal versus anneal time t at 600 °C.

EXPERIMENTAL RESULTS

The investigations have shown that the amplitude of the DLTS peak associated with an A center does not depend on the temperature in the untreated material. It becomes temperature-dependent after only a 1-h anneal at $T_a=600$ °C. Consequently, interstitial oxygen is uniformly distributed in the untreated material, and local oxygen-enriched zones form in the material after prolonged anneals at $T_a=600$ °C. Figure 2 shows the calculated values of the total concentration of A centers in local clusters (N_t) (Fig. 2a) and the characteristic radius (R) of those clusters (Fig. 2b) as functions of the duration of heat treatment t. The ratio of N_t to the measured concentration of A centers N_a in the untreated material ($N_a=1\times10^{14}$ cm^{-3}) characterizes the factor by which the oxygen concentration in the cluster exceeds the average oxygen concentration in the host crystal. Oxygen atoms involved in the composition of the SiO_2 phase do not participate in the formation of A centers and therefore disappear from the field of view of the given method of investigation. The dependence of the concentration of A centers in local clusters on the anneal time exhibits a nonmonotonic behavior (Fig. 2a): It increases in the initial interval, then at anneal times greater than 10 h a decrease in the concentration in the clusters is observed, and after annealing for 96 h it essentially attains the average value throughout the crystal. The concentration of newly formed local clusters,

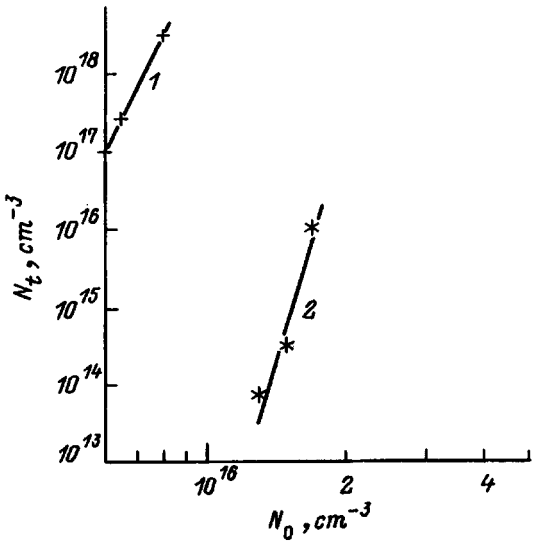

FIG. 3. Total concentration of A centers in a cluster N_t versus oxygen content N_O in the crystal for two anneal regimes. *1* — 600 °C, 10 h; *2* — 720 °C, 8 h.

which is equal to the concentration of oxygen precipitates observed at $T_a = 600$ °C ($\sim 10^{12}$ cm^{-3}), is used to calculate R. The characteristic radius of oxygen precipitates at the experimental temperature[1] is used for the value of R at large anneal times ($t = 96$ h. Figure 3 shows N_t as a function of the initial oxygen concentration N_O in the crystal for various anneal regimes. The value of N_t increases as the oxygen concentration is increased and decreases as the anneal temperature is increased.

Figure 4 illustrates the influence of the hydrostatic pressure P on the process of formation of oxygen agglomerates. The variation of N_t as the pressure is increased during various heat treatments (Fig. 4a) and the variation of the concentration of already-formed oxygen precipitates N_{Op} at $T_a = 960$ °C (Fig. 4b), determined by selective etching, indicates that the influence of hydrostatic pressure is quite strong, beginning at $P = 10^{-2}$ GPa. According to selective etching data, the etch pits decrease abruptly in size at pressures $P \geqslant 10^{-2}$ GPa. The precipitates formed at lower temperatures in this case are not exposed by selective etching.

A 96-h anneal at 600 °C ultimately leads, on the whole, to the formation of precipitates in the form of inclusions of the SiO_2 phase surrounded by an oxygen-depleted zone (Fig. 1). The results of additional anneals of crystals containing previously introduced precipitates at the same temperature but different pressures are shown in Fig. 5. We see that the application of a pressure ~ 1.0 GPa increase N_t, i.e., the application of pressure once again produces local oxygen-enriched zones.

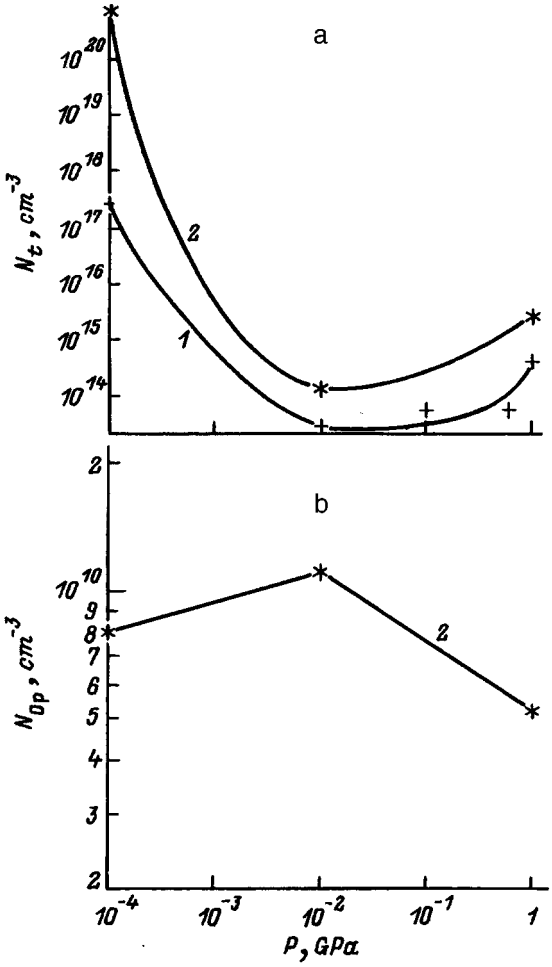

FIG. 4. Total concentration of A centers in a cluster N_t (a) and density of observable oxygen precipitates N_{Op} (b) a: *1* — $N_O = 6.5 \times 10^{17}$ cm^{-3}, $T_a = 650$ °C, $t = 10$ h; *2* — $N_O = 8 \times 10^{17}$ cm^{-3}, $T_a = 960$ °C, $t = 5$ h.

DISCUSSION

One of the main experimental results obtained in the study is the observation of local clusters of interstitial oxygen atoms after several hours of annealing. These clusters become increasingly dense as the anneal time is increased, the quantity of oxygen captured by them increasing as their sizes decrease. The decrease in N_t for $t > 10$ h is probably attributable to the onset of formation of the SiO_2 phase, since this anneal time corresponds to the initiation time of oxygen precipitates (the delay time is 10–15 h at 600 °C). The results imply that the SiO_2 phase appears when a certain critical oxygen concentration is reached in the cluster region.

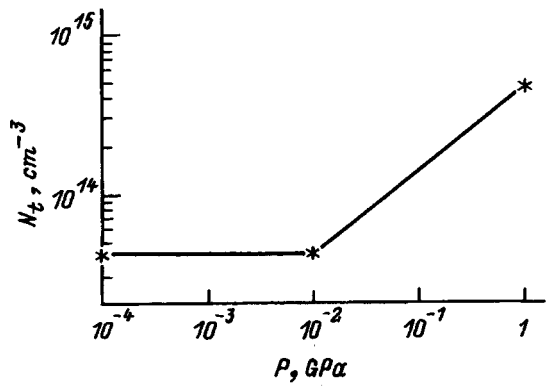

FIG. 5. Total concentration of A centers in a cluster N_t versus applied hydrostatic pressure P during an additional 5-h anneal, at the same temperature, of oxygen precipitates formed at 650 °C after 96 h.

We need to call attention to the fact that the relative concentration of oxygen in the cluster N_t, evaluated at $t=10$ h, like certain values of N_t for other anneal regimes and a different oxygen content in silicon (Figs. 2 and 3), is too high. This excess was not observed in an investigation of the processes of decomposition of previously formed precipitates by a similar method.[10] The cause of the excessive values of N_t is more likely attributable to a discrepancy between the true oxygen distribution in the cluster and the given modeling of the oxygen precipitate nucleus by a spherical object. Judging from the data, the true oxygen distribution is characterized by the substantially greater relative contribution of the surface in comparison with the volume. Moreover, after 1 h at $T_a=600$ °C, given the usual diffusion coefficient, an oxygen atom is displaced by ~ 70 Å when the average atomic spacing is ~ 100 Å. Even if we assume an accelerated diffusion of oxygen (usually acceleration by a factor of 2 or 3 is considered[13]), the probability of a relatively large number of oxygen atoms clustering together in a local zone is low. These contradictions can be resolved by assuming that the oxygen precipitate nucleus comprises a fairly loosely consolidated formation, for example, branched oxygen chains. The formation of such chains requires far greater displacements of the oxygen atoms. Fraundorf *et al.*[14] also postulate the existence at 600 °C of metastable nuclei, which are no longer SiO_2 phase and which have a high surface-to-volume ratio.

Further indirect evidence in support of the stated hypothesis is contained in data on the existence of a fine structure of oxygen precipitates,[15] which, being ''disk-shaped'' on the whole with a characteristic diameter ~ 2000 Å (formation regime at 650 °C and 216 h), consists of very small spherical precipitates of diameter ~ 20 Å. But if the oxygen atoms (and the A centers following them) form various more or less complex chains, this process should be manifested in the emergence of a logarithmic dependence of the fraction of charged A centers N_a on the duration of the filling pulse τ in DLTS measurements. In the case of a spherical cluster such a dependence occurs only for clusters of very large diameter (>500 Å for the material used here). Measurements have shown that such a dependence $N_a(\tau)$ is indeed observed (Fig. 6). The value of N_t and the average distance between neighboring A centers r_a have been estimated (by analogy with Refs. 16 and 17) from the data in Fig. 6 on the assumption that the oxygen precipitate nuclei are in the form of an elementary chain of oxygen atoms . These quantities are equal to (respectively) 5×10^{14} cm^{-3} and 12 Å after a 5-h anneal and are equal to 5.3×10^{16} cm^{-3} and 4 Å after a 10-h anneal. The actual structure of the oxygen precipitate nucleus is more likely a certain configuration intermediate between a chain and a spherical object. Consequently, the reported numerical characteristics of the oxygen precipitates represent upper (spherical approximation) and lower (chain approximation) bounds in relation to the true characteristics of the oxygen precipitates.

It follows from the selective etching data that the application of hydrostatic pressure leads to the formation of finer oxygen precipitates. The abrupt decrease in N_t (or, more precisely, the loss of the temperature dependence of the concentration of A centers) already at $P\approx 10^{-2}$ GPa indicates that pressure stimulates transition to the SiO_2 phase, and a 10-h heat treatment at $T_a=600$ °C at $P\geqslant 10^{-2}$ GPa is enough to terminate the transition $\langle$clustering of oxygen atoms$\rangle\rightarrow SiO_2$ phase. However, at the maximum pressure of 1.0 GPa there is a certain increase in N_t with a simultaneous reduction in the density of observed etch pits. This effect can be identified with the fact the dimensions of the newly formed oxygen precipitates have become even smaller, so that some of them are no longer observable by selective etching, and there has possibly been a shift toward the stabilization of such clusters, in which the necessary oxygen concentration for transition to the SiO_2 phase has not yet been attained. An analogous situation is encountered in the annealing of already-formed oxygen precipitates (Fig. 4).

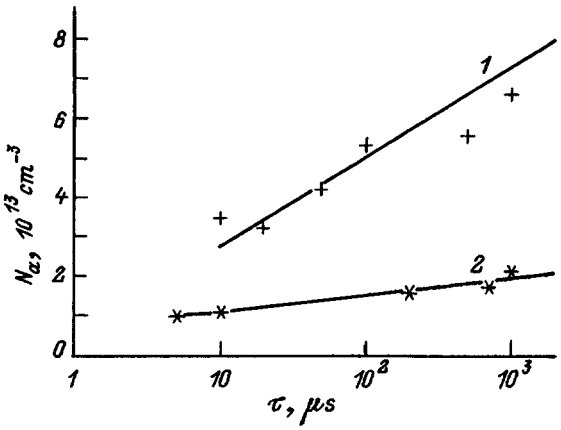

FIG. 6. Concentration of A centers in a crystal annealed at 600 °C for 10 h (graph *1*) and bombarded by electrons at a flux of 8×10^{14} cm^{-2} (graph *2*) versus duration of the filling pulse.

CONCLUSIONS

The results discussed in the article show that the formation of oxygen precipitates passes through a stage of formation of interstitial oxygen clusters, most likely with a branched-chain structure typical of large surface-to-volume ratio. Oxygen accumulates in these local regions with the passage of time. The SiO_2 phase most likely begins to form when a certain critical oxygen concentration is reached. Hydrostatic pressure applied in the nucleation stage of oxygen precipitates also results in the formation of finer oxygen precipitates.

This work has received support from the Russian Fund for Fundamental Research, Grant No. 95-02-05082-a, and from the Polish Committee for Scientific Research, Grant No. 8T11B04809.

[1] A. Borghesi, B. Pivac, A. Sassella, and A. Stella, J. Appl. Phys. **77**, 4169 (1995).
[2] J. Vanhellemont and C. Claeys, J. Appl. Phys. **71**, 1073 (1992).
[3] S. W. Hu, Mater. Res. Soc. Symp. Proc. **59**, 249 (1986).
[4] N. Inoue, K. Wada, and J. Osaka, J. Cryst. Growth **84**, 21 (1987).
[5] G. S. Oehrlein, J. L. Lindstrom, and J. M. Corbett, Appl. Phys. Lett. **40**, 241 (1982).
[6] A. J. R. de Kock and W. M. Van de Wijgert, Appl. Phys. Lett. **38**, 888 (1981).
[7] T. Y. Tan and C. Y. Kung, J. Appl. Phys. **59**, 917 (1986).

[8] *Defect Control in Semiconductors: Proceedings of the International Conference on the Science and Technology of Defect Control in Semiconductors*, Tokyo, 1989, K. Sumino (Ed.), North-Holland, Amsterdam-New York (1990), p. 239.
[9] H. Harada, T. Abe, and J. Chikawa, in *Semiconductor Silicon*, H. R. Huff, T. Abe, and B. O. Kolsen (Eds.), Electrochem. Soc., Pennington, N.Y. (1986), p. 76.
[10] I. V. Antonova, A. Misiuk, V. P. Popov, S. S. Shaimeev, and L. I. Fedina, Physica B **225**, 251 (1996).
[11] I. V. Antonova, A. V. Vasil'ev, V. I. Panov, and S. S. Shaĭmeev, Fiz. Tekh. Poluprovodn. **22**, 998 (1988) [Sov. Phys. Semicond. **22**, 630 (1988)].
[12] I. V. Antonova and S. S. Shaĭmeev, Fiz. Tekh. Poluprovodn. **25**, 847 (1991) [Sov. Phys. Semicond. **25**, 513 (1991)].
[13] S. A. McQuaid, M. J. Binns, C. A. Londos, J. H. Tucker, A. R. Brown, and R. C. Newman, J. Appl. Phys. **77**, 1427 (1995).
[14] P. Fraundorf, G. K. Fraundorf, and R. A. Craven, in *VLSI Science and Technology 1985*, W. M. Bullis and S. Broydo (Eds.), Electrochem. Soc., Pennington, N.Y. (1985), p. 436.
[15] R. Bouchard, J. R. Schneider, S. Gupta, S. Messolaras, R. J. Stewart, H. Nadasawa, and W. Zulehner, J. Appl. Phys. **77**, 553 (1995).
[16] P. Omling, E. R. Weber, Z. Montelius, H. Alexander, and J. Michel, Phys. Rev. B **32**, 6571 (1985).
[17] V. V. Kveder, Yu. A. Osipyan, W. Schroter, and G. Zoth, Phys. Status Solidi A **72**, 701 (1982).

Translated by James S. Wood

Transient photoelectric effect in pure, high-resistivity, highly biased metal-semiconductor and metal-insulator-semiconductor structures

B. I. Reznikov

A. F. Ioffe Physicotechnical Institute, Russian Academy of Sciences, 194021 St. Petersburg, Russia
(Submitted December 26, 1996; accepted for publication February 10, 1997)
Fiz. Tekh. Poluprovodn. **31**, 1003–1010 (August 1997)

The relaxation dynamics of the electric field and the current during the illumination of high-resistivity, slightly doped (essentially pure), highly biased, symmetrical metal-semiconductor and metal-insulator-semiconductor structures with monochromatic light in the fundamental band is investigated. The system of transport equations is solved in the drift-diffusion approximation, and the Poisson equation is solved. The emission and surface recombination of carriers are taken into account at the semiconductor boundaries. It is shown that when illumination is turned on (off), the field in the structure relaxes monotonically to a steady-state distribution. The field and current rise times at the start of illumination are approximately equal to the drift time for holes T_{dr} calculated from the mean field $E_e = V/d$ and does not depend on the light intensity I_i, the absorption coefficient, or the interface tunneling transmissivities $T_{n,p}$. The current and field decay times at the cessation of illumination increase as I_i is increased and as $T_{n,p}$ decreases, but are always of the same order of magnitude as t_{dr}. In the presence of strong absorption and at an intensity higher than the intensity scale characterizing the region of weak field shielding, the time dependence of the total current is nonmonotonic. When surface traps are filled, carriers begin to accumulate near the electrodes, causing the field to undergo an abrupt change near the anode at sufficiently high intensities I_i and low transmissivities $T_{n,p}$. © *1997 American Institute of Physics.* [S1063-7826(97)03208-0]

1. INTRODUCTION

Metal-semiconductor-metal (MSM) structures utilizing high-resistivity, wide-gap, compensated crystals (e.g., CdTe, HgI_2, and C) have a variety of applications. In particular, they form the elemental basis of radiation (light, x-ray, γ-ray) detectors[1] and light-controlled optoelectronic devices designed for fiber-optic communication lines, information processing systems, and systems for the recording of optical image signals.[2] The operation of these devices is based on the variation of the electric field distribution when the structure is illuminated. Theoretical and applied considerations have stimulated experimental work on the transient photoelectric effect and relaxation processes in high-resistivity (semi-insulating) CdTe crystals and have shown that the light-stimulated variation of the field in a crystal can be attributed to the space charge of free photogenerated carriers.[3] Theoretical studies for pure crystals[4–7] have refined the quantitative laws of shielding against an external field. The way that this phenomenon is related to the free-carrier space charge distinguishes it fundamentally from charge-exchange processes between two systems of discrete levels (populated donors and empty traps). The latter processes have been investigated in connection with the application of sillenite ($Bi_{12}SiO_{20}$ and $Bi_{12}GeO_{20}$) crystals as an electrooptical medium for writing holograms and information in space-time light modulators[8] and in connection with the experimental observation of an alternating oscillating space-charge distribution in these crystals.[9] The results of theoretical studies of electric field relaxation in a crystal containing deep-level impurities and subjected to stress and illumination in impurity-band light are given in Refs. 9–12. This work is based on a drift monopolar model with simplified boundary conditions. Several dozen papers have been published on this topic and are surveyed in Ref. 12.

The basic laws of the steady-state photoelectric effect in pure, high-resistivity crystals are embodied in three principles.[4]

1. The distribution of the field in the high-resistivity structure depends on the ratio between the illumination intensity I_i and the characteristic scale $I_* = (8/9) j_* / e$ (where $j_* = e\mu_p V^2/4\pi d^3$ is the space-charge-limited current, and d is the width of the structure).

2. At low intensities $I_i \ll I_*$ the values of the fields around the electrodes E_0 and E_d differ very little from the mean field $E_e = V/d$. The boundary values of the field and the current depend linearly on the intensity, and the distribution $E(x)$ is linear.

3. As the field at the illuminated surface increases, E_0 decreases and can become much weaker than E_e. The field E_d around the dark electrode increases. At average intensities $I_i \geqslant I_*$ the field $E_0 \ll E_e$, the field $E_d = (3/2)E_e$, the current is close to j_*, and the distribution $E(x)$ obeys a square-root law.

The major importance of the speed and response time of devices mandates the timeliness of studying relaxation processes in pure, high-resistivity structures. Numerical simulation must be used, because experiments are limited in both spatial and temporal resolution with respect to electric fields. The identification and investigation of the basic ''pure'' structure model stems from the need to separate phenomena inherent in high-resistivity crystals from the influence of deep impurity levels. The presence of the latter, even in minute quantities, exerts a significant influence on the dy-

namics and characteristics of the photoelectric effect in high-resistivity structures.[3]

By far most of the papers published to date on the transient characteristics of photodiodes have either been confined to special cases amenable to analytical solution or have solved special problems, usually with the aid of major simplifications. One of the first studies to be concerned with the smearing of a step pulse of electrons in a crystal containing traps[13] embraced all the basic features of the drift monopolar model subsequently used for the analysis in Refs. 9–11. In later studies, for example, in the paper of Ref. 14 allowance has been made for volume diffusion, surface recombination, and charge trapped by surface levels. In particular, the influence of the intensity of the incident radiation, the optical thickness of the layer, and volume recombination on the field distribution has been analyzed for the dimensionless system of transport equations, which contains twelve parameters. Photoelectric processes in a silicon diode at a high excitation level have been investigated[15] on the basis of a complete formulation of the drift-diffusion approximation. The closest to the present study is the work of Iverson and Smith,[16] who have investigated field and current relaxation in a structure containing impurity levels when the incident light is turned on and off. However, their investigation deals with the case of weak light absorption in the crystal and ohmic-contact boundary conditions, which correspond to an infinite recombination rate.

The objective of the present study is to give a detailed description of field and current relaxation in pure, high-resistivity crystals and to analyze the influence of the governing parameters on the dynamics of transient processes.

2. STATEMENT OF THE PROBLEM

2.1. We consider a highly biased, high-resistivity metal-insulator-semiconductor (MIS) structure $0 \leqslant x \leqslant d$, which has an equilibrium hole density p_* in its interior and is illuminated by monochromatic light of wavelength in the fundamental absorption region ($\hbar\nu > E_g$) through a semitransparent anode $x=0$. A voltage V much higher than the contact potential between the semiconductor and the metal is applied to the structure. For a structure containing deep impurity levels, in general, the distributions of the densities of electrons $n(x)$ and holes $p(x)$ and the electric field $E(x)$ are described by a system comprising the equations of continuity and the Poisson equation

$$\frac{\partial n}{\partial t}+\frac{\partial q_n}{\partial x}=G-R_n, \tag{1}$$

$$\frac{\partial p}{\partial t}+\frac{\partial q_p}{\partial x}=G-R_p, \tag{2}$$

$$\frac{\partial E}{\partial x}=\frac{4\pi e}{\varepsilon}[p-p_*-n+n_*-N_t(f-f_*)]. \tag{3}$$

In the drift-diffusion approximation the carrier fluxes q_n and q_p have the standard form

$$q_n=-D_n\frac{\partial n}{\partial x}-\mu_n E n, \tag{4}$$

$$q_p=-D_p\frac{\partial p}{\partial x}+\mu_p E p. \tag{5}$$

The rate of production of electrons and holes by external radiation is

$$G=\alpha I_i \exp(-\alpha x) \tag{6}$$

(I_i is the intensity of the light entering the sample, and α is the light absorption coefficient). We consider the general case of a high-resistivity, compensated semiconductor containing, in addition to shallow donors and acceptors, a single impurity level that obeys Shockley–Read statistics. Recombination processes of the band-to-band type are ignored, and the expressions for the heat generation rate-recombination R_n and R_p are written with allowance for the trapping of carriers by the deep impurity level and their emission into the corresponding band of the semiconductor:[17]

$$R_n=\alpha_n N_t[n(1-f)-n_1 f], \tag{7}$$

$$R_p=\alpha_p N_t[pf-p_1(1-f)]. \tag{8}$$

Here $\alpha_{n,p}=\langle\sigma_{n,p}v_{n,p}\rangle$ are the velocity-averaged capture coefficients at the impurity level ($v_{n,p}$ and $\sigma_{n,p}$ are the thermal velocities of electrons and holes and their impurity capture cross sections), and $f=n^-/N_t$ is the filling factor of the deep impurity level, which is equal to the ratio of the negative charge density n^- to the density of impurity levels N_t. The quantities n_1 and p_1, which depend on the energy of the impurity level $\varepsilon_t=E_t-E_c$, are given by the expressions $n_1=N_c\exp(-\varepsilon_t/kT)$ and $p_1=N_v\exp[-(E_g-\varepsilon_t)/kT]$. It is evident from Eqs. (1)–(3) and the definitions (7) and (8) that the deep impurity levels determine the recombination rate and the bound charge. The degree of filling of the impurity in equilibrium is determined from the condition $R_p=0$ and is equal to $f_*=p_1(p_1+p_*)$.

In the transient (time-dependent) case the variation of the bound charge density is proportional to the difference between the fluxes R_n and R_p:

$$N_t\frac{\partial f}{\partial t}=R_n-R_p=N_t\frac{f_{st}-f}{\tau}, \tag{9}$$

where

$$f_{st}=\frac{\alpha_n n+\alpha_p p_1}{\alpha_n(n+n_1)+\alpha_p(p+p_1)},$$

$$\tau^{-1}=\alpha_n(n+n_1)+\alpha_p(p+p_1). \tag{10}$$

The emission of carriers and their recombination through a single surface level are taken into account at the semiconductor-metal interface by an approach similar to that in Ref. 18:

$$q_n(0)=-V_{n0}^T(n_0-n_0^{eq})-q_{sn}(0), \tag{11}$$

$$q_p(0)=-V_{p0}^T(p_0-p_0^{eq})-q_{sp}(0), \tag{12}$$

$$q_n(d)=V_{nd}^T(n_d-n_d^{eq})+q_{sn}(d), \tag{13}$$

$$q_p(d)=V_{pd}^T(p_d-p_d^{eq})+q_{sp}(d). \tag{14}$$

Here n^{eq} and p^{eq} are the equilibrium densities of electrons and holes at the interfaces, $V_{n,p}^T=V_{n,p}T_{n,p}$ are the rates of

carrier exchange across the interface, which are proportional to the thermionic emission rates into the metal $V_{n,p}=(1/4)v_{n,p}$ and the interface tunneling transmissivities (tunneling probabilities) $T_{n,p}$. The latter take into account the decrease in the carrier exchange rates across the interface due to the presence of the insulating layers and depend exponentially on a function combining the thickness of the insulating layer, the height of the tunneling barrier, the voltage drop across the layer, and other quantities.[19] In lieu of reliable information on these quantities, the dependence of $T_{n,p}$ on the film characteristics is not specified in detail, and the tunneling transmissivity is used as an input parameter.

The recombination fluxes on the surface are proportional to the surface recombination rates at the interface $s_{n,p}=\langle \alpha_{n,p}N_s\rangle$:

$$q_{sn}=s_n[n(1-f_s)-n_{1s}f_s], \tag{15}$$

$$q_{sp}=s_p[pf_s-p_{1s}(1-f_s)], \tag{16}$$

where the variation of the degree of filling of the impurity levels on the surface is proportional to the difference in the recombination fluxes:

$$N_s\frac{\partial f_s}{\partial t}=q_{sn}-q_{sp}. \tag{17}$$

The external voltage source imposes the following condition on the field distribution in the semiconductor:

$$\int_0^d E(x)dx=V. \tag{18}$$

Because the insulating film is not thick, and because of the surface charge density, the potential drop on the insulator and the surface-charge field are disregarded in Eq. (18).

2.2. The basic equations are written on a nonequilibrium numerical grid with tighter bunching of the mesh at the endpoints of the interval in the region of high gradients. An implicit time approximation of first-order accuracy is used. Finite-difference expressions of second-order accuracy for the carrier fluxes are written using relations proposed by Scharfetter and Gummel.[20] The nonlinear three-point system of difference equations is linearized and solved by a vector forward/backward (Gaussian-type) elimination scheme.[21] The nonlinearity of the problem is handled by Newton's method. The solution obtained on the preceding time layer is used as the initial approximation. The computational error and choice of time step are monitored from the invariance of the total current through the structure and the closeness of the numerical value of the total current calculated from the difference equations to its value obtained by integrating the equation

$$j=e(q_p-q_n)+\varepsilon/4\pi\partial E/\partial t$$

with respect to the width of the structure.

3. RESULTS FOR PURE STRUCTURES

3.1. We first investigate the relaxation dynamics of the field and the current when the illumination of the structure on a CdTe base is turned on and off. We adopt the following set of parameters for our basic model: $d=0.28$, $V=400$ volts, $p_*=10^8$ cm^{-3}, $s_n=s_p=10^6$ cm/s, $T_n=T_p=1$. The intensity does not depend on the time and has the value $I_i=2\times10^{15}$ cm$^{-2}\cdot$s^{-1}. The light absorption coefficient is $\alpha=10^4$ cm^{-1}.

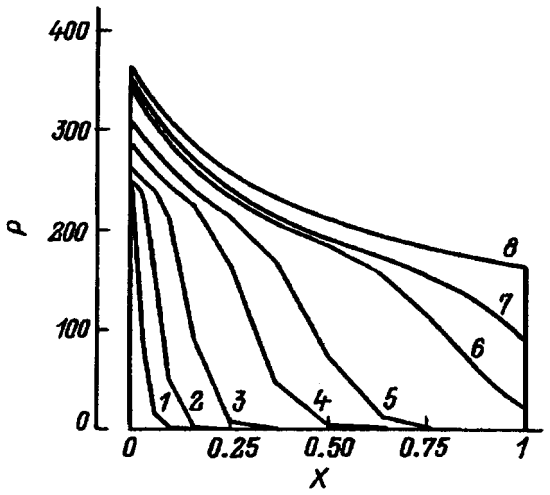

FIG. 1. Distribution of the hole density ($P=p/p_*$, $X=x/d$) in the structure for $I_i=2\times10^{15}$ cm$^{-2}\cdot$s^{-1}, $\alpha=10^4$ cm^{-1}. Elapsed time after light is turned on: *1*) $t=0.12$ μs; *2*) 0.3 μs; *3*) 0.61 μs; *4*) 1.22 μs; *5*) 1.82 μs; *6*) 3.04 μs; *7*) 3.65 μs; *8*) 9.12 μs.

The initial conditions include the steady-state distribution functions for *n*, *p*, and *E* in the dark case, obtained in the numerical solution of the system (1)–(3) for $\partial/\partial t=0$ and $I_i=0$. At $t=0$ the distributions of *n*, *p*, and *E* in the interior of the structure are almost uniform. Near the electrodes we have boundary conditions for electrons and holes, where their densities suffer a discontinuity, but for $T_n=T_p=1$ they do not differ much, either at the boundaries or in the interior, from the equilibrium values n^{eq} and p^{eq} at the boundaries of the crystal.

The qualitative pattern of the photoelectric effect is depicted as follows. When the illumination is turned on, electron-hole pairs are generated in a zone having a width of several absorption lengths ($\sim3\times10^{-4}$ cm$\ll d$). The exponential decay of the radiation intensity into the depth of the sample and the transport of carriers across the surface at thermal velocities instantly produces nonmonotonic, peaked distributions of the densities *n* and *p* around the illuminated anode. In the initial stage photogeneration causes the surface and maximum carrier densities to increase with time. The electric field separates them, making electrons and holes drift toward the electrodes of opposite sign. Figure 1 shows profiles of $P(X)=p/p_*$, $X=x/d$, from which it is apparent how the leading edge of the hole density distribution moves toward the cathode, so that a positive space-charge density wave propagates into the depth of the sample. The pattern of propagation is shown at times comparable with the hole drift time in a static field $t_{dr}=d/(\mu_pE_e)$, which is equal to 3.92 μs for the adopted values of the parameters. It is also evident from the figure that once the leading edge of the density distribution arrives at the surface, a diffusion boundary sheath is formed around the cathode, and the distribution $p(x)$ in the anode zone of the structure becomes weakly

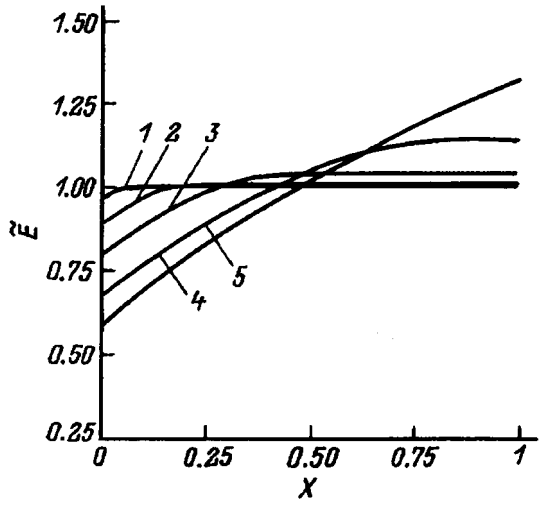

FIG. 2. Electric field distribution ($\widetilde{E}=E/E_e$, $E_e=V/d$) in the structure for $I_i=2\times10^{15}$ cm$^{-2}\cdot$s^{-1}, $\alpha=10^4$ cm^{-1}. Elapsed time after light is turned on: *1*) $t=0.18$ μs; *2*) 0.61 μs; *3*) 1.22 μs; *4*) 2.43 μs; *5*) 9.12 μs.

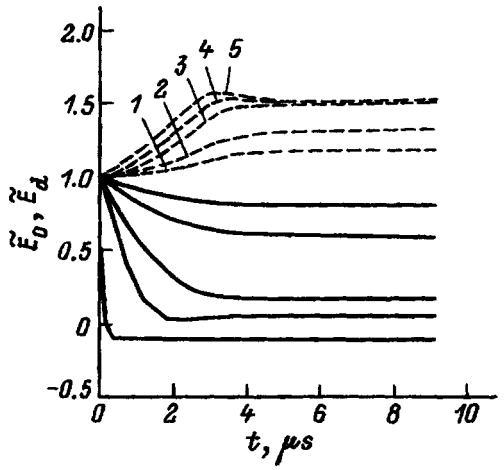

FIG. 3. Time dependence of the boundary values of the electric field $\widetilde{E}_0$ (solid curves) and $\widetilde{E}_d$ (dashed curves) for $\alpha=10^4$ cm^{-1}. Illumination intensity: *1*) $I_i=1\times10^{15}$ cm$^{-2}\cdot$s^{-1}; *2*) 2×10^{15} cm$^{-2}\cdot$s^{-1}; *3*) 5×10^{15} cm$^{-2}\cdot$s^{-1}; *4*) 10×10^{15} cm$^{-2}\cdot$s^{-1}; *5*) 100×10^{15} cm$^{-2}\cdot$s^{-1}.

time-dependent. Because of the thinness of the electrode sheaths, the hole distributions in them have the appearance of abrupt steps.

The time variation of the field distribution is shown in Fig. 2. It is evident that the distortion of the field distribution is associated with the arrival of the space-charge density wave and that the restructuring of the field in the cathode zone occurs later than processes in the vicinity of the anode. Since the potential difference on the structure is positive and the space-charge density in the sample interior is positive, the field decreases monotonically around the anode and increases monotonically around the cathode. The curvature of the field distribution is negative. The relaxation of the field is essentially terminated when the leading edge of the hole density distribution arrives at the surface. The field relaxation time is somewhat shorter than the relaxation time of the hole density distribution.

The time lag between processes in the anode and cathode zones of the structure is evident in Fig. 3, which shows the time variations of the boundary fields $\widetilde{E}_0=E_0/E_e$ and $\widetilde{E}_d=E_d/E_e$ for various radiation intensities. It is obvious from the figure that as the radiation intensity increases:

- the steady-state boundary values of the field around the anode are attained far more quickly;
- the time at which the steady state is attained decreases for the field $\widetilde{E}_0$ and is essentially constant for the field $\widetilde{E}_d$, whose time dependence becomes nonmonotonic;
- the steady-state value of the field around the anode decreases and, at sufficiently high intensities, becomes negative (inversion of the field[5]).

The radiation intensity also significantly influences the behavior of the total current as a function of time. It is evident from Fig. 4 that the rate of increase of j and the qualitative characteristics of the functions $j(t)$ differ for ''low'' ($I_i<5\times10^{15}$ cm$^{-2}\cdot$s^{-1}) and ''high'' ($I_i>5\times10^{15}$ cm$^{-2}\cdot$s^{-1}) intensities. In the first case the total current increases almost linearly with time, approaching the steady-state value from below. In the second case the total current passes through the steady-state value, approaching it from above. A kink in the $j(t)$ curve is noticeable at early times. The current relaxation time is practically the same in both cases, since it is determined by the time at which a steady-state field distribution is attained throughout the entire structure and is therefore close to the dark-field drift time of holes.

In the interpretation of the behavior of $j(t)$ it must be borne in mind that at times much shorter than t_{dr} the total current mainly comprises the displacement current, and the dynamics of its growth is governed by the variation of the field at the illuminated surface. The slowing of the growth of the total current at small times, manifested as a kink of the $j(t)$ curve, and the approximate equidistance of all the curves are attributable to the completion of formation of the small-field region in the anode part of the structure and a

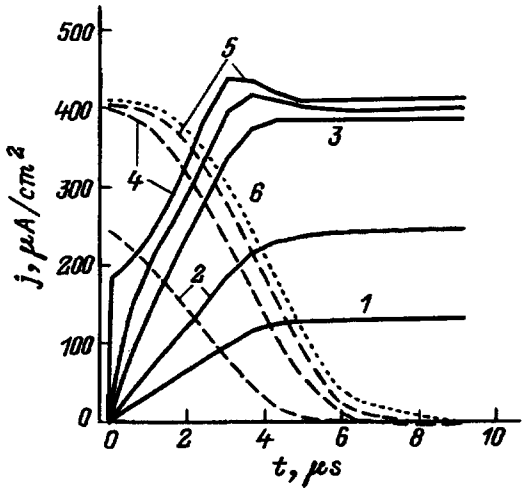

FIG. 4. Time dependence of the total current j when light is turned on (solid curves) and off (dashed curves), $\alpha=10^4$ cm^{-1}. Illumination intensity: *1*) $I_i=1\times10^{15}$ cm$^{-2}\cdot$s^{-1}; *2*) 2×10^{15} cm$^{-2}\cdot$s^{-1}; *3*) 5×10^{15} cm$^{-2}\cdot$s^{-1}; *4*) 10×10^{15} cm$^{-2}\cdot$s^{-1}; *5*) 100×10^{15} cm$^{-2}\cdot$s^{-1}. Curve *6* corresponds to $T_{n,p}=10^{-4}$ at $I_i=10^{16}$ cm$^{-2}\cdot$s^{-1}.

reduction in the relative contribution of the displacement current to the total current. We note that for intensities $I_i > I_*$ the steady-state value of the total current is close to the value j_*, which is equal to 370 μA/cm^2 in the given situation.

The prominences of the $j(t)$ curve near the steady-state value are associated with the sensitivity of the distribution $E(x)$ to the radiation intensity in high-resistivity structures and the substantial reduction of the field in and around the carrier-generating zone when I_i is much higher than the scale I_* characterizing the upper boundary of the linear region.[4]

In the given situation we have $I_* = 2 \times 10^{15}$ cm$^{-2} \cdot$ s^{-1}. In the linear case $I_i < I_*$ the field in the structure does not change very much, and the hole drift velocity in the photogeneration region does not depend on the time. As a result, the hole density in the interior increases monotonically with time (Fig. 1), as does the total current. In the nonlinear case, owing to the reduction of the field near the anode and its increase in the cathode zone, the incoming hole flux becomes smaller than the outgoing flux, while the hole density deep within the structure attains a maximum and begins to drop slightly. This behavior causes E_d and the total current do decrease very slightly.

We note that before the leading edge of the hole density distribution reaches the interface, the displacement current j_D comprises a sizable fraction of the total current. The conduction current varies substantially through the structure, where the difference $j - j_D$ is negative near the illuminated anode and is positive around the cathode. For this reason, the quasisteady-state approach based on the postulated identity of the total current and the drift component of the hole conduction current is invalid before the field distribution relaxes to the steady state ($t < t_{dr}$).

Upon cessation of photogeneration (dashed curves in Fig. 4) the electric field pulls carriers from the crystal. A hole-density wave of diminishing amplitude propagates from the anode to the cathode, and a positive space charge emanates from the structure. The field in the anode zone becomes more uniform and increases in strength. The field around the cathode decreases. The total current decays monotonically toward its thermal value. It is significant that, since the initial field distribution is nonuniform and since its degree of shielding depends strongly on the intensity, the characteristic time for the dark field to become established and for the current to decay is longer than the relaxation time after the removal of illumination and depends on the intensity. The asymmetry of the current–time curves at the activation and cessation of illumination is clearly evident in Fig. 4.

3.2. The transient process exhibits a somewhat different pattern when the absorption coefficient α is not too high, so that $\alpha d < 10$. In this case carriers are generated over a much broader range. Figure 5 shows the $P(X)$ profiles at various times for $I_i = 10^{16}$ cm$^{-2} \cdot$ s^{-1} and $\alpha = 10$ cm^{-1}. We see that the hole density in the interior of the structure increases as a result of volume photogeneration rather than drift flux as in the case $\alpha d \gg 1$ (Fig. 1). A diffusion layer is formed around the cathode immediately after the start of illumination. At intensities $I_i < I_*$, which correspond to a slight decrease in the field, the maximum of the hole density increases and

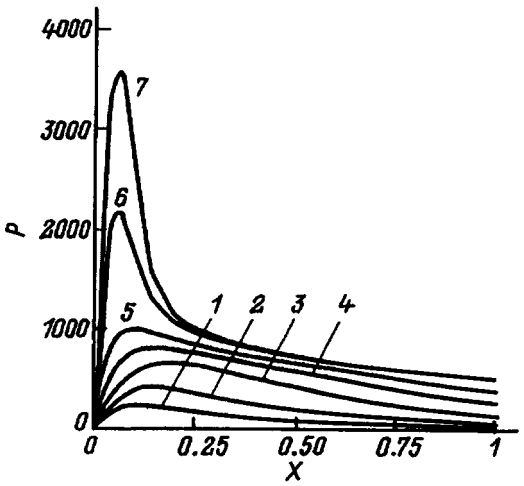

FIG. 5. Distribution of the hole density ($P = p/p_*$, $X = x/d$) in the structure for $I_i = 10^{16}$ cm$^{-2} \cdot$ s^{-1}, $\alpha = 10$ cm^{-1}. Elapsed time after light is turned on: *1*) $t = 0.3$ μs; *2*) 0.61 μs; *3*) 1.22 μs; *4*) 1.82 μs; *5*) 2.43 μs; *6*) 4.25 μs; *7*) 6.08 μs.

shifts toward the cathode, tending to its steady-state position. At intensities $I_i > I_*$, which correspond to an appreciable reduction in the field near the anode, the maximum of the hole density initially shifts toward the cathode but then, because of diffusion, moves toward the anode, the distribution $P(x)$ acquiring a sharper profile (Fig. 5). As the intensity increases, the diffusion effects intensify, and electrons penetrate the interior on account of the attenuation of the field. In the vicinity of the anode, after a time of the order of t_{dr} a negative space-charge region is formed, along with a quasineutral layer, whose width is much greater than that of the generation zone. The relaxation dynamics of the field distribution in the case $I_i > I_*$ is shown in Fig. 6. In contrast with the case of strong absorption (Fig. 2), the distribution $E(x)$ permeates the entire structure all at once, and the rates

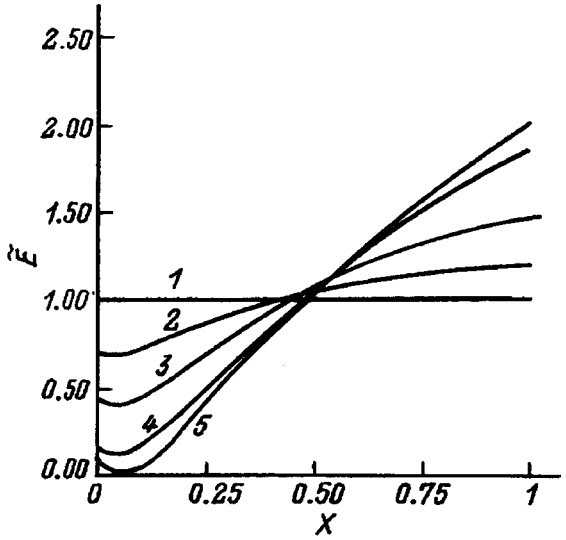

FIG. 6. Electric field distribution ($\tilde{E} = E/E_e$, $E_e = V/d$) in the structure for $I_i = 10^{16}$ cm$^{-2} \cdot$ s^{-1}, $\alpha = 10$ cm^{-1}. Elapsed time after light is turned on: *1*) $t = 0$; *2*) 0.61 μs; *3*) 1.22 μs; *4*) 2.43 μs; *5*) 6.08 μs.

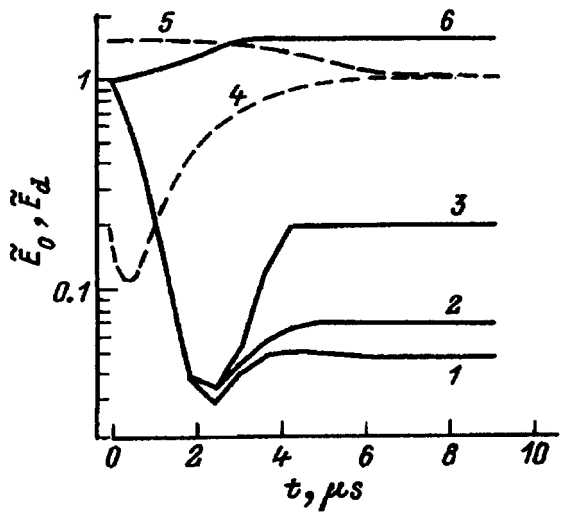

FIG. 7. Time dependence of the boundary values of the electric field $\widetilde{E}_0$ (curves *1–4*) and $\widetilde{E}_d$ (curves *5* and *6*) when illumination is turned on (solid curves *1–3* and *6*) and off (dashed curves *4* and *5*), $I_i=10^{16}$ cm$^{-2}\cdot$s^{-1}, $\alpha=10$ cm^{-1}. Interface tunneling transmissivities: *1*) $T_{n,p}=10^{-2}$; *2*) 10^{-3}; *3–5*) 10^{-4}; *6*) $1–10^{-4}$.

of change of the field boundary values $\widetilde{E}_0$ and $\widetilde{E}_d$ are approximately identical. The total current increases monotonically to its steady-state value even with strong shielding of the field around the illuminated anode.

The onset of the field minimum, which shifts slightly toward the cathode with passing time, and the presence of the strong shielding region deep in the interior are typical of the given case of moderate optical thicknesses and is not related to the presence of the space charge of the deep-level impurity. It is interesting that the $E(x)$ curves shown in Fig. 6 are qualitatively similar to the experimentally measured field distributions in $Bi_{12}GeO_{20}$ crystals for $\alpha d=9$ (Ref. 22).

3.3. Real metal-semiconductor structures have a thin insulating layer at the interface, and its presence significantly reduces the emission flux of carriers across the interface, making surface recombination the primary mechanism controlling the number of electrons in the vicinity of the anode. It is evident from relations (11) and (15) that the recombination flux q_{sn} on the surface is proportional to the recombination rate (surface-level capture coefficient) and the number of unfilled traps. The flux q_{sn} decreases as the traps fill up, and when the rate of emission of electrons across the interface falls below their drift velocity, a layer of enhanced negative charge density of electrons forms near the anode

A drop in the transmissivity below a certain limit, which depends on the illumination intensity and the surface recombination rate, makes the charge density so high that the field around the anode acquires a discontinuity commensurate with the magnitude of the field itself. Consequently, in the case of MISIM structures having a reduced tunneling transmissivity near the electrodes it is possible to encounter new phenomena associated with carrier accumulation. Figure 7 shows the time dependence of $\widetilde{E}_0$ and $\widetilde{E}_d$ for $\alpha=10^4$ cm^{-1} and various interface tunneling transmissivities. It is evident from the figure that when the interface tunneling transmissivity is lower than 10^{-3} (the carrier exchange rate has a value $V_n^T\approx10^4$ cm/s and is much lower than the electron drift velocities in the interior), accumulation effects become significant, and the near-anode field begins to increase. Hole accumulation also takes place near the cathode, but the positive charge density is not as great, and the field $\widetilde{E}_d$ does not increase. When illumination is turned on (curve *4* in Fig. 7), the surface field decreases at first as electrons move away, but then it begins to increase as a result of the leakage of positive charge from the system. Since carrier accumulation effects influence the field in a narrow layer of thickness $l_E=kT/eE_e$, this behavior does not affect the propagation of the hole-density wave in the interior or the relaxation time of the current to its steady-state value. The $\widetilde{E}_d(t)$ and $j(t)$ curves associated with the start of illumination scarcely differ from the case $T_{n,p}=1$. Upon cessation of illumination (curve *6* in Fig. 4), the relaxation time of the dark current increases somewhat but has the same order of magnitude as the hole drift time.

4. CONCLUSIONS AND DISCUSSION OF THE RESULTS

The results of simulation of the transient photoelectric effect in a pure, highly biased, high-resistivity crystal illuminated from the anode side by monochromatic light indicate the following general laws of the transient processes.

- When the illumination is turned on (off), the field varies monotonically at all points of the structure, relaxing to the steady-state distribution.
- The field and current relaxation times at the start of illumination are approximately equal to the drift time for holes, calculated from the mean field, and do not depend on the illumination intensity, the absorption coefficient, or the tunneling transmissivity of the interface.
- During the hole drift time the displacement current comprises a sizable fraction of the total current and differs sharply from the conduction current.
- The particular features of the time dependence of the total current are determined by the ratio between the illumination intensity and the characteristic scale I_* corresponding to the upper end of the range of weak shielding of the field around the illuminated anode. For $I_i>I_*$ in the case of strong absorption, $\alpha d\gg1$, the $\widetilde{E}_d(t)$ and $j(t)$ curves are nonmonotonic, and the total current tends to its steady-state value from above. In the case of volume photogeneration, $\alpha d\simeq1$, the total current increases monotonically to its steady-state value independently of the intensity.
- When the illumination is turned off, the current decreases monotonically to its steady-state value, and the relaxation time increases somewhat as the intensity and the tunneling transmissivity of the interface increase.
- In the presence of a reduced interface tunneling transmissivity and almost complete initial filling of the traps, carrier accumulation sets in near the electrodes, imparting a discontinuity to the field around the anode at sufficiently high illumination intensities and low transmissivities ($T_{n,p}\leqslant10^{-3}$ at $I_i\geqslant10^{16}$ cm$^{-2}\cdot$s^{-1}).

Let us compare the theoretical results obtained on the basis of the model of the photoelectric effect for a pure,

high-resistivity structure with the experimental data.[3] Several conclusions are fully consistent with the experimental results: The field varies monotonically when the illuminating light is turned on and off, the rate of change of the field near the boundaries of the structure increases as the intensity is increased, and the relaxation time of the field distribution does not depend on the interface tunneling transmissivity results. The monotonicity of the time variation of the field distribution attests to the weak influence of recombination and the capture by an impurity on the space charge in the experiment discussed here. This conclusion is further supported by the fact that the main variations of the field and the current take place in the first 5–10 μs, which is close to the value $(1–2)t_{dr}$. The fact that the field distribution and the time dependence of the total current do not depend on the tunneling transmissivity of the interfaces at the start of illumination indicates the weak influence of processes in the electrode sheaths and the boundary conditions for the densities of electrons and holes as long as these processes do not lead to new phenomena affecting conditions throughout the entire thickness of the structure.

On the other hand, the model of a pure crystal with strong absorption gives two fundamental differences from the experimental data. First, the measured steady-state field distributions have a positive curvature, whereas the calculated distributions have a negative curvature. Second, the experimentally recorded relaxation time at the start of illumination for structures with tunneling-thin layers is approximately 20 μs, which is several times greater than t_{dr}. Moreover, the relaxation time of the dark distribution in a structure with lowered tunneling transmissivity increases by roughly an order of magnitude.[3] In our opinion, these two differences indicate that the investigated samples have a deep-level impurity whose space charge is comparable with the space charge of free photocarriers and influences the shape of the electric field distribution and the time dependences. The inclusion of this charge and an analysis of the influence of recombination through deep impurity levels on the transient characteristic of high-resistivity structures will be the object of a special investigation.

[1] E. N. Arkad'eva, L. V. Maslova, O. A. Matveev, S. V. Prokof'ev, S. M. Ryvkin, and A. Kh. Khusainov, Dokl. Akad. Nauk SSSR **221**, 77 (1975) [Sov. Phys. Dokl. **20**, 211 (1975)].
[2] P. G. Kasherininov, A. V. Kichaev, Yu. N. Perepelitsin, Yu. O. Semenov, and I. D. Yaroshetskiĭ, Élektrosvyaz', No. 10, 37 (1990).
[3] P. G. Kasherininov, A. V. Kichaev, and A. A. Tomasov, Fiz. Tekh. Poluprovodn. **29**, 2092 (1995) [Semiconductors **29**, 1092 (1995)].
[4] P. G. Kasherininov, B. I. Reznikov, and G. V. Tsarenko, Fiz. Tekh. Poluprovodn. **26**, 1480 (1992) [Sov. Phys. Semicond. **26**, 832 (1992)].
[5] B. I. Reznikov and G. V. Tsarenkov, Fiz. Tekh. Poluprovodn. **27**, 1262 (1993) [Semiconductors **27**, 699 (1993)].
[6] B. I. Reznikov and G. V. Tsarenkov, Fiz. Tekh. Poluprovodn. **31**, 23 (1997) [Semiconductors **27**, 19 (1993)].
[7] B. I. Reznikov and G. V. Tsarenkov, in *Proceedings of the Fourth International Seminar on Simulation of Devices and Technologies*, CEFIM–University of Pretoria (1995), p. 58.
[8] M. P. Petrov, S. I. Stepanov, and A. V. Khomenko, *Photosensitive Electrooptical Media in Holography and Optical Information Processing* [in Russian], Nauka, Leningrad (1983).
[9] V. N. Astratov, A. V. Il'inskiĭ, and V. A. Kiselev, Fiz. Tverd. Tela (Leningrad) **26**, 2843 (1984) [Sov. Phys. Solid State **26**, 1720 (1984)].
[10] V. V. Bryksin, L. I. Korovin, and Y. K. Kuz'min, Fiz. Tverd. Tela (Leningrad) **28**, 2728 (1986) [Sov. Phys. Solid State **28**, 1528 (1986)].
[11] A. S. Furman, Fiz. Tekh. Poluprovodn. **22**, 2138 (1988) [Sov. Phys. Semicond. **22**, 1350 (1988)].
[12] V. N. Astratov and A. V. Il'inskiĭ, FTI Preprint No. 1091 [in Russian], A. F. Ioffe Physicotechnical Institute of the Academy of Sciences of the USSR, Leningrad (1986).
[13] A. I. Rudenko, Fiz. Tekh. Poluprovodn. **5**, 2383 (1971) [Sov. Phys. Semicond. **5**, 2097 (1971)].
[14] N. V. Klimova, Mikroélektronika **10**, 457 (1981).
[15] N. A. Kudryashov, S. S. Kucherenko, and Yu. I. Sytsyko, Mat. Model. **1**, 1 (1989).
[16] A. E. Iverson and D. L. Smith, IEEE Trans. Electron Devices **ED-34**, 2098 (1987).
[17] V. L. Bonch-Bruevich and S. G. Kalashnikov, *Physics of Semiconductors* [in Russian], Nauka, Moscow (1977)
[18] B. I. Reznikov and G. V. Tsarenkov, Fiz. Tekh. Poluprovodn. **25**, 1922 (1991) [Sov. Phys. Semicond. **25**, 1158 (1991)].
[19] J. G. Simmons and G. W. Taylor, Solid–State Electron. **29**, 287 (1986).
[20] D. L. Scharfetter and H. K. Gummel, IEEE Trans. Electron Devices **ED-16**, 64 (1969).
[21] A. A. Samarskiĭ, *Introduction to the Theory of Differencing Schemes* [in Russian], Nauka, Moscow (1971).
[22] I. T. Ovchinnikov and É. V. Yanshin, Pis'ma Zh. Tekh. Fiz. **8**, 355 (1982) [Sov. Tech. Phys. Lett. **8**, 153 (1982)].

Translated by James S. Wood

Injection currents in mixed-layer $Ga_{0.5}In_{1.5}S_3$ single crystals

I. M. Askerov and F. Yu. Asadov

Azerbaidzhan Structural Engineering University, 370073 Baku, Azerbaidzhan
(Submitted February 4, 1997; accepted for publication February 10, 1997)
Fiz. Tekh. Poluprovodn. **31**, 1011–1012 (August 1997)

Single crystals of $Ga_{0.5}In_{1.5}S_3$ are prepared by chemical transport reaction, and the current-voltage characteristics and temperature dependence of the electrical conductivity are investigated. It is shown that the current transmission mechanism in an In-$Ga_{0.5}In_{1.5}S_3$-In structure is associated with monopolar injection. © *1997 American Institute of Physics.* [S1063-7826(97)03308-5]

The crystal structures of layered materials based on solid solutions of the type $(Ga, In)_2S_3$ are of considerable interest in the physics of semiconductors.[1–8] The investigation of phase formation in the system Ga–In–S has resulted in the synthesis and x-ray structural analysis of a number of single-crystal phases of general composition $(Ga, In)_2S_3$ (Refs. 4–8). The configuration of the majority of the phases investigated in this system classifies them as layered structures. Of special interest in this series of structures are mixed-layer (interstratified) structures synthesized from electroneutral stacks having dissimilar internal structures and compositions.

The first representative of semiconductors with a mixed-layer structure is $Ga_{1.73}In_{2.94}S_7$ (Ref. 8) consisting of two-level and three-level stacks in the ratio 1:1. A second example of a semiconductor with a mixed-layer structure is $Ga_{0.5}In_{1.5}S_3$ (Ref. 9) consisting of analogous two-level and three-level stacks, but in the ratio 1:2.

The $Ga_{0.5}In_{1.5}S_3$ single crystals were prepared by chemical transport reaction. The orange-colored, as-grown, laminated crystals had perfect cohesion in the (001) plane. The improved crystallographic parameters had the values $a=3.814(2)$ Å, $c=100.04(3)$ Å, $U=1260.4(1)$ Å, space group $R3m$, $Z=11$, and $R=0.069$. The stacks of the $Ga_{0.5}In_{1.5}S_3$ crystal were joined through tetrahedral and octahedral interstack sites randomly occupied by Ga and In metal ions.

Here we give the results of an investigation of the current-voltage (I–V) characteristics and the temperature dependence of the electrical conductivity $\sigma(T)$ in these single crystals.

The single crystals had n-type conductivity with a resistivity of $5\times10^{10}\Omega\cdot$cm and a 237-eV band gap at $T=293$ K.

The following intervals are distinguished on the I-V characteristic of an In–$Ga_{0.5}In_{1.5}S_3$–In structure at various temperatures: a linear interval ($I\sim U$), a quadratic interval ($I\sim U^2$), and an interval in which the current rises abruptly ($I\sim U^n$, $n=3$–7). A sharp rise of the current in semiconductors is attributed to the filling and emptying of traps.[10] In the first case the relations $I\sim U^3$ and $U\sim L^2$ hold between the current, the voltage, and the interelectrode spacing L. In both cases the capture ratio $\theta=n_0/n_t\ll1$, where n_0 is the density of free carriers, and n_t is the density of trapped carriers injected from the electrode. When detrapping is induced by the electric field, the relations $I\sim U^3$ and $U\sim L$ are observed. It has been shown[10] that the following relations hold for structures fabricated with different interelectrode spacings ($L_1\neq L_2$) by the same technology in the trapping case:

$$\frac{U_f(L_1)}{U_f(L_2)}=\left(\frac{L_1}{L_2}\right)^2$$

and in the detrapping case:

$$\frac{U_E(L_1)}{U_E(L_2)}=\frac{L_1}{L_2}.$$

The second case prevails in our investigated structure and is shown in Fig. 1. According to the resulting data, we can conclude that the interval of the sharp current rise in our structure is associated with the emptying of filled traps by the electric field. In this case the depth and density of the traps are determined from the temperature dependence of the capture ratio $\theta(T)$. According to Refs. 9 and 10, the capture ratio is related to the depth and density of the traps by the equation

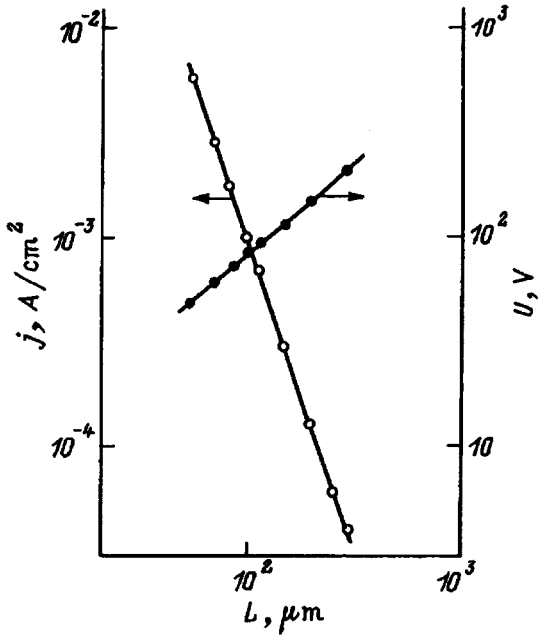

FIG. 1. Current density j (from the quadratic interval of the I–V characteristic and voltage U versus interelectrode spacing L.

 1063-7826/97/080864-02$10.00

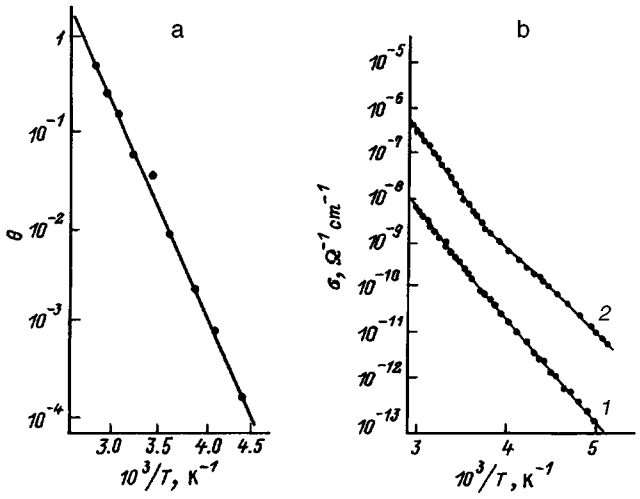

FIG. 2. Capture ratio θ (a) and electrical conductivity σ (b) versus temperature. *1*) Electric field $E=10^3$ V/cm; *2*) $E=10^4$ V/cm.

$$\theta=\frac{N_c}{gN_t}\exp\frac{E_t-E_c}{kT}.$$

Here N_c is the effective density of states in the conduction band, and g is the spin degeneracy factor ($g=2$). Figure 2a shows the temperature dependence of the capture ratio as a graph of $\log\theta-10^3/T$. The depth of the traps is determined from the slope of the line, $E_t=0.45$ eV), and the trap density is determined from intersection of the line with the $\log\theta$ axis at $10^3/T=0$: $N_t=2\times10^{12}$ cm^{-3}. In calculating the trap parameters, the effective density of states, the carrier mobility, and the dielectric constant are assumed to have the values 10^{19} eV/cm^{-3}, $\mu=20$ cm^2/(V·s), and $\varepsilon=8$, respectively.[11,12] The trap depth E_t can also be determined from the temperature dependence of the conductivity $\sigma(T)$ (Fig. 2b). At the voltage corresponding to Ohm's law (curve *1*) and in the nonlinear interval (curve *2*) the $\sigma(T)$ curve exhibits two straight lines with activation energies of 0.45 eV and 0.55 eV.

In summary, on the basis of an analysis of the current-voltage characteristics at various temperatures and electric fields we have shown that the current transmission mechanism in an In–$Ga_{0.5}In_{1.5}S_3$–In structure is attributable to monopolar injection.

[1] M. I. Zartarova and R. S. Gamidov, Izv. Akad. Nauk SSSR Neorg. Mater. **5**, 369 (1969).
[2] V. P. Ambros, I. Ya. Andronchik, V. P. Mushinskiĭ, and N. M. Pavlenko, *Aspects of the Chemistry and Physics of Semiconductors of Complex Composition* [in Russian], Uzhgorod (1970).
[3] V. P. Ambros and V. P. Mushinskiĭ, Izv. Akad. Nauk SSSR Neorg. Mater. **8**, 1310 (1972).
[4] I. R. Amiraslanov, G. G. Guseĭnov, Kh. S. Mamedov, and A. S. Kuliev, Kristallografiya **33**, 767 (1988) [Sov. Phys. Crystallogr. **33**, 452 (1988)].
[5] T. Kh. Azizov, G. G. Guseĭnov, G. M. Niftiev, and I. R. Amiraslanov, Dokl. Akad. Nauk Az. SSR **12**, 25 (1985).
[6] I. R. Amiraslanov, T. Kh. Azizov, G. G. Guseĭnov, A. S. Kuliev, and G. M. Niftiev, Izv. Akad. Nauk SSSR Neorg. Mater. **24**, 723 (1988).
[7] I. R. Amiraslanov, G. G. Guseĭnov, A. S. Kuliev, and Kh. S. Mamedov, in *Collected Abstracts of the Tenth European Crystallographic Meeting*, Warsaw (1986), p. 456.
[8] I. R. Amiraslanov, F. Yu. Asadov, A. A. Musaev, and G. G. Guseĭnov, Kristallografiya **34**, 1012 (1989) [Sov. Phys. Crystallogr. **34**, 611 (1989)].
[9] I. R. Amiraslanov, F. Yu. Asadov, A. A. Musaev, and A. S. Kuliev, in *Proceedings of the First All-Union Conference on the Crystal Chemistry of Inorganic and Coordination Compounds* [in Russian], Vladivostok (1989), p. 108.
[10] M. A. Lampert and P. Mark, *Current Injection in Solids*, Academic Press, New York (1970) [Russian trans., Mir, Moscow (1973)].
[11] Yu. S. Ryabinkin, Fiz. Tverd. Tela (Leningrad) **6**, 2989 (1964) [Sov. Phys. Solid State **6**, 2382 (1964)].
[12] R. N. Bude, J. Appl. Phys. **33**, 1733 (1960).

Translated by James S. Wood

Conversion of red and infrared luminescence centers as a result of electron bombardment and annealing of CdS and CdS:Cu single crystals

G. E. Davidyuk, N. S. Bogdanyuk, A. P. Shavarova, and A. A. Fedonyuk

L. Ukrainki Volynskiĭ State University, 263009 Lutsk, Ukraine
(Submitted June 3, 1996; accepted for publication September 10, 1996)
Fiz. Tekh. Poluprovodn. **31**, 1013–1016 (August 1997)

The luminescence centers and their conversion as a result of electron bombardment and annealing in CdS single crystals which were not specially doped and which were doped with copper have been investigated. The Cu atoms, which interact mainly with defects in the cadmium sublattice, form Cu_{Cd}, which are responsible for luminescence at wavelengths $\lambda_m = 0.98-1.00$ μm. At annealing temperatures above 50 °C, conversion of the defect complexes, which are responsible for the green ($\lambda_m = 0.514$ μm), red ($\lambda_m = 0.72\mu$m), and infrared ($\lambda_m = 0.98$ μm) luminescence, occurs as a result of an increase in the mobility of point defects in the cadmium and sulfur sublattices of CdS:Cu. © *1997 American Institute of Physics.* [S1063-7826(97)00107-5]

Silver- and copper-doped II–VI compounds are components of many commercial crystal phosphors. Most luminescence centers in these materials are due to defect-impurity complexes, whose nature has not been completely determined. Promising methods for determining the formation mechanisms and nature of optically active centers in binary compounds are radiation physics methods, which make it possble to vary the density of the intrinsic defects in the experimental objects at comparatively low temperatures. In the present work, we investigated luminescence centers and their conversion as a result of electron bombardment and annealing in cadmium sulfide single crystals which were not specially doped and which were doped with copper. These single crystals, according to many parameters, are regarded as model compounds in the group of II–VI wide-gap chalcogenide semiconductors. To avoid uncontrollable impurities from appreciably affecting the defect-formation processes under irradiation, we employed samples with a comparatively high doping level (copper densities $N_{Cu} \simeq 10^{18}$ cm^{-3}) and high irradiation doses ($\Phi > 10^{17}$ cm^{-2}), so that the density of copper and radiation defects exceeded the background uncontrollable-impurity density. To simplify the analysis of the interaction of the copper atoms with the radiation defects, the experimental samples were bombarded by electrons with energy $E \simeq 1$ MeV, when, as is well known,[1], the dominant primary radiation defects are the simple point defects — Frenkel' pairs, formed approximately in equal densities in both sublattices in CdS.[2] During irradiation, the samples were cooled by liquid-nitrogen vapor and their temperature did not rise above 10–15 °C. The synthesis conditions of the experimental material and the irradiation technique are described in Refs. 3–5.

The dose dependences of the intensities I, which are known for the red and infrared luminescence bands of cadmium sulfide single crystals, are shown in Fig. 1.

Electron bombardment of undoped, high-resistance (resistivity $\rho = 10^{10}-10^{11}$ $\Omega\cdot$cm) CdS single crystals, grown from specially purified powder, exhibit bands of almost constant intensity with maxima at the wavelengths $\lambda_m = 1.03$ μm (curve *5*) and $\lambda_m = 0.72$ μm (curve *4*), indicating a low rate of introduction of free cadmium vacancies (V_{Cd}), which are responsible for the $\lambda_m = 1.03$-μm band[6] and the $\lambda_m = 0.72$-μm band associated with the complex $V_{Cd}^- - V_S^+$.[5,7,8] We did not observe an appreciable increase in the optical quenching of photoconductivity (OQP) as a result of the small change in the density of ''slow'' recombination centers, for which V_{Cd} are also responsible.

Irradiation of CdS:Cu single crystals leads to completely different results (Fig. 1, curves *1–3*). As the irradiation dose increases, the intensity of the luminescence band with $\lambda_m = 0.98$ μm increases (Fig. 1, curve *1*); the increase is accompanied by an increase in the OQP (in the regions 0.95–1 and 1.4–1.6 μm) and in the resistance of the irradiated sample (by almost five orders of magnitude after irradiation with a dose $\Phi \simeq 2\times 10^{17}$ cm^{-2}). This confirms our assumption in Ref. 9 that as a result of irradiation, the interstitial mobile copper atoms (Cu_i), which are donors, interact with the radiation-implanted V_{Cd}, during which the acceptor Cu_{Cd} centers (copper occupying cation sites in the CdS lattice), which are responsible for the luminescence band with $\lambda_m = 0.98$ μm and OQP, are formed. This mechanism of the interaction of Cu atoms with radiation defects in the cadmium sublattice explains the high rate of introduction of Cu_{Cd} centers in CdS:Cu single crystals as compared with the pure samples, where free V_{Cd} rapidly annihilate with interstitial cadmium atoms (Cd_i). It should be noted that in the luminescence excitation spectrum of an electron-irradiated CdS:Cu sample ($\Phi \simeq 2\times 10^{17}$ cm^{-2}) the intensity of the impurity band at 0.498 μm ($T = 77$ K) is two times higher than that of the 0.68 to 0.70-μm band observed before irradiation. This attests to the formation of complexes of shallow donors (apparently Cd_i) with Cu_{Cd} centers, i.e., donor-acceptor pairs responsible for the $\lambda_m = 0.98$ μm luminescence band. The formation of such complexes in photochemical reactions in CdS:Cu single crystals was observed in Ref. 10.

The conversion of the red-luminescence centers as a result of electron bombardment of Cu-doped CdS single crystals (Fig. 1, curves *2* and *3*) is described in Ref. 5 and agrees well with the above-examined mechanism of the interaction

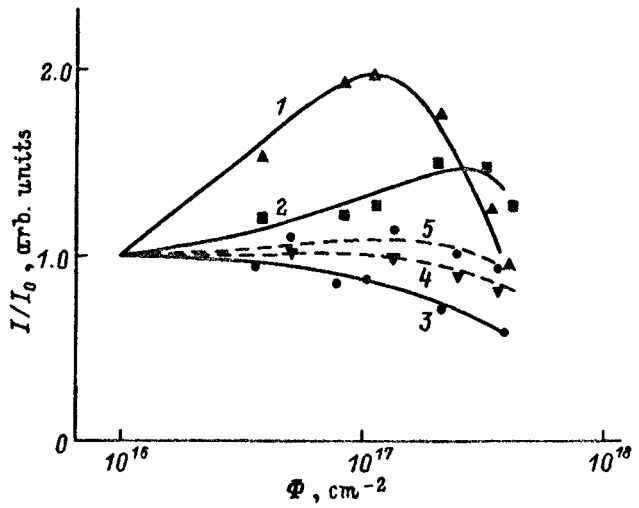

FIG. 1. Relative intensities I/I_0 of the luminescence bands of CdS:Cu (1–3) and CdS (4, 5) versus the dose of irradiation with electrons with energy $E=1.2$ MeV. λ_m, μm: *1* — 0.98, *2, 4* — 0.72, *3* — 0.808, *5* — 1.03. I, I_0 — intensities of the luminescence of irradiated and unirradiated samples, respectively.

of Cu atoms with the intrinsic lattice defects in these compounds.

The decrease in the intensity of all luminescence bands and the photosensitivity of the irradiated sample at high electron doses is apparently due to several factors. Nonradiative ''fast'' recombination centers, along with radiative recombination centers, are introduced as a result of electron bombardment. As they accumulate, a substantial fraction of the recombination flux of nonequilibrium carriers is redistributed to them.[3] Examples of such centers are interstitial-atom precipitates, the formation of which at high electron-irradiation intensities was observed directly with an electron microscope.[11] Moreover, as the density of the radiation defects increases, the screening action of some defects by the fields of other defects increases, which directly results in a change in the carrier trapping cross sections of recombination centers and possibly increases the role of nonradiative transitions or Auger processes, which decrease the quantum yield and the photosensitivity of strongly irradiated samples. Concentration quenching of luminescence in many crystal phosphors has been widely reported in the literature.[12]

As has been shown in many studies (see, for example, Ref. 13), V_{Cd} and V_S in CdS are immobile at room temperature, although during irradiation they can possess an appreciable mobility as a result of the strong excitation of the lattice. This apparently explains the formation of $Cu^-_{Cd}V^+_S$ complexes, which are responsible for luminescence with $\lambda_m=0.72$ μm[5] (Fig. 1, curve *2*), in CdS:Cu as a result of electron bombardment.

The rate of introduction of green-luminescence ($\lambda_m=0.514$ μm) centers, for which interstitial sulfur atoms (S_i) are responsible, is virtually identical in the undoped and doped samples.[3] Comparing the results of isochronous annealing of these centers in CdS:Cu (Figs. 2 and 3) with the results of annealing in undoped crystals (Fig. 2 in Ref. 4) shows that these processes follow the same scheme. These facts apparently can all be explained if it is assumed that the Cu atoms mainly interact with intrinsic defects in the cadmium sublattice of CdS single crystals. Annealing of red and infrared luminescence centers in undoped samples is different from that in doped samples. Isochronous annealing of irradiated undoped crystals to a temperature $T_a=150$ °C has virtually no effect on the intensities of the $\lambda_m=1.03$ μm and $\lambda_M=0.72$ μm luminescence (Fig. 3, curves *5* and *6*). A similar annealing of the irradiated CdS:Cu crystals results in a substantial change in the intensities of the intrared ($\lambda_M=0.98$ μm) and red ($\lambda_m=0.72$ μm) luminescence bands (Figs. 2 and 3). Up to temperatures $T_a=80-100$ °C, the intensity of the green-luminescence band increases, and this increase is accompanied by a synchronous increase in the intensity of the $\lambda_m=0.72$-μm band and a decrease in the intensity of the $\lambda_m=0.98$-μm band (Fig. 2, curves *1–4* and Fig. 3, curves *1–3*).

The increase in the intensity of the green-luminescence band can be explained by a decay of the associated (bound) Frenkel' pairs in the sulfur sublattice, which are formed, to-

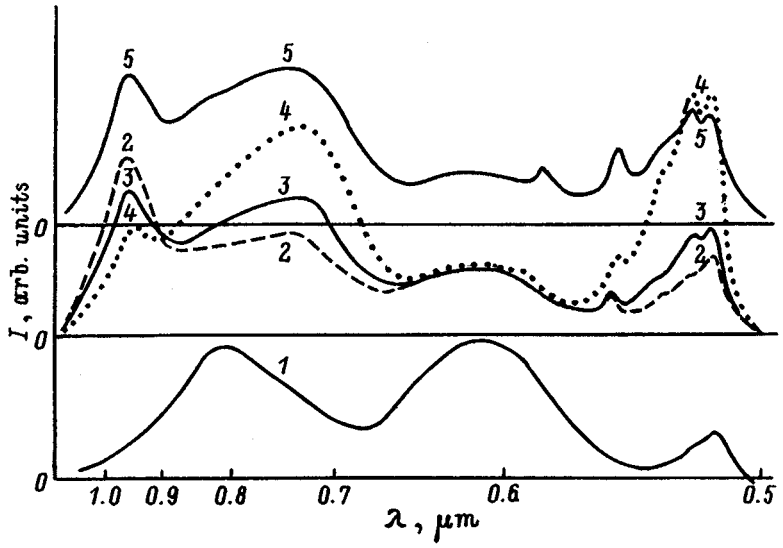

FIG. 2. Luminescence spectra of CdS:Cu single crystals: *1* — Not bombarded by electrons; *2* — bombarded by electrons with $E=1.2$ MeV and $\Phi=2\times10^{17}$ cm^{-2}, and *3–5* — after irradiation and annealing at temperatures $T_a=60$ (*3*), 100 (*4*), and 150 (*5*) °C. The irradiated samples were annealed at each temperature for $\tau=10$ min. The measurements were performed at the temperature $T=77$ K.

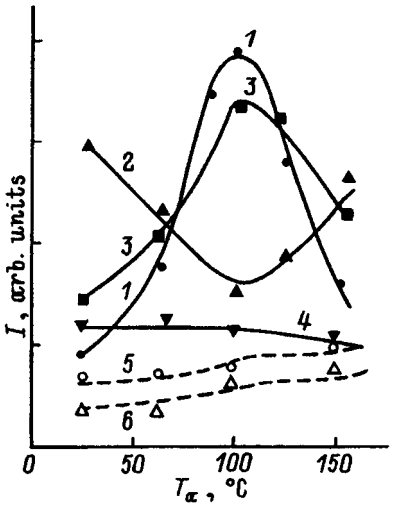

FIG. 3. Intensities I of the luminescence bands of CdS:Cu (*1–4*) and CdS (*5, 6*) single crystals bombarded by electrons ($E=1.2$ MeV, $\Phi=2\times10^{17}$ cm^{-2}) versus the temperature of isochronous annealing. The duration of the annealing is $\tau=10$ min. The measurements were performed at temperature $T=77$ K. λ_m, μm: *1* — 0.51, *2* — 0.98, *3, 5* — 0.72, *4* — 0.605, *6* — 1.03.

gether with separated pairs, as a result of electron bombardment of CdS and CdS:Cu single crystals. As a result of the mutual screening of the fields of V_{S^+} and S_{i^-}, the bound Frenkel' pairs apparently do not appear in the radiation, and they most likely function as ''fast'' nonradiative recombination centers, as is indicated by the increase in the photosensitivity as a result of annealing of the irradiated samples. Our results are confirmed by investigations of the luminescence of CdS single crystals doped with the rare-earth ions Yb^{3+} and Tm^{3+}.[13] The appearance of new lines and the change in the relative intensities of the lines, known for CdS, at $T_a=47-107$ °C, can be attributed to the migration of defects, which arise when sulfur atoms are displaced, and to their binding with a rare-earth ion.

At $T_a>40$ °C, free S_i and V_S appear in the sulfur sublattice as a result of the decomposition of bound Frenkel' pairs. Interacting with one another according to the reaction $Cu_{Cd}^{-}+V_S^{+}\rightarrow Cu_{Cd}^{-}V_S^{+}$, V_S and Cu_{Cd} form centers which are responsible for the $\lambda_m=0.72$-μm luminescence band, whose intensity increases with annealing up to 100 °C. As the Cu_{Cd} density decreases, the intensity of $\lambda_m=0.98$ μm radiation also decreases (Fig. 2, curves *2–4*, and Fig. 3, curves *1–3*).

At temperatures above 100 °C, the intensity of the green luminescence (Figs. 2 and 3) apparently decreases as a result of an increase in the mobility of S_i and the migration of S_i to different sinks, which could be V_S, and accumulation of defects, dislocations, and apparently $Cu_{Cd}^{-}V_S^{+}$ centers. The ''annihilation'' of sulfur atoms with vacancies at centers of red luminescence $Cu_{Cd}^{-}V_S^{+}+S_i^{-}\rightarrow Cu_{Cd}$ results in a decrease in the intensity of the $\lambda_m=0.72$-μm radiation and an increase in the intensity of $\lambda_m=0.98$-μm luminescence (Fig. 2, curve *5*, and Fig. 3, curves *1–3*).

In summary, as a result of electron bombardment of CdS:Cu single crystals, the Cu atoms mainly interact with defects in the cadmium sublattice, forming Cu_{Cd} centers which are responsible for the $\lambda_m=0.98-100$ μm luminescence. At temperatures above 50 °C, conversion of the defect complexes, which are responsible for the green ($\lambda_m=0.514$ μm), red ($\lambda_m=0.72$ μm), and infrared ($\lambda_m=0.98$ μm) luminescence bands, occurs as a result of an increase in the mobility of point defects in the cadmium and sulfur sublattices in CdS:Cu.

[1] V. V. Emtsev and T. V. Mashovets, *Impurities and Point Defects in Semiconductors* [in Russian], Radio i svyaz', Moscow, 1981.
[2] R. O. Chester, J. Appl. Phys. **38**, 1745 (1967).
[3] G. E. Davidyuk, N. S. Bogdanyuk, and A. P. Shavarova, Fiz. Tekh. Poluprovodn. **28**, 2056 (1994) [Semiconductors **28**, 1132 (1994)].
[4] N. S. Bogdanyuk, G. E. Davidyuk, and A. P. Shavarova, Fiz. Tekh. Poluprovodn. **29**, 201 (1995) [Semiconductors **29**, 99 (1995)].
[5] N. S. Bodanyuk, G. E. Davidyuk, and A. P. Shavarova, Fiz. Tekh. Poluprovodn. **29**, 357 (1995) [Semiconductors **29**, 181 (1995)].
[6] B. A. Kulp, Phys. Rev. **125**, 1865 (1965).
[7] I. B. Ermolovich, G. I. Matvievskaya, G. S. Pekar', and M. K. Sheĭnkman, Ukr. Fiz. Zh. **18**, 733 (1973).
[8] J. E. Ralph, Phys. Status Solidi A **53**, 611 (1979).
[9] A. P. Galushka, G. E. Davidyuk, V. T. Mak, V. I. Kuts, and N. S. Bogdanyuk, Fiz. Tekh. Poluprovodn. **9**, 2174 (1975) [Sov. Phys. Semicond. **9**, 1413 (1975)].
[10] S. S. Ostapenko, M. K. Sheĭnkman, and Yu. N. Emirov, Fiz. Tekh. Poluprovodn. **15**, 1747 (1981) [Sov. Phys. Semicond. **15**, 1013 (1981)].
[11] T. Yoshiie, H. Jwanaga, N. Shibata, M. Ichihara, K. Suzuki, and S. Takekchi, in *Def. Rad. Effects. Semicond (Proc. 11th Int. Conf.*, Bristol–London, 1981, p. 443).
[12] A. M. Gurvich, *Introduction to the Physical Chemistry of Crystal Phosphors* [in Russian], Vyssh. Shk., Moscow, 1982.
[13] G. D. Watkins, in *Point Defects in Solids* [Russian trans., Mir, Moscow, 1979], p. 221.

Translated by M. E. Alferieff

Acceptors in $Cd_{1-x}Mn_xTe$ ($x<0.1$)

A. I. Vlasenko, V. N. Babentsov, Z. K. Vlasenko, and S. V. Svechnikov

Institute of Semiconductor Physics, Ukrainian National Academy of Sciences, 252650 Kiev, Ukraine

I. M. Rarenko, Z. I. Zakharuk, E. S. Nikonyuk, and V. L. Shlyakhovyĭ

Chernovtsy State University, Chernovtsy, Ukraine

(Submitted August 7, 1996; accepted for publication October 25, 1996)
Fiz. Tekh. Poluprovodn. **31**, 1017–1020 (August 1997)

Acceptor defects, which control conductivity and recombination in $Cd_{1-x}Mn_xTe$ ($0\leqslant x\leqslant 0.1$), have been observed experimentally and investigated by electric and luminescence methods. The energy levels of the defects and the composition dependence of the energy levels have been determined. The physicochemical nature of these defects is discussed. © *1997 American Institute of Physics.* [S1063-7826(97)00607-8]

Semimagnetic semiconductor materials $Cd_{1-x}Mn_xTe$ are of interest for a number of reasons. A number of their parameters, primarily parameters such as the band gap, index of refraction, absorption coefficient, and others, depend on the manganese concentration and can be changed by a magnetic field.[1,2] The possibility of obtaining large-diameter, highly perfect, degradation-resistant plates makes these materials promising for optical devices for controlling high-power laser radiation in phototransducers and other elements of integrated opto- and microelectronics, for applications as substrates for epitaxial growth of variable band gap $Cd_{1-x}Mn_xTe$ layers,[3] for preparing quantum structures which effectively localize charge carriers,[4] and for other applications. This makes it important to investigate the energy structure of intrinsic and extrinsic defects in this material and their interaction and evolution.

It is well known that in single crystals with the composition $x<0.4$ the band gap $E_g<2$ eV and the photoluminescence (PO) spectrum of the crystals is qualitatively similar to the PL spectrum of *p*-type CdTe, the difference being that the PL bands in it are strongly broadened due to the composition fluctuations and the presence of structural defects.[3,5,6] In crystals with $0.4<x<0.7$ the band in the photon energy range ~ 2 eV, which is associated with the intracenter the transitions in Mn^{2+} ions, dominates the PL.[2]

There is virtually no published information on the effect of manganese on the conductivity in CdTe and on the energy position of acceptor levels in $Cd_{1-x}Mn_xTe$.

In this article we report the results of an experimental study of the the effect of Mn impurity on the conductivity of CdTe and determine the energy levels and nature of the acceptor states in $Cd_{1-x}Mn_xTe$ ($x<0.1$).

SAMPLE PREPARATION AND EXPERIMENTAL PROCEDURE

Bulk CdTe:Mn single crystals, just as the solid solutions $Cd_{1-x}Mn_xTe$ ($0.01\leqslant x\leqslant 0.1$), were grown by a modified Bridgman method in rotating tilted (with respect to the horizontal plane) cells, where the crystallization front moved relative to the melt. This made possible mixing of the melt and equalization of its composition and temperature over the entire volume during rotation; this cannot be done with a vertical arrangement of the container. Upon doping CdTe with superstoichiometric Mn and preparing dilute solid solutions $Cd_{1-x}Mn_xTe$ ($0\leqslant x\leqslant 0.02$), we introduced the Mn into the initial charges in the form of a Cd-based dopants, taking into account the required quantity of Cd in the final charge (this increased the concentration of the embedded Mn).

The measurements of the Hall constant R_H and the conductivity σ were performed by the standard methods on square-shaped samples in the temperature range 77–300 K. The PL spectra were measured on fresh-cleavage faces of the sample with excitation by a 15-mW He–Ne laser ($\lambda=632.8$ nm) at $T=77$ K; a FÉU-62 photomultiplier was used as a radiation detector. The structural perfection of the crystals was monitored by Berg–Barret and Lang x-ray topographic methods and the microanalysis of the composition was performed with a REM-101 M electron microscope–microanalyzer.

EXPERIMENTAL RESULTS AND DISCUSSION

We obtained *n*-CdTe with electron density $n\leqslant 10^{15}$ cm^{-3} with Mn density N_{Mn} in the melt up to 10^{19} cm^{-3}. Increasing N_{Mn} above $\approx 10^{19}$ cm^{-3} changed the conductivity of the material to *p*-type with hole density $p\approx 10^{15}$ cm^{-3} (Fig. 1).

A similar change in the conductivity type $n\rightarrow p$ can be obtained by annealing undoped *n*-CdTe in an evacuated cell by rediffusion of Cd from the volume and formation of cadmium vacancies, which are filled with group-I atoms that form singly charged acceptors at the cadmium sites.[7] In the case of doping with manganese from the melt, no additional cadmium vacancies are formed and the change in conductivity type $n\rightarrow p$ can occur as a result of the diffusion of group-I atoms, present at interstices, from the volume of the crystal and their migration into the doping solution or to sinks and a decrease in the density of residual donors as a result of this circumstance.

Although, according to the data of Ref. 8, the mechanism of single embedding of atoms prevails in CdTe:Mn with manganese impurity density $N_{Mn}\leqslant 5\times 10^{19}$ cm^{-3}, it has not been ruled out that for densities $N_{Mn}>10^{19}$ cm^{-3} Mn-enriched regions or manganese microprecipitates, which can

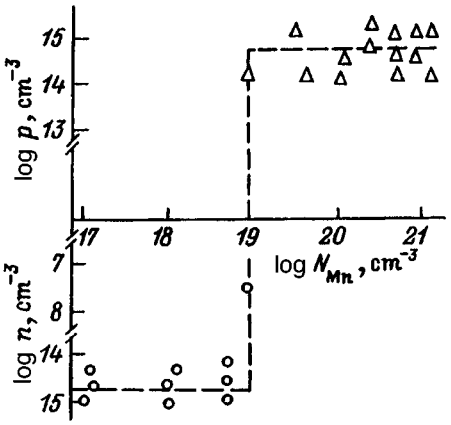

FIG. 1. Carrier density in CdTe:Mn versus the manganese density N_{Mn} in the melt ($T \approx 300$ K).

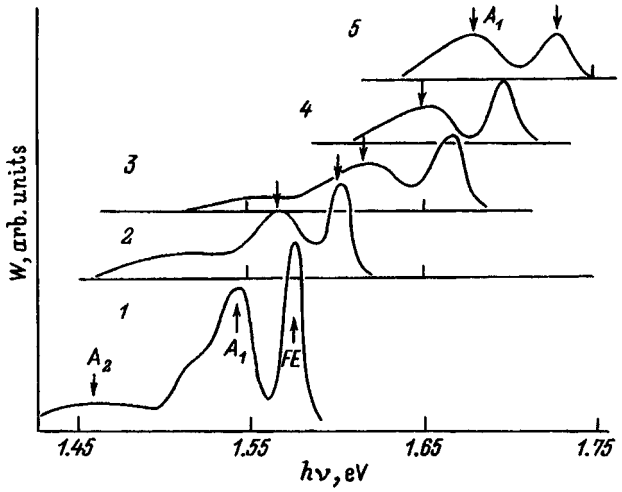

FIG. 3. PL spectra at 77 K of CdTe:Mn (*1*) and $Cd_{1-x}Mn_xTe$ (*2–5*) single crystals with different compositions x,%: *2* — 2, *3* — 6, *4* — 8, *5* — 10.

play the role of getters or sinks for the uncontrollable background donor impurity located at interstices, are formed. Then, as the *n*-CdTe:Mn is cooled to room temperature, the donor density in the volume decreases and overcompensation of CdTe:Mn into *p*-type material occurs, similarly to the manner in which this was observed in Ref. 5 during storage of *n*-CdTe obtained by annealing in Cd vapor. It should be noted that in Ref. 6, in the investigation of sublimation of crystals during annealing, Mn-enriched ($x \approx 0.5$) precipitates were observed on the boundaries of structural defects in CdMnTe solid solutions ($x \approx 0.2$). Evidence supporting this hypothesis could be data on the temperature dependences of the Hall mobility μ_H in CdTe:Mn crystals after annealing in melt with different N_{Mn} density (Fig. 2). For $N_{\mathrm{Mn}} > 10^{18}$ cm^{-3} these data fall on the curves which are displaced almost parallel to one another, which could indicate the formation of local nonuniformities in the crystal.[9] In CdTe:Mn crystals, just as in CdHgTe, such nonuniformities can arise as a result of the formation of overcompensated regions, precipitations of a second phase, and for other reasons.[10] We were not able to observe such regions by means of x-ray microanalysis; in principle, this does not rule out finely dispersed Mn precipitates (with average precipitate sizes $\leqslant 1$ μm, wich are not observable by local probing with an electron beam $\approx 2-3$ μm in diameter).

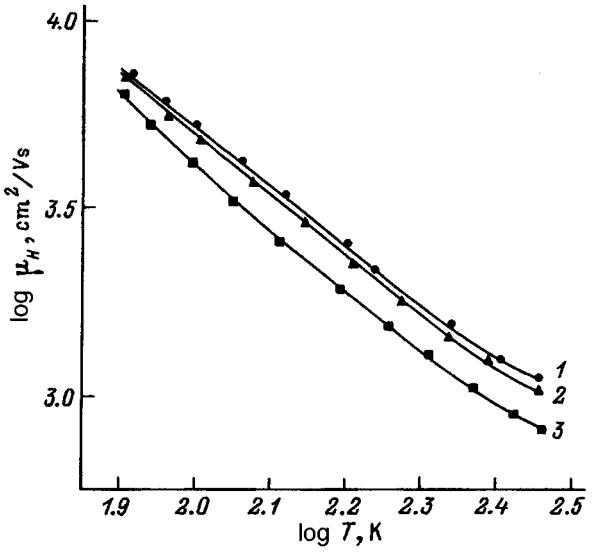

FIG. 2. Temperature dependences of the Hall mobility μ_H for CdTe:Mn crystals with Mn density in the melt: *1* — $N_{\mathrm{Mn}} \cong 10^{17}$ cm^{-3}, $n_{0300\,\mathrm{K}} \cong 4\times10^{14}$ cm^{-3}; *2* — $N_{\mathrm{Mn}} \cong 10^{18}$ cm^{-3}, $n_{0300\,\mathrm{K}} \cong 1.8\times10^{14}$ cm^{-3}; *3* — $N_{\mathrm{Mn}} \cong 5\times10^{18}$ cm^{-3}, $n_{0300\,\mathrm{K}} \cong 7.2\times10^{14}$ cm^{-3}.

It has not been ruled out that complex acceptor-type associates, including Mn atoms, uncontrollable impurity, and intrinsic point defects are formed during doping of crystals in the density range $N_{\mathrm{Mn}} > 10^{19}$ cm^{-3} and with decreasing scattering between separate Mn atoms. It has also not been ruled out that the change in the type of conductivity is due to the increasing compensating action of uncontrollable impurities present in the initial Mn with increasing Mn content in the doping solution. At the same time, other processes can also dominate.

Three emission bands are observed in the PL spectrum at 77 K of most $Cd_{1-x}Mn_xTe$ samples with $x < 0.02$ (Fig. 3). The high-energy band (*FE*) is due to radiative decay of excitons. The change in the position of this band, to within the binding energy of the exciton (~ 10 meV in CdTe), characterizes the increase in the band gap in $Cd_{1-x}Mn_xTe$ with increasing x relative to the band gap in CdTe. The best agreement between the experimental data and calculations is obtained with $E_g(x)$ approximated by the expression $E_g = 1.58(1+0.92x)$ eV. The longer wavelength band A_1 is due, just as in undoped *p*-type CdTe, to radiative recombination of an electron from the conduction band with a hole trapped in a shallow acceptor level A_1. For $0 < x < 0.1$ the accuracy with which the depth of the level E_{A1} in the band gap is determined is limited by the accuracy with which the position of the emission and absorption bands of a free exciton is determined, which, because of broadening of the bands in the solid solution, is 5–6 meV.[1,11] The value of E_{A1} for $x < 0.05$ found from the PL spectrum depends on the composition [approximation gives the expression $E_{A1} \approx 0.032(1+8x)$ eV] and saturates — $E_{A1} \approx 50$ meV for $x > 0.05$.

The emission band A_2, which is attributable to the transition of an electron from the conduction band to an acceptor

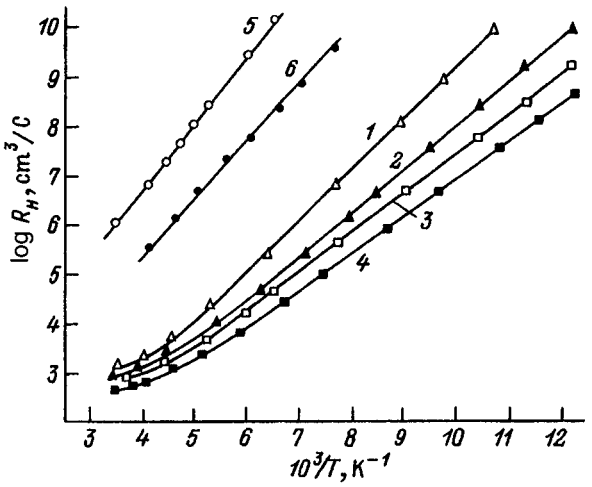

FIG. 4. Temperature dependences of the Hall coefficient of $Cd_{1-x}Mn_x$ Te single crystals with different compositions x,%: *1* — 10, *2* — 6, *3* — 4, *4* — 2 (samples in whose PL spectra three bands are observed), *5* — 10, 6 — 2 (PL in these samples is very weak).

with the thermal ionization energy E_{A2}, was clearly observed only in CdTe:Mn and $Cd_{1-x}Mn_xTe$ ($x<0.02$) samples. The position of its maximum differs from E_g by the energy $E_{A2}\approx 120\pm 5$ meV, which is virtually identical to the value E_{A2} determined from the temperature dependence of the Hall coefficient $R_H(T)-E_{A2}\approx 0.125$ eV with $x\approx 0.02$ (Fig. 4). The dependence $E_{A2}(x)$ in this region of compositions x is approximated by the expression $E_{A2}\approx 0.125(1+5x)$ eV.

A PL spectrum containing only a very weak *FE* band with intensity an order of magnitude lower than in the typical PL spectrum was observed in some $Cd_{1-x}Mn_xTe$ samples. For these samples the temperature dependence of the Hall coefficient gives the ionization energy of acceptor A_3 ($E_{A3}=215$ meV for $x=0.02$) (Fig. 4). The variation of E_{A3} with composition in this range of values of x is described by the expression $E_{A3}=0.215(1+1.1x)$ eV. In CdTe the PL band with an energy of about 200 meV is observed, as a rule, in crystals with a low degree of structural perfection.

Let us assume that in $Cd_{1-x}Mn_xTe$, just as in $Hg_{1-x}Cd_xTe$,[12] E_g changes primarily as a result of a change in the energy position of the conduction band bottom. In this case the absence of a change in E_{A1} and E_{A3} (for $x\leqslant 0.05$) with increasing x can be explained by the fact that the common anion rule also applies to acceptors, which are defects in the cation sublattice (V_{Cd}, Mn_{Cd}, etc.), whose nearest-neighbor environment (four tellurium atoms) does not depend on the composition of the solid solution. In *p*-type CdTe the acceptor with ionization energy 50 meV is Li_{Cd},[13] which apparently is also found in $Cd_{1-x}Mn_xTe$. According to data from Ref. 14, the energy position of the Mn level in CdTe, which is split off from the valence band, is approximately ≈ 36 meV. Therefore, the change in E_{A1} from ≈ 32 up to ≈ 50 meV with increasing x ($0\leqslant x\leqslant 0.05$), just as the establishment of the nature of E_{A1}, requires further study.

In structurally perfect *n*-type CdTe there are no acceptors with $E_{A3}\approx 215$ meV. Therefore, it is possible that in $Cd_{1-x}Mn_xTe$ such an acceptor is a complex consisting of group-I atoms in the cadmium sublattice (Cu_{Cd}, Ag_{Cd}) and Mn atoms that lie next to one another.

In the case of the acceptor A_2, whose energy E_{A2} in the range $0<x<0.1$ varies quite strongly ($\geqslant 60$ meV), it is known that in CdTe it corresponds to a donor-acceptor complex.[15] In $Cd_{1-x}Mn_xTe$ the quantity E_{A2}, just as E_g, increases with x (E_g increases as a result of a change in the energy of the conduction band bottom). Therefore, in the solid solution E_{A2} can increase with x if the acceptor includes a defect of the cation sublattice and a nearby shallow donor defect, whose energy level is determined by the states of the conduction band.

In conclusion, it should also be noted that the investigation of $Cd_{1-x}Mn_xTe$ crystals ($0.01\leqslant x\leqslant 0.1$) by the Berg–Barret and Lang x-ray topographic methods has shown that the structural and mechanical characteristics of such crystals are much better than those of pure CdTe crystals.

CONCLUSIONS

A change in the conductivity type $n\rightarrow p$ in CdTe:Mn on doping from a solution with dopant densities $N_{Mn}\approx 10^{19}$ cm^{-3} was observed. In $Cd_{1-x}Mn_xTe$ ($x<0.1$) the composition dependence of the band gap was determined, the energies of the levels of the acceptor defects were determined, approximate expressions for their composition dependences were presented, and the physicochemical nature of these defects was discussed.

[1] K. Y. Lay, H. Neff, and R. J. Bachmann, Phys. Status Solidi A **92**, 567 (1985).
[2] P. N. Bukivskiĭ, Yu. P. Gnatenko, and A. Kh. Rozhko, JETP Lett. **61**, 386 (1995).
[3] W. M. Higgins, G. N. Pultz, R. G. Roy, and R. G. Lancaster, J. Vac. Sci. Technol. A **7**, 271 (1989).
[4] B. P. Zakharchenya, A. V. Kudinov, and Yu. G. Kusraev, JETP Lett. **63**, 256 (1996).
[5] V. N. Babentsov, A. I. Vlasenko, and N. I. Tarbaev, Fiz. Tekh. Poluprovodn. **29**, 1563 (1995) [Semiconductors **29**, 813 (1995)].
[6] A. V. Savitskiĭ, N. I. Ilashchuk, O. A. Parfenyuk, and K. S. Ul'yanitskiĭ, in *Abstracts of Reports at the 2nd Ukrainian Onference on ''Materials Engineering and the Physics of Semiconductor Phases with Variable Composition* [in Russian], September 21–24, 1993, Zezhin, 1993, p. 192.
[7] V. N. Babentsov, L. V. Rashkovetskiĭ, E. A. Sal'kov, and N. I. Tarabaev, Fiz. Tekh. Poluprovodn. **26**, 1088 (1992) [Sov. Phys. Semicond. **26**, 608 (1992)].
[8] P. I. Babiĭ, N. P. Gavaleshko, Yu. P. Gnatenko *et al.*, Preprint No. 3, Institute of Physics, Ukrainian SSR Academy of Sciences, Kiev, 1983.
[9] M. V. Alekseenko, E. N. Arkad'eva, and O. A. Matveev, Fiz. Tekh. Poluprovodn. **4**, 414 (1970) [Sov. Phys. Semicond. **4**, 347 (1970)].
[10] A.I. Vlasenko, A. V. Lyubchenko, and E. A. Sal'kov, Ukr. Fiz. Zh. **25**, 1317 (1980).
[11] V. F. Agekyan, A. Yu. Serov, Yu. A. Stepanov, and Le Thai Lai, Fiz. Tverd. Tela (Leningrad) **37**, 1090 (1995) [Phys. Solid State **37**, 592 (1995)].
[12] S. P. Kovalczyk, J. T. Cheung, E. A. Kraut, and R. W. Grant, Phys. Rev. Lett. **56**, 1605 (1986).
[13] E. Molva, J. R. Chamonal, and J. L. Pautra, PSS B **109**, 635 (1982).
[14] V. I. Sokolov, Neorg. Mater. **31**, 1310 (1995).
[15] N. V. Agrinskaya, E. N. Arkad'eva, and O. A. Matveev, Fiz. Tekh. Poluprovodn. **5**, 869 (1971) [Sov. Phys. Semicond. **5**, 767 (1971)].

Translated by M. E. Alferieff

Energy spectrum of *n*-type $Pb_{1-x}Sn_xTe$ ($x=0.22$) bombarded by neutrons

E. P. Skipetrov, A. N. Nekrasova, and A. V. Ryazanov

M. V. Lomonosov Moscow State University, 119899 Moscow, Russia
(Submitted April 24, 1996; accepted for publication January 22, 1997)
Fiz. Tekh. Poluprovodn. **31**, 1021–1023 (August 1997)

The effect of hydrostatic pressure ($P \leqslant 12$ kbar) on the electrical properties of *n*-type $Pb_{1-x}Sn_xTe$ ($x=0.22$) bombarded by electrons ($T \approx 300$ K, $E=6$ MeV, $\Phi = 7.7\times 10^{17}$ cm^{-2}) has been investigated. The restructuring of the energy spectrum of electron-irradiated alloys under pressure has been investigated. The parameters of a model of the energy spectrum of charge carriers in electron-irradiated *n*-type $Pb_{1-x}Sn_xTe$ ($x=0.22$) have been determined on the basis of the experimental data obtained. © *1997 American Institute of Physics.* [S1063-7826(97)03307-3]

It is now known that bombardment of $Pb_{1-x}Sn_xTe$ ($x \approx 0.2$) alloys by electrons leads to the appearance of a donor-type resonance level E_d in the conduction band and a band of acceptor-type resonance states E_a located near the valence-band top.[1–3] External pressure changes the relative arrangement of the edges of the allowed bands and the radiation levels, inducing in this manner a change in the charge-carrier density in the allowed bands because of the redistribution of electrons between bands and localized states. This method made it possible to obtain the most reliable information about the parameters of deep radiation levels in *p*-type $Pb_{1-x}Sn_xTe$ ($x=0.2$) alloys.[2,3] At the same time, electron-irradiated *n*-type alloys and alloys with a different tin content under pressure have still not been investigated, and the parameters of the energy spectrum of radiation defects in these materials are still not known.

In the present work we investigated the effect of hydrostatic pressure on the electrical properties of electron-irradiated alloy *n*-$Pb_{1-x}Sn_xTe$ ($x=0.22$) at $T \approx 300$ K with electron energy $E=6$ MeV and electron flux $\Phi \leqslant 8.4\times 10^{17}$ cm^{-2}. The sample method of preparing the samples for the measurements and the main parameters of the samples are presented in Ref. 4. In each sample, before and after bombardment, the temperature dependences of the resistivity and the Hall coefficient ($4.2 \leqslant T \leqslant 300$ K, $B \leqslant 0.04$ *T*), as well as the Shubnikov–de Haas effect and the field dependences of the Hall coefficient ($T=4.2$ K, $B \leqslant 6$ T, $B \parallel \langle 100 \rangle$) were investigated. For measurements under hydrostatic pressure ($P \leqslant 12$ kbar) a *S*-22 sample ($n_0 = 1.5\times 10^{16}$ cm^{-3}, $\Phi = 7.7\times 10^{17}$ cm^{-2}) with tin content $x=0.22$ was chosen. In this sample *n–p* conversion was observed under irradiation and at the maximum irradiation fluxes the Fermi level was found to lie in the valence band.

It was determined that under pressure the resistivity of the *S*-22 sample at $T=4.2$ K decreases by almost two orders of magnitude and passes through a minimum at pressure $P \approx 9$ kbar, corresponding to a transition of the alloy with $x=0.22$ through a gapless state. The temperature dependences of the resistivity changed form qualitatively and at maximum pressures they are of a metallic character typical of undoped $Pb_{1-x}Sn_xTe$ crystals (Fig. 1). The Hall coefficient at low temperatures decreases continuously under pressure approximately by an order of magnitude and nearly saturates at $P > 6$ kbar. The character of the temperature and field dependences of the Hall coefficient remains unchanged under pressure.[4]

The results obtained indicate that the free-hole density increases under pressure. Figure 2 shows the pressure dependence of the hole density, calculated according to the value of the Hall coefficient in weak magnetic fields at $T=4.2$ K. The most rapid changes of the hole density are observed at low pressures, and for $P > 6$ kbar the function $p(P)$ nearly saturates. Such changes in the hole density under pressure have been observed before in investigations of electron-irradiated *p*-$Pb_{1-x}Sn_xTe$ ($x=0.2$) samples[2,3] and are attributed to a redistribution of the electrons between the valence band and the resonance band of radiation defects E_a (Fig. 3). The characteristic form of the pressure dependence of the hole density (rapid increase and saturation) makes it possible to determine the main parameters of the model of the energy spectrum by comparing the experimental and computed functions $p(P)$ for an electron-irradiated alloy.

These calculations were based on the width of the resonance band $\sigma = 4$ meV and the generation rate of acceptor-type radiation defects $dN_a/d\Phi = 1.7$ cm^{-1}, characteristic of the previously investigated alloy *p*-$Pb_{1-x}Sn_xTe$ $\times (x=0.2)$.[1–3] It was assumed that just as in the electron-irradiated alloys $Pb_{1-x}Sn_xTe$ (the results of the investigations are presented in Refs. 5 and 6), the change in the free charge carrier density and composition of the alloy should not greatly influence the values of these parameters. On the other hand, the change in the tin content in the alloy can appreciably influence the position of the acceptor band E_a relative to the valence band top. For this reason, the main purpose of this calculation was to determine the energy position of the resonance band E_a. Finally, the value of the difference generation rate of defects $d(N_a - N_d)/d\Phi$, determined from the position of the *n–p* conversion point for the sample *S*-22 and the rate of decrease of the electron density, calculated according to the change in the period of the Shubnikov oscillations in the samples *Nn*-4 and 5,[4] were used to estimate the generation rate $dN_d/d\Phi$ of donor-type defects.

The theoretical pressure dependences $p(P)$ were constructed taking into account the fact that when the energy spectrum of the irradiated alloy is restructured under pres-

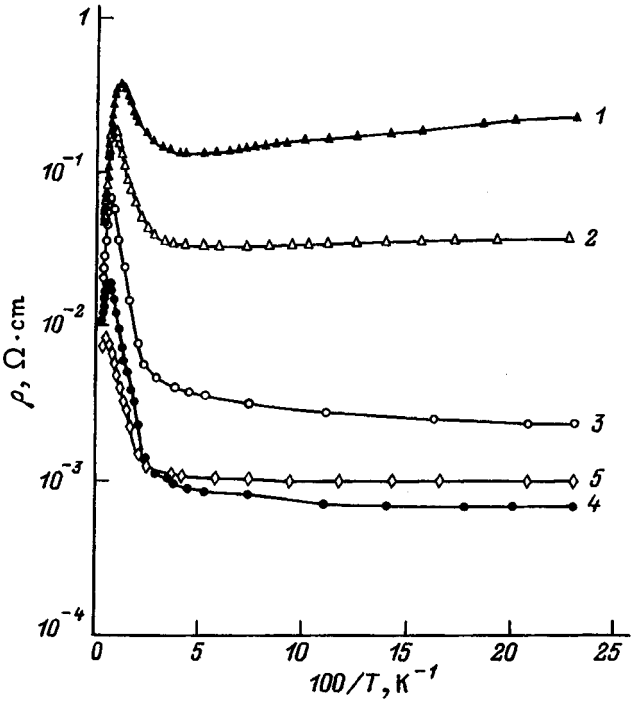

FIG. 1. Temperature dependences of the resistivity of sample *S*-22 bombarded by electrons ($\Phi = 710^{17}$ cm^{-2}) at different pressures. *P*, kbar: *1* — 0, *2* — 0.3, *3* — 1.9, *4* — 6.7, *5* — 11.8.

sure, the sum of the hole densities p in the valence band and p_a in the resonance band remains constant:

$$p(P)+p_a(P)=p(0)+p_a(0), \tag{1}$$

or, since $p_a(P)=N_a-n_a(P)$ and $p_a(0)=N_a-n_a(0)$, we obtain

$$p(P)=p(0)+[n_a(P)-n_a(0)], \tag{2}$$

where

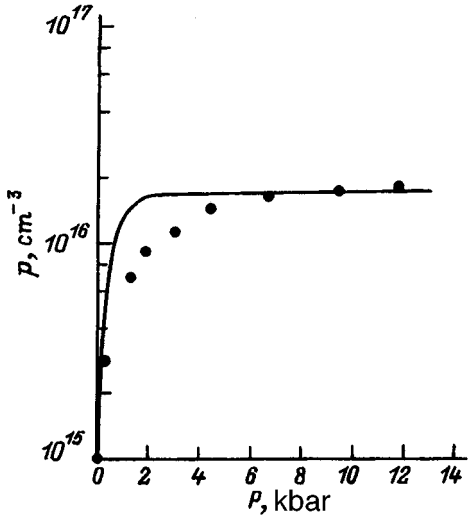

FIG. 2. Hole densities versus pressure at $T=4.2$ K for sample *S*-22 bombarded by electrons ($\Phi = 7.7\times10^{17}$cm^{-2}). Dots — experiment, solid line — calculation with the parameters $E_v-E_a=9.3$ meV, $\sigma=4$ meV, $dN_a/s\Phi=1.7$ cm^{-1}.

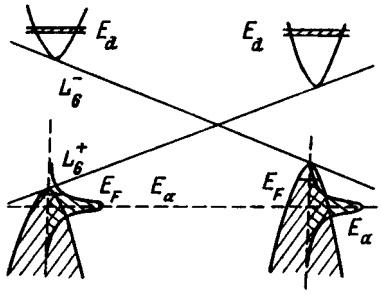

FIG. 3. Diagram of the pressure-induced restructuring of the energy spectrum.

$$n_a(P)=\int_{-\infty}^{E_F(P)} g_a(E)dE,$$

$$g_a(E)=\frac{N_a}{\sigma\sqrt{2\pi}}\exp\left[-\frac{(E-E_a)^2}{2\sigma^2}\right], \tag{3}$$

$N_a=\Phi(dN_a/d\Phi)$, $G_a(E)$ is the density of states in the resonance band in the form of a Gaussian-type curve, E_a is the center and σ the width of the resonance band, and E_F is the Fermi energy, calculated in Kane's two-band model with the parameters presented in Ref. 7. The best agreement between theory and experiment was achieved under the assumption that the position of the center of the resonance band E_a remains unchanged relative to the center of the band gap in the alloy under pressure (Fig. 3) and for the following parameters of the model:

$$E_v-E_a=9.3\text{meV}, \quad \sigma=4 \text{ mev}, \quad dN_a/d\Phi=1.7 \text{ cm}^{-1}. \tag{4}$$

It should be noted that the method chosen for the calculation gives automatic agreement between the computational results and the experimental data at atmospheric pressure, and agreement near maximum pressures is obtained by varying the position of the resonance band E_a. For intermediate pressures the computed hole densities are much higher than the experimental values (Fig. 2). This deviation of the theoretical curves from the experimental points was discussed previously in an analysis of the experimental data obtained for electron-irradiated alloys p-$Pb_{1-x}Sn_xTe$ ($x=0.2$), and it was attributed to a deviation of the density of states in the resonance band from the Gaussian form.[3]

It should also be noted that in the experimental alloy $Pb_{1-x}Sn_xTe$ ($x=0.22$) the resonance band E_a was found to lie somewhat lower than in the previously investigated alloys $Pb_{1-x}Sn_xTe$ ($x=0.2$), for which the average value of E_v-E_a was $E_v-E_a\approx5.3$ meV. This suggests that in the alloys $Pb_{1-x}Sn_xTe$ the position of the band of radiation defects E_a relative to the center of the band gap does not depend on the composition.

We thank A. M. Musalitin for irradiating the samples with high-energy electrons.

This work was supported by the Russian Fund for Fundamental Research under Grants Nos. 96-02-18325 and 96-02-16275.

[1] N. B. Brandt, E. P. Skipetrov, and A. G. Khorosh, Fiz. Tekh. Poluprovodn. **24**, 51 (1990) [Sov. Phys. Semicond. **24**, 31 (1990)].
[2] A. N. Nekrasova, E. P. Skipetrov, and A. G. Khorosh, Fiz. Tekh. Vys. davleniĭ **2**, 107 (1992).
[3] N. B. Brandt, E. P. Skipetrov, and A. G. Khorosh, Fiz. Tekh. Poluprovodn. **26**, 888 (1992) [Sov. Phys. Semicond. **26**, 500 (1992)].
[4] E. P. Skipetrov and A. N. Nekrasova, Fiz. Tekh. Poluprovodn. **31**, 257 (1997) [Semiconductors **31**, 207 (1997)].
[5] N. B. Brandt, V. N. Doropeĭ, V. P. Dubkov, and E. P. Skipetrov, Fiz. Tekh. Poluprovodn. **22**, 1462 (1988) [Sov. Phys. Semicond. **22**, 925 (1988)].
[6] B. B. Kovalev and E. P. Skipetrov, Fiz. Tekh. Poluprovodn. **24**, 1379 (1990) [Sov. Phys. Semicond. **24**, 866 (1990)].
[7] B. A. Akimov, R. S. Vadkhva, B. P. Zlomanov, L. I. Rabova, and S. M. Chudinov, Fiz. Tekh. Poluprovodn. **11**, 1077 (1977) [Sov. Phys. Semicond. **11**, 637 (1977)].

Translated by M. E. Alferieff